Attosecond spectroscopy : study of the photoionization dynamics of atomic gases close to resonances

Christina-Anastasia Alexandridi

UNIVERSITÉ PARIS SUD
Comprendre le monde, construire l'avenir

Attosecond spectroscopy: Study of the photoionization dynamics of atomic gases close to resonances

Thèse de doctorat de l'Université Paris-Saclay
préparée à l'Université Paris-Sud

École doctorale n°572 Ondes et Matière (EDOM)
Spécialité de doctorat: Milieux dilués et optique fondamentale

Thèse présentée et soutenue à Gif-sur-Yvette, le 19 décembre 2018, par

Mme Christina-Anastasia Alexandridi

Composition du Jury :

M. Pascal Lablanquie Directeur de Recherche, CNRS, UPMC (LCPMR)	Président et Rapporteur
M. Eric Constant Directeur de Recherche, CNRS, Institut Lumière Matière (iLM)	Rapporteur
Mme Amelle Zair Maître de Conférence, King's College London	Examinateur
M. Dimitris Charalambidis Professeur, University of Crete	Examinateur
M. John Bozek Maître de Recherche, SOLEIL synchrotron	Examinateur
M. Pascal Salières Directeur de recherche, CEA (LIDYL)	Directeur de thèse

ATTOSECOND SPECTROSCOPY: STUDY OF THE PHOTOIONIZATION DYNAMICS OF ATOMIC GASES CLOSE TO RESONANCES

Printed in Paris, 2018

Commissariat à l'Energie Atomique
Direction de la Recherche Fondamentale
Institut Rayonnement Matière Saclay
Laboratoire Interactions, Dynamique et Lasers
Bâtiment 522
F–91191 Gif-sur-Yvette
France

http://iramis.cea.fr/LIDYL/index.php

This thesis was typeset with the LaTeX-system and the memoir class, using a model developed by the smart people of the Atomfysik division at Lund University and modified by the previous students of the Attosecond group at CEA Saclay.

LIST OF PUBLICATIONS

The following article was published during this thesis. The full version is available at the end of the manuscript.

ABBREVIATIONS

APT	Attosecond Pulse Train
ATI	Above Threshold Ionization
CCD	Charge Coupled Device
CFT	Cumulative Fourier Transform
CM	Cooper Minimum
COLTRIMS	Cold Target Recoil Ion Momentum Scpetroscopy
EWP	Electron Wave Packet
FAB	Femtosecond-Attosecond Beamlines
FROG	Frequency Resolved Optical Gating
FT	Fourier Transform
FWHM	Full Width at Half Maximum
GVD	Group Velocity Dispersion
HE-TOPAS	High Energy Tunable Optical Parametric Amplifier
HHG	High Harmonic Generation
IAP	Isolated Attosecond Pulse
IR	Infra-Red
LDA	Local-Density Approximation
MBES	Magnetic Bottle Electron Spectrometer
MCP	Micro Channel Plate
MCHF	Multi-Configuration Hartree-Fock
MIR	Middle Infra-Red
OPA	Optical Parametric Amplifier
PECD	PhotoElectron Circular Dichroism
PLFA	Plateforme Laser Femtoseconde Accordable
RABBIT	Reconstruction of Attosecond harmonic Beating by Interference of Two-photon Transitions
RPA	Random Phase Approximation
RPAE	Random Phase Approximation with Exchange
RRPA	Relativistic Random Phase Approximation
SFA	Strong Field Approximation
STFT	Short Time Fourier Transform
TDLDA	Time-Dependent Local-Density Approximation
TDSE	Time Dependent Schrödinger Equation
TSI	Two Sources Interferometry
VMI	Velocity Map Imaging spectrometer

VUV	Vacuum Ultra-Violet
WV	Wigner-Ville
XUV	eXtreme Ultra-Violet

ABSTRACT

The interaction of intense laser pulses with atomic and molecular gases results in exceptionally short bursts of XUV light, through the process of high-order harmonic generation of the fundamental laser frequency. This ultrashort radiation, in the attosecond (10^{-18} s) range, allows detailed investigations of ultrafast electron dynamics in matter. The work of this thesis consists in studying the photoionization delays close to different types of resonances, using the Rainbow RABBIT technique. This is a two-color interferometric technique (XUV + IR) that allows access to the time required for the electron to escape the atomic potential with high resolution. We are particularly interested in two cases: i) autoionizing resonances which are spectrally narrow (tens of meV) and ii) Cooper-type minima which have a spectral width of some eV. The effect of these continuum structures on the corresponding ionization dynamics is studied.

More specifically, we investigate the sp2+ and sp3+ autoionizing resonances in helium and the 3s4p autoionizing resonance in argon. In the case of helium, we introduce different time-frequency representations of the emitted electron wave packet (EWP) such as the Gabor and Wigner representations that give more insight into the corresponding ionization dynamics. Moreover, tuning the driving laser allows us to excite simultaneously the two above-mentioned resonances in a coherent way and thus to create a complex two-electron wave packet, whose complicated dynamics is reconstructed. In the case of argon, Rainbow RABBIT allows us to resolve the spin-orbit (s-o) splitting (180 meV) in the measured spectral amplitude and phase of the resonant EWP. Furthermore, we isolate the two S-O contributions by implementing a numeric technique, allowing the reconstruction of the temporal buildup of the 3s4p resonance for the J=3/2 component.

The Cooper minimum (CM) in argon is then investigated, where we measure the difference in ionization delays between electrons emitted from the 3s and 3p shells over a large energy range (up to 68 eV) for the first time. Our measurements reveal a previously unknown change of sign of the 3s-3p delay at 41 eV, just on the edge of the spectral region of the CM in the 3s channel. A maximum delay difference is obtained at 47 eV, position of the 3p CM. These experimental results are compared with different theoretical models that predict widely conflicting results, in particular in the 3s CM that is due to inter-shell correlation, and is thus particularly difficult to simulate accurately. Our measurements thus provide stringent tests for advanced theories describing electron correlation effects.

SYNTHÈSE

L'interaction de puissantes impulsions laser avec des gaz atomiques ou moléculaires entraîne l'émission de flashs exceptionnellement brefs de lumière dans l'extrême ultraviolet (XUV) grâce au processus de génération d'harmoniques d'ordre élevé (GHOE) de la fréquence laser fondamentale. Ce rayonnement ultrabref, dans la gamme attoseconde (10^{-18} s), permet des investigations détaillées de la dynamique électronique ultra-rapide dans la matière. Le travail de cette thèse a consisté à étudier les délais de photoionisation au voisinage de différents types de résonances, en utilisant la technique Rainbow RABBIT. Il s'agit d'une technique interférométrique à deux couleurs (XUV + IR) qui permet d'accéder au temps nécessaire à l'électron pour s'échapper du potentiel atomique avec une haute résolution. Nous nous intéressons particulièrement à deux cas: i) les résonances auto-ionisantes spectralement étroites (dizaines de meV) et ii) les minima de type Cooper ayant une largeur spectrale de quelques eV. L'effet de ces structures du continuum sur la dynamique d'ionisation correspondante est étudié.

Plus précisément, nous étudions les résonances auto-ionisantes sp2+ et sp3+ dans l'hélium et la résonance auto-ionisante 3s4p dans l'argon. Dans le cas de l'hélium, nous introduisons différentes représentations temps-fréquence du paquet d'ondes électroniques (POE) émis, telles que les représentations de Gabor et de Wigner, qui permettent de mieux comprendre la dynamique d'ionisation correspondante. De plus, l'accordabilité du laser fondamental nous permet d'exciter simultanément les deux résonances susmentionnées de manière cohérente et de créer ainsi un paquet d'ondes à deux électrons, dont la dynamique complexe est reconstruite. Dans le cas de l'argon, Rainbow RABBIT nous permet de résoudre la séparation spin-orbite (180 meV) dans l'amplitude spectrale et la phase mesurées du POE résonant. De plus, nous isolons les deux contributions spin-orbite en mettant en œuvre une technique numérique, permettant la reconstruction de la dynamique temporelle de la résonance 3s4p pour la composante J = 3/2.

Nous étudions ensuite le minimum de Cooper (CM) dans l'argon, où nous mesurons la différence de retards d'ionisation entre les électrons émis par les couches 3s et 3p sur une large gamme d'énergie (jusqu'à 68 eV) pour la première fois. Nos mesures révèlent un changement de signe du retard 3s-3p à 41 eV auparavant inconnu, juste au bord de la région spectrale du CM dans le canal 3s. Une différence de retard maximale est obtenue à 47 eV, position du CM 3p. Ces résultats expérimentaux sont comparés à différents modèles théoriques, qui prédisent des résultats très contradictoires, en particulier dans le CM 3s, en raison de la corrélation inter-couches, qui est particulièrement difficile à simuler avec précision. Nos mesures fournissent ainsi des tests sévères pour les théories avancées décrivant les effets de corrélation électronique.

CONTENTS

Part I

Introduction

CHAPTER 1

INTRODUCTION

This thesis is dedicated to the study of ionization dynamics, meaning the movement of electrons as they escape their parent atom after interaction with light and the subsequent rearrangement of the electronic cloud. Monitoring these processes can give us insight into information about the atomic structure as well as features like resonances, electron-electron interaction and so on. In order to access these information we use pump-probe techniques such as the RABBIT method where we use XUV light to pump the system and then IR pulses to probe and record the induced dynamics. The idea behind the operating principle of this type of sophisticated experiments can be compared to chrono-photography.

In Figure 1.1 (a) there is one of the first photos of Paris, taken by Louis Daguerre in 1838, showing Boulevard du Temple. Even though, it is a quite busy street, the photo shows only two men near the bottom left corner, where one of them apparently is having his boots polished by the other. This is of course due to the

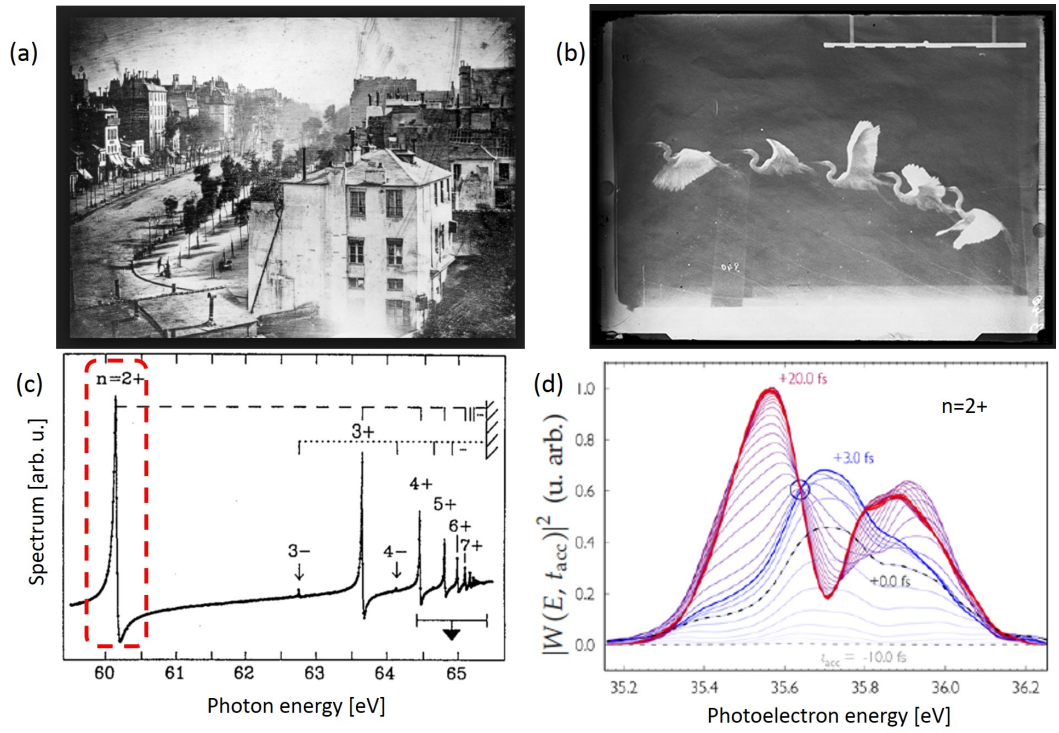

Figure 1.1: (a) Paris by Louis Daguerre (1838), (b)Flapping heron by Étienne-Jules Marey (around 1870), (c) Helium absorption spectrum with Fano resonances (1996 [Domke et al., 1996]), (d) Temporal reconstruction of the sp2+ Fano resonance in helium (2016 [Gruson et al., 2016a]).

fact that the exposure lasted for several minutes and thus the moving traffic left no trace on the photographic film, while the two men remained in one place long enough to be visible. Around 30 years later the british photographer Eadweard J. Muybridge and french physiologist Étienne-Jules Marey, introduced the idea of chrono-photography. There by using an 'ultra-fast' shutter, thus smaller exposure time, they were able to record the movement of a flapping heron as shown in Figure 1.1 (b). In their case 'ultra-fast' meant anything the human eye could no longer resolve, i.e. milliseconds (1×10^{-3}s).

In the same spirit, Figure 1.1 (c) shows the absorption spectrum of helium in a synchrotron experiment where a family of Fano resonances is visible. This is a static picture that shows only the last step/result of the autoionization process which is these asymmetric -non Lorentzian line shapes. On the other hand in Figure 1.1 (d) one can see the 'chrono-photography' of the first of these resonances and its build-up in time, which reveals the dynamics behind it. The 'exposure time' for this photo is now only some hundreds of attoseconds (1×10^{-18}s). So how did we go from millisecond down to attosecond temporal resolution?

Dynamics or movement in quantum systems arises when two eigenstates, $|\phi_1\rangle$ and $|\phi_2\rangle$, with energies differing by ΔE are superposed coherently. A beating term will appear with a half-period of $\tau = \pi\hbar/\Delta E$, giving the fundamental time-scale of dynamics between the two states. The mass of the nuclei leads to typical energy distances between vibrational states of ~10 meV, and thus the time resolution necessary to observe such dynamics is τ ~100 fs. Electronic bound states are much further apart and consequently much faster dynamics are expected. For ΔE >2 eV, the fundamental time-scale of dynamics becomes smaller than a femtosecond. Attosecond pulses that have a duration of about 100 attosecond, will thus, allow us to observe electron dynamics as demonstrated 8 years ago by Schultze *et al.* [Schultze et al., 2014], who performed the first measurement of delays between photoelectrons from different atomic orbitals. But how can we generate so short pulses?

High Harmonic Generation

In the case of a pulse with a duration of 100 as, the relation $\Delta\omega\Delta t = 4ln2$ requires that the spectrum has a width greater than or equal to 18 eV (equal if the pulse is 'Fourier limited'), the central energy must then be at least 9 eV, which falls in the region of vacuum ultraviolet (VUV: 10 - 200 nm) / extreme ultraviolet (XUV: 10 - 100 nm). One way to produce such large spectra is based on the high order harmonic generation process (HHG), especially in gases. This strongly nonlinear process is accessible thanks to the significant increase of the laser pulse energy (see the Brabec and Krausz review [Brabec and Krausz, 2000]), making it possible to achieve intensities of the order of $10^{15}W/cm^2$. Under these conditions, the electric field is comparable to the electrostatic field seen by an electron in an outer atomic orbital.

HHG in gases was discovered in the 80's, almost simultaneously by Ferray et al.

[Ferray et al., 1988] at CEA-Saclay and McPherson et al. [McPherson et al., 1987] at the University of Rochester. This highly non-linear process results from the interaction between an intense electric field, generally linearly polarized, and a set of atoms or molecules in the gas phase. The emitted spectrum can extend over several tens or hundreds of electronvolts, even up to keV (Popmintchev *et al* [Popmintchev et al., 2012]). The spectrum is composed of three parts: a so-called perturbative region, where the intensity of the harmonics produced decreases rapidly, a region called 'plateau', where the intensity of the harmonics is constant and finally the cutoff region, where the intensity decreases quickly until the signal goes out completely.

HHG in gases can be described by a semi-classical 'three-step' model (Corkum [Corkum, 1993], Lewenstein *et al* [Lewenstein et al., 1994], Schafer *et al* [Schafer et al., 1993]): tunnel ionisation of the atom into the laser field, acceleration of the ejected electron by the laser field and radiative recombination of the electron with the ionic core, with the excess energy being released in the form of an attosecond light pulse in the XUV. In a laser field with several optical cycles, the harmonic emission corresponds to a train of attosecond pulses spaced by an optical half-period, perfectly synchronized with the fundamental field (Hentschel *et al.* [Hentschel et al., 2001], Mairesse *et al.* [Mairesse et al., 2003b], Paul *et al.* [Paul et al., 2001], Tzallas *et al.* [Tzallas et al., 2003]). It is also possible to generate isolated attosecond pulses using different techniques (Sansone *et al.* [Sansone et al., 2006], Sola *et al.* [Sola et al., 2006]). The characteristics of the XUV light generated by HHG were intensively studied during the 1990's, notably in order to improve the IR / XUV conversion efficiency. The emission is coherent both spatially and temporally, in the sense that the phase of the XUV field varies regularly in space and time, with small divergence, typically a few mrad.

Attosecond science

Attosecond physics can be divided into two main categories (Salieres *et al.* [Salières et al., 2012]). The first, adapts the techniques used in femtosecond science to the attosecond scale. Thus in a pump-probe scheme, XUV attosecond pulses-isolated or in the form of a pulse train- are used to pump and/or probe the system under study. These can be atoms or molecules in the gas, liquid or solid state. There, the XUV light can excite the system to a continuum (ionization) or to a bound state (dissociation). When the pump-probe scheme uses the XUV light to photoionize the system under study, then one can access the amplitude and phase of the emitted electron wave packet with the help of interferometric techniques like: RABBIT (Muller *et al.* [Muller, 2002]), attosecond streaking (Itatani *et al.* [Itatani et al., 2002]), FROG-CRAB (Mairesse and Quéré [Mairesse and Quéré, 2005]). These type of measurements enable us to extract information about the intra-atomic/molecular dynamics.

The above techniques have served in the study of the attosecond dynamics of numerous systems (Calegari *et al.* [Calegari et al., 2014], Eckle *et al.* [Eckle et al., 2008],

Mauritsson *et al.* [Mauritsson et al., 2008], Sansone *et al.* [Sansone et al., 2010], Sola *et al.* [Sola et al., 2006], Uiberacker *et al.* [Uiberacker et al., 2007]). The RABBIT technique plays a prominent role, especially for time-resolved studies. This method was initially developed for the measurement of the spectral phase of the emitted harmonics which allows the reconstruction of the attosecond pulse train in the time domain (Paul *et al.* [Paul et al., 2001]). However it was soon shown that RABBIT could also be used to characterize the electron wave packets produced by the two-photon ionization (XUV-pump + IR-probe), of an atomic/molecular system (Mauritsson *et al.* [Mauritsson et al., 2005]). For example, in the case of photoionization in a 'flat' continuum, meaning resonance-free, the RABBIT method has allowed the extraction of the ionization delays of electron wave packets emitted from different atomic shells, showing that there is a difference of some hundreds of attoseconds between them (Klünder *et al.* [Klünder et al., 2011]).

The RABBIT technique can also be used to study the ionization delays in the vicinity of a resonance. A first study was carried out by Haessler *et al.* [Haessler et al., 2009], who studied the photoionization of the N_2 molecule near an autoionization resonance. There a phase shift of 0.9π rad has been observed for the electrons produced in the ionization channels corresponding to the $X^2\Sigma_g^+$, $v'=1$ and $v'=2$ states of the molecular ion. The authors observe that the phase of the two-photon transition amplitude varies significantly around the resonance. Later on the same group of Saclay, by using an energy-resolved version of the RABBIT method namely the Rainbow RABBIT technique were able to access the evolution of this phase in the vicinity of the sp2+ autoionization resonance in the helium atom by tuning the generation wavelength. The authors also showed that by choosing precisely the experimental parameters, it is possible to completely measure the phase variation around the resonance with a single measurement (Gruson *et al.* [Gruson et al., 2016a]). Several studies of the dynamics associated with resonances have been performed both theoretically (Chu and Lin [Chu and Lin, 2012], Morishita *et al.* [Morishita et al., 2007], Tong and Lin [Tong and Lin, 2005], Wikkenhauser *et al.* [Wickenhauser et al., 2005], Zhao and Lin [Zhao and Lin, 2005]) and experimentally (Gilbertson *et al.* [Gilbertson et al., 2010], Mauritsson *et al.* [Mauritsson et al., 2010], Ott *et al.* [Ott et al., 2013a],[Kaldun et al., 2016]). These studies have made it possible to trace back the life time of the studied resonances and confirm the experimental spectroscopic results. Furthermore, the buildup in time of such resonances becomes observable, bringing new information on the dynamics of the ionization process.

The second direction of attosecond physics, is Harmonic spectroscopy developed notably at CEA-Saclay. Like classical linear or weakly nonlinear spectroscopy, strongly nonlinear harmonic spectroscopy extracts information about the radiating system by characterizing completely, in amplitude, in phase and in polarization, the harmonic emission induced in the system by a fundamental laser pulse. High Harmonic spectroscopy can act as a probe in the time-resolved studies mentioned in the previous paragraphs, with the pump being supplied independently by a first pulse. High Harmonic spectroscopy can also be considered as a variant of the pump-probe scheme, when one wants to study in particular the dynamics in-

duced by strong field ionization. To better understand this, let's take the three-step model. The first step is the pump pulse that induces tunnel ionization of the system. The excursion of the electron wave packet into the continuum can be seen as the pump-probe delay, during which the ionized system evolves. Finally, the radiative recombination of the electron wave packet with the parent ion acts as an ultrashort probe. This 'self-probe' scheme then makes it possible to extract information on the structure and/or the dynamics of the tunnel ionization and the ionized system. Many studies have been performed using this technique revealing rotational dynamics (Jin *et al.* [Jin et al., 2012], Levesque *et al.* [Levesque et al., 2007a], Vozzi *et al.* [Vozzi et al., 2005]), vibrational nuclear dynamics (Li *et al.* [Li et al., 2008], Wagner *et al.* [Wagner et al., 2006]) or even dissociation dynamics (Haessler *et al.* [Haessler et al., 2009], Tehlar *et al.* [Tehlar, 2013], Worner *et al.* [Wörner et al., 2010], Mairesse *et al.* [Mairesse et al., 2010], Cireasa *et al.* [Cireasa et al., 2015], Bruner *et al.* [Bruner et al., 2016]).

Harmonic spectroscopy also provides access to the ultra-fast electron dynamics, for example by following the evolution of the spatial structure of an electronic valence orbital in the ion. The reconstruction of molecular orbitals was originally proposed by Itatani *et al.* [Itatani et al., 2004]. It is based on the fact that the electron wave functions of the highest occupied orbitals (HOMO) involved in the HHG, are contained in the recombination dipole. In the case of small linear molecules that we are able to laser-align, we can then reconstruct not only the time-dependent orbital in the molecular ion, but also the HOMO stationary orbitals that have been ionized. Several experiments have indeed allowed the reconstruction of the HOMO of N_2 (Haessler *et al.* [Haessler et al., 2010]) and CO_2 (Vozzi *et al.* [Vozzi et al., 2012]) from the measurement of the amplitude and the spectral phase of the harmonic emission from these molecules.

Thesis Outline

The aim of the work presented in this thesis is to enrich our knowledge regarding the atomic photoionization dynamics in the presence of strong structural features as well as to assess and improve the existing theoretical models. As it will be detailed later on, the presence of a resonance can alter significantly the ionization dynamics of a system as well as the interpretation of the measured ionization time delays. The studied structures were the Fano autoinizing resonances and the Cooper minimum. Both are the result of different physical processes and involve inter- and intra-shell electron correlation effects. Fano resonances have a spectral width of some tens of meV on the contrary, Cooper minimum (in argon) is a feature that spreads along almost 15 eV. By using the Rainbow RABBIT interferometric technique we were able to measure the corresponding ionization delays in both cases showing also the robustness and versatility of the technique. The manuscript is organized as follows:

In the first part we give an overview of both the theoretical background of the HHG process, which is the tool, and the photoionization dynamics which is the subject of study. In Chapters 2, we present the simple semi-classical model that accounts for

the main characteristics of the harmonic radiation that are also detailed, as well as its more complex quantum-mechanical counterpart. In Chapter 3 a detailed description of the fundamental concepts of collision theory necessary to interpret Wigner's photoionization delays, is conducted. Then a connection with the delays measured by RABBIT interferometry is discussed.

The second part consists of the description of our experimental tools. Chapter 4 details the technical aspects of the two beam-lines used in our experiments, the one in AttoLab and the one in Lund University. Further on, in Chapter 4.1, we explain in detail the Rainbow RABBIT method and compare with the standard RABBIT technique.

The last part includes the experimental work on Fano resonances and the Cooper minimum. In Chapter 6 we first discuss the results of the study of the sp2+ Fano resonance in helium. Its transition amplitude and phase measured by the Rainbow RABBIT method allow us to reconstruct the dynamics of the ejected EWP (Electron Wave Packet) from the Fano resonance in the time domain and different representation methods were also explored. The intensity dependence of the EWP's phase and line shape of the resonance is studied. The dynamics of the complex EWP resulting from simultaneous excitation of the sp2+ and the next Fano resonance, namely the sp3+, is also presented. The 3s4p Fano resonance in argon was also studied where the resolution in the measured spectral phase of the two spin-orbit components was achieved. These measurements were carried out in collaboration with the team of Anne L'Huillier in Lund University, Sweden.

Finally, Chapter 7 presents the results of the first experiment performed in Attolab, CEA-Orme des merisiers, where the ionization delay differences between the 3s and 3p ionization channels of argon are measured in a large energy range including the effect of the Cooper minima on both channels. These results are then compared with various theories.

MEDEA project

This thesis work has been a part of the MEDEA network (MEDEA) . MEDEA is a Marie Skłodowska-Curie Innovative Training Networks (ITN-ETN) funded in the framework of the HORIZON 2020 program. The main objective of MEDEA is to create a platform where Early Stage Researchers receive an interdisciplinary and intersectoral comprehensive research training in one of the major field of Photonics that is contributed by leading universities and research centers, and by keyplayer companies in the development and commercialization of state-of-the-art ultrafast laser sources and detection systems.

Part II

Theoretical background

CHAPTER 2

HIGH HARMONIC GENERATION

High order Harmonic Generation (HHG) is a strong field, highly non-linear phenomenon observed for the first time in 1987 by McPherson *et al* [McPherson et al., 1987] and Ferray *et al* [Ferray et al., 1988]. By submitting an atomic or molecular gas to a laser field with high enough intensity and in good phase matching conditions, the generation of harmonics that are odd multiples of the driving field's frequency can be observed. It is this phenomenon of HHG that served as the basic tool for the photoionization studies of this thesis. In this part, we are going to display the main theoretical aspects of this non-linear process starting with the microscopic interpretation of the effect and continuing with the macroscopic conditions necessary for this process to take place.

2.1 Microscopic effects

2.1.1 Semi-classical approximation: *The three-step model*

The semi-classical model of high order harmonic generation was proposed in 1993 by Schafer *et al.* [Schafer et al., 1993] and Corkum [Corkum, 1993] and allows a qualitative understanding of the phenomenon. Briefly, the interaction between an intense laser field and an atom or a molecule distorts the potential felt by the electrons of the system. An electron wave packet (EWP) can then be emitted by tunnel ionization (1). Then the released EWP is accelerated by the laser field (2) and finally, when the field changes sign, the wave packet is brought back to the parent ion with which it can recombine by emitting the accumulated kinetic energy in the field, in the form of an extreme ultraviolet (XUV) photon (3). In the following, these three different stages are going to be detailed.

1. Tunnel ionization Let us consider an isolated atom in its ground state. An electron in this state is subjected to the Coulomb potential of the nucleus, $V_0(x) = -1/|x|$, where x is the distance between the electron and the nucleus (Figure 2.1 (a)). In the presence of a linearly polarized (along the x-axis, $\hat{x}$) electric field $E(t) = E_0 cos(\omega t)\hat{x}$ with angular frequency ω, the total potential V(x,t) felt by the electron will become:

$$V(x,t) = V_0(x) + xE(t) \tag{2.1}$$

There are different schemes of ionization due to the influence of the laser. The electron can be ionized from the simultaneous absorption of several photons corre-

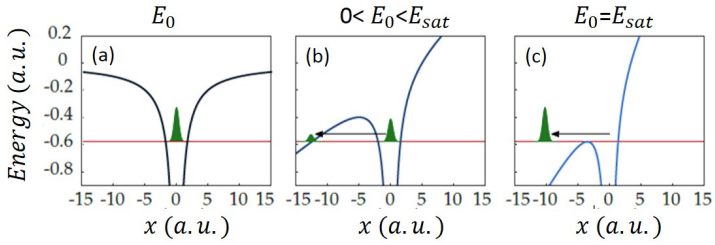

Figure 2.1: Potential felt by an electron in argon, Ip = 15.76 eV = 0.58 a.u., in the absence of an electric field (a), in the presence of a field E_0= 0.04 a.u. (I = $5.5\times10^{13} W/cm^2$) (b) and in the presence of a field at the saturation illumination of argon $E_0 = E_{sat}$ = 0.084 a.u. (I = 2.4 $\times10^{14} W/cm^2$) (c). Adapted from Ref. [Barreau, 2017].

sponding to an energy greater than the ionization potential, which is referred to as multi-photon ionization. If the absorbed number of photons is larger than the minimum number required to reach the ionization threshold, Above Threshold Ionization (ATI) takes place. When the electric field is comparable to the binding electric field between the nucleus and the electron, it distorts the potential. This "intra-atomic" field can be estimated as $E_{atom} = \frac{e}{4\pi\epsilon_0 a_0^2} \sim 5\times10^{11} V/m$ that corresponds to an intensity of $I_{atom} \sim 3.5\times10^{16} W/cm^2$, where a_0 is the Bohr radius, ϵ_0 is the vacuum permeability and e the charge of the electron. Thus, in the presence of an intense laser field of the order of $I \sim 10^{14} W/cm^2$, the interaction with the electric field is no longer perturbative. In that case, the laser field lowers the potential barrier felt by the electron and part of the EWP can cross it by tunneling with a probability that depends on its height and width, as well as the time that the barrier is lowered (Figure 2.1 (b)). In the extreme case of Figure 2.1 (c), the laser field is intense enough to completely remove the potential barrier [Augst et al., 1989],[Bauer and Mulser, 1999]. Ionization will be completed when the potential barrier is fully suppressed, below the fundamental energy of the electron, meaning that for x < 0 :

$$\frac{\partial V}{\partial x} = -\frac{1}{x^2} + E_0 = 0 \tag{2.2}$$

The maximum of the barrier is obtained when $\frac{\partial V}{\partial x} = 0$, which results in $x_m = -1/\sqrt{E_0}$ and writes $V(x_m) = -2\sqrt{E_0} = -I_p$. Thus the intensity needed to suppress the potential barrier will be :

$$I_{sat} = \frac{I_p^4}{16}$$
$$I_{sat}[W/cm^2] = 4\times10^9 I_p^4[eV] \tag{2.3}$$

The various saturation intensities for different gases commonly used in HHG are listed in Table 2.1.1. For the HHG process to be effective, the laser intensity must

be lower than the saturation intensity so that the ground state is not completely "emptied".

	I_p [eV]	I_{sat} $[W/cm^2]$
He	24.58	14.62
Ne	21.56	8.65
Ar	15.76	2.47
Kr	14.00	1.54
Xe	12.13	0.87

Table 2.1: Ionization potential I_p and saturation intensities I_{sat} for different gases, commonly used in HHG.

The image above, for a quasi-static field should be complemented in the case of an oscillating laser field due to the fact that tunnel ionization also depends on the time during which the barrier is lowered, proportional to the laser field. To distinguish various ionization regimes of the light matter interaction, we then introduce the Keldysh parameter [Keldysh et al., 1965]:

$$\gamma = \sqrt{\frac{I_p}{2U_p}} = \omega\frac{2I_p}{I} = \frac{T_{tunel}}{T}, \tag{2.4}$$

where I_p is the ionization potential, I = E^2 is the intensity of the laser field, $U_p = E^2/4\omega^2 \propto I\lambda^2$ is the ponderomotive potential, i.e. the mean quiver energy of a free electron in the laser field. $T_{tunnel} = 2\pi\frac{\sqrt{2m_eI_p}}{eE}$ is the ionization time needed for an electron to cross the Coulomb barrier, and the period of the oscillation, $T = 2\pi/\omega$. When $\gamma < 1$ we are in the tunnel ionization regime. For example, in the case of argon with a laser field centered at 800 nm and of intensity $2\times10^{14}W/cm^2$ it will be: U_p=12 eV and γ= 0.8. This falls well in the tunnel ionization regime.

2. Acceleration by the laser field After the tunnel ionization process, the electron is found in the continuum, accelerated by the linearly polarized laser field $E(t)$. At this point, it is assumed that its dynamics is governed only by the laser field which is strong enough that allow us to neglect the effect of the long-range tail of the atomic potential. Due to the strength of the laser field we can use a classical description of the EWP's dynamics. The only force acting on the electron now is the Lorentz force and thus the equation of motion is then written as:

$$m\ddot{x} = -eE_0cos(\omega t) \tag{2.5}$$

For the initial conditions, we note as t_i the moment when the EWP is ionized, and we suppose that $x(t_i) = 0$ and $\dot{x}(t_i) = 0$, meaning that we neglect the movement across the barrier and that all its kinetic energy is lost while crossing the barrier. By integrating equation 2.5 we obtain:

$$\dot{x}(t) = u(t) = -\frac{eE_0}{m\omega}[sin(\omega t) - sin(\omega_{ti})] \tag{2.6}$$

and

$$x(t) = \frac{eE_0}{m\omega^2}[cos(\omega t) - cos(\omega t_i)] + \frac{eE_0}{m\omega} sin(\omega t_i)(t - t_i) \tag{2.7}$$

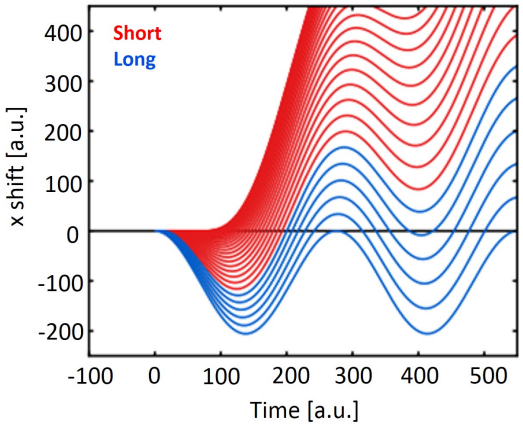

Figure 2.2: Electron oscillation after ionization driven by the laser field. Adapted from [Schoun, 2015]

From equation 2.7, we obtain the electron trajectories corresponding to different ionization times t_i, as shown in Figure 2.2. For ionization times such that ωt_i corresponds to [0, π / 2] and [π, 3 π / 2], the electron follows a closed path and returns to the origin. For ωt_i corresponding to [π / 2, π] and [3π / 2,2π], the electron drifts away and does not return to the parent ion. Moreover, some trajectories indicate several recollisions. However the spreading of the EWP, increases with time so that it reduces the importance of the later collisions. Phase matching effects also decrease the contribution of longer trajectories to the macroscopic signal. Therefore, we only consider the first recollisions.

3. Recombination The last step is the "radiative" recombination of the electron with the parent ion, converting the kinetic energy E_k of the EWP into a high energy photon $\hbar\omega = I_p + E_k$. In recombination, we associate a recombination time t_r, obtained as a function of the ionization time t_i by solving the equation $x(t) = 0$ from equation 2.7. This recombination time t_r makes it possible to go back to the energy $E_k = mu^2(t_r)/2$. Figure 2.3 shows the evolution of E_k as a function of time, for different pairs of (t_i, t_r). This curve makes it possible to extract the maximum energy that an electron acquires, and thus a photon can have:

$$\hbar\omega_{max} = I_p + 3.17U_p \tag{2.8}$$

This is the so-called cut-off law and was first determined empirically by Krause *et al.* [Krause et al., 1992]. The expression 2.8 of the maximum energy, known as the cutoff energy, indicates that the extent of the HHG spectrum depends on the medium (I_p) but also the intensity and wavelength of the laser via $U_p \propto I\lambda^2$. By increasing the intensity, the position of the cut-off is shifted; however, one is quickly limited by the saturation intensity I_{sat} of the ionized medium. One can then increase the driving laser's wavelength towards the midIR, for example at 3.9 nm which will

shift the position of the cut-off energy at 1.6 keV. However, this increase of the spectrum is accompanied by a decrease of the generation efficiency. By increasing the wavelength, the time spent by the electron in the continuum is increased. The associated wave packet will therefore spread spatially decreasing the recombination efficiency. The λ dependence of the generation efficiency is not yet fully characterized, but the different simulations / experiments indicate an evolution in $\lambda^{-(5-9)}$ [Shan and Chang, 2001], [Tate et al., 2007], [Popmintchev et al., 2009], [Shiner et al., 2009]. By optimizing the phase matching, it is possible to go towards a λ^{-2} dependency [Popmintchev T.].

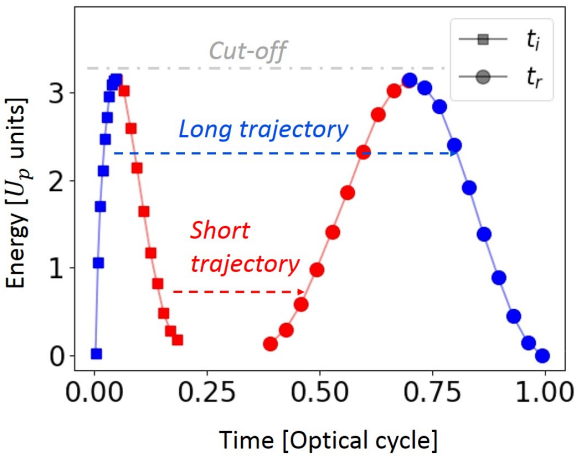

Figure 2.3: Kinetic energy at recollision as a function of the ionization (squares) and recombination times (circles) calculated by the semi-classical model, for a driving pulse centered at 800 nm with I= $2.5\times10^{14} W/cm^2$. Two examples of short (red) and long (blue) trajectories are given. The position of the cut-off is plotted in grey.

In Figure 2.3 we observe two pairs of (t_i, t_r) that correspond to two different trajectories leading to the same kinetic energy. These trajectories are called short and long trajectory, respectively. The first corresponds to short propagation times in the continuum, which increases with the harmonic order. The second corresponds to the case where the electron is ionized near the maximum of the electric field and has a propagation time which decreases with the harmonic order. The harmonics emitted during these different trajectories have distinct properties, which will be detailed later.

High order Harmonic spectrum This three-step process is repeated coherently at each extreme of the electric field, thus each half-cycle with a change of sign of the induced dipole. It therefore, has a periodicity of $T/2$, where T =$2\pi/\omega$ is the period of the generation laser. This temporal periodicity is reflected in the spectral domain by a periodicity of 2ω. Due to the centro-symmetric nature of the generation medium, only the odd harmonics are emitted. Thus, for a sufficiently long laser pulse (several cycles), the spectrum obtained consists of a comb of odd harmonics separated by 2ω as shown in Figure 2.4.

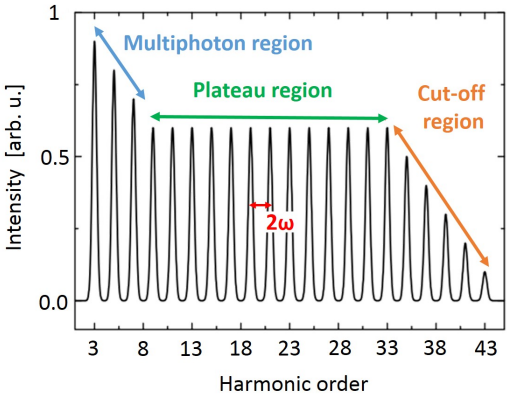

Figure 2.4: Schematic visualization of a high order harmonic spectrum [Salières and Lewenstein, 2001].

In this model, the step of tunnel ionization is treated quantum mechanically, while the dynamics of the free electron in the field are treated in a classical way, hence its 'semi-classical' name. In this way we have a simple picture of the process which allows access to important quantities such as cutoff energy and ionization and recombination times. However, the HHG process is the result of the interference between part of the ionized EWP and its remaining part in the ground state. Thus, in order to study this process in detail and verify the validity of the semi-classical model, it is necessary to compare it to a more rigorous fully quantum mechanical model.

2.1.2 Quantum mechanical description: the model of Lewenstein

The quantum mechanical treatment of the HHG process was developed in 1994 by Maciej Lewenstein [Lewenstein et al., 1994]. This model justifies the assumptions used before in the semi-classical model and allows to take into account quantum effects such as tunnel ionization, the diffusion of the EWP and interferences between quantum paths. Here we briefly describe the basics of this model.

We consider an atom in the approximation of a single active electron interacting with the laser field $\vec{E}(t)$ linearly polarized along the $\hat{x}$ direction. The electronic dynamics is described by the Schrödinger equation (in atomic units):

$$i\frac{\partial}{\partial t}|\psi(\vec{x},t)\rangle = \left(-\frac{1}{2}\nabla^2 + V_0(\vec{x}) - E_0 x cos(\omega t)\right)|\psi(\vec{x},t)\rangle \tag{2.9}$$

In the Strong Field Approximation (SFA), one makes the following assumptions:
1. Among the bound states, only the ground state contributes to the high-order harmonic radiation. The other bound states are neglected.
2. The depletion of the ground state is considered negligible in the first step.

3. The electrons in the continuum states are seen as free electrons that are only affected by the laser field, and ignore the Coulomb potential of the ionic core.

This allows to calculate the wavefunction $\psi(x,t)$, and then the dipole moment $x(t) = \langle\psi(t)|x|\psi(t)\rangle$. This model gives the $x(t_r)$ at the moment of recombination as:

$$x(t_r) = i\int_0^{t_r} dt_i \int d^3\vec{p}\ \underbrace{\vec{d}^{\,*}_{\vec{p}+\vec{A}(t_r)}}_{C}\ \underbrace{e^{iS(\vec{p},t_i,t_r)}}_{B}\ \underbrace{\vec{E}(t_i)\,\vec{d}_{\vec{p}+\vec{A}(t_i)} + c.c.}_{A}, \tag{2.10}$$

where $\vec{p}$ is the canonical momentum, $\vec{d}$ is the dipole matrix element for bound-free transitions and $\vec{A}$ is the vector potential associated with electric field $\vec{E}$. $S(\vec{p},t_i,t_r)$ is the quasi-classical action. The effects of the atomic potential are assumed to be small between t_i and t_r so that $S(\vec{p},t_i,t_r)$ actually describes the motion of an electron freely moving in the laser field with a constant momentum $\vec{p}$.

Equation 2.10 recovers and justifies the semi-classical three-step model. More specifically:

A First, $\vec{E}(t_i)\,\vec{d}_{\vec{d}+\vec{A}(t_i)}$ represents the probability amplitude for the laser-induced transition to the continuum state with momentum $\vec{p}$ at time t_i.

B Next, the EWP gains kinetic energy during the laser oscillation and acquires an extra phase:

$$S(\vec{p},t_i,t_r) = -\int_{t_i}^{t_r}\left(I_p + \frac{(\vec{p}+\vec{A}(t))^2}{2}\right)dt \tag{2.11}$$

.

C Finally, $\vec{d}^{\,*}_{\vec{p}+\vec{A}(t_r)}$ indicates that the electronic wave function eventually recombines to the ground state at time t_r and releases the energy in the form of photon emission.

The Fourier transform of equation 2.10 will be:

$$x(\Omega) = \int dt_r \int dt_i \int d^3\vec{p}\, b(t_r,t_i,\vec{p})\, e^{\overbrace{[iS(\vec{p},t_i,t_r)+i\Omega t_r]}^{i\phi_\Omega(\vec{p},t_i,t_r)}} \tag{2.12}$$

In this expression, the sum is performed on all the ionization, recombination times and all the canonical momenta, meaning on all the electronic trajectories. This enormous number of possible paths makes the calculation difficult. The calculation is simplified if the sum is only made on the trajectories that contribute significantly to the emission. In order to determine these contributions, the saddle point approximation is applied. The phase of the integral in expression 2.12 varies much faster

than its amplitude. For a path whose phase varies very rapidly, the various contributions cancel out in the sum, making the contribution of this path negligible. The main trajectories then correspond to the points where the phase does not vary along the three variables $\vec{p}$, t_i and t_r. This condition results in the following equations:

$$\frac{\partial \phi_\Omega(\vec{p},t_i,t_r)}{\partial t_i} = I_p + \frac{(\vec{p}^2 + \vec{A}(t_i))^2}{2} = 0 \tag{2.13}$$

$$\frac{\partial \phi_\Omega(\vec{p},t_i,t_r)}{\partial t_r} = -I_p - \frac{(\vec{p}^2 + \vec{A}(t_r))^2}{2} + \Omega = 0 \tag{2.14}$$

$$\nabla_{\vec{p}} \phi_\Omega(\vec{p},t_i,t_r) = -x(t_r) + x(t_i) = 0 \tag{2.15}$$

These three conditions correspond to the assumptions made in the semi-classical description of the HHG: equation 2.15 states that the dominating quantum paths correspond to closed trajectories. Equation 2.13 means the kinetic energy of the tunneling electron is negative at the ionization time t_i so that the real part of the initial velocity is 0, as it is foreseen by the classical description. This imaginary-valued velocity can be obtained if t_i is complex, which can be seen as a trace of the tunnel ionization process [Zhao and Lein, 2013]. This has important consequences since all quantities will then be complex. In particular, the imaginary part of the action will give the well known Keldysh exponential factor characteristic of tunnel ionization. Finally, equation 2.14 implies that the energy of the emitted photon is the sum of the electron kinetic energy and the binding energy, which corresponds to the energy conservation law at recombination. By solving these three equations we get triplets of $(\vec{p}, t_i, t_r)$, from which we find the relation between t_i, t_r and the photon energy, as plotted in Figure 2.5.

The simple semi-classical model turns out to be in reasonable agreement in the plateau region but, obviously, the more rigorous quantum mechanical calculation yields a more precise description, i.e. the quantum calculation leads to the generation of more high harmonic orders than the classical simulation by taking the effects of quantum tunneling and quantum diffusion into account [Lewenstein et al., 1994]. The cutoff energy given by the quantum calculation is $E_{max} \approx 3.17U_p + 1.32I_p$, for $I_p \ll U_p$.

2.1.3 HHG Temporal structure

In the previous paragraphs, we have seen that the harmonic emission in the spectral domain, is made of a large number of frequencies, odd multiples of the fundamental laser frequency. The spectral bandwidth emitted, supports pulses with attosecond duration [Farkas and Tóth, 1992] [Harris et al., 1993], if all emitted spectral components have the proper phase relationship. Here we consider a spectrum composed of N monochromatic harmonics of spectral amplitude $\mathcal{E}_n$ and spectral phase ϕ_n. The temporal profile of the emission is then written as :

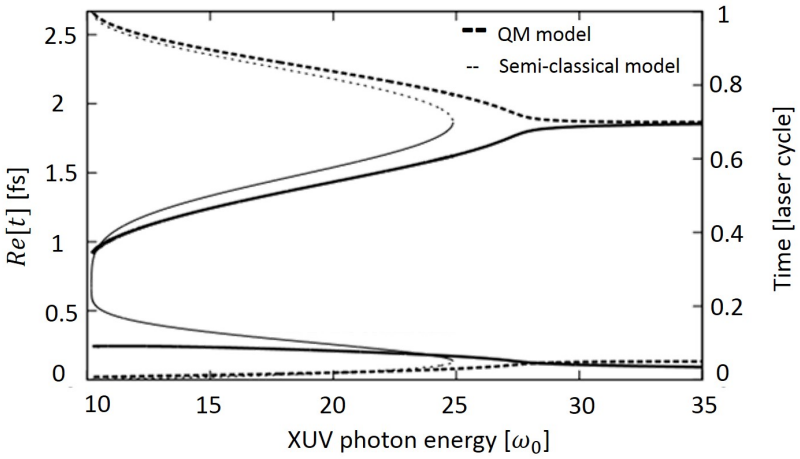

Figure 2.5: Ionization and recombination times as a function of the photon energy. Thick and thin lines correspond to quantum and classical calculations respectively. Full and dashed lines mark the short and long trajectories. The calculation was performed in argon with I_p=15.76 eV with a laser centered at 800 nm and intensity I=1.2×$10^{14} W/cm^2$. The trajectories are calculated by Thierry Auguste.

$$I(t) = \left| \sum_{n=1}^{n} \mathcal{E}_n e^{-in\omega t + i\phi_n} \right|^2 \tag{2.16}$$

If ϕ_n is constant for every n, the pulse is Fourier transform limited. Its duration is then minimal given its spectral width. This case is illustrated in Figure 2.6: the pulse corresponding to a harmonic spectrum of total bandwidth N where each harmonic has a width $\delta\omega$, is an attosecond pulse train. The temporal width of the train is $1/\delta\omega$, and each pulse in the attosecond pulse train has a duration of $1/N$. If ϕ_n is linear with n, the time profile is the same as before, but has a temporal offset of $t_e = \partial\phi_n/\partial\omega$, this group delay is also called "emission time". If ϕ_n has another behavior, then the pulse is longer than the duration given by the Fourier limit. In that case the different spectral components of the pulse are not emitted at the same time. $t_e(\omega_n)$ is then the group delay associated with the frequency ω_n. In the extreme case where the phase between each harmonic is random, the light emission becomes continuous. Therefore in order, to study the harmonics and the attosecond pulses it is important to know the spectral phase.

Two types of spectral phases are to be considered: the phase relationship between consecutive harmonics that influences the pulses duration in the train, and the spectral phase of a given harmonic which globally modifies the train. These two phases are responsible for the attosecond frequency derivative, the so-called attochirp and the harmonic frequency derivative also called harmonic/femto-chirp , respectively.

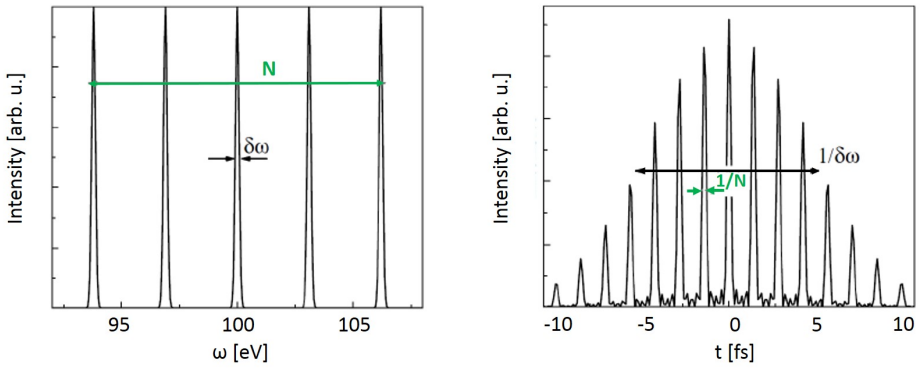

Figure 2.6: Temporal structure of a Fourier limited harmonic comb. Taken from [Mairesse, 2005] .

2.1.4 Attosecond temporal structure: Attochirp

The two models presented previously show that the different harmonics are not emitted at the same time (Figures 2.5 and 2.3) where for short/long trajectories, high energies are emitted after/ before the low energies. Ref. [Mairesse, 2005] shows that $t_e(\omega_n)$ is directly connected to the recombination time $t_n(\omega_n)$. As part of the Lewenstein model, the variation of t_e with the harmonic order is linear in the plateau, with an opposite slope for both families of trajectories, and constant in the cut-off. So, provided that we have selected a type of trajectories, the harmonic phase is quadratic in the plateau and linear in the cut-off. This spectral phase can be measured (e.g. with the RABBIT method described later in the thesis), and the measurement for the short trajectories are in very good agreement with the theoretical model (Figure 2.7) [Mairesse et al., 2003a], [Mairesse et al., 2004]. The attochirp is intrinsically linked to the HHG process: in a half cycle, the frequencies emitted correspond to different electronic trajectories and are therefore not synchronized.

The attochirp in the plateau corresponds to a quadratic spectral phase and therefore to a temporal widening of the attosecond pulses in the train. However, we note that by selecting spectrally only the harmonics of the cut-off region, whose spectral phase is linear, makes it possible to obtain Fourier limited pulses but whose duration can not be very short due to the exponential decay of the harmonic intensity. Note that this linear group delay can be partially compensated if the pulse is propagated through a metallic filter of opposite group delay. This method can be used to compress the attosecond pulses [López-Martens et al., 2005], [Gustafsson et al., 2007]. The shortest pulse measured up to now is 43 as by Gaumnitz *et al.* [Gaumnitz et al., 2017]. Another possible method used for the compression of this group delay is the use of chirped mirrors [Morlens et al., 2005], [Bourassin-Bouchet et al., 2011].

In Figure 2.7 (a) Mairesse *et al.* [Mairesse et al., 2004] measured the effect of the driving laser intensity on the attochirp. There, the slope $t_e(\omega_n)$ decreases as the intensity increases in the case of short trajectories. This can be simply explained by

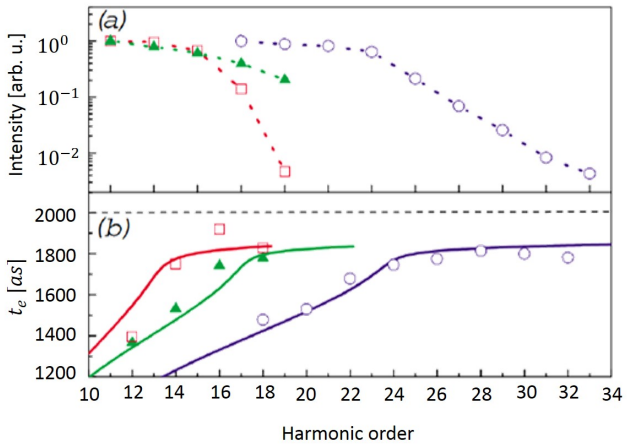

Figure 2.7: (a) Intensity and (b) emission time of harmonics generated in xenon at $3 \times 10^{13} W/cm^2$ (red) and $6 \times 10^{13} W/cm^2$ (green), and in argon at $9 \times 10^{13} W/cm^2$ (blue). RABBIT measurements are shown in symbols and the continuous lines correspond to the recombination times for the calculated short trajectory with the Lewenstein model. Taken from [Mairesse et al., 2004].

the cut-off law where $U_p \propto I$. Thus, as the intensity increases the cut-off energy increases and thus the slope of $t_r(\omega_n)$ decreases as the absolute value of $t_e(\omega_n) \propto 1/I$ for both trajectory families. The generation of shorter attosecond pulses is therefore favored at high intensity.

2.1.5 Femtosecond temporal structure: Harmonic chirp

For a given harmonic, the spectral phase of a trajectory j is given by the following dipole phase:

$$\phi_n^j = \omega_n t_r^j - \int_{t_i^j}^{t_r^j} I_p + \frac{(\vec{p}^{\,j} + \vec{A}(t))^2}{2} dt \tag{2.17}$$

The second term represents the phase accumulated by the EWP along the considered path and depends on the laser intensity through the vector potential $\vec{A}(t)$. Figure 2.8 (a) shows SFA calculations for the intensity dependence of the phase of harmonic 19 for both trajectories. For a low intensity, harmonic 19 is in the cut-off region and thus the two trajectories are mixed. For both trajectories, ϕ_n^j is approximately linear with the intensity with a proportionality coefficient dependent on the considered trajectory, $\phi_n^j = -\alpha_n^j \times I$ with $\alpha_n^{short} \ll \alpha_n^{long}$.

In the HHG process with a femtosecond laser pulse, the laser intensity varies at the scale of the envelope $I(t)$, which implies a modification of the dipole phase. The harmonic femtosecond emission is thus not Fourier limited but has a chirp proportional to α_n [Salières et al., 1995]. This harmonic chirp is intrinsically linked to the variation of the laser intensity at the femtosecond envelope scale. From a

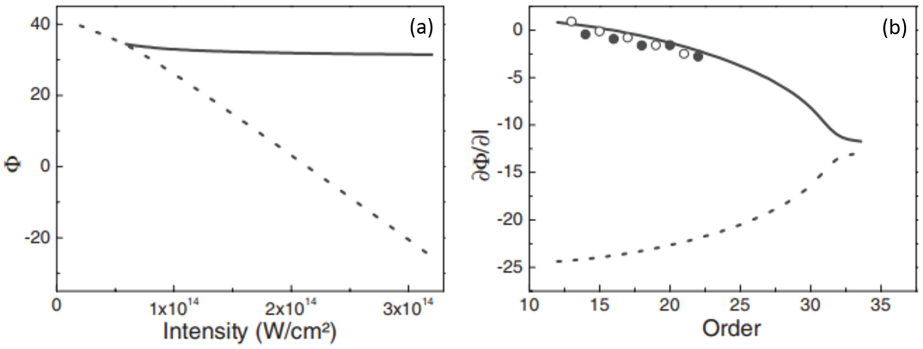

Figure 2.8: SFA calculations (a) Variation of the phase ϕ_n^j with the laser intensity for H19 generated in argon by 800 nm. (b) Variation of $\partial\phi_n^i/\partial I = -\alpha_n^j$ as a function of the harmonic order for $1.5 \times 10^{14} W/cm^2$. The short trajectory is in solid line and the long trajectory in dashed lines. Taken from [Varjú et al., 2005].

half-cycle to the other, the electron trajectories leading to the emission of a photon with a given energy, are modified. Within the attosecond pulse train, one observes a change in the spacing of the pulses in the train [Varjú et al., 2005]. In practice, atto- and harmonic- chirp are both present, as shown in Figure 2.9.

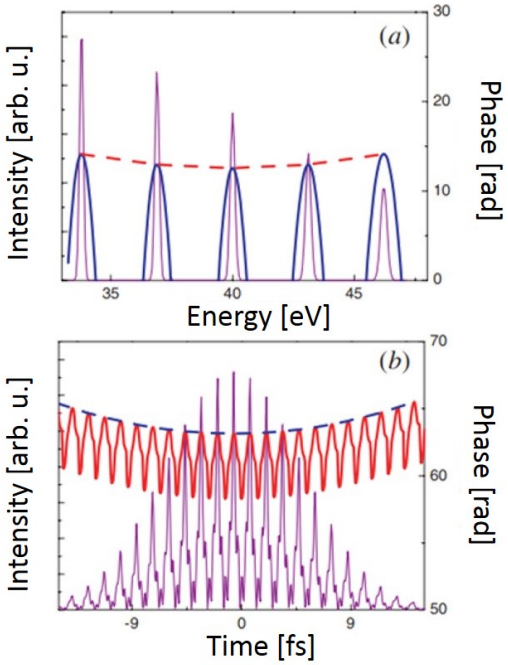

Figure 2.9: Illustration of the simultaneous presence of harmonic and attochirps in the spectral and temporal domains. (a) Spectral intensity (purple, left scale) and phase (solid blue, right scale) for a group of 5 harmonics of slowly decreasing amplitudes. The dashed red line connects the phases at the central harmonic frequencies. (b) Corresponding temporal intensity (purple, left scale) and phase (solid red, right scale). The dashed blue line connects the phases corresponding to the peaks of the attosecond pulses. Taken from [Varjú et al., 2005].

The chirp is very different for the two trajectories, since α_n^j is very different for short trajectories and long. For a given harmonic, the contribution of the long trajectory will present a much larger spectral broadening than that of the short trajectory, which makes it possible to differentiate these two contributions with a spectrometer [Zaïr et al., 2008]. Moreover, for a Gaussian beam, the intensity also presents a radial modulation $I(r)$. The intensity dependence of the induced dipole phase is also different for short and long trajectories. For the lowest harmonics, the short trajectories have a divergence much lower than the long ones [Bellini et al., 1998]. When the harmonic order increases, the divergence of short/long trajectories increases/decreases until they mix at the cut-off.

2.2 Macroscopic effects

The spatio–temporal characteristics of XUV pulses produced via HHG, depend not only on the single atom response, but are affected by amplitude and phase variations across the three dimensional nonlinear medium. Macroscopic aspects of the HHG process, including dispersion, absorption and phase matching effects, commonly denote effects arising from the propagation of the XUV field and the generating laser field along the optical axis $\hat{z}$ through the nonlinear medium.

As illustrated in Figure 2.10, if the different microscopic contributions are not in phase, destructive interference will prevent the efficient XUV emission in a specific direction (1D approach). Let us consider the propagation equation of the total harmonic field $\vec{E}(r,t) = \sum_n \mathcal{E}_n e^{i(\vec{k}_n \cdot \vec{r} - n\omega t)}$ in the P_n^{NL} non-linear polarization medium. In the paraxial and slowly varying envelope approximations (which consists of the assumption that the temporal variations of the envelope of the IR probe field are negligible at the optical cycle scale), we have:

$$\Delta_\perp \mathcal{E}_n + 2ik_n \frac{\partial \mathcal{E}_n}{\partial z} = -\frac{n^2\omega^2}{\epsilon_0 c^2} P_n^{NL} e^{i(n\vec{k}_1 - \vec{k}_n)z} \tag{2.18}$$

The phase mismatch is given by the quantity $\Delta\vec{k}(n) = n\vec{k}_1 - \vec{k}n + \nabla \arg[P_n^{NL}]$. This last term contains the variation of the nonlinear dipole phase (equation 2.17) in the medium (in particular due to the geometric variation of the laser intensity in the focal region).

The influence of phase mismatching on the HHG can be demonstrated simply by a one-dimensional model. For $\mathcal{E}_n(z)$, the harmonic signal S_n is the coherent sum on all the atoms of the medium of length L:

$$S_n \propto \left| \int_0^L x_n e^{i(\Delta k + i\eta_n)(L-z)} \rho dz \right|^2, \tag{2.19}$$

where x_n is the dipole amplitude corresponding to harmonic n, ρ the density and η_n the absorption coefficient of the medium at the energy of harmonic n. If x_n, Δ, ρ and η_n do not depend on z, S_n becomes [Constant et al., 1999], [Heyl, 2014]:

$$S_n \propto |d_n|^2 \, e^{-\eta_n L} \frac{cosh(\eta_n L) - cos(\Delta k L)}{\Delta k^2 + \eta_n^2} \tag{2.20}$$

Finally, for $\eta_n \to 0$ we get:

$$S_n \propto |d_n|^2 \, L^2 \left(\frac{sin(\Delta k L/2\pi)}{\Delta k L/2\pi} \right) \tag{2.21}$$

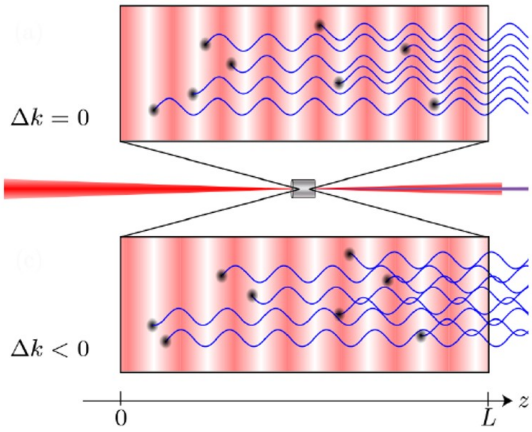

Figure 2.10: Phase-matched (first row) and non phase-matched (second row) harmonic generation, illustrated using the example of second harmonic generation. The red shading indicates the fundamental field. Taken from [Heyl, 2014] .

For $\Delta k = 0$ (perfect phase matching), the harmonic signal increases with L^2. In contrast, if $\Delta k \neq 0$, at a constant medium length the harmonic intensity is very sensitive to Δk. Optimization of the HHG therefore requires phase matching, $\Delta \vec{k} = \vec{0}$.

We can summarize the most important quantities to determine the generation efficiency as:

1. The length L of the medium.
2. The coherence length $L_c = 1/\Delta k$
3. The absorption length $L_{abs} = 1/\eta_n = 1/(\sigma\rho)$, where σ is the absorption cross-section.
4. The amplification length L_{ampl} on which the dipole x_n has a significant amplitude.

The relative value of these different lengths will determine the macroscopic emission.

2.2.1 Phase matching

For a gas medium, the phase mismatch is the sum of four contributions [Balcou et al., 1997]:

$$\Delta\vec{k} = \Delta\vec{k}_a + \vec{k}_{el} + \vec{k}_{foc} + \vec{k}^{traj}_{dip} \tag{2.22}$$

For convenience we consider only the $\Delta\vec{k}$ component along z, the propagation direction of the field. Δk_a is the phase mismatch due to atomic dispersion, and is expressed as a function of the refractive indices of the medium at the fundamental $\mathcal{N}_1$ and harmonic frequency $\mathcal{N}_n$, $\Delta k_a = n\frac{\omega}{c}(\mathcal{N}_1 - \mathcal{N}_n)$. In general $\mathcal{N}_n < 1 < \mathcal{N}_1$, thus $\Delta k_a > 0$. This term depends on the density of neutral gas atoms in the medium and thus of the generation pressure. $\Delta\vec{k}_{el}$ is the phase mismatch due to scattering by the free electrons of the medium (produced by ionization), of density N_e. Its expression is analogous to the previous term by replacing the refractive indices by the index of refraction of the plasma

$$\Delta k_a = n\frac{\omega}{c}(\mathcal{N}_1^e - \mathcal{N}_n^e) \tag{2.23}$$

with

$$\mathcal{N}_n^e = \sqrt{1 - \frac{\omega_p^2}{\omega_n^2}} \approx 1 - \frac{\omega_p^2}{2\omega_n^2} \tag{2.24}$$

where $\omega_p^2 = \frac{e^2}{m\epsilon_0}N_e$ is the plasma frequency. By replacing it in equation 2.23 we finally obtain:

$$\Delta k_{el} \approx \frac{q\omega\omega_p^2}{2c}\left(\frac{1}{\omega_n^2} - \frac{1}{\omega^2}\right) < 0 \tag{2.25}$$

This term depends on the density of free electrons in the medium an thus the generation gas density and the intensity. Δk_{foc} is the phase mismatch due to the Gouy phase. The focus of the laser beam used for the HHG induces a longitudinal phase, which for a Gaussian beam is written $\arctan(z/z_R)$ with z_R the Rayleigh length. Δk^{traj}_{dip} is the phase mismatch due to the dipole phase ϕ_n^j from 2.17. This term comes from the single atom response that was presented previously and depends on the considered trajectory. We also have:

$$\Delta k^{dip}_{traj} = -\alpha^j\frac{\partial I}{\partial z} \tag{2.26}$$

This contribution changes sign on either sides of the generation beam's focal point with $\Delta k^{dip}_{traj} \propto sign(z) > 0$ after the focus and $\Delta k^{dip}_{traj} < 0$ before the focus. This term depends on the relative position of the generation medium and the focal point, and is different for the two trajectory families.

To summarize, the experimental parameters to optimize the phase matching in the HHG process are the gas pressure, the laser intensity and the conditions of the focus [Kazamias et al., 2011]. The phase matching is also a good way to isolate the

contribution of a type of trajectories (usually the short ones): when the gas jet is placed after the focus the short trajectories are favored, while long trajectories are favored when the jet is placed before the focus [Salières et al., 1995], [Antoine et al., 1996], [Balcou et al., 1997].

2.2.2 Accessing the recombination moment

If only the contribution of the short trajectories is selected, the macroscopic HHG emission is a replica of the single atom response, which is supported by theoretical investigations [Ruchon et al., 2008] and numerous experimental results [Mairesse et al., 2003b], [Doumy et al., 2009], [Dudovich et al., 2006], [Goulielmakis et al., 2008], [Varjú et al., 2005]. In this case based on the SFA, the harmonic emission can be written as the quantum version of the three-step model [Ivanov et al., 1996], [Le et al., 2008a], [Levesque et al., 2007b]:

$$\mathcal{E}_n(\Omega) = 2\pi\Omega^2 a_n(k) d_{rec} \tag{2.27}$$

with $\Omega = k^2/2 + I_p$ the emitted XUV frequency, k the kinetic energy of the electron, $a_n(k)$ the complex amplitudes and $d_{rec} = \langle \psi_i | z | \psi_k^+ \rangle$ the recombination dipole matrix element between the initial bound state ψ_i and the continuum state ψ_k^+. For accessing d_{rec} one needs to calibrate for the $g_n(k) = 2\pi\Omega^2$ and $a_n(k)$ factors. In the case of diatomic or linear molecules, Itatani *et al.* [Itatani et al., 2004] suggested the calibration of the harmonic emission of the wanted molecule with that of a reference atom of same I_p and in the same generation condition, and whose dipole matrix element can be calculated precisely. In the case that we investigate in Chapter 7.2, we are interested in measuring the d_{rec} of an atom, then the reference will be a molecule with similar ionization potential I_p. If the experimental conditions are kept unchanged then one gets:

$$S_n^{atom}(\Omega) = \frac{\mathcal{E}_n^{atom}(\omega) e^{i\phi_{XUV}^{atom}(\omega)}}{\mathcal{E}_n^{mol}(\omega,\theta) e^{i\phi_{XUV}^{mol}(\omega,\theta)}} = \frac{d_{rec}^{atom}}{T(\theta) d_{rec}^{mol}(\theta)} \tag{2.28}$$

$$d_{rec}^{atom} = \frac{\mathcal{E}_n^{atom}(\omega)}{\mathcal{E}_n^{mol}(\omega,\theta)} T(\theta) d_{rec}^{mol}(\theta) e^{i(\phi_{XUV}^{atom}(\omega) - \phi_{XUV}^{mol}(\omega,\theta))} \tag{2.29}$$

where the g_n and a_n factors cancel out, with only the $T(\theta)$ factor, corresponding to the dependence of the ionization rate with θ, the alignment angle of the molecule with respect to the laser field. From equation 2.29 becomes clear that one needs to completely characterize the phases $\phi_{XUV}^{atom}(\omega) - \phi_{XUV}^{mol}(\omega,\theta)$, which can be achieved either by Two Source Interferometry [Lin, 2013] or by the RABBIT technique with which one can measure the spectral phases (i.e. ω dependence) by performing separate scans for the reference molecule and the atom respectively.

CHAPTER 3

PHOTOIONIZATION DYNAMICS

In his first article of 1905, Albert Einstein lays the foundations of modern quantum mechanics by explaining the photoelectric effect [Einstein, 1905]. When a system absorbs a photon of energy greater than its ionization potential, an electron is emitted. For a long time, the emission of the photoelectron is considered a quasi-instantaneous phenomenon. If the one-photon transition is instantaneous, the "exit time" of the electron from the potential is not. This became clear in the 1950's with the development of scattering theory. When a particle (i.e. an electron) is scattered by a potential, the associated wave packet is asymptotically out of phase with respect to that of a free particle of same energy. The spectral derivative of this phase is homogeneous to a group delay and can be interpreted as a delay between the scattered particle and the free particle [Wigner, 1955]. These tiny delays have remained theoretical until the advent of attosecond spectroscopy.

In this chapter, we will present the results of the scattering theory by a potential that leads to the definition of the Wigner delay. Then we will connect this delay to the quantities measured in two-color photo-ionization experiments that will help the interpretation of our experimental results presented later on.

In the last part of this chapter a brief presentation of some of the most well-established theoretical models that describe the one-photon ionization process including electron-correlation effects, will also be briefly presented.

3.1 Scattering in a central potential

We consider an electron wave packet (EWP) in the continuum (energy $E > 0$) as the superposition of "monochromatic" continuum states with amplitudes $a(E)$

$$\Psi(t,r) = \int_0^{+\infty} a(E)\psi(E,r)e^{iEt/\hbar}dE \tag{3.1}$$

where Ψ is the solution of the time-dependent Schrödinger equation

$$i\hbar\frac{\partial\Psi}{\partial t} = \left[-\frac{\hbar^2}{2\mu}\nabla^2 + V(r)\right]\Psi(t,r) \tag{3.2}$$

It is assumed here that the potential V is independent of time and corresponds only to the interaction with the scattering center. It is also assumed that the potential V is central, meaning that it depends only on the distance r between the electron and the

scattering center. The states there are therefore solutions of the time-independent Schrödinger equation, expressed in spherical coordinates of the electron (r,θ,ϕ) in reference with the system's center of mass, which is almost the center of the ion in the case of an interaction between an electron and an ion. μ corresponds to the reduced mass of the system which in this case is almost equal to the electron mass.

In order to study the scattering of the EWP of equation 3.1 in a potential V, one needs to know the stationary states ψ

$$[\underbrace{\hat{H}_0 + V}_{\hat{H}}]\psi(r,\theta,\phi) = E\psi(r,\theta,\phi) \tag{3.3}$$

$$[-\frac{\hbar^2}{2\mu}\nabla^2 + V(r)]\psi(r,\theta,\phi) = E\psi(r,\theta,\phi) \tag{3.4}$$

In spherical coordinates, the Laplacian will write:

$$\Delta\psi(r,\theta,\phi) = \frac{1}{r}\frac{\partial^2}{\partial r^2}(r\psi) + \frac{1}{r^2}\underbrace{\left(\frac{1}{sin\theta}\frac{\partial}{\partial\theta}(sin\theta\frac{\partial\psi}{\partial\theta}) + \frac{1}{sin^2\theta}\frac{\partial^2\psi}{\partial\phi^2}\right)}_{-\hat{L}^2/\hbar^2\psi} \tag{3.5}$$

Comparing the previous expression with that of the angular momentum operator $\hat{L}^2$, we get a new expression for the eigenfunctions, where a centrifugal term appears:

$$\left[-\frac{\hbar^2}{2\mu}\frac{1}{r}\frac{\partial^2}{\partial r^2}r + \frac{1}{2\mu r^2}\hat{L}^2 + V(r)\right]\psi(r,\theta,\phi) = E\psi(r,\theta,\phi) \tag{3.6}$$

The angular momentum operator $\hat{L}$ acts only on the angular variables θ and ϕ. The angular dependence of the Hamiltonian is therefore entirely contained in the $\hat{L}^2$ term. This Hamiltonian commutes with the operators $\hat{L}^2$ and $\hat{L}_z$. We can then look for a basis of the particle states space, consisting of the common eigenfunctions, to the three observables $\hat{H}$, $\hat{L}^2$ and $\hat{L}_z$ with the respective eigenvalues $\hbar^2k^2/2\mu$, $l(l+1)\hbar^2$ and $m\hbar$. The eigenfunctions common to $\hat{L}^2$ and $\hat{L}_z$ are well known and are the spherical harmonics $Y_l^m(\theta,\phi)$. So the solutions of equation 3.6 will have the form:

$$\psi(r,\theta,\phi) = R(r)Y_l^m(\theta,\phi) \tag{3.7}$$

the corresponding wave functions ψ will be called partial waves. By putting this expression in equation 3.6, we obtain the radial expression:

$$\left(-\frac{\hbar^2}{2\mu}\frac{1}{r}\frac{d^2}{dr^2}r + \frac{l(l+1)\hbar^2}{2\mu r^2} + V(r) \right) R(r) = ER(r) \tag{3.8}$$

The particular case where V is a Coulombic potential ($\propto 1/r$) requires a particular treatment. Nevertheless, the study of the partial waves, solutions of expression 3.6 in the case of a V potential at short range - meaning a decrease faster than 1/r at infinity - allows an approach of the phase shift concept due to the scattering on the potential V.

In this section, we will first study the solutions of equation 3.6 in the case where V is zero, known as the free spherical waves. We will then study solutions in the case where the potential V is a short-range potential, and their long-range asymptotic behavior r. We will highlight the existence of a phase shift $\delta_{E,l}$ between the free spherical waves and the partial waves introduced by the scattering by the potential V which will finally lead us to the definition of the Wigner delays.

3.1.1 Free spherical waves

At long distance r from the scattering center, it is expected that the electron will not feel the effects of short-range potential V. The solutions of equation 3.6 must therefore have an asymptotic behavior similar to free spherical waves $\psi^{(0)}(r,\theta,\phi) = R^{(0)}(r)Y_l^m(\theta,\phi)$, eigenfunctions of the Hamiltonian $\hat{H}_0$. One would need therefore to solve the radial equation 3.8 for V = 0:

$$\left(-\frac{\hbar^2}{2\mu}\frac{1}{r}\frac{d^2}{dr^2}r + \frac{l(l+1)\hbar^2}{2\mu r^2} \right) R^{(0)}(r) = ER^{(0)}(r) \tag{3.9}$$

It can be shown, noting that the radial equation can be reduced to the spherical Bessel equation, that the solutions of equation 3.6 are of the form:

$$\psi^{(0)}_{k,l,m}(r,\theta,\phi) = \sqrt{\frac{2k^2}{\pi}} j_l(kr) Y_l^m(\theta,\phi) \tag{3.10}$$

with k, l and m parameterizing the eigenvalues of the potential-free Hamiltonian $\hat{H}_0$, $\hat{L}^2$ and $\hat{L}_z$:

$$\hat{H}_0 \psi^{(0)}_{k,l,m}(r,\theta,\phi) = \frac{\hbar^2 k^2}{2\mu} \psi^{(0)}_{k,l,m}(r,\theta,\phi) \tag{3.11}$$

$$\hat{L}^2 \psi^{(0)}_{k,l,m}(r,\theta,\phi) = l(l+1)\hbar^2 \psi^{(0)}_{k,l,m}(r,\theta,\phi) \tag{3.12}$$

$$\hat{L}_z \psi^{(0)}_{k,l,m}(r,\theta,\phi) = m\hbar \psi^{(0)}_{k,l,m}(r,\theta,\phi) \tag{3.13}$$

and j_l a spherical Bessel function defined as

$$j_l(\rho) = (-1)^l \rho^2 \left(\frac{1}{\rho}\frac{d}{d\rho}\right)^l \frac{sin\rho}{\rho} \tag{3.14}$$

The first three spherical Bessel functions j_0, j_1 and j_2 are represented in Figure 3.1. Note that the function j_0 is identified with the cardinal sinus function.

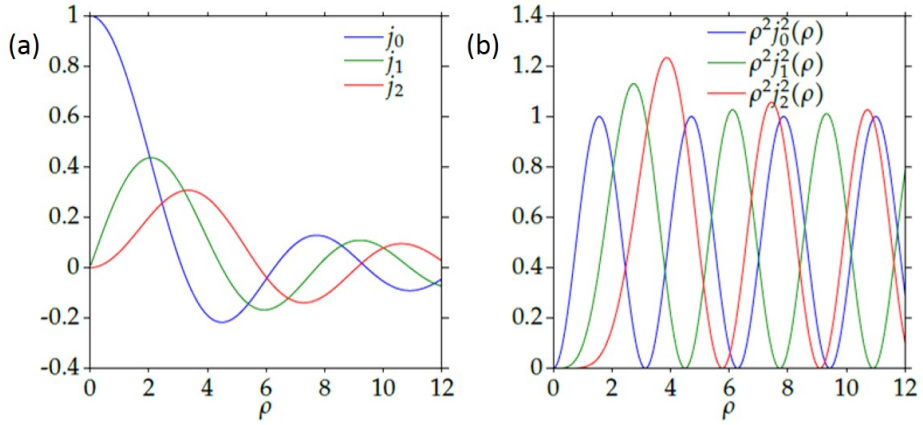

Figure 3.1: Spherical Bessel functions $j_l(\rho)$ (a) and $\rho^2 j_l^2(\rho)$, giving the radial dependence of the probability of presence in the state $|\psi^{(0)}_{k,l,m}\rangle$ (b) for l=0,1,2. Taken from Ref. [Barreau, 2017].

The angular dependence of the free spherical wave is contained in the spherical harmonic $Y_l^m(\theta,\phi)$. It is therefore fixed by the quantum numbers l and m and not by the energy ($\propto k^2$). In the state $|\psi^{(0)}_{k,l,m}\rangle$ the probability of finding the particle in a solid angle $d\Omega_0$ around a given direction (θ_0,ϕ_0) and between r and $r+dr$ is proportional to $r^2 j_l^2(kr)\left|Y_l^m(\theta_0,\phi_0)\right|^2 dr d\Omega_0$. The function $\rho^2 j_l^2(\rho)$ is presented in Figure 3.1. This function takes small values for $\rho < \sqrt{l(l+1)}$. In the state $|\psi^{(0)}_{k,l,m}\rangle$, the probability of finding the particle in $r < \frac{1}{r}\sqrt{l(l+1)}$, is therefore almost zero. This means that the particle is almost insensitive to what happens in a sphere of center $\mathcal{O}$ and radius $\frac{1}{k}\sqrt{l(l+1)}$. A potential of shorter range than this radius will then have no influence on the wave. This critical distance can be interpreted semi-classically as an impact parameter.

Asymptotic behavior We want to determine the behavior of the long-distance wave function of the scattering center $\psi^{(0)}_{k,l,m}(r \to +\infty,\theta,\phi)$, which is the asymptotic behavior of the spherical Bessel functions. By applying the operator $(\frac{1}{\rho}\frac{d}{d\rho})$ a first time to the function $\frac{sin\rho}{\rho}$, $j_l(\rho)$ will be:

$$j_l(\rho) = (-1)^l \rho^l \left(\frac{1}{\rho}\frac{d}{d\rho}\right)^{l-1} \left(\frac{cos\rho}{\rho^2} - \frac{sin\rho}{\rho^3}\right) \tag{3.15}$$

For $\rho \to +\infty$, we get $\frac{sin\rho}{\rho^3} \ll \frac{cos\rho}{\rho^2}$. If we apply the operator $(\frac{1}{\rho}\frac{d}{d\rho})$ once more, the dominant term will come again from the derivative of the cosine. Thus

$$j_l(\rho \to +\infty) \sim (-1)^l \rho^l \frac{1}{\rho^l}\frac{1}{\rho}\Big(\frac{d}{d\rho}\Big)^l sin\rho \tag{3.16}$$

With $\Big(\frac{d}{d\rho}\Big)^l sin\rho = (-1)^l sin(\rho - l\pi/2)$, we finally obtain

$$j_l(\rho \to +\infty) \sim \frac{1}{\rho} sin(\rho - l\pi/2) \tag{3.17}$$

The asymptotic behavior of the free spherical wave $\psi^{(0)}_{k,l,m}(r,\theta,\phi)$ is therefore:

$$\psi^{(0)}_{k,l,m}(r \to +\infty,\theta,\phi) \sim \sqrt{\frac{2k^2}{\pi}} Y^m_l(\theta,\phi) \frac{sin(kr - l\pi/2)}{kr} \tag{3.18}$$

which is a real function that can be written in a complex form in order to interpret its expression as a wave :

$$\psi^{(0)}_{k,l,m}(r \to +\infty,\theta,\phi) \sim -\sqrt{\frac{2k^2}{\pi}} Y^m_l(\theta,\phi) \frac{e^{-ikr}e^{il\pi/2} - e^{ikr}e^{-il\pi/2}}{2ikr} \tag{3.19}$$

For $r \to +\infty$, $\psi^{(0)}_{k,l,m}$ is the superposition of an incoming e^{-ikr}/r and an outgoing e^{+ikr}/r spherical wave whose relative phase is $l\pi$.

3.1.2 Partial waves

We are now interested in solving equation equation 3.8 in the general case of a central potential V(r) at a short range, meaning decreasing more rapidly than $1/r$ for $r \to +\infty$.

For $R(r) = \frac{1}{r}u(r)$, equation 3.8 becomes:

$$\Big(-\frac{\hbar^2}{2\mu}\frac{d^2}{dr^2} + \frac{l(l+1)}{2\mu r^2} + V(r)\Big)u(r) = \frac{\hbar^2 k^2}{2\mu}u(r) \tag{3.20}$$

to which the initial condition, $u(r = 0) = 0$, must be added .

Asymptotic behavior The centrifugal potential and the potential $V(r)$ at short range, are negligible and the previous equation becomes:

$$\frac{d^2u}{dr^2} + k^2 u(r) \approx 0 \tag{3.21}$$

the general solution of which writes:

$$u(r \to +\infty) \sim Acos(kr) + Bsin(kr) \tag{3.22}$$

If the potential V is real, we can find real solutions u and therefore choose the constants A,B $\in R$. We can then rewrite:

$$u(r \to +\infty) \sim \sqrt{A^2 + B^2}(sin\beta_l cos(kr) + cos\beta_l sin(kr)) \tag{3.23}$$

and with $sin\beta_l = \frac{A}{\sqrt{A^2+B^2}}$ and $cos\beta_l = \frac{B}{\sqrt{A^2+B^2}}$ it will become:

$$u(r \to +\infty) \sim Csin(kr - \beta_l) \tag{3.24}$$

The scattering phase β_l is determined by the continuity of equation's 3.20 solution, vanishing in $r = 0$. In the case of a zero potential V, we showed previously that the scattering phase β_l is equal to $l\pi/2$. We can then choose this value as a reference by defining the phase shift $\delta_{E,l}$ such that:

$$u(r \to +\infty) \sim Csin(kr - l\pi/2 + \delta_{E,l}) \tag{3.25}$$

$\delta_{E,l}$ depends on the angular momentum l and energy E.

In order now to interpret physically the meaning of this dephasing we inject the previous expression of u in the general expression of the wave function and obtain the asymptotic expression of the partial wave $\psi_{k,l,m}(r \to +\infty,\theta,\phi)$:

$$\psi_{k,l,m}(r \to +\infty,\theta,\phi) \sim CY_l^m(\theta,\phi)\frac{sin(kr - l\pi/2 + \delta_{E,l})}{r} \tag{3.26}$$

or else, by multiplying by a phase factor $e^{i\delta_{E,l}}$, and by choosing the constant C to facilitate comparison with the asymptotic expression of the spherical free wave of equation 3.19

$$\psi_{k,l,m}(r \to +\infty,\theta,\phi) \sim CY_l^m(\theta,\phi)\frac{e^{-ikr}e^{il\pi/2} - e^{ikr}e^{-il\pi/2}e^{2\delta_{E,l}}}{2ikr} \tag{3.27}$$

In the same way as for the case of the free spherical wave of equation 3.19, the partial wave for $r \to +\infty$ is the superposition of an incoming e^{-ikr}/r and an outgoing e^{ikr}/r spherical wave, which are out of phase by $l\pi + 2\delta_{E,l}$. We can interpret this expression as follows. The incoming wave is identical to that of the free particle case, and approaches the area of action of the potential V being more and more

disturbed by the potential. After reversing direction and being transformed into an outgoing wave, it has accumulated a phase shift $2\delta_{E,l}$ with respect to the free outgoing wave which would have been obtained in the case of $V = 0$. This $2\delta_{E,l}$ dephasing, is a very important quantity since it characterizes the whole effect of the potential on the particle with angular momentum l and energy E. For example, it is possible to express the scattering cross section as a function of $2\delta_{E,l}$ [Cohen-Tannoudji et al., 1973].

The theory of scattering by a central potential presented previously originates from the scattering theory where a wave moving in the direction of positive r "from the left to the right ", and scattered by a potential located in $r = 0$ has a phase shift $2\delta_{E,l}$ in $r \to +\infty$, compared to the same wave propagating without any potential.

Scattering in a Coulombic potential For a Coulombic potential created by an ion of charge Z which is proportional to Z/r, the previous analytical treatment of short-range potentials does not apply. However, it can be shown that the scattering phase on a Coulombic potential is expressed as [Friedrich, 1991]:

$$\Phi_{k,l}(r) = \frac{Zln(2kr)}{k} - l\frac{\pi}{2} + \underbrace{\sigma_{k,l} + \delta_{k,l}}_{\eta_{k,l}} \tag{3.28}$$

where $\sigma_{k,l}$ is the Coulomb phase, due to the long-range potential and is defined by

$$\sigma_{k,l} = arg\big[\Gamma(l+1-\frac{iZ}{k})\big] \tag{3.29}$$

with function Γ being:

$$\Gamma(z+1) = \int_0^{+\infty} t^z e^{-t} dt \tag{3.30}$$

and $\delta_{k,l}$ the dephasing due to the short-range potential. The phase $\Phi_{k,l}(r)$ depends on the distance r at the scattering center, even for $r \to +\infty$. Thus the long-range Coulombic potential deforms the wave function, even at great distance from the ion.

3.1.3 Wigner delay

Taking now the case of the short-range potential, according to the above, for $r \to +\infty$ we can rewrite the radial part of the outgoing wave as:

$$\Psi^-(t,r) \propto \frac{1}{r}\sum_l \int_0^{+\infty} |A_l(E)| e^{i(kr+2\delta_{E,l})} e^{-iEt/\hbar} dE \tag{3.31}$$

which is dephased by $2\delta_{E,l}$ compared to the EWP not scattered by the potential EWP:

$$\Psi^{-}_{V=0} \propto \frac{1}{r}\sum_{l}\int_{0}^{+\infty}|A_l(E)|e^{ikr}e^{-iEt/\hbar}dE \tag{3.32}$$

These two integrals contain terms that oscillate rapidly with energy. The most important contribution will therefore be due to the points where the phase is stationary. Deriving the phases of equation 3.31 and 3.32, we obtain the following relations:

$$r\frac{dk}{dE} + 2\frac{d\delta_{E,l}}{dE} - \frac{t}{\hbar} = 0 \tag{3.33}$$

$$r\frac{dk}{dE} - \frac{t}{\hbar} = 0 \tag{3.34}$$

which gives

$$t = \frac{r}{v} + 2\hbar\frac{d\delta_{E,l}}{dE} \tag{3.35}$$

$$t = \frac{r}{v} \tag{3.36}$$

The scattered EWP is temporally shifted compared to a free one by the quantity:

$$\tau_W = 2\hbar\frac{d\delta_{E,l}}{dE} \tag{3.37}$$

, where τ_W is the so-called Wigner delay [Eisenbud, 1948], [Wigner, 1955], [Smith, 1960].

For the better understanding of the Wigner delay it would be instructive to see an example of a weak potential. By using the semi-classical Brillouin-Kramers-Wentzel approximation to solve the Schrödinger equation for an electron subjected to a potential V, the phase shift $\delta_{E,l}$ will be [Friedrich, 1991], [Dahlström et al., 2012]:

$$\delta_{E,l}(E) = \frac{1}{\hbar}lim_{x\to+\infty}\int_{-\infty}^{x}\left(\sqrt{2m(E-V(x'))} - \sqrt{2mE}\right)dx'. \tag{3.38}$$

For a $V \ll E$, we have $\sqrt{2m(E-V(x'))} \approx \sqrt{2mE}\left(1 - \frac{V(x')}{2E}\right)$ from where

$$\delta_{E,l}(E) \approx -\frac{1}{\hbar}\sqrt{\frac{m}{2E}}\int_{-\infty}^{+\infty}V(x')dx' = -\frac{1}{\hbar}\sqrt{\frac{m}{2E}}I_v \tag{3.39}$$

where the integral of the potential I_v, is defined to be independent of the energy. The corresponding Wigner delay is then calculated as

$$\tau_W = 2\hbar \frac{d\delta_{E,l}}{dE} = \sqrt{\frac{m}{2}} \frac{I_v}{E^{3/2}} \tag{3.40}$$

For an attractive potential we have $I_v < 0$ so $\tau_W < 0$. This means that the electron scattered by the potential, is ahead of the free electron. Indeed, at a constant energy, the kinetic energy of the scattered electron is greater when it passes near an attractive potential compared to the case of a zero potential. The delay introduced is even greater when the potential is important. We also note that the Wigner delay is proportional to $E^{-3/2}$, meaning that an electron will be more affected by the potential if its energy is low.

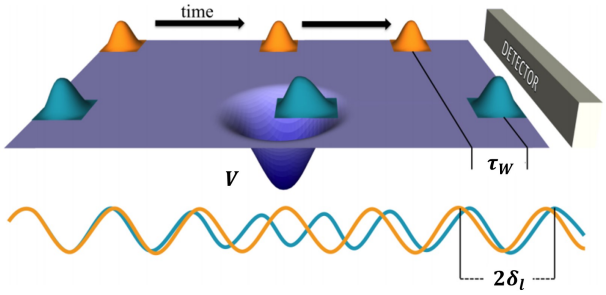

Figure 3.2: Schematic representation of the Wigner time delay. As the electron wave packet (blue symbols) scatters off the potential, it acquires a phase shift η compared to a reference free electron (orange symbols). This phase shift is related to the time elapsed between the detection of the scattered EWP and the detection of the unscattered free electron, called the Wigner time delay . Taken from [Argenti et al., 2017].

3.2 Measuring the photoionization delays

3.2.1 Photoionization delays and one-photon transition matrix

During the photo-ionization process, the electron is "released" into the ion potential and scatters out of it. The measurement of the time of photo-ionization consists in determining the time taken by the electron to be emitted, which means the time between the absorption of the photon and the exit of the electron from the atomic potential. The question that arises now is how this time delay is connected to the Wigner delay and the scattering phase. In the following section the work of Dahlström *et al.* [Dahlström et al., 2012], Guenot *et al.* [Guénot et al., 2012] and Argenti *et al.* [Argenti et al., 2017] on this subject will be presented. Atomic units are used throughout this section.

Lets consider the case of an atom in its ground state $|\psi_g\rangle$ ionized by a XUV $E(t)$ pulse, centered at $t_{XUV} = 0$. E is polarized along the z direction, is monochromatic and Fourier limited; its spectrum is centered at $E_0 - E_g$, where E_0 and E_g are the energies of the final and fundamental state, respectively. The Fourier transform of $E(t)$ is noted as $\tilde{E}(\Omega)$. We choose as eigenfunctions of the continuum (of energy $E = k^2/2 > 0$) in the absence of an electric field, the functions $|\psi^-_{\vec{k}}\rangle$, that correspond to the outgoing waves. The ionized EWP is then written as

$$|\Psi(t)\rangle = -i\sqrt{2\pi}\int |\psi^-_k\rangle e^{-iEt} M^{(1)}_k dE \tag{3.41}$$

where $M^{(1)}_k$ is the transition dipole between $|\psi_g\rangle$ and $|\psi^-_{\vec{k}}\rangle$. In the frame of the first-order perturbation theory and the dipole approximation we get:

$$M^{(1)}_k = i\langle\psi_{\vec{k}}| - z\tilde{E}(\Omega)|\psi_g\rangle = -i\tilde{E}(\Omega)\langle\psi_{\vec{k}}|z|\psi_g\rangle \tag{3.42}$$

The wave function of the ground state is separated into a radial and an angular part :

$$\psi_g(\vec{r}) = R_{n_g,l_g}(r)Y^{m_g}_{l_g}(\theta,\phi) \tag{3.43}$$

We have seen previously that the functions $|\psi_{\vec{k}}\rangle$ are not plane waves, but scattering waves. We use their decomposition in partial waves [Landau and Lifshitz, 1977]:

$$\psi_{\vec{k}}(\vec{r}) = (8\pi)^{3/2}\sum_{L,M} i^L e^{-i\delta_{k,L}} Y^{M*}_L(\vec{k}) Y^M_L(\theta,\phi) R_{k,L}(r) \tag{3.44}$$

By substituting equation 3.43 and 3.44 in expression 3.42 and by using the expression of the operator in spherical coordinates $z = rcos\theta$ and separating the angular and radial parts, we will have:

$$\begin{aligned} M^{(1)}_k = -i\tilde{E}(\Omega)(8\pi)^{3/2}\sum_{L,M} i^{-L} e^{i\delta_{k,L}} Y^M_L(\vec{k})\langle Y^M_L(\theta,\phi)|cos\theta|Y^{m_g}_{l_g}(\theta,\phi)\rangle \\ \times\langle R_{k,L}(r)|r|R_{n_g,l_g}(r)\rangle \end{aligned} \tag{3.45}$$

With $cos\theta = \sqrt{\frac{4\pi}{3}}Y^0_1(\theta)$, we obtain according to the $3j$ Wigner symbols [Landau and Lifshitz, 1977]:

$$\langle Y_L^M(\theta,\phi)|Y_1^0(\theta)|Y_{l_g}^{m_g}(\theta,\phi)\rangle = (-1)^{-M}\sqrt{2L+1}\sqrt{2l_g+1}\times\begin{bmatrix} L & 1 & l_g \\ 0 & 0 & 0\end{bmatrix}\begin{bmatrix} L & 1 & l_g \\ -M & 0 & m_g\end{bmatrix} \tag{3.46}$$

The selection rules for the one-photon transition impose $L = l_g \pm 1$ and $M = m_g$. The transition matrix $M_k^{(1)}$ will then become:

$$M_k^{(1)} \propto \sum_{L=l_g\pm1;M=m_g} (-1)^{-M} i^{-L} e^{i\delta_{k,L}} Y_L^M(\vec{k})\sqrt{2L+1}\sqrt{2l_g+1}\times \tag{3.47}$$

$$\begin{bmatrix} L & 1 & l_g \\ 0 & 0 & 0\end{bmatrix}\begin{bmatrix} L & 1 & l_g \\ -M & 0 & m_g\end{bmatrix}\langle R_{k,L}(r)|r|R_{n_g,l_g}(r)\rangle \tag{3.48}$$

The radial matrix element and the 3j-symbols are real [Cohen-Tannoudji et al., 1973]. If we consider only one ionisation channel, the matrix element is simplified. This situation occurs in the case of ionization of an s electron or if the transition $L = l_g + 1$ is favored compared to the $L = l_g - 1$ one, according to the propensity rule [Fano, 1985]. We then have the following simple relation between the transition matrix element and the scattering phase of the continuum state:

$$Arg M_k^{(1)} = \delta_{k,L} + cste \tag{3.49}$$

which gives the photoionization delay:

$$\tau = \frac{\partial arg M_k^{(1)}}{\partial \omega} = \frac{1}{2}\tau_W \tag{3.50}$$

The photoionization delay is half the Wigner delay. The photoionization process can then be interpreted as a semi-scattering event. This delay is much shorter than the resolution of any electronic detector used experimentally and thus seems impossible to measure directly.

3.2.2 Two-photon transition matrix

The first measurements of photo-ionisation delays were possible thanks to the development of the RABBIT (Reconstruction of Attosecond Beating by Interference of two-photon Transitions) technique [Véniard et al., 1995], [Paul et al., 2001], [Muller, 2002] or the attosecond streaking method [Kienberger et al., 2004], [Goulielmakis et al., 2004].

These two methods include a second electric field which is used as probe of the photoionization process. The question that arises now is how one can access the information about the one-photon ionization process from a two-photon measurement. Throughout this thesis the RABBIT technique (experimental implementation detailed in Chapter 4.1 is used. In this method the dressing field can be treated in a perturbative way. The formalism of Marcus Dahlström [Dahlström et al., 2013] and the team of Richard Taïeb of LCPMR Paris are used.

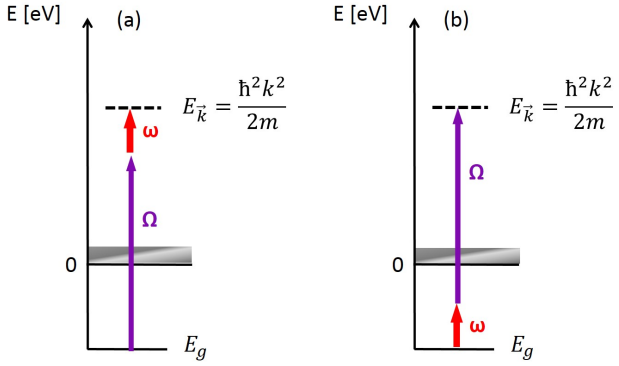

Figure 3.3: XUV-IR two-photon ionization from the initial state with energy E_g to a continuum state with energy $E_{\vec{k}}$. Two quantum paths lead to $\vec{k}$: a photon of energy Ω is absorbed first (a) or second (b). The second path is negligible compared to the first one.

We consider the two-color ionization process outlined in Figure 3.3. The initial energy system E_g is ionized by the absorption of a photon of energy Ω and a photon of energy ω. In general in the RABBIT interferometry we have $\Omega > \omega$, the first being an XUV and the second an IR photon. The IR photon can be absorbed first or second. However, there are very few states below the ionization threshold, which makes the absorption of the IR photon first a negligible process. We will thus focus on the two-photon process described in Figure 3.3 (a).

The XUV and IR fields are both polarized in the z direction that is chosen as the quantization axis. According to the second-order perturbation theory, the two-photon transition element corresponding to the absorption of the XUV photon followed by the IR photon, is written as the sum-integral on all the intermediate energy states E_v (discrete for $E_v < 0$ and continuum for $E_v > 0$):

$$M^{(2)}_{\vec{k}} = -iE_\Omega E_\omega \lim_{\epsilon \to 0^+} \sum\!\!\!\!\!\!\int_v \frac{\langle \vec{k}|z|v\rangle\langle v|z|g\rangle}{E_g + \Omega - E_v + i\epsilon} \tag{3.51}$$

As before, we separate the ground state wave function in the radial and angular part (equation 3.43):

$$M^{(2)}_{\vec{k}} = \frac{4\pi}{3i}(8\pi)^{3/2}E_\Omega E_\omega \sum_{L,M}(-i)^L e^{i\eta_L(\vec{k})}Y_L^M(\vec{k})\sum_{\lambda,\mu}\langle Y_L^M|Y_1^0|Y_L^\mu\rangle\langle Y_\lambda^\mu|Y_1^0|Y_{l_g}^{m_g}\rangle\times$$
$$\left[\sum_{v,E_v<}\frac{\langle R_{k,L}|r|R_{v,\lambda}\rangle\langle R_{v,\lambda}|r|R_{n_g,l_g}\rangle}{E_g+\Omega-E_v}+\lim_{\epsilon\to 0^+}\int_0^{+\infty}dE_v\frac{\langle R_{k,L}|r|R_{v,\lambda}\rangle\langle R_{v,\lambda}|r|R_{n_g,l_g}\rangle}{E_g+\Omega-E_v+i\epsilon}\right] \quad (3.52)$$

The intermediate states are characterized by the quantum numbers v, λ and μ. The angular moment of intermediate and final states obey the selection rules, allowing dipole transitions only for $\lambda = l_g \pm 1$, $L = l_g$ or $l_g \pm 2$ and $M = \mu = m_g$. The term in square brackets in equation 3.52 will be later noted as $T_{L,\lambda,l_g}(k)$. It corresponds to the radial part of the transition amplitude, in which we have separated the contribution of the discrete states under the ionization threshold (in the sum) and the states of the continuum (in the integral). In RABBIT interferometry , the energy of the XUV photon is greater than the ionization potential of the atom $\Omega > |E_g|$, therefore greater than the energy of the discrete states below the threshold. We have then the denominator of the first term : $E_g + \Omega - E_v$, to be positive and large, which makes the contribution of the discrete states in $T_{L,\lambda,l_g}(k)$ negligible compared to that of the continuum states. In the integral, the denominator is pure imaginary for the moment κ such that $E_\kappa = \kappa^2/2 = E_g + \Omega$. We then obtain the following expression for the integral, where $\mathcal{P}$ represents the Cauchy principal value :

$$\lim_{\epsilon\to 0^+}\int_0^{+\infty}dE_v\frac{\langle R_{k,L}|r|R_{v,\lambda}\rangle\langle R_{v,\lambda}|r|R_{n_g,l_g}\rangle}{E_g+\Omega-E_v+i\epsilon} =$$
$$\mathcal{P}\int_0^{+\infty}dE_v\frac{\langle R_{\kappa,L}|r|R_{v,\lambda}\rangle\langle R_{v,\lambda}|r|R_{n_g,l_g}}{E_g+\Omega-E_v} - i\pi\langle R_{k,L}|r|R_{\kappa,L}\rangle\langle R_{\kappa,\lambda}|r|R_{n_g,l_g}\rangle \quad (3.53)$$

The calculation of $T_{L,\lambda,l_g}(k)$, and in particular of its phase, is a complex task analytically and numerically. M. Dahlström [Dahlström et al., 2013] therefore developed an approximation to compute the $T_{L,\lambda,l_g}(k)$, based on the analysis of the asymptotic behavior of the radial functions, similar to the analysis presented in sections 3.1.1 and 3.

Asymptotic behavior One can re-write $T_{L,\lambda,l_g}(k)$ under the form

$$T_{L,\lambda,l_g} = \langle R_{k,L}|r|\rho_{\kappa,\lambda}\rangle \quad (3.54)$$

where $\rho_{\kappa,\lambda}(r)$ is a scattering wave function whose expression is given by identification with equation 3.52

$$\rho_{\kappa,\lambda}(r) = \sum_{v,E_v<0} \frac{R_{v,\lambda}(r)\langle R_{v,\lambda}|r|R_{n_g,l_g}\rangle}{E_\kappa - E_v}$$
$$+\mathcal{P}\int_0^{+\infty} dE_v \frac{R_{v,\lambda}(r)\langle R_{v,\lambda}|r|R_{n_g,l_g}\rangle}{E_\kappa - E_L} - i\pi R_{\kappa,\lambda}|r|R_{n_g,l_g}\rangle \tag{3.55}$$

In the case of scattering on a Coulombic potential, it has been shown that for $r \to +\infty$ the radial part of the wave function of the final state is written as:

$$R_{k,L}(r \to +\infty) \sim \frac{C_k}{r} sin(kr + \Phi_{k,L}(r)), \tag{3.56}$$

where the dephasing $\Phi_{k,L}(r)$ is given by equation 3.28. According to the previous paragraph, the contribution of the discrete states to $\rho_{\kappa,\lambda}(r)$ is negligible compared to that of the continuum states, thus:

$$\mathrm{R}\,e[\rho_{\kappa,\lambda}(r)] \approx \mathcal{P}\int_0^{+\infty} dE_v \frac{R_{v,\lambda}(r)\langle R_{v,\lambda}|r|R_{n_g,l_g}\rangle}{E_\kappa - E_v} \tag{3.57}$$

We then, extend the integration to $-\infty$ and replace $R_{v,\lambda}$ by its asymptotic form

$$\mathrm{R}\,e[\rho_{\kappa,\lambda}(r \to +\infty)] \approx \mathcal{P}\int_{-\infty}^{+\infty} dE_v \frac{C_\kappa}{r} sin(\kappa r + \Phi_{\kappa,\lambda}(r)) \frac{\langle R_{v,\lambda}|r|R_{n_g,l_g}\rangle}{E_\kappa - E_n} \tag{3.58}$$
$$\mathrm{R}\,e[\rho_{\kappa,\lambda}(r \to +\infty)] \approx -\frac{\pi C_\kappa}{r} cos(\kappa r + \Phi_{\kappa,\lambda}(r))\langle R_{\kappa,\lambda}|r|R_{n_g,l_g}\rangle \tag{3.59}$$

The asymptotic form of the imaginary part of $\rho_{\kappa,\lambda}$ is obtained by simply replacing expression 3.56 into 3.55:

$$\mathrm{Im}[\rho_{\kappa,\lambda}(\to +\infty)] \approx -\frac{\pi C_\kappa}{r} sin(\kappa r + \Phi_{\kappa,\lambda}(r))\langle R_{\kappa,\lambda}|r|R_{n_g,l_g}\rangle \tag{3.60}$$

Finally, the asymptotic form of $\rho_{\kappa,\lambda}$ will become:

$$\rho_{\kappa,\lambda}(r \to +\infty) \approx -\frac{\pi C_\kappa}{r} e^{i(\kappa r + \Phi_{\kappa,\lambda}(r))}\langle R_{\kappa,\lambda}|r|R_{n_g,l_g}\rangle \tag{3.61}$$

By replacing equation 3.61 and 3.56 into equation 3.54 one gets:

$$T_{L,\lambda,l_g}(k) \approx -\pi C_k C_\kappa \langle R_{\kappa,\lambda}|r|R_{n_g,l_g}\rangle \int_0^{+\infty} \frac{sin(kr + \Phi_{k,L}(r))}{r} r \frac{e^{i(\kappa r + \Phi_{\kappa,\lambda}(r))}}{r} r^2 dr \tag{3.62}$$

By expressing the sine in the integral in an exponential form, we will obtain a sum of two oscillating terms : $e^{i((\kappa+k)r + \Phi_{\kappa,\lambda}(r) + \Phi_{k,L}(r))}$ and $e^{i((\kappa-k)r + \Phi_{\kappa,\lambda}(r) - \Phi_{k,L}(r))}$. In RABBIT interferometry, the energy $\hbar\omega$ of the IR photon that is absorbed after the XUV photon, is equal to the energy difference between the intermediate and final states.

This energy is much smaller than the energy of the final state $k^2/2 - \kappa^2/2 = \omega \ll k^2/2$. Thus the term $\propto e^{i(\kappa+k)}$ oscillates more rapidly than the second term $\propto e^{i(\kappa-k)}$ and subsequently the integral is simplified as:

$$T_{L,\lambda,l_g}(k) \approx -C_k C_\kappa \langle R_{\kappa,\lambda}|r|R_{n_g,l_g}\rangle \int_0^{+\infty} -\frac{1}{2i} e^{i((\kappa-l)r+\Phi_{\kappa,\lambda}(r)-\Phi_{k,L}(r))} r dr \tag{3.63}$$

By replacing the dephasings with their expressions, after changing variable and using the integral expression of the Gamma function defined by the equation 3.30, one obtains:

$$\int_0^{+\infty} e^{i((\kappa-k)r+\Phi_{\kappa,\lambda}-\Phi_{k,L})} r dr = \int_0^{+\infty} r e^{i(\kappa-k)r} e^{i\left(\frac{Zln2\kappa r}{\kappa}\frac{Zln2kr}{k}\right)} e^{i(\eta_\lambda-\eta_L)} e^{i\pi/2}(L-\lambda) dr \tag{3.64}$$

$$= \frac{(2\kappa)^{iZ/\kappa}}{(2k)^{iZ/k}} e^{i(\eta_\lambda-\eta_L)} i^{L-\lambda} \int_0^{+\infty} r^{1+iZ(1/\kappa-1/k)} e^{i(\kappa-k)r} dr \tag{3.65}$$

$$= \frac{(2\kappa)^{iZ/\kappa}}{(2k)^{iZ/k}} e^{i(\eta_\lambda-\eta_L)} i^{L-\lambda} \left(\frac{i}{\kappa-k}\right)^{2+iZ(\frac{1}{\kappa}-\frac{1}{k})} \Gamma\left(2+iZ(\frac{1}{\kappa}-\frac{1}{k})\right) \tag{3.66}$$

Noticing that $i^{iZ(1/\kappa-1/k)} = e^{-\pi/2} Z(1/\kappa - 1/k)$, we obtain the final asymptotic expression of the radial transition element:

$$\begin{aligned} T_{L,\lambda,l_g}(k) \approx \frac{\pi}{2} C_k C_\kappa \langle R_{\kappa,\lambda}|r|R_{n_g,l_g}\rangle \frac{e^{-\frac{\pi}{2}Z(\frac{1}{\kappa}-\frac{1}{k})}}{(\kappa-k)^2} \\ \times e^{i(\eta_\lambda-\eta_L)} i^{L-\lambda+1} \frac{(2\kappa)^{iZ/\kappa}}{(2k)^{iZ/k}} \Gamma\left(2+iZ(\frac{1}{\kappa}-\frac{1}{k})\right)(\kappa-k)^{-iZ\left(\frac{1}{\kappa}-\frac{1}{k}\right)} \end{aligned} \tag{3.67}$$

The first line of this expression is real and contains an exponential term which describes the transition between two continuum states κ and k. The exponential decreases with the energy of the dressing IR photon $\omega = k^2/2 - \kappa^2/2$ and at a fixed photon energy ω, the exponential increases with the final angular moment k.

Phase From the previous expression we deduce the phase of the radial transition matrix element as:

$$arg T_{L,\lambda,l_g}(k) = \frac{\pi}{2}(L-\lambda+1) + \eta_\lambda - \eta_L + \underbrace{arg\left(\frac{(2\kappa)^{iZ/\kappa}}{(2k)^{iZ/k}} \frac{\Gamma\left(2+iZ(\frac{1}{\kappa}-\frac{1}{k})\right)}{(\kappa-k)^{iZ(\frac{1}{\kappa}-\frac{1}{k})}}\right)}_{\phi_{cc}(k,\kappa)}, \tag{3.68}$$

where the phase ϕ_{cc} is related to the transition between the intermediate state and the final continuum of a Coulombic potential. This means that it doesn't depend neither on the initial state nor on the XUV field. It is a measurement induced quantity and is considered global [Dahlström et al., 2013]. It is now possible to express the phase of the total two-photon transition matrix 3.52 as:

$$arg M_{\vec{k}}^{(2)} = arg Y_L^{m_g}(k) + \phi_\Omega + \phi_\omega - \lambda\frac{\pi}{2} + \eta_\lambda(\kappa) + \phi_{cc}(k,\kappa), \tag{3.69}$$

where ϕ_Ω and ϕ_ω are the phases of the XUV and IR fields respectively. The phase terms due to the final state L, compensate for each other and do not contribute in the final expression 3.69. Thus, surprisingly, except for the contribution of the spherical harmonic, the terms contained in expression 3.69 depend solely on the intermediate state, meaning the one-photon transition.

3.2.3 Phase and delay measured by RABBIT interferometry

The RABBIT technique measures the phase difference between two two-photon transitions. More specifically, the absorption of a harmonic followed by the absorption of a dressing photon which will interfere with the absorption of the next harmonic followed by the stimulated emission of an other dressing photon as is schematically outlined in Figure 3.4.

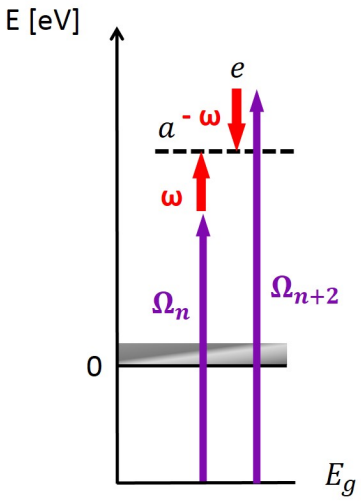

Figure 3.4: Two-photon quantum paths interfering in RABBIT interferometry: the absorption of the XUV photon of energy Ω_n followed by the absorption of IR photon of energy $\omega(a)$ and the absorption of the XUV photon of energy Ω_{n+2} followed by the stimulated emission of the IR photon of energy $\omega(e)$ leads to the same final state.

The signal of a sideband is then expressed as a function of the two-photon transition matrix elements as:

$$S_{SB} \propto |M^{\alpha} + M^{e}|^2 = |M^{\alpha}|^2 + |M^{e}|^2 + 2|M^{\alpha}||M^{e}|cos[arg(M^{\alpha}M^{e*})] \tag{3.70}$$

Assuming that only one intermediate angular momentum contributes to the transition in both paths α and e and taking into account equation 3.69 we obtain:

$$arg(M^{\alpha}M^{e*}) \approx 2\omega\tau + \phi_{\Omega_{n+2}} - \phi_{\Omega_n} + \eta_L(\kappa_{n+2}) - \eta_L(\kappa_n) + \phi_{cc}(\kappa_{n+2}) - \phi_{cc}(\kappa_n) \tag{3.71}$$

with $\phi_{\Omega_{n+2}} - \phi_{\Omega_n}$ the spectral phase difference between two consecutive harmonics and τ the delay between the IR and XUV pulses. By dividing by 2ω the phase of the oscillating component at 2ω, in a RABBIT spectrogram, we obtain an approximation of the group delays.

$$\tau_{RABBIT} \approx t_{XUV} + \tau_W + \tau_{cc}, \tag{3.72}$$

where t_{XUV} is the harmonic group delay (Chapter 2), τ_W the Wigner delay and τ_{cc} the continuum-continuum, measurement-induced delay.

So, in the case of an unstructured continuum, there is a simple relation between the phase of the two-photon transition amplitude and the photoionization delay. During a RABBIT measurement, this delay can be directly measured with an additional "continuum-continuum" delay. These developments allowed the interpretation of two-color attosecond photoionization experiments in terms of photoionization delays.

Part III

Experimental Apparatus and Methods

CHAPTER 4

EXPERIMENTAL APPARATUS FOR XUV+IR PHOTOIONIZATION SPECTROSCOPY

The experiments presented in this thesis have been performed on two different laser facilities: ATTOLab in Saclay, France and the Lund Attosecond Science Center (LASC) in Sweden. In this chapter, the RABBIT method will be first presented, followed by a detailed description of the 1 kHz (SE1) beam-line in ATTOlab and the 1 kHz beam-line in Lund.

4.1 RABBIT technique

In the attosecond spectroscopy field, the 'reconstruction of attosecond beating by interference of two-photon transitions', also know as the RABBIT technique, plays a prominent role. Historically, the first to introduce the RABBIT scheme was Veniard *et al.* [Véniard et al., 1996] in 1996 where it was theoretically shown that by changing the delay τ between a XUV pump and a weaker IR probe pulse, the intensity of the so called sidebands oscillates. These oscillations contain valuable information for both the XUV ionizing radiation and the target atom. Later on, Paul *et al.* [Paul et al., 2001] in 2001 and Muller [Muller, 2002] in 2002, demonstrated experimentally the technique for the first time.

The principle of the method is recalled schematically in Figure 4.1. A comb of coherent harmonics is used to ionize the system of interest creating one-photon EWPs. After adding a weak IR field ($\sim 10^{11} W/cm^2$) we create two-photon replicas of the initial EWPs that will now interfere giving rise to the so-called sidebands (SB) that lie $\pm\hbar\omega_0$ between the harmonic peaks. Their intensity oscillates with $2\omega_0$ frequency as a function of the delay τ between the XUV and IR pulses as given by equation 3.70 which in order to facilitate readability, is rewritten here as :

$$S_{n+1}(\tau,E) = |M_n(E)|^2 + |M_{n+2}(E)|^2 \\ +2|M_n(E)||M_{n+2}(E)|cos(2\omega_0\tau + \Delta\phi_{XUV}(E) + \Delta\phi_{atom}(E)), \quad (4.1)$$

where $M_n(E)$,$M_{n+2}(E)$ are the transition amplitudes of the two-photon EWPs after absorbing/emitting a dressing IR photon, ω_0 is the driving laser frequency. In Chapter 3.2.3 it was shown (equation 3.71) that the measured phase by the RABBIT method consists of i) the phase difference between two consecutive harmonics $\Delta\phi_{XUV} = \phi_{\Omega n+2} - \phi_{\Omega n}$, ii) the difference between the scattering phases of the one-photon EWPs produced by harmonics n and n+2 respectively, $\Delta\eta_{scat} = \eta_L(\kappa_{n+2}) - \eta_L(\kappa_n)$ and finally iii) the term $\Delta\phi_{cc} = \phi_{cc}(\kappa_{n+2}) - \phi_{cc}(\kappa_n)$ which is called the 'continuum-continuum phase' and is due to the absorption/emission of the

dressing IR photon. Thus in total the measured RABBIT phase is $\phi_{RABBIT} = \Delta\phi_{XUV} + \overbrace{\Delta\eta_{scat} + \Delta\phi_{cc}}^{\Delta\phi_{atom}}$. $\Delta\phi_{XUV}$ is connected to the atttochirp (Chapter 2.1.4) while $\Delta\eta_{scat}$ is intrinsic to the target atom and $\Delta\phi_{cc}$ is a small and constant quantity which becomes important for lower energies especially in angle resolved measurements when more than one ionization channels are present.

To access the spectral phase of the $2\omega_0$ oscillations ($\Delta\phi_{XUV} + \Delta\phi_{atom}$) one may integrate $S_{n+1}(\tau,E)$ over the energy inside each sideband and then apply a Fourier transform to the oscillating signal.

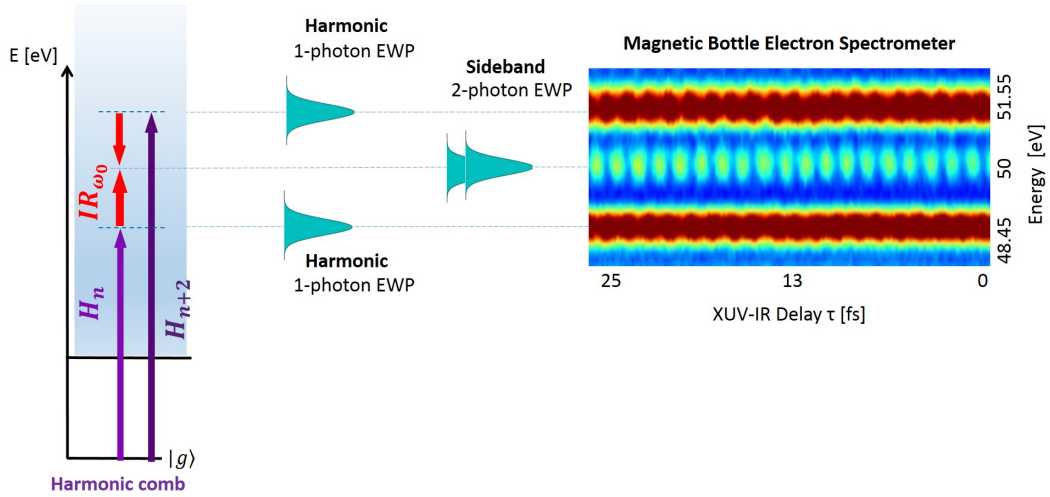

Figure 4.1: RABBIT principle: The two different quantum paths $(n+2) - IR$ and $(n) + IR$, end up at the same energy and their interference creates the oscillating SB signal.

The RABBIT method was initially developed as a characterization tool of the Attosecond Pulse Trains (APT) generated from focusing an intense ($\sim 10^{14} W/cm^2$) ultrashort IR pulse into a gas medium. If $\Delta\phi_{atom}$ is known or considered negligible then one has direct access to $\Delta\phi_{XUV}$. In combination with the measured harmonic intensities the reconstruction of the initial harmonic comb is achieved [Paul et al., 2001], [Mairesse et al., 2003a], [Muller, 2002],[Agostini and DiMauro, 2004]. However, it was soon demonstrated ([Mauritsson et al., 2005]) that the same method could also be used for the study of the photo-ionization dynamics of the detection atomic gas by measuring the atomic phases $\Delta\phi_{atom}$ if now the harmonic phase is known. In this way, by measuring the spectral phase and amplitude of the ionized EWP it is possible to reconstruct the dynamics of the photo-emission event ([Guénot et al., 2012], [Klünder et al., 2011], [Haessler et al., 2009], [Dahlström and Lindroth, 2014]).

4.2 SE1 beam line in ATTOlab

ATTOlab is a consortium between nine laboratories situated on the plateau of Saclay, France, dedicated to the interdisciplinary studies of ultra-fast electronic and nuclear dynamics at femtosecond and attosecond timescales in systems in the gas, condensed and plasma phase (Attolab). The experimental site at CEA-l'Orme-les-merisiers, inaugurated officially in February 2017, is specialized in gas phase and solid state studies. It consists of two Femtosecond-Attosecond Beamlines (FAB1 and FAB10), each including an IR femtosecond laser and a HHG-based attosecond XUV source, respectively at 1 kHz (SE1) and 10 kHz (SE10) repetition rates, coupled to experimental end-stations (Figure 4.2).

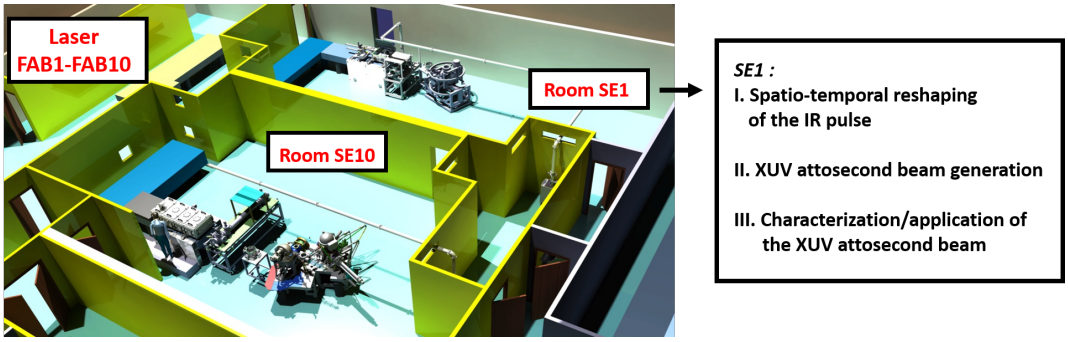

Figure 4.2: overall view of the experimental space: hall for FAB1-FAB10 lasers, experimental rooms with HHG attosecond sources and endstations (SE1, SE10)

The experiments presented in Chapter 7 were the first to be realized in the SE1 beam-line driven by the FAB1 laser (25 fs duration,15 mJ per pulse, centered at 800 nm, with carrier-envelope phase stabilization).

4.2.1 FAB1 and FAB10 dual laser system

This laser system has been developed by Amplitude Technologies in collaboration with CEA Saclay within the joint laboratory Impulse. An original full water-cooled 10 kHz front-end is used to seed different amplification stages. The front-end output is split in two parts, seeding simultaneously two beam-lines operating respectively at 1 and 10 kHz. Figure 4.3 (b) shows schematically the outline of the 10 kHz front-end where CEP-stable pulses from a Rainbow CEP4 (Femtolasers) oscillator are temporally stretched by an Öffner-triplet stretcher. In order to optimize the pulse duration and correct the CEP slow drift, a Dazzler module (acousto-optic programmable dispersive filter - AOPDF) that provides a dispersion compensation is placed after the stretcher. Next, a 6-pass amplifier boosts the pulse energy up to 50 nJ when pumped with 15 W. The pulses are then amplified in a double Ti:Sa crystal regenerative cavity. Gain narrowing effects during the amplification are counter-counted by the use of an intracavity Mazzler (acousto-optic programmable gain filter - AOPGF). Next, a double Ti:Sa crystal pre-amplifier is used. When pumped

with 25 W this pre-amplifier can provide pulses with 7 W power after a two-crystal single pass.

The front-end output pulses are then seeded into two high energy amplifiers as it is shown in Figure 4.3 (a). 30% of the energy is sent to a Pockels cell to reduce the pulse repetition rate from 10 kHz to 1 kHz, resulting in 180 μJ. These pulses are firstly amplified to 4.3 mJ in a water cooled 5-pass pre-amplifier and further boosted up to 23 mJ with 70 W of pump power in the 4-pass main cryo-cooled amplification stage. The rest of the output power from 10 kHz front-end, corresponding to 5.1 W , is sent to the 10 kHz main cryo-cooled amplifier. With 100 W pump power, 28 W output is achieved at 10 kHz. After an expansion telescope, each amplified laser beam is send to a CEP (carrier envelope phase)-compatible reflection grating-based compressor. For a full description of the system and its detailed characteristics consult [Golinelli et al., 2018]. The FAB1 laser beam after the compressor delivers pulses centered at 800 nm with 25 fs duration, 15 mJ energy, with energy stability of 0.8% (rms) and shot-to-shot CEP stability of 350 mrad at 1kHz repetition rate.

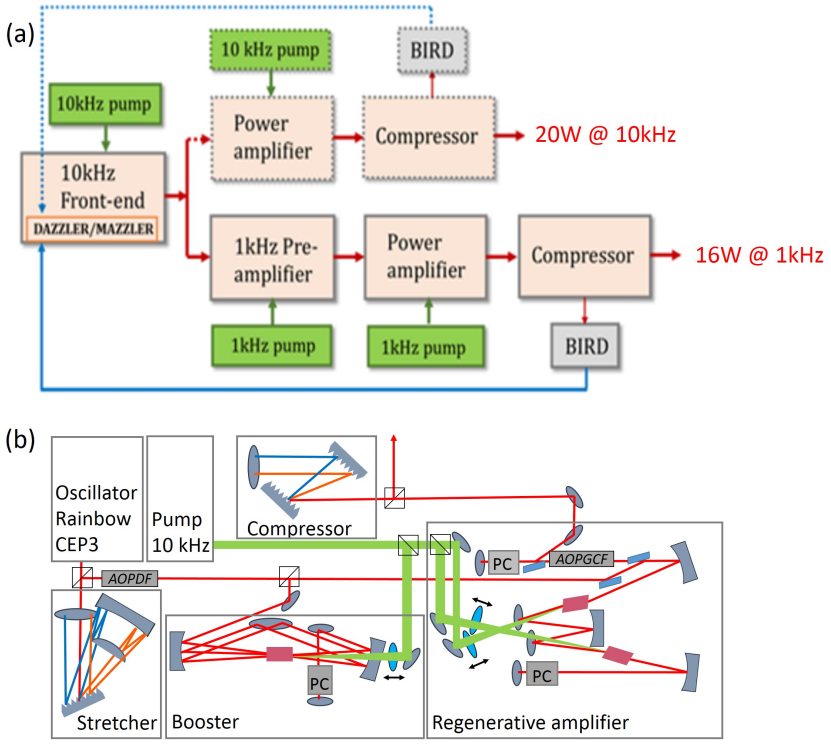

Figure 4.3: (a) Schematic representation of the FAB1-FAB10 dual laser system. (b) Scheme of the 10 kHz laser front-end. PC – Pockels cell. The amplifiers are pumped by two 10 kHz Continuum MESA lasers. Amplified pulses can be compressed by a grating-based compressor or seeded in the main amplifiers as in the layout presented in (a) [Golinelli et al., 2018].

4.2.2 SE1 attosecond beam-line

As it is demonstrated in Figure 4.2, the initial beam is split into two parts: the IR spatiotemporal shaping line for the generation of single attosecond pulses and the beam-line for the generation and characterization of attosecond pulse trains and photoionization spectroscopy studies. The latter consists mainly of the RABBIT experimental apparatus

Figure 4.4 shows the schematic outline of the attosecond pulse train beam-line. Before the initial beam enters the main configuration, it passes through an attenuator consisting of a rotatable half-wave plate and two reflective polarizers setting an s-polarization. This enables the control of the incoming energy and allows its adjustment in a range of 0.8 mJ to 9.4 mJ, according to the needs of each experiment. The main set up [Weber et al., 2015] consists of a Mach-Zehnder interferometer where a part of the incoming beam is used for the generation of the attosecond pulse train and the rest is used as a probe. More specifically, 90% of the initial beam is focused by a f = 2000 mm lens into a gas cell of 3mm - 10 mm length, placed on a translation stage (path 1, Figure 4.4). An anti-reflective coated silica plate, set at grazing incidence (78.5°), is used to transmit the strong generating IR beam and to reflect the generated XUV light. By turning the silica plate, the XUV beam can then either be directed to an XUV spectrometer (path 2, Figure 4.4) or to the time-of-flight electron spectrometer (path 3, Figure 4.4).

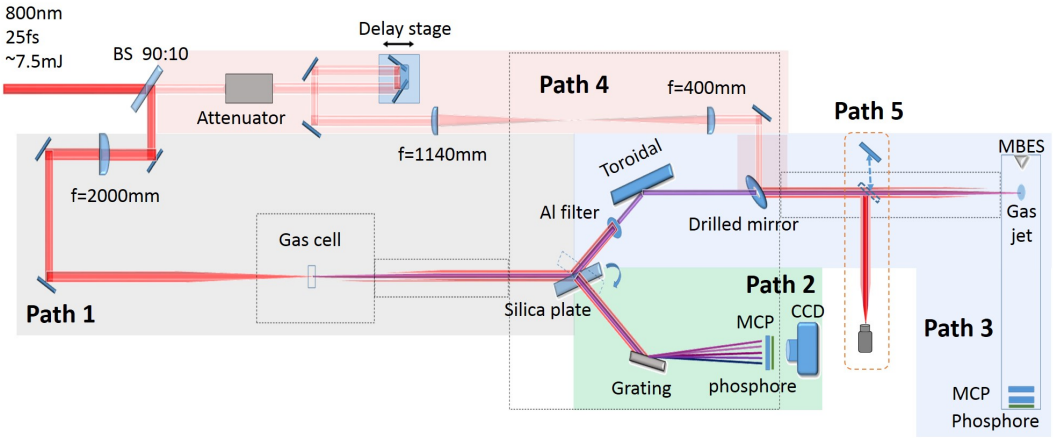

Figure 4.4: SE1 beam line for XUV generation and characterization/application.

The XUV spectrometer consists of a concave grating which will focus each harmonic in the range 15–100 eV (in order to image the full spectrum one needs to move the detector perpendicularly to the beam propagation direction) on a position sensitive detector made of two micro-channel plates (MCPs) in chevron configuration coupled to a phosphor screen. A micro-channel plate is a slab made from highly resistive material of typically 2 mm thickness with a regular array of tiny tubes or slots (microchannels) leading from one face to the opposite, densely distributed over the whole surface. The microchannels are typically approximately 6-10 micrometers in diameter and spaced apart by approximately 15 μm. 'Chevron con-

figuration' means that our MCP detectors consist of two microchannel plates with angled channels rotated 180° from each other producing a v-like (chevron) shape. In a chevron MCP the electrons that exit the first plate start the cascade in the next plate. The angle between the channels reduces ion feedback in the device, as well as producing significantly more gain at a given voltage compared to a straight channel MCP.

The 2D fluorescence signal , showing the spectrum in the horizontal direction and the spatial profile in the vertical direction, will then be recorded with a cooled CCD (charge-coupled device) camera. A system like this gives the possibility of fine tuning the generation parameters in order to optimize the spatio-spectral characteristics of the produced XUV radiation before using it for photoionization experiments. Path 3 (Figure 4.4) indicates the second option where the silica plate is rotated to reflect the XUV beam through a filter that removes the remaining IR light (usually 200 nm thick aluminum filters are used due to their high transmission between ~ 20-73 eV), towards a gold coated toroidal mirror (f=500mm). Used in the 2f-2f configuration, this mirror refocuses the beam in a gas jet in the interaction region of a 2m-long MBES (Magentic bottle electron spectrometer , see chapter 4.2.3 below), where it produces photo-ionization.

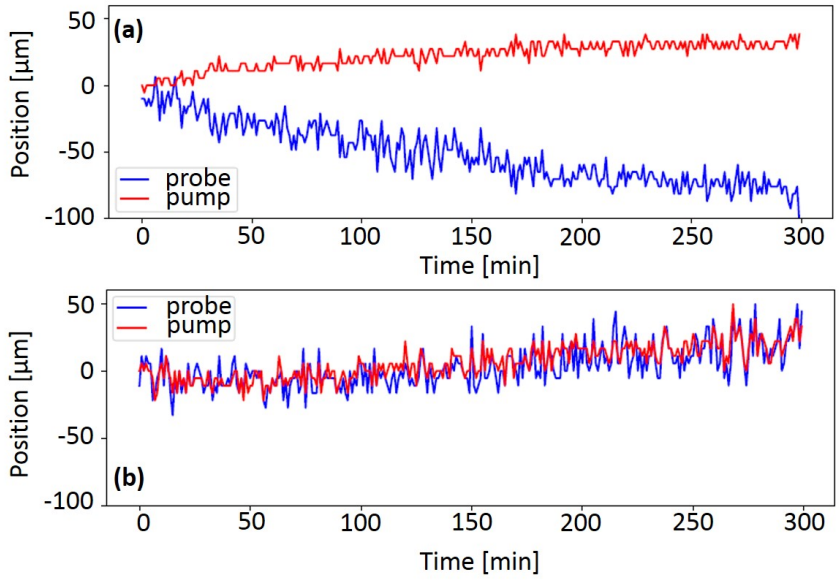

Figure 4.5: Pointing stability of the pump and probe beams when the number of reflections between the two arms is uneven (a) or even (b)[Platzer, 2017].

The produced photoelectrons are then collected and guided by magnetic fields towards a pair of MCPs and a phosphor plate. In order to record a cleaner signal with the less possible ringing and other noise contamination a bandpass filter is added after the second MCP.

The remaining 10% of the initial beam is used as a probe as is shown in path 4 (Figure 4.4). In order to be able to adjust the pulse energy to the experimental conditions, an attenuator identical to the one discussed above is mounted in the beam

path. The pulse then passes through a delay line for fine adjustment and scan of the probe delay by translating a set of two mirrors. Coarse adjustment is provided by a microcontrole translation while fine by a piezo-electric actuator with a 75 μm range and 2 nm resolution. The dressing IR beam is then focused and recombined with the XUV beam by a drilled mirror (d=2 mm) that reflects the IR and transmits the XUV. This recombination mirror is placed on a three axis translation stage with remote control, that enables its alignment under vacuum directly on the XUV beam. In order however, to find the best spatial overlap between the pump and the probe beam, after removing the gas cell and the Al filter, thus letting only the generating IR beam through, a mirror is inserted into the common path. In this way the two co-propagating beams are now focusing outside the vacuum chamber and it is possible to image both their foci by the same IR camera (path 5 of Figure 4.4) and adjust accordingly the position of the drilled mirror to maximize their interference.

A big challenge for this kind of experiments is to achieve good spatio-temporal stability between the two long (~ 4 m) arms of the interferometer. Since the physical processes we are interested in measuring are of the order of some tens-hundreds of attoseconds the stability of our interferometer should be of the same order or less. Many sources of beam path fluctuations may occur. Our 1 kHz intense laser system is susceptible of long term fluctuations. Moreover, slow temperature variations as well as vibrations from the location of the experimental setup in the building and from the vacuum pumping system may arise.

To solve these issues, we took care to setup our beam-line with the best possible passive stabilization. In order to avoid all these instability sources, we installed a single main optical table supporting all the beam steering of the beam-line. Optics are clamped on thick posts of the minimum possible height in order to reduce vibrations. Vacuum chambers are fixed, using a bridge like design, on two heavy sand filled steel containers to decouple turbo pumps' vibrations from the optical setup. Vacuum chambers are therefore connected to the main optical table only through the floor. The optical breadboard inside the square chamber (path 4 and 2) rests on four feet mounted on the optical table and is only connected to the vacuum chamber through highly flexible bellows used as vacuum seals (for more details see Ref [Weber et al., 2015]). The entire beam-line is also covered in order to isolate the system during the measurements.

Additionally, in order to achieve better stability between the two interferometric arms the number of reflections for the two paths should be even. A configuration of two lenses with f_1 = 1140 mm and f_2 = 400 is chosen (path 4, Figure 4.4). The first lens is placed on a translation stage (outside the vacuum chamber) which enables us to move the lens in the beam propagation direction to ensure the best possible overlap between the IR and XUV foci. The stability of the system is measured by using path 5 of Figure 4.4 to image the vertical displacement of the IR foci of the pump and probe beam over time. In Figure 4.5 the spatial stability of the system is plotted for the case of uneven (a) and even (b) reflections between the two arms. In the case of uneven reflections, the probe arm consists of one lens (f = 1140 mm) and

an additional mirror as is shown in Figure 4.6.

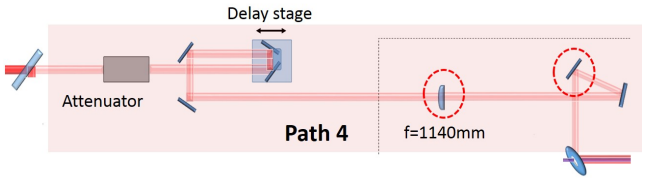

Figure 4.6: Dressing arm for the 'uneven reflection' configuration.

In Figure 4.5 (a), we notice that after a few hours, the foci move in opposite directions and are separated by more than 100 μm, which is of the same order of magnitude as the focal spot. However, this drift is corrected in Figure 4.5 (b), where the two beams move in the same way and thus remain superimposed during the experiment.

In order now to estimate the corresponding temporal stability of the system, we superimpose the two foci, and introduce a fixed delay τ between the two arms. We then measure the spectrum of the two overlapped beams using an IR spectrometer. In the spectral domain the sum of the two identical beams will give :

$$S(\omega) = A(\omega)e^{i\phi(\omega)} + A(\omega)e^{i\phi(\omega)}e^{i\omega\tau} = A(\omega)e^{i\phi(\omega)}(1 + e^{i\omega\tau}) \tag{4.2}$$

,where $A(\omega)$ and $\phi(\omega)$ are the spectral amplitude and phase of the first pulse. The spectral intensity measured by the spectrometer will be :

$$|S(\omega)|^2 = |A(\omega)|^2 \left|1 + e^{i\omega\tau}\right|^2 = 4\,|A(\omega)|^2\,(1 + cos\omega\tau) \tag{4.3}$$

which corresponds to the spectral intensity of a single pulse $|A(\omega)|^2$ modulated by a factor $(1 + cos\omega\tau)$ due to which spectral fringes appear. By Fourier transforming equation 4.3, we thus obtain the delay τ which is the quantity plotted in Figure 4.7. The corresponding temporal stability is ~ 3 fs over three hours. In a usual RABBIT measurement the signal for each delay is accumulated for 1000 laser shots, so for a typical delay range of 26 fs with 0.1 fs sampling, we need ~3 minutes to record a full RABBIT trace. This means that the spatio-temporal stability of the system is satisfactory for this type of measurements.

4.2.3 Detection of photoelectrons: Magnetic Bottle Electron Spectrometer (MBES)

The results of this thesis have been obtained by detecting the photoelectrons using a magnetic bottle electron spectrometer. In this instrument the kinetic energy of the photoelectrons, is analyzed by determining the photoelectron flight-time in a drift tube. The main advantage of this instrument is its high collection efficiency, which is enabled by a magnetic field designed to direct the electrons towards the

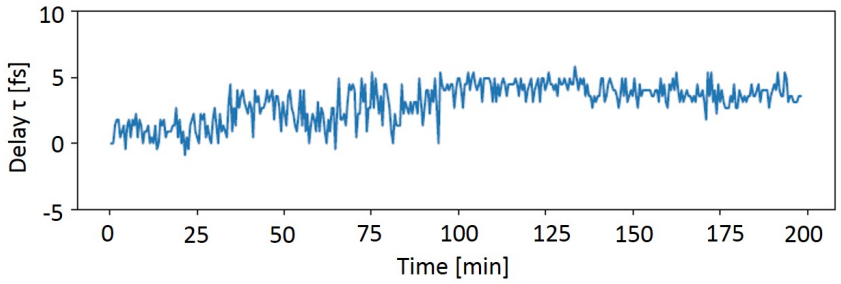

Figure 4.7: Delay drift between the pump and the probe pulse over three hours [Platzer, 2017].

microchannel plates at the end of the drift tube, independently of their emission angle and without altering their kinetic energy [Kruit and Read, 1983].

The scheme of the MBES used in SE1 beam line is shown in Figure 4.8. It consists of a 2m long flight tube which is wrapped with a sheet of μ-material (a material with very large magnetic permeability) to shield the magnetic field of the earth. A permanent magnet that creates a strong magnetic field of ~1 T close to the gas target and a solenoid wrapped around the drift tube that creates a weak homogeneous magnetic field of ~1 mT, are used in order to create the 'bottle' type field that allows to collect electrons ejected over a large angle. Additionally, electrodes that provide a retarding/accelerating electric field are placed close to the entrance of the drift tube and are used for the optimization of the system's resolution. Finally there is the detector which consists of a set of MCPs and a phosphor screen in the end of the tube.

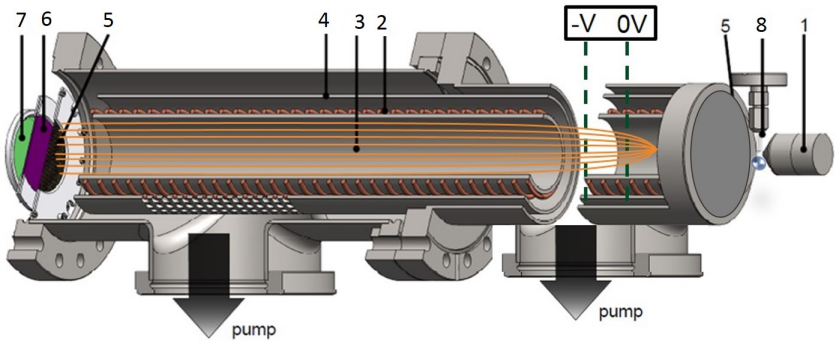

Figure 4.8: Design of the MBES electron spectrometer: (1) permanent magnet with a soft iron cone mounted inside the vacuum chamber enabling a 4π sr collection angle , (2) solenoid, (3) drift tube, (4) μ-metal shield, (5) copper mesh, (6) double-stack of MCP, (7) phosphor screen coupled to an analog-to-digital converter Agilent DP1400 with a 500 ps resolution, (8) nozzle to introduce the sample. The orange lines are the schematic outline of the guiding magnetic field. Figure adapted from [Kothe et al., 2013].

Its working principle is simple and based on the free-field time-of-flight electron spectrometer: depending on its velocity, an electron will arrive on the detector at a

specific time t

$$E_{kin} = \frac{m_e}{2}\frac{L^2}{(t-t_0)^2} \tag{4.4}$$

where $E_{kin} = E_{ph} - E_{Ip}$, E_{ph} is the photon energy, E_{Ip} is the ionization energy of the gas target, m_e is the electron mass, L is the time-of-flight tube length and t_0 accounts for the time offset of the trigger (usually the time resolution of the detector and the electronics is on the order of 100 ps to 1 ns). To make the transition from the temporal domain to the energy domain, a Jacobian transform function is used and in combination with equation 4.4 we obtain the calibration function 4.5

$$I(E_{kin})dE_{kin} = I(t)dt \rightarrow I(E_{kin}) = \frac{L\sqrt{m_e}}{(2E_{kin})^{3/2}}I(t) \tag{4.5}$$

where $I(E_{kin})$ and $I(t)$ are the intensities of the peaks in the spectral and temporal domain respectively. From equation 4.5 derives that the relative energy resolution will be:

$$\frac{\Delta E}{E} = \frac{2}{L}\sqrt{\frac{2E}{m_e}}\Delta t. \tag{4.6}$$

It becomes clear that it depends on both the temporal resolution Δt that is constrained to the reaction time of the detection electronics (~1 ns) and the length of the flight tube. The MBES used for the experiments in Chapter 7 has $\Delta E/E$ ~ 1.9% resulting in an energy resolution ΔE of 190 meV at 10 eV electron energy (Attolab) whereas the one used for the experiments described in Chapter 6 has a resolution of 89 ±5 meV at 10 eV (Lund).

An alternative way to increase the resolution of the spectrometer is to decrease the effective energy of the traveling photoelectrons. This can be done by slowing down the electron before it enters the tube by applying a bias voltage between the gas interaction region and the drift tube (Figure 4.8). The drawback in this case is that electrons with initial energy less than the bias voltage cannot enter the drift tube [Chang].

As stated earlier, the main advantage of this instrument in comparison with its simple field-free version is the large collection angle of 4π sr while at the same time maintaining the high energy resolution. This is achieved by the 'bottle' shaped magnetic field. An electron emitted in the interaction region with speed v and a velocity component perpendicular to the magnetic field lines, $v\sin(\theta_i)$, will follow a helical trajectory. In a plane perpendicular to the magnetic field lines, the electron will travel in a circular, cyclotron motion with a radius

$$r_i = \frac{vm\sin(\theta_i)}{eB_i} \tag{4.7}$$

while drifting into the parallel-field region, due to its longitudinal velocity component. If the variation of the magnetic field that the electron experiences changes negligibly during one revolution of the cyclotron motion, the component of the electron angular momentum that is parallel to the magnetic field lines is conserved.

We can therefore equate the final angular momentum of the cyclotron motion in the homogeneous field of the drift region, with the initial angular momentum,

$$r_i mv \sin(\theta_i) = r_f mv \sin(\theta_f), \tag{4.8}$$

which together with equation 4.7 gives a relation between the initial and the final traveling angles relative to the magnetic field lines,

$$\frac{\sin(\theta_f)}{\sin(\theta_i)} = \sqrt{\frac{B_f}{B_i}} \tag{4.9}$$

The momentum of the electron is thus essentially parallel to the lines once it reaches the drift region. The transition from the high to the low field region should be made relatively short, a few mm, so that the travel time of the electron from the interaction region to the detector is a good measure of the particle speed, independently of the emission angle from the target. However, the transition should not be made over too short distance. The magnetic field gradient then becomes too large for the adiabatic approximation to be valid, i.e. the magnetic field strength changes significantly during one revolution of the electron cyclotron motion [Roedig, 2012].

4.2.4 A typical RABBIT measurement from SE1 beam line

In Figure 4.9 we show a typical RABBIT measurement using the experimental apparatus described above where we used neon as the generation and detection gas. In Figure 4.9 (a) the RABBIT spectrogram along with its integrated signal over the delays (yellow line) are shown. The sidebands' intensity is kept lower than the harmonics' one in order to remain in the perturbative region where the RABBIT analysis described in Chapter 4.1 is valid. By integrating the electron signal over the sideband energy width for each sideband, we get oscillating curves like the one shown in Figure4.9 (b) for SB38. The Fourier transform with respect to delay exhibits a peak at $2\omega_0$, as shown in (d). The spectral phase at this peak for each sideband is reported in Figure4.9 (c). It contains the spectral phase of the ionizing harmonics (or rather their group delay as well as the 'atomic' phase delay of the ionized target) , as explained in Chapter 2. In the case where the latter is negligible (neon target gas), we can use the information on the former to reconstruct the corresponding APT [Mairesse et al., 2003a], [Paul et al., 2001] in Figure 4.10.

One of the criteria of the measurement's quality is the spatio-temporal overlap between the pump and the probe beams which is mirrored on the quality of the sidebands' oscillations and subsequently on the form of the $2\omega_0$ peak. A well defined and well centered around 2ω without any sidelobes peak, as the one in Figure 4.9 (d) is the desired result. Measuring the ratio between the 0^{th} and 2^{nd} order peak we derive the contrast of the sideband oscillations which is typically around 0.52.

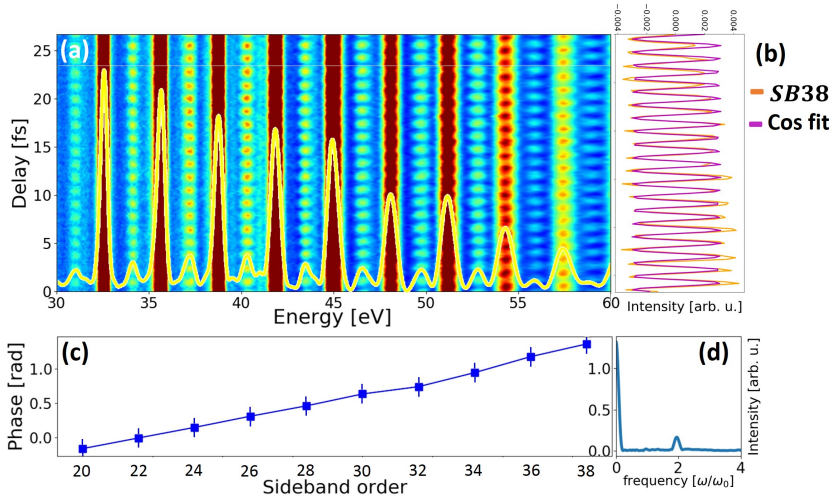

Figure 4.9: (a) RABBIT spectrogram for harmonics generated and detected in neon, with the corresponding delay-integrated signal shown in yellow. (b) The energy-integrated signal of sideband 38 (orange line) along with its cosine fit (magenta line). (c) The spectral phases (see Chapter 4.1) of each sideband and (d) the intensity of the Fourier transform of the signal in (b).

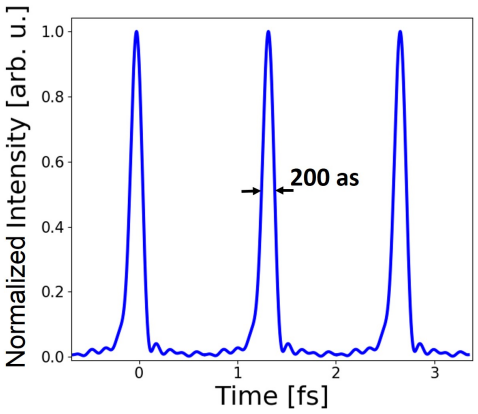

Figure 4.10: Reconstruction of the attosecond pulse train (APT) from harmonics H21-H39 and their corresponding spectral phases from Figure 4.9. The pulses are separated by a half laser period, i.e. 1.3 fs and have a duration of about 200 as at FWHM.

4.3 Beam line in Lund University

The experimental work discussed in Chapter 6 was performed in collaboration with Lund university and the group of Anne L'Huillier. In this section the 1kHz laser-chain and the RABBIT apparatus of the Lund beam-line will be presented.

1 kHz laser-chain

Figure 4.11 displays the schematic outline of the 1kHz CPA laser-chain in Lund. A KLM-mode-locked Ti:sapphire CEP-stable, RAINBOW oscillator from Femtolasers delivers 7 fs long pulses of 2.5 nJ energy that are then stretched in a single grating configuration stretcher. A Dazzler is then used to reshape and also limit the bandwidth of the seed pulses. The spectral width of the final pulses is ~100 nm (corresponds to Fourier transform limited pulses of 20 fs) that can be reduced down to ~50 nm. In this way longer pulses are generated along with the possibility of tuning the central wavelength of the final pulse. For the first amplification stage a multi-pass amplifier increases the pulse's energy up to about 250 nJ. A pulse picker is then used to reduce the pulse repetition rate and let only the wanted pulses pass in the second amplification stage. This consists of the regenerative amplifier combined with a Mazzler which operates as a spectral amplitude filter. After traveling 14 round-trips in the regenerative amplifier, the ~0.5 mJ pulse passes through the last amplification stage that consists of two 3-pass amplifiers, ending up with an energy of 6 mJ per pulse. Finally, the pulse is recompressed via a double pass on a grating pair in parallel configuration giving pulses with 20 fs duration, 3.5 mJ energy and 1kHz repetition rate.

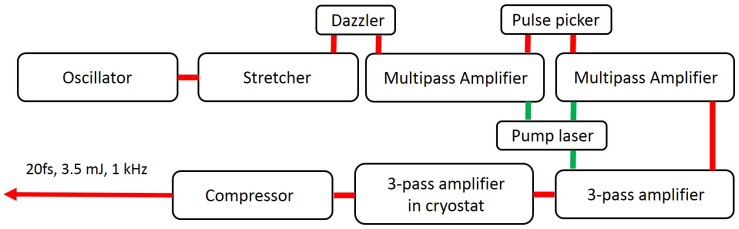

Figure 4.11: Outline of the 1 kHz CPA laser chain in Lund. Adapted from [Kroon, 2016].

RABBIT set up

The main design of the set up is very similar to the one in Attolab. The optical set up is schematically outlined in Figure 4.12. The initial beam is split by a 70:30 beam splitter and the most energetic part of the beam is used to generate the harmonics (pump beam) while the rest of the power is used as the probe beam. In the pump arm, the beam is first focused by an on-axis spherical mirror (f=50cm) into a pulsed gas cell, then the XUV is separated by a thin foil from the remaining IR and is refocused by a gold coated toroidal mirror (f=30 cm) in the interaction region of the MBES. The remaining 30% of the IR pulse goes into the probe arm of the interferometer and after passing through a piezo-controlled delay stage, the outer part of the beam is reflected off the recombination mirror and overlapped in time and space with the XUV beam in the MBES. The harmonics are simultaneously monitored on an XUV spectrometer mounted after the MBES.

The set up there is stabilized in two ways: 1. The initial IR beam is actively stabilized with an Aligna 4d beam pointing system at a frequency of 100 Hz. 2. A second interfometer is added to the beam-line in order to monitor and control the probe pulse delay (yellow beam-path in Figure 4.12). The part of the probe beam

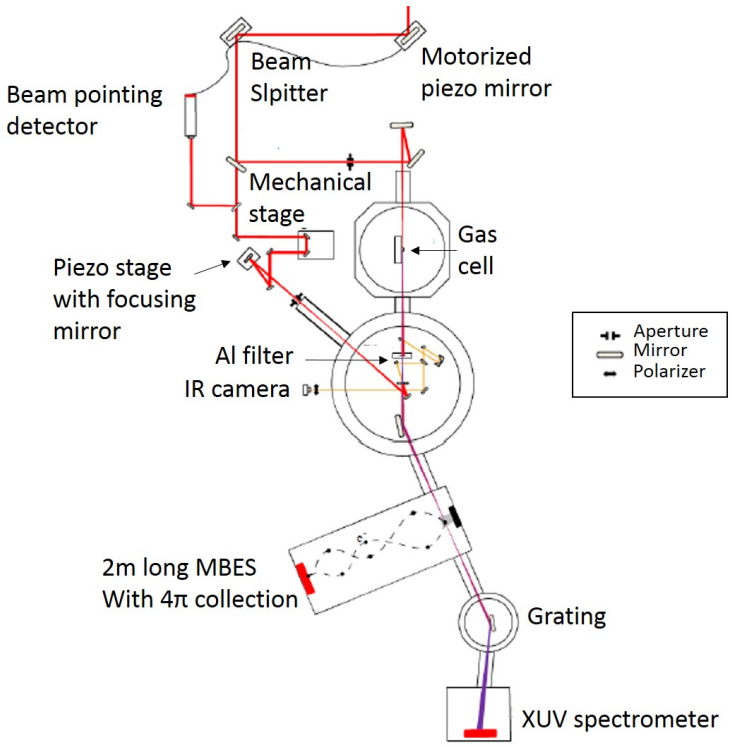

Figure 4.12: Attosecond beamline with RABBIT setup in Lund University. Adapted from [Marcus et al., 2017].

that leaks through the hole in the recombination mirror is combined on a beam splitter with a part of the generation beam picked off by a small d-shaped mirror. The two beams are then sent to a camera. The spatial interference pattern is then used in a feed-back loop that controls the piezo-electric delay stage of the probe arm. Thus for a measurement of 6 minutes the rms in the measured delay drops from 200 as to 50 as when the active stabilization is switched on.

CHAPTER 5

RAINBOW RABBIT METHOD

5.1 Rainbow RABBIT principle

Even though the 'classic' RABBIT technique detailed in Chapter 4.1, is well established and widely used it has a main drawback when it comes to cases of spectrally narrow features such as resonances. In such an occasion the phase *inside* the sidebands involving transitions through the resonant harmonic (Figure 5.1) will not be flat, on the contrary, it will have fast variations.When the atomic phase varies slowly in between two harmonic orders, the RABBIT technique allows a precise access to it with a sampling of 3 eV (for 800 nm fundamental wavelength). When faster variations occur, due to structural features such as Cooper minima or resonances, a finer sampling can be obtained by tuning the driving wavelength and performing RABBIT scans for different wavelengths. This is the approach chosen by Klünder *et al.* [Klünder et al., 2011]. However, when fast phase variation occur *within* the sideband width, the integration of the signal over this width, intrinsic to the RABBIT technique, leads to a smearing of the phase information. This restricts the access to the full ionization dynamics of the corresponding system.

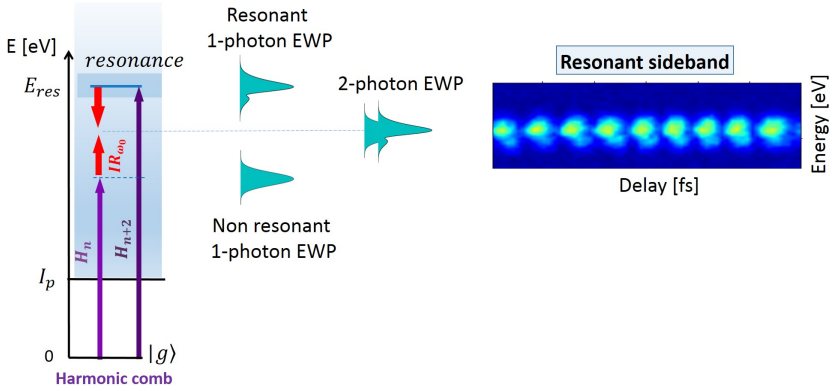

Figure 5.1: Schematic representation of the excitation of a spectrally narrow resonance by harmonic n+2. The spectral phase and amplitude of the structured resonant one-photon EWP will be 'transferred' to the resonant two-photon EWP (n+2 -IR), that interferes with the non-resonant EWP (n+IR). The sideband encodes the interference between these two quantum paths.

A solution to this challenge was proposed for the first time by Gruson and coworkers [Gruson et al., 2016a] who developed the spectrally resolved version of this technique, known as the Rainbow RABBIT. Its principle is shown schematically in Figure 5.2. In contrast to the regular RABBIT, in order to extract the corresponding

spectral phases and amplitudes a Fourier transform is applied on the $2\omega_0$ oscillations at each energy E inside the sideband's spectral width.

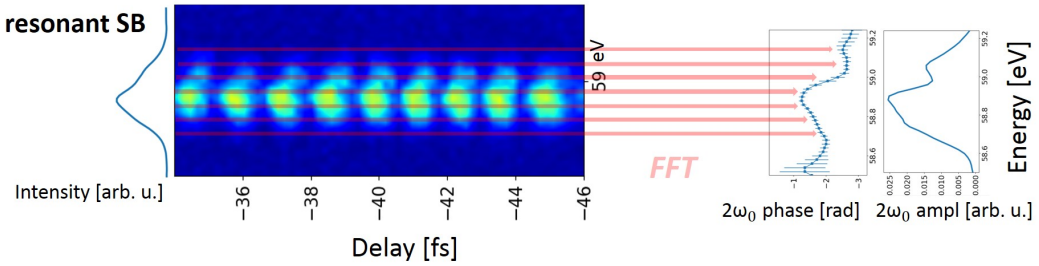

Figure 5.2: Rainbow RABBIT principle on a resonant sideband: For each energy in the spectral width of the sideband, a fourier transform is applied and the total evolution of the spectral phase and amplitude can be retrieved.

To make the difference between the two methods more clear let us consider $S_{(n+1)}(\tau,E)$ the signal of a resonant sideband. Monitoring its $2\omega_0$ oscillations as τ varies, gives access to the total phase $\Phi_{(n+1),tot}(E) = \Delta\phi_{(n+1),XUV}(E) + \Delta\phi_{(n+1),atom}(E)$. Assuming the variations of the harmonic phase difference $\Delta\phi_{(n+1),XUV}(E) = \phi_{(n+2),XUV}(E) - \phi_{(n),XUV}(E)$ over the sideband width to be very small and considering that for $\Delta\phi_{(n+1),atom}(E) = \phi_{(n+2)-1,atom}(E) - \phi_{(n)+1,atom}(E)$, the atomic phase $\phi_{(n)+1,atom}(E)$ varies smoothly since it is related to the transition through the non resonant harmonic H_n (Figure 5.1), the phase measured with the Rainbow RABBIT method will eventually become $\Phi_{(n+1),tot}(E) \propto \phi_{(n+2)-1,atom}(E) + constant$. Similarly, the phase measured in the sideband 'above' the resonant harmonic H_{n+2} writes: $\Phi_{(n+3),tot}(E) \propto -\phi_{(n+2)+1,atom}(E) + constant$. These phases correspond to the intrinsic phases of the resonant 2-photon EWPs.

On the other hand, the phase measured by the 'classic' RABBIT can be written as $\overline{\Phi_{(n+1),tot}} = arg_{2\omega_0}[FT_\tau(\int S_{(n+1)}(\tau,E)dE)] = \Delta\overline{\phi_{(n+1),XUV}} - \Delta\overline{\phi_{(n+1),atom}}$. The 'mean' phases in this equation are not equivalent to the averages over the sideband width of the corresponding spectrally-resolved phases. In non-resonant conditions (small $\Delta\overline{\phi_{(n+1),atom}}$), the RABBIT phase is dominated by the mean phase difference of consecutive harmonics. The latter displays a linear spectral variation inherited from the harmonic generation process, and related to the so-called attochirp (see Chapter 2.1.4). In order to correct $\overline{\Phi_{(n+1),tot}}$ from this contribution and access the atomic phase $\Delta\overline{\phi_{(n+1),atom}}$, it is needed to measure the RABBIT phase of nonresonant sidebands and interpolate in order to get a trustable estimate of the attochirp that is very sensitive to the actual generation conditions. The mean scattering phase $\Delta\overline{\phi_{(n+1),atom}}$ then appears in the measurement as a deviation from this linear spectral variation (Figure 5.3). Note that the sideband phase variation induced by the attochirp within the sideband width is very small so that is does not affect the energy-resolved phase $\Phi_{(n+1),tot}(E)$ measured by the Rainbow RABBIT except for a shift of the phase origin [Gruson et al., 2016b].

Figure 5.3, demonstrates schematically the above discussion for the case of sp2+ Fano resonance in helium. This resonance occurs at 60.15 eV and has a narrow spec-

tral width of 37 meV (for comparison the spectral width of our sidebands is ~1 eV). When using the 'classic' RABBIT method, we measure the sideband phases $\overline{\Phi_{n+1,tot}}$, with the magenta dashed line being the linear slope due to the term $\Delta\overline{\phi_{(n+1),XUV}}$ that is related to the attochirp as mentioned above. The deviation of the blue circles from the magenta line then, corresponds to the energy-integrated atomic phase $\Delta\overline{\phi_{(n+1),atom}}$. For a driving wavelength of 800 nm, the resonant sidebands are SB38 and SB40. The presence of the resonance is then clear with the corresponding sideband phases exhibiting a symmetric deviation from the linear behavior of about 0.5 rad. The insets show the same measurement conducted by the Rainbow RABBIT method. Here the energy-resolved atomic phase $\Delta\phi_{(n+1),atom}(E)$ within each sideband is directly measured. Now the entire evolution of this phase is recorded within the two resonant sidebands and shows an abrupt jump of ±1.4 rad . Note that the nonresonant ones exhibit a flat behavior as expected.

In order to access the spectral variation of $\Delta\overline{\phi_{n+1,atom}}$ around the resonance with the standard RABBIT, a number of traces have to be recorded when tuning the driving wavelength so that the resonant harmonic H_n scans the resonance, as first performed by Kotur *et al.* [Kotur et al., 2016].

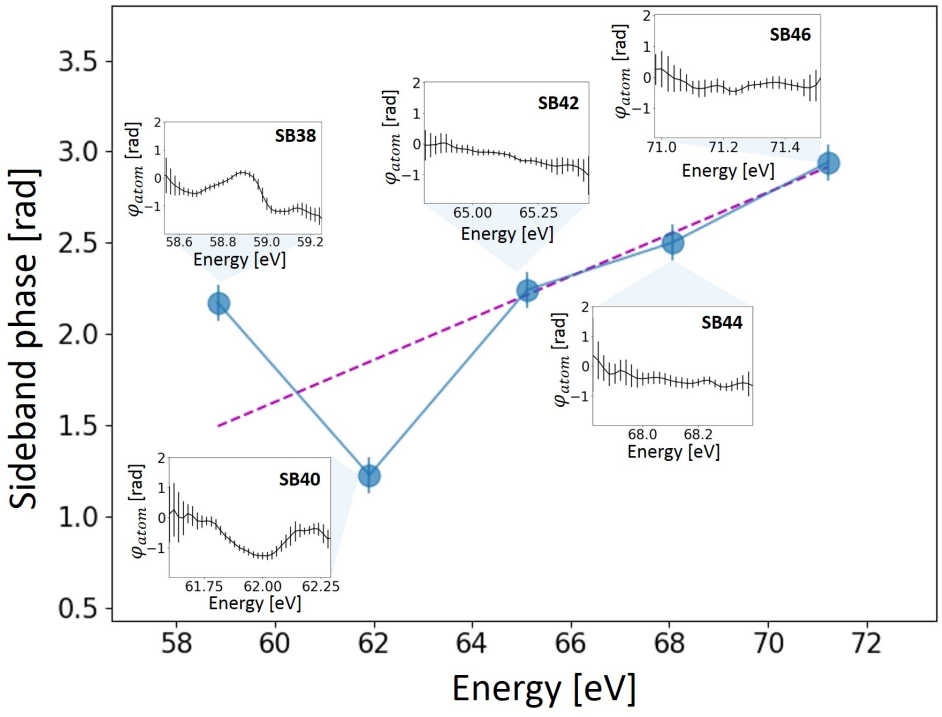

Figure 5.3: Classic RABBIT phase measurement for the sp2+ Fano resonance in helium. The insets show the corresponding Rainbow RABBIT measurements. For a driving wavelength of 800 nm, the resonance is excited by H39.

In the same spirit Gruson *et al.* [Gruson et al., 2016b] by using the tunability of an OPA, they scanned the resonance and for each wavelength measured the phase of

the resonant sidebands with the 'classic' RABBIT. For the driving wavelengths used (λ= 1305 nm -1285 nm) the resonant sidebands are SB62 and SB64. The variation of $\Delta\overline{\phi_{(n+1),atom}}$ inferred from the SB62 and SB64 RABBIT phases at several driving wavelengths is plotted in Figure 5.4 against each sideband's central energy. The comparison with the spectrally-resolved analysis is instructive: the phase jump occurring when H63 scans the resonance is much broader and of smaller amplitude in the RABBIT measurement than in the spectrally resolved one. This is a consequence of the integration of the signal over the sideband spectral bandwidth (dominated by the 400-meV width of the resonant harmonic H63), which 'dilutes' the phase distortions that occur within the much narrower resonance width. The phase at the maximum of the resonant amplitude thus plays a dominant role in determining the spectral variation of $\Delta\overline{\phi_{(n+1),atom}}$ that consequently does not reflect the actual shape of $\Delta\phi_{(n+1),atom}(E)$. In these conditions, $\Delta\overline{\phi_{(n+1),atom}}$ is therefore only approximately representative of the full EWP phase. Using harmonics spectrally much narrower than the resonance width and finely tuning the driving wavelength would allow performing more accurate measurements of $\Delta\phi_{(n+1),atom}(E)$.

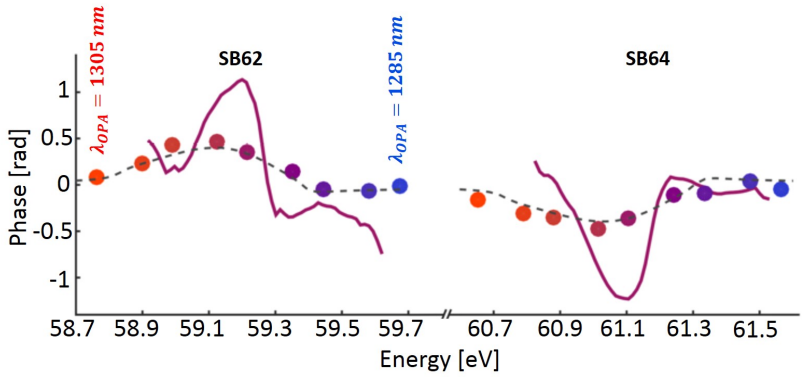

Figure 5.4: Experimental (colored circles) and theoretical (black dashed line) phase $\Delta\overline{\phi_{(n+1),atom}}$ extracted from RABBIT scans at different OPA wavelengths for SB62 and SB64, as compared to the experimental (violet line) phase $\Delta\phi_{(n+1),atom}(E)$ measured with the spectrally-resolved technique at λ_{OPA} = 1295 nm. All these phases are directly obtained from the phase of the sidebands after removal of the linear group delay of the exciting harmonic radiation, which sets the phase origin to 0. For the experimental $\Delta\overline{\phi_{(n+1),atom}}$, each point corresponds to a generating wavelength. The energy axis is the corresponding SB62/ SB64 central energy for each wavelength. Figure taken from Ref. [Gruson et al., 2016b].

5.2 Reconstruction of the two-photon EWP in the spectral domain

Here we will discuss how from the spectral amplitudes and phases measured by the Rainbow RABBIT one can access the resonant two-photon EWP. To facilitate the discussion we will consider the specific case where a resonance is involved as

depicted in Figure 5.1

The measured spectrogram provides SB signals S_{n+1} resulting from the coherent superposition of two different two-photon EWPs. If the exciting harmonic and IR fields had finite short pulse durations, the corresponding transition amplitudes would be calculated by convolving the two-photon transition matrix element with the field spectra (see Chapter 6.2.1.3 for details). In the case where the spectral width of the IR field is much smaller than the harmonic and resonance widths, one recovers a simplified expression for the sideband intensity where the different phase contributions are nicely separated [Véniard et al., 1996].

We then rewrite equation 4.1:

$$S_{(n+1)}(\tau,E) = |M^{(2)}_{(n)+1}(E)|^2 + |M^{(2)}_{(n+2)-1}(E)|^2$$
$$+2|M^{(2)}_{(n)+1}(E)||M^{(2)}_{(n+2)-1}(E)|cos(2\omega_0\tau + \Delta\phi_{(n+1),XUV}(E) + \Delta\phi_{(n+1),atom}(E)), \quad (5.1)$$

where $M^{(2)}_{(n)+1}(E)$ and $M^{(2)}_{(n+2)-1}(E)$ are the two-photon transition amplitudes associated with the two paths and the two phase terms write: $\Delta\phi_{(n+1),XUV}(E) = \phi_{(n+2),XUV}(E+\hbar\omega_0) - \phi_{(n),XUV}(E-\hbar\omega_0)$ and $\Delta\phi_{(n+1),atom}(E) = \phi_{(n+2)-1,atom}(E) - \phi_{(n)+1,atom}(E)$. In this interferometric scheme, we consider the resonant $M_{(n+2)-1}(E)$ to be probed by the non-resonant $M_{(n)+1}(E)$. The aim is thus to retrieve $|M_{(n+2)-1}(E)|$ and $\phi_{(n+2)-1,atom}(E)$ out of the measurements and access the 'intrinsic' two-photon EWP that would result from Fourier- limited excitation:

$$M^{(2)}_{(n+2)-1}(E) = |M^{(2)}_{(n+2)-1}(E)|e^{i\phi_{(n+2)-1,atom}(E)} \quad (5.2)$$

Phase As stated earlier $\Phi_{(n+1),tot}(E) = \Delta\phi_{(n+1),XUV}(E) + \Delta\phi_{(n+1),atom}(E) \propto \phi_{(n+2)-1,atom}(E)$. For this relation to be valid,some approximations were made

we assumed that the variations within the sideband spectral width, the harmonic phase difference is negligible and that the 'non-resonant' atomic phase $\phi_{(n)+1,atom}$ is also small compared to the 'resonant' $\phi_{(n+2)-1,atom}$.

i) As stated above, we assumed the variations within the sideband spectral width of the harmonic phase difference $\Delta\phi_{(n+1),XUV}(E)$ to be very small as compared to the variations of the atomic phase difference $\Delta\phi_{(n+1),atom}(E)$ – since the latter is strongly affected by the resonant transition through harmonic $H_{(n+2)}$. We therefore neglect $\Delta\phi_{(n+1),XUV}(E)$ and consider $\Phi_{(n+1),tot}(E) = \phi_{(n+2)-1,atom}(E) - \phi_{(n)+1,atom}(E)$.

ii) Since the transition through harmonic $H_{(n)}$ involves a smooth continuum, we expect the variations of $\phi_{(n)+1,atom}$ to be very small compared to the resonance-driven ones of $\phi_{(n+2)-1,atom}$ so that we neglect it. Subsequently, we consider the mea-

sured Rainbow RABBIT phase to be the phase of the probed EWP: $\Phi_{(n+1),tot}(E) \propto \phi_{(n+2)-1,atom}(E)$.

Amplitude The Rainbow RABBIT trace provides the intensity of each sideband averaged over the delay τ:

$$I_{(n+1)}(E) = \left|M^{(2)}_{(n)+1}(E)\right|^2 + \left|M^{(2)}_{(n+2)-1}(E)\right|^2 \tag{5.3}$$

as well as its $2\omega_0$-oscillation amplitude:

$$A_{(n+1)}(E) = 2|M^{(2)}_{(n)+1}(E)||M^{(2)}_{(n+2)-1}(E)|. \tag{5.4}$$

In principle, this set of equations gives access to the modulus of the two interfering EWP, $|M^{(2)}_{(n)+1}(E)|$ and $|M^{(2)}_{(n+2)-1}(E)|$. However, the presence of a spurious background in the spectra may prevent the accurate evaluation of the average intensity $I_{(n+1)}(E)$, such that approximate methods relying solely on the $2\omega_0$-component of the sidebands could be more efficient for retrieving $|M^{(2)}_{(n+2)-1}(E)|$.

A first approach is to assume that the non-resonant EWP $|M^{(2)}_{(n)+1}(E)|$ displays a smooth gaussian shape, so that its variations within the width of the resonant EWP could be neglected, which means:

$$A_{(n+1)}(E) \propto |M^{(2)}_{(n+2)-1}(E)| \tag{5.5}$$

An alternative method consists in calibrating the EWP of interest using a neighboring non-resonant sideband, with assumptions reminiscent of the soft-photon approximation [Maquet and Taïeb, 2007]. For sideband $S_{(n-1)}(E)$ equation 5.4 will be:

$$A_{(n-1)}(E - 2\hbar\omega) = 2|M^{(2)}_{(n)-1}(E - 2\hbar\omega)||M^{(2)}_{(n-2)+1}(E - 2\hbar\omega)| \tag{5.6}$$

with the two paths '(n)-1' and '(n-2)+1' being non-resonant. Far from the ionization threshold, one can consider the amplitudes of the two paths involving the same harmonic equal and simply shifted by the energy of two IR photons

$$|M^{(2)}_{(n)+1}(E)| \approx |M^{(2)}_{(n)-1}(E - 2\hbar\omega)|. \tag{5.7}$$

In addition, if the harmonics $H_{(n)}$ and $H_{(n)-2}$ have similar profiles, we can approximate:

$$|M^{(2)}_{(n)-1}(E - 2\hbar\omega)| \approx |M^{(2)}_{(n-2)+1}(E - 2\hbar\omega)|. \tag{5.8}$$

Thus, the 2ω amplitude of sideband $S_{(n-1)}$ can be written as:

$$A_{(n-1)}(E - 2\hbar\omega) = 2\left|M^{(2)}_{(n)+1}(E - 2\hbar\omega)\right|^2. \tag{5.9}$$

After inserting equation 5.9 in 5.4, one finally gets:

$$|M^{(2)}_{(n+2)-1}(E)| = \frac{A_{(n+1)}(E)}{2|M^{(2)}_{(n)+1}(E-2\hbar\omega)|} \tag{5.10}$$

$$\Downarrow$$

$$|M^{(2)}_{(n+2)-1}(E)| = \frac{A_{(n+1)}(E)}{\sqrt{2A_{(n-1)}(E-2\hbar\omega)}}. \tag{5.11}$$

This approach is in principle more accurate, but it is expected that the corresponding amplitude will be more sensitive to the experimental noise and possible spectral resolution variations of the electron spectrometer [Gruson et al., 2016b].

The Rainbow RABBIT method is utilized throughout this thesis. Its implementation in different experimental set ups and conditions did not alter neither the procedure nor the physical meaning of the results showing its robustness. Additionally, it is a versatile technique since it can serve various measurement purposes. For example in Chapter 6 Rainbow RABBIT is used to measure the spectral phases and amplitudes in the vicinity of autoionizing resonances as in [Gruson et al., 2016a],[Busto et al., 2018] and [Kotur et al., 2015]. In Chapter 7 on the other hand, the technique is used to spectrally isolate the contribution of the almost overlapping 3s and 3p ionization channels of argon close to the corresponding two Cooper minima. Nevertheless there are still a number of different experimental aspects that could affect the phase and amplitude extraction that will be discussed in detail in the following Chapter (see section 6.2.1).

Part IV

Ionization dynamics close to strong structural features

CHAPTER 6

AUTOIONIZING DYNAMICS IN HELIUM AND ARGON

Autoionizing dynamics is a topic of broad and current interest in attosecond science, since it can serve as a fine probe of electron-electron interactions. An autoionizing resonance can be seen as the result of a quantum interference. In Figure 6.1, the case of the sp2+ resonance at 60.15 eV in helium, is schematically shown as an example. After the absorption of an XUV photon of such energy by the helium atom there are two possibilities: (1) One of the electrons can be sent directly to the continuum leaving the rest of the system in the He^{+1} state or (2) both electrons will be excited to the sp2+ (also written as 2s2p) doubly excited state that is coupled to the $1s$ continuum by configuration interaction. It will decay with a 17 fs lifetime by liberating one electron to the continuum and returning the other one to the $He^{+}1s$ state. These direct and indirect ionization paths end up at the same final energy and interfere.

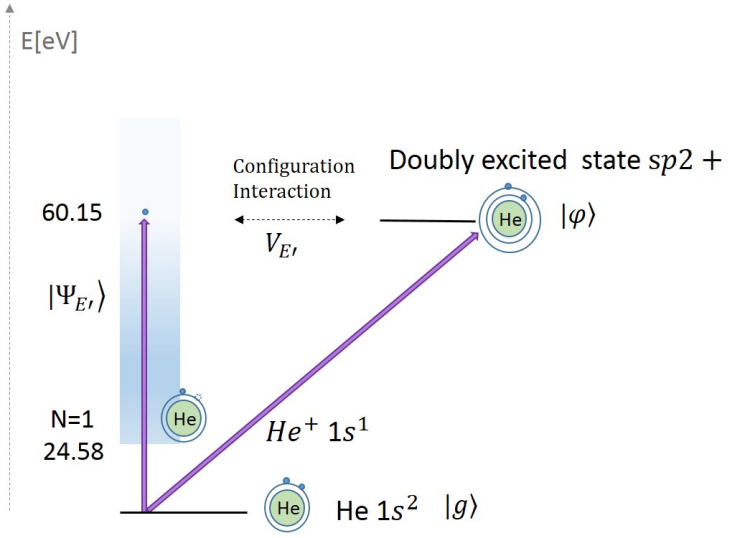

Figure 6.1: Schematic representation of the sp2+ autoionizing resonance in helium. Where $|\Psi_{E'}\rangle$ are the continuum states, $V_{E'}$ is the configuration interaction matrix element and $|\phi\rangle$ and $|g\rangle$ are the discrete and ground state respectively.

Historically, the first observation of an autoinizing resonance, was in 1935 when H. Beutler [Beutler, 1935] measured the absorption spectra of argon, krypton and xenon and observed unusual asymmetric peak profiles as presented in Figure 6.2. However, it was not until almost thirty years later that a theoretical explanation of this phenomenon was published by Ugo Fano using configuration interaction in [Fano, 1961] (this was actually an upgraded version of his first paper [Fano, 1935]

published in 1935 in Italy). Since then, a vast number of studies both theoretical and experimental has been performed concerning this type of resonances, today known as the 'Fano resonances'. A broad spectrum of scientific areas is covered; from attosecond atomic and molecular spectroscopy ([Gruson et al., 2016a], [**?**]) to studies where Fano resonances have been utilized as potential candidates to build a wide range of biomedical sensors probed by THz radiation ([Singh et al., 2014]). For a review of the generality and wide applicability of the Fano formalism from molecules and nanostructures to surfaces, see the review article of Ref. [Miroshnichenko et al., 2010].

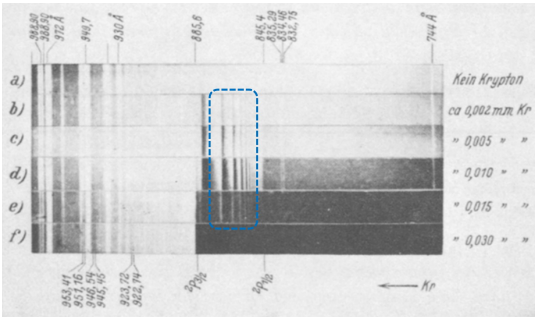

Figure 6.2: Krypton absorption spectra measured by [Beutler, 1935].

In this chapter the photoionization dynamics in the vicinity of different Fano resonances in the simple system of helium as well as in the more complex argon atom will be studied. The chapter is structured as follows:

First, the principles of Fano's theoretical model will be briefly presented. Then, we concentrate on the *helium* atom and by using the prototype example of the sp2+ resonance, a detailed study of the effect of different experimental parameters on the retrieved spectral amplitudes and phases by the Rainbow RABBIT method will be presented. Since Rainbow RABBIT is used throughout this thesis, it is of great importance to be able to disentangle the physical processes from the measurement-induced features that could lead to the misinterpretation of the measured EWP dynamics. Later on, Rainbow RABBIT measurements close to the independently ionized single resonances sp2+ and sp3+ are presented along with different types of representation of the corresponding ionization dynamics (i.e. temporal reconstruction of the ejected EWP, Gabor and Wigner-Ville representations). The effect of the increasing dressing beam intensity on the line-shape of the sp2+ resonance as well as on the spectral phase of the resonant EWP is also studied. Finally, the dynamics of the complex EWP created after the simultaneous excitation of both sp2+ and sp3+ resonances is presented.

The second part of the chapter is dedicated to *argon* and the study of the ionization dynamics around the 3s4p Fano resonance. The main complexity of this system comes from its spin-orbit splitting of only 180 meV. We first discuss a method to isolate numerically the two S-O components and then the measured Rainbow RABBIT phases and amplitudes, resolved for each S-O component are presented along with the temporal reconstruction of the resonant EWP. Finally, our preliminary sim-

ulations developed in order to better understand the measured spectral phases are detailed.

6.1 Theoretical aspects

6.1.1 Fano's original work

Eigenfunctions

In this section the formalism of [Fano, 1961] and [Maquet, 2015] will be used.
Fano's theory of configuration interaction describes an atomic system that consists of a discrete state $|\phi\rangle$ which is coupled to a continuum with states $|\psi_{E'}\rangle$, by $V_{E'}$. This means that the energy E_ϕ of the bound state is degenerate with the energetic spectrum E of the continuum states. Neither $|\phi\rangle$ nor $|\psi_{E'}\rangle$ are eigenstates of the complete system. However, these states can be chosen as a full basis set into which the new eigenstate $|\Psi_E\rangle$ is expanded. In Fano's original treatment, the problem is described in a time independent manner, expressed in the energy domain.

In the absence of any external field the Hamiltonian $\hat{H}_0$ needs to be diagonalized, one has:

$$\langle\phi|\hat{H}_0|\phi\rangle = E_\phi \tag{6.1}$$
$$\langle\psi_{E'}|\hat{H}_0|\psi_{E''}\rangle = E'\delta(E'' - E') \tag{6.2}$$
$$\langle\psi_{E'}|\hat{H}_0|\phi\rangle = V_{E'} \tag{6.3}$$

with δ being the Dirac function. The off-diagonal term $V_{E'}$ is the configuration interaction matrix element which describes the interaction of the discrete state at energy E_ϕ with a continuum state at energy E', therefore in general depends on E'. The eigenstates $|\Psi_E\rangle$ of the system can be expanded in a complete basis set of this form:

$$|\Psi_E\rangle = a_E|\phi\rangle + \int b_{E'}|\psi_{E'}\rangle dE' \tag{6.4}$$

and the task now will be to define the energy-dependent expansion coefficients a_E and $b_{E'}$ which are determined as solutions of this system of equations:

$$a_E E_\phi + \int b_{E'} V^*_{E'} dE' = E a_E \tag{6.5}$$
$$a_E V_{E'} + b_{E'} E' = E b_{E'} \tag{6.6}$$

.

This will result in the following formal solution of $b_{E'}$ involving the z(E) function to be determined:

$$b_{E'} = \left(\frac{1}{E - E'} + z(E)\delta(E - E') \right) V_{E'} a_E \tag{6.7}$$

To determine the function z(E) one needs to substitute $b_{E'}$ given in equation 6.7 in the expression 6.5 which will now become:

$$a_E E_\phi + a_E \underbrace{\mathcal{P} \int \frac{|V_{E'}|^2}{E - E'} dE'}_{F(E)} + a_E z(E) \int \delta(E - E') |V_{E'}|^2 dE' = E a_E \tag{6.8}$$

$$z(E) = \frac{E - E_\phi - \mathcal{P} \int \frac{|V_{E'}|^2}{E - E'} dE'}{|V_{E'}|^2}, \tag{6.9}$$

with F(E) being the energy shift between the resonance position and E_ϕ and $\mathcal{P}$ denotes the principle value of the integral, i.e. circumventing the pole at E=E′ via integration in the complex plane. To find a_E, one needs to normalize the $|\Psi_E\rangle$ which in its final form will be:

$$|a_E|^2 = \frac{1}{|V_E|^2 (\pi^2 + z(E)^2)} = \frac{|V_E|^2}{(E - E_\phi - F(E))^2 + \pi^2 |V_E|^4} \tag{6.10}$$

which can be seen as a Lorentzian with FWHM given by $\Gamma = 2\pi |V_E|^2$. If the states $\psi_{E'}$ are represented by wavefunctions with asymptotic behavior then at large distance r we can write:

$$\psi_{E'}(r \to \text{inf}) \propto \frac{1}{r} sin(k(E')r + \delta). \tag{6.11}$$

Inserting equation 6.11 in equation 6.7 will give the following result:

$$\begin{aligned} \int b_{E'} |\psi_{E'}\rangle dE' &\propto \int b_{E'} sin(k(E')r + \delta) dE' \\ &\propto \mathcal{P} \int V_{E'} a_E sin(k(E')r + \delta) dE' \\ + \int V_{E'} a_E sin(k(E')r + \delta) z(E) \delta(E - E') dE' \end{aligned} \tag{6.12}$$

and if $V_{E'}$ cancels out quickly for $E' \neq E$ then equation 6.12 will become:

$$\int b_{E'} |\psi_{E'}\rangle dE' \propto V_E a_E [-\pi cos(k(E)r + \delta) + z(E) sin(k(E)r + \delta)] \tag{6.13}$$

which after defining $tan(\Delta) = -\frac{\pi}{z(E)} = -\frac{\pi|V_E|^2}{E-E_\phi-F(E)} = -\frac{\Gamma/2}{E-E_\phi-F(E)}$ can be rewritten as:

$$\int b_{E'}|\Psi_{E'}\rangle dE' \propto V_E a_E sin(k(E)r + \delta + \Delta)] \tag{6.14}$$

with the Δ being interpreted as the phase shift due to the configuration interaction of $|\psi_{E'}\rangle$ with the discrete state $|\phi\rangle$. By using the phase shift Δ one can rewrite the expressions of a_E and $b_{E'}$ as:

$$|a_E|^2 = \frac{1}{|V_E|^2 \pi^2(1 + 1/tan^2\Delta)} \tag{6.15}$$

hence

$$a_E = \frac{sin\Delta}{\pi V_E} \quad \text{and} \quad b_{E'} = \frac{V_{E'} sin\Delta}{\pi V_E}\frac{1}{E-E'} - cos\Delta\delta(E-E'). \tag{6.16}$$

Finally, the wavefunction $|\Psi_E\rangle$ will become:

$$|\Psi_E\rangle = \frac{sin\Delta}{\pi V_E}|\phi\rangle + \int \left[\frac{V_{E'} sin\Delta}{\pi V_E}\frac{1}{E-E'} - cos\Delta\delta(E-E')\right]|\psi_{E'}\rangle dE' \tag{6.17}$$

Cross-section

The excitation probability of the stationary state $|\Psi_E\rangle$, may be represented as the square matrix element of a transition operator $\hat{T}$ between an initial state $|g\rangle$ and the Fano resonance $|\Psi_E\rangle$:

$$\langle\Psi_E|\hat{T}|g\rangle = \frac{sin\Delta}{\pi V_E^*}\langle\phi|\hat{T}|g\rangle + \frac{sin\Delta}{\pi V_E^*}\mathcal{P}\int dE'\frac{V_{E'}}{E-E'}\langle\psi_{E'}|\hat{T}|g\rangle - cos\Delta\langle\psi_E|\hat{T}|g\rangle \tag{6.18}$$

$$= \frac{sin\Delta}{\pi V_E^*}\langle\Phi|\hat{T}|g\rangle - cos\Delta\langle\psi_E|\hat{T}|g\rangle \tag{6.19}$$

where

$$|\Phi\rangle = |\phi\rangle + \mathcal{P}\int dE'\frac{V_{E'}}{E-E'}|\psi_{E'}\rangle \tag{6.20}$$

represents the discrete state $|\phi\rangle$ modified by a mixture with the continuum states due to configuration interaction. Thus the cross-section will be

$$\sigma \propto \left|\langle \Psi_E|\hat{T}|g\rangle\right|^2 \tag{6.21}$$

$$\propto \left|\frac{sin\Delta}{\pi V_E^*}\langle\Phi|\hat{T}|g\rangle - cos\Delta\langle\psi_E|\hat{T}|g\rangle\right|^2 \tag{6.22}$$

$$\propto \left|\langle\psi_E|\hat{T}|g\rangle\right|^2 \times \left|\frac{sin\Delta}{\pi V_E^*}\frac{\langle\Phi|\hat{T}|g\rangle}{\langle\psi_E|\hat{T}|g\rangle} - cos\Delta\right|^2. \tag{6.23}$$

By defining $\sigma_0 \propto \left|\langle\psi_E|\hat{T}|g\rangle\right|^2$ and introducing the q asymmetry parameter as

$$q = \frac{1}{\pi V_E^*}\frac{\langle\Phi|\hat{T}|g\rangle}{\langle\psi_E|\hat{T}|g\rangle} \tag{6.24}$$

equation 6.23 becomes $\sigma = \sigma_0 \left|qsin\Delta - cos\Delta\right|^2$. Fano defines also the reduced energy ϵ as

$$\epsilon = -cos\Delta = \frac{E - E_\phi - F(E)}{\pi\left|V_E\right|^2} = \frac{E - E_\phi - F(E)}{\Gamma/2}. \tag{6.25}$$

Finally, the Fano profile is obtained by taking into account that $sin^2\Delta = 1/(1 + cos^2\Delta)$ as:

$$\sigma = \sigma_0\frac{(q+\epsilon)^2}{1+\epsilon^2} \tag{6.26}$$

Thus, the cross-section is defined by only the three parameters q, the resonant energy $E_R = E_\phi + F(E)$ and its spectral width Γ. By writing equation 6.24 in this way

$$\frac{1}{2}\pi q^2 = \frac{\left|\langle\Phi|\hat{T}|g\rangle\right|^2}{\left|\langle\psi_E|\hat{T}|g\rangle\right|^2\Gamma}, \tag{6.27}$$

it now becomes clear that the q parameter characterizes the ratio between the transition probabilities to the continuum-modified discrete state and to the continuum states. Different values of q correspond to different line profiles as is shown on Figure 6.3. One can see that the larger the q value the more asymmetric the line shape with the maximum value corresponding to $\epsilon = 1/q$ and the minimum to $\epsilon = -q$. The direction of the asymmetry has to do with the sign of the q parameter: when q is negative then the asymmetric peak falls at negative reduced energy values whereas positive q results in an asymmetric peak at the positive reduced energy side. In the particular case where $q = 0$ the cross-section takes the form of a well known 'window resonance' or 'anti-resonance'.

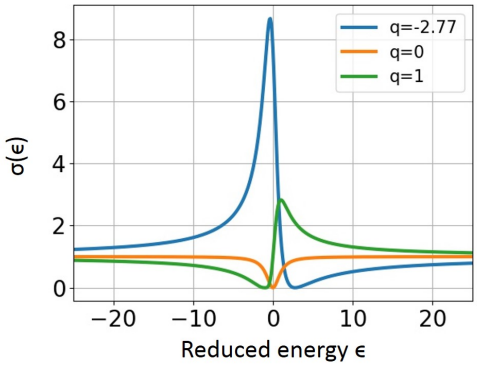

Figure 6.3: Absorption cross-sections for different q values.

6.1.2 Phase properties of the Fano transition amplitude

According to the work of [Jiménez-Galán et al., 2016], the Fano characteristic wave function can be written as:

$$|\Psi_E\rangle = \frac{\epsilon}{\epsilon - i}|\psi_E\rangle + \frac{1}{\pi V_E}\frac{1}{\epsilon - i}|\Phi\rangle \tag{6.28}$$

and thus the transition amplitude between the ground state $|g\rangle$ and $|\Psi_E\rangle$ will be:

$$M_k^{(1)} = \langle\Psi_E|\hat{T}|g\rangle = \frac{\epsilon}{\epsilon + i}\langle\psi_E|\hat{T}|g\rangle + \frac{1}{\pi V_E^*}\frac{1}{\epsilon + i}\langle\Phi_E|\hat{T}|g\rangle \tag{6.29}$$

$$= \langle\psi_E|\hat{T}|g\rangle\left(\frac{\epsilon + q}{\epsilon + i}\right) \tag{6.30}$$

$$= \langle\psi_E|\hat{T}|g\rangle \times \mathcal{R}(\epsilon). \tag{6.31}$$

One can see that the absolute value of this expression is the same as the Fano cross-section given by equation 6.26, however this form exposes its physical meaning [Gruson et al., 2016a]:

$$\mathcal{R}(\epsilon) = \frac{\epsilon + q}{\epsilon + i} = 1 + \frac{q - i}{\epsilon + i} \tag{6.32}$$

$$\Downarrow$$

$$|\mathcal{R}(\epsilon)|^2 = \left(1 + \frac{q^2 + 1}{1 + \epsilon^2} + \frac{2(q\epsilon - 1)}{1 + \epsilon^2}\right). \tag{6.33}$$

Equation 6.33 consists of three terms: the first term is a unit which corresponds to the contribution of the continuum, the second term is a Lorenzian that corresponds to the discrete state. The third term is due to the interference between the two former terms. The dipole phase will be:

$$\arg M_k^{(1)} = \arg \mathcal{R}(\epsilon) = \arctan \epsilon - \pi\Theta(\epsilon + q) + \pi/2 \tag{6.34}$$

where Θ is the so-called Heaviside function. In Figure 6.4 (b) we plot this phase for different q parameters.
The resonant Fano factor $\mathcal{R}(\epsilon)$ can be rewritten as a function of $(\epsilon - i)/(\epsilon + i)$:

$$\mathcal{R}(\epsilon) = \frac{1 - iq}{2} + \frac{1 + iq}{2}\frac{\epsilon - i}{\epsilon + i}. \tag{6.35}$$

This re-writing puts forward the fact that the trajectory of $\mathcal{R}(\epsilon)$ in the complex plane is a circle of center $1/2 - iq/2$, of radius $r = \sqrt{1+q^2}/2$, ending at 1 for $\epsilon = \pm\infty$ and intercepting the origin at $\epsilon = -q$. Figure 6.4 (a) illustrates the trajectories followed by $\mathcal{R}(\epsilon)$ for different values of q. Value $q = -2.77$ corresponds to the sp2+ resonance of helium, one of the cases that will be studied later in this chapter.

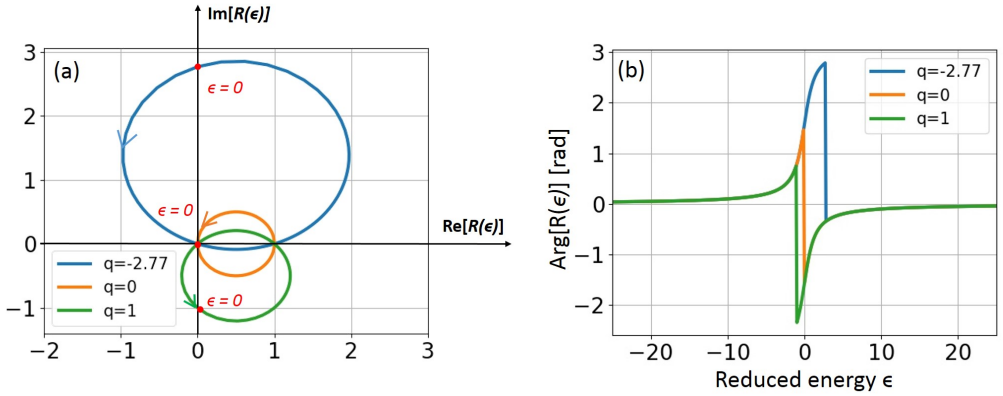

Figure 6.4: (a) Trajectories of the resonant Fano factor $\mathcal{R}(\epsilon)$ in the complex plane as a function of the reduced energy ϵ around the resonance ($\epsilon = 0$) and the corresponding phases (b) for different q values. Figure adapted from [Jiménez-Galán et al., 2016].

6.1.3 Resonant two-photon transition amplitude

In the previous section, the phase of the one-photon transition in the vicinity of a Fano resonance was extracted according to the work of Fano and its interpretation by [Jiménez-Galán et al., 2016]. This phase information however is lost in classic absorption spectroscopy experiments where it is possible to measure only the cross-section. On the contrary, the RABBIT technique presented in Chapter 4.1, provides access to the phase of the two-photon dipole matrix element. In specific cases where the continuum is flat and the atomic potential is described as Coulombic, these phases can be related to the corresponding one-photon dipole phases. The link between the one- and two-photon dipole matrix phase in the vicinity of a Fano resonance has been studied extensively by the group of F. Martin. In this section the specific work of [Jiménez-Galán et al., 2016], and [Jiménez-Galán et al., 2014] will be briefly presented.

Here, one seeks a simple expression of the two-photon photoionization matrix element $M^{(2)}_{\vec{k}}$, which can be obtained by using second-order time-dependent pertur-

bation theory. This will be :

$$M^{(2)}_{\vec{k},Fano} = \frac{1}{i}\mathcal{E}_\Omega\mathcal{E}_\omega \lim_{a\to 0^+} \sum\!\!\!\!\!\!\int \frac{\langle\vec{k}|z|\Psi_E\rangle\langle\Psi_E|z|g\rangle}{E_g+\Omega-E_v+i\alpha}, \tag{6.36}$$

where $|\vec{k}\rangle$ and $|\Psi_E\rangle$ are the final and intermediate states respectively, $\mathcal{E}_\Omega$,$\mathcal{E}_\omega$ are the spectral amplitudes of the XUV and IR fields and Ω, ω denote the XUV and IR photon frequencies. After replacing $|\Psi_E\rangle$ (equation 6.28) in expression 6.36 and by considering the case of a resonant two-photon transition where the XUV photon is absorbed before the IR probe photon, following a long demonstration it can be shown that in the case where there is no resonance in the final state, the expression of the two-photon transition amplitude will be:

$$M^{(2)}_{\vec{k},Fano} \approx \frac{1}{i}\mathcal{E}_\Omega\mathcal{E}_\omega \frac{\langle\vec{k}|z|\psi_E\rangle\langle\psi_E|z|g\rangle}{\omega} \times \frac{\epsilon+q(1-\gamma)+i\gamma}{\epsilon+i}. \tag{6.37}$$

For this expression to be valid another important condition that should be fulfilled is that the duration of both XUV and IR pulses should be greater than the lifetime of the intermediate resonant state. A new parameter γ is introduced as:

$$\gamma = \frac{\langle\vec{k}|z|\phi\rangle}{\langle\vec{k}|z|\psi_E\rangle V_E/\omega}. \tag{6.38}$$

γ measures the ratio of the two transitions between the resonance and the final continuum. More specifically, the direct transition between the bound state and the continuum $\langle\vec{k}|z|\phi\rangle$ and the indirect transition that passes through the intermediate continuum involving the coupling between the bound state $|\phi\rangle$ and $|\psi_E\rangle$ followed by the radiative transition between between $|\psi_E\rangle$ and $|\vec{k}\rangle$, $\langle\vec{k}|z|\psi_E\rangle V_E/\omega$.

By comparing the result of equation 6.37 with the corresponding one-photon case (equation 6.30), one can clearly see the similarity. Thus we introduce a complex q effective parameter:

$$q_{eff} = q(1-\gamma)+i\gamma \tag{6.39}$$

which will result also in an effective resonant Fano factor:

$$\mathcal{R}_{eff}(\epsilon) = \frac{\epsilon+q_{eff}}{\epsilon+i} \tag{6.40}$$

$$= \gamma + (1-\gamma)\frac{\epsilon+q}{\epsilon+i} \tag{6.41}$$

$$= \gamma + (1-\gamma)\times\mathcal{R}(\epsilon). \tag{6.42}$$

The trajectories in the complex plane as well as the evolution of the phase for different values of γ and $q = 1$ are shown in Figure 6.5. If $\gamma = 0$ (orange curve), the intermediate bound state is not radiatively coupled with the state of the final continuum. In this case, we find $q_{eff} = q$ and thus the results of the one-photon case. However, when $\gamma \neq 0$, the complex trajectories no longer pass through the origin. In the case where $\gamma < 0$ (blue curve), the circle is widened compared to the case of $\gamma = 0$ and it cuts the real axis for $\epsilon = \gamma$ and 1, thus encircling the origin. In this case,

the two-photon transition phase has a sudden variation of 2π. Finally, when $\gamma > 0$ (green curve), the circle is contracted and misses the origin.

Moreover, since the value of γ is proportional to ω, the sign of γ for the emission of the second photon (IR) is opposite to that for absorption. In this case, both the complete 2π phase excursion and the finite phase excursion are present simultaneously and are observable on the two sidebands on either side of the resonance: $q^{\pm}_{eff} = q \mp 2(q - i)\beta\omega/\Gamma$, where β is a pure number that depends solely on the properties of the atomic system and is connected to γ by the expression: $\gamma = \frac{\omega\beta}{\Gamma/2}$.

Finally, the corresponding phases will be:

$$\arg M^{(2)}_{\vec{k},Fano} \approx \arg M^{(2)}_{\vec{k}} + \arg[\mathcal{R}_{eff}] \tag{6.43}$$

where

$$M^{(2)}_{\vec{k},Fano} \approx -\frac{1}{i}\mathcal{E}_{\Omega}\mathcal{E}_{\omega}\frac{\langle\vec{k}|z|\psi_E\rangle\langle\psi_E|z|g\rangle}{\omega} \times \mathcal{R}_{eff}, \tag{6.44}$$

with $M^{(2)}_{\vec{k}}$ being a two-photon transition element that involves only continuum states.

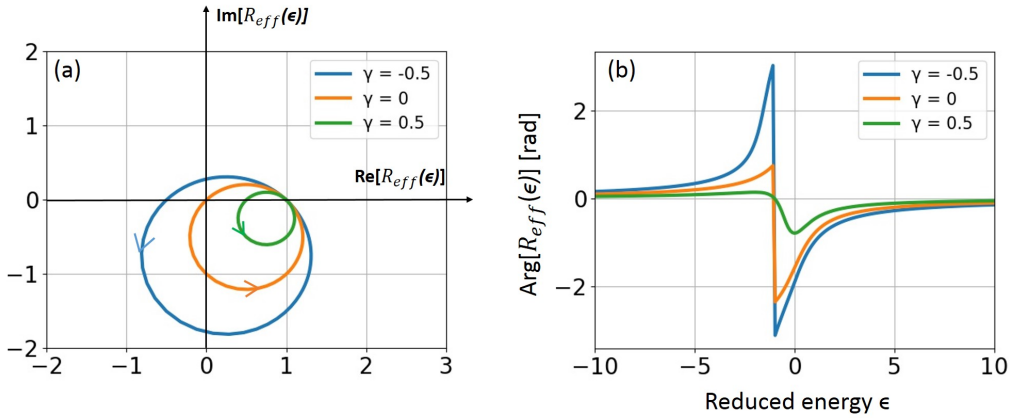

Figure 6.5: (a) Trajectories of the effective resonant Fano factor $\mathcal{R}_{eff}(\epsilon)$ in the complex plane as a function of the reduced energy ϵ around the resonance ($\epsilon = 0$) and the corresponding phases (b) for different γ values with constant q=1.

Multichannel case

The results obtained thus far are valid only for the case of a single intermediate and a single final continuum channel. However, when the Fano resonance is coupled to several continua, the system can be shown to be equivalent to an "interactive" continuum and a "non-interactive" continuum. So for the two-photon transition, one has:

$$M^{(2)}_{\vec{k},multichannel} \propto r + \frac{\epsilon + q_{eff}}{\epsilon + i} \tag{6.45}$$

with

$$r = \frac{\langle \vec{k}|z|\Psi_E^{non-int}\rangle\langle\Psi_E^{non-int}|z|g\rangle}{\langle \vec{k}|z|\Psi_E^{int}\rangle\langle\Psi_E^{int}|z|g\rangle}. \tag{6.46}$$

The constant term r expresses the strength of the dipolar coupling to the final continuum through 'non-interactive' intermediate continuum relative to the one through the 'interactive' continuum. The phase of $M^{(2)}_{\vec{k},multichannel}$ thus depends on the coupling with different continua [Jiménez-Galán et al., 2016].

6.1.4 Non monochromatic pulses

When non monochromatic XUV and IR pulses are used, they will obviously contain more frequency components than Ω_0 and ω_0, respectively. Therefore, for a given final energy in the sideband, the energy conservation condition will be satisfied by several different pairs of frequency components, which results in separate contributions that interfere to give rise to the total transition amplitude. A schematic representation of the effect is shown in Figure 6.6.

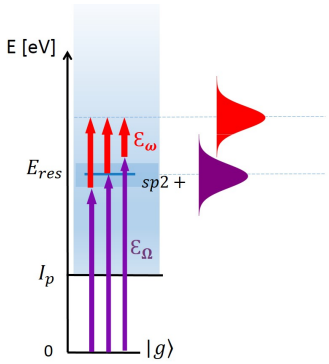

Figure 6.6: Schematic representation of the finite pulses effect. When the XUV and IR pulses are not monochromatic then many different energy combinations Ω+ω can lead to the same final state.

Jiménez-Galàn *et al.* [Jiménez-Galán et al., 2016] showed analytically that in the simple case of a non-resonant sideband, the finite pulse effects can be described as the convolution of the spectral envelopes of the harmonic and dressing beams with the harmonic pulse. However, this is not the case when intermediate resonant states are involved, because the two-photon transition matrix element has a sharp frequency dependence. In order to account for these effects one needs to sum coherently the contributions for all the possible combinations of the XUV+IR (Ω+ω) pulses for every final energy E_f in the resonant sideband. The two-photon transition amplitude of equation 6.36 will now become:

$$M^{(2)}_{\vec{k},Fano} \approx \frac{1}{i}\lim_{a\to 0^+}\int dE\mathcal{E}_\omega(E_f-E)\mathcal{E}_\Omega(E)\frac{\langle\vec{k}|z|\Psi_E\rangle\langle\Psi_E|z|g\rangle}{E_g+\Omega-E+i\alpha}. \tag{6.47}$$

6.2 Helium

The asymmetric Fano line shapes in helium were measured for the first time by Maden and Codling [Madden and Codling, 1963] a couple of years after the publication of the theoretical work of Fano. According to the theoretical explanation of Fano the autoionizing resonances are a very good example of electron-electron interaction however the synchrotron measurements of absorption spectroscopy experiments did not allow phase measurements and thus the study of the ionization dynamics of a system like this was only relying on theoretical models.

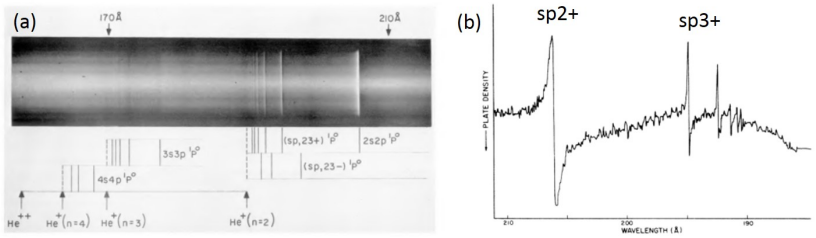

Figure 6.7: Absorption spectra of helium where the asymmetric line shapes of autoionization resonances are visible: (a) taken from Ref. [Madden and Codling, 1965] and (b)from Ref. [Madden and Codling, 1963].

Since then and with the advent of the XUV table top sources the Fano resonances in helium have been well studied. In 2014, Ott *et al.* [Ott et al., 2014] by performing transient absorption experiments were able to monitor the decay of a complex 2-electron wave packet including the effect of the sp2+ and sp3+ resonances. Two years later Gruson *et al.* [Gruson et al., 2016a] by using the Rainbow RABBIT method measured the spectral phase and amplitude of the ejected resonant EWP and reconstructed the build up of the resonance in the time domain. This study revealed a fast variation of the spectral phases as was predicted by theory [Jiménez-Galán et al., 2014], something that was previously measured in the case of argon [Kotur et al., 2016] . At the same time Kaldun *et al.* [Kaldun et al., 2016] could also study the buildup of the resonance using transient absorption experiments.

In the following subsections, after a study on the effect of different experimental parameters on our measurement technique, the Rainbow RABBIT, in the same context as the experiment of Gruson *et al.* we will study the dynamics of the sp2+ and sp3+ autoionization in helium, the influence of the intensity of dressing field on the line profiles and the corresponding spectral phases. A study on the simultaneous excitation of both resonances (sp2+ and sp3+) and their corresponding dynamics, will also be presented. The experiments that will be presented in this chapter are

a collaboration with the group of Anne L'Huillier from Lund University and the group of Reimund Feifel from Gotemburg University.

6.2.1 Study of the experimental limiting factors on Rainbow RABBIT measurements: *example on sp2+ Fano resonance in helium*

This section presents a detailed study on the influence of the experimental conditions on the spectral phase and amplitude extraction procedure via the Rainbow RABBIT technique. This will help to get a clear view on the potentials and drawbacks of the technique and could also serve as a 'textbook' for future experiments. The full mapping of the method is of great importance in order to distinguish the physical from the measurement-induced effects. We will study the influence of the following parameters: the spectrometer resolution, the spectral width of the resonant harmonic and the dressing pulses' as well as the energy position of the resonant harmonic. We will see that they can potentially distort both the retrieved spectral phase and amplitude and may lead later on to a misinterpretation of the corresponding dynamics. These aspects will be studied both theoretically and experimentally in the following sections. The Rainbow RABBIT algorithm used in this thesis was written in Python by Margherita Turconi based on the initial Matlab code of Thierry Ruchon.

As was detailed earlier in Chapter 5.1 the main advantage of this method is its capability of accessing directly the full evolution of the intrinsic atomic phase (Chapter 3) of the system under study, by spectrally resolving the $2\omega_0$ oscillations of the corresponding sidebands. This property becomes very useful in cases that involve spectrally narrow features as resonances that cause fast variations in the phase and structured amplitudes. For example in [Gruson et al., 2016a] and [Busto et al., 2018] the Rainbow RABBIT method was used to study the sp2+ autoionizing resonance of helium. As was already discussed earlier in this chapter, autoionization occurs when a system is excited in structured spectral regions where resonant states are embedded into a continuum. The system can then either be directly ionized or transiently remain in the resonant bound state before ionizing. The interference between these two quantum paths will give rise to a spectral amplitude with the characteristic asymmetric Fano line shape [Domke et al., 1996] and a spectral phase that exhibits a π jump around the resonance. These characteristics along with its small spectral width (Γ = 37meV), make the sp2+ resonance, the perfect candidate for this study. However these results are rather general, applicable to any case with similar features.

Simulation of a RABBIT spectrogram

In order to simulate a RABBIT trace of a resonant sideband, we use equation 4.1

rewritten as:

$$SB_R(\tau,E) = |M_{NR}|^2 + |M_R|^2 + 2|M_R||M_{NR}|cos(2\omega_0\tau + \underbrace{\Delta\phi_{XUV} + \Delta\phi_{atom}}_{\Delta\phi_{total}}). \tag{6.48}$$

As was discussed earlier in this chapter, the resonant two-photon transition amplitude (equation 6.37) is given by : $M_R \propto \mathcal{E}_{n+2}\mathcal{R}_{eff}$, with $\mathcal{R}_{eff}(\epsilon) = \frac{\epsilon+q_{eff}}{\epsilon+i}$ from equation 6.40 being the effective Fano factor expressed as a function of the reduced energy ϵ. The nonresonant two-photon transition amplitude is: $M_{NR} \propto \mathcal{E}_n$, with $\mathcal{E}_{n+2}$ and $\mathcal{E}_n$ being the electric fields of the resonant and nonresonant harmonic respectively. We then describe the ionizing harmonics as Gaussians:

$$\mathcal{E}_{harm}(E) = \frac{1}{s_{harm}\sqrt{2\pi}} e^{-(E-E_{harm})^2/2s_{harm}^2} \tag{6.49}$$

with

$$s_{harm} = \frac{FWHM_{harm}}{2\sqrt{2ln2}} \tag{6.50}$$

where E_{harm} is the central energy of the harmonic. For the purpose of this study the resonant harmonic will be scanned around the resonance: $E_{sp2+} = 60.15$ eV. The central energy of the resonant harmonic will then be called E_{tun}. The harmonic spectral width in intensity, $FWHM_{harm}$, will also be varied.

Since the phase between consecutive harmonics, in the Rainbow RABBIT analysis doesn't affect the extracted intra-harmonic phase apart from adding a global offset we assume here $\Delta\phi_{XUV} = 0$. This means that $\Delta\phi_{total} = arg[M_R] - arg[M_{NR}] \approx \Delta\phi_{atom} = arg[\mathcal{R}_{eff}]$. Here we consider the case where we excite the resonance from below. In the opposite case where the resonance is excited from above we would have $\Delta\phi_{atom} = -arg[\mathcal{R}_{eff}]$.

In Figure 6.8 we plot the experimentally measured RABBIT trace of the resonant sideband 38 and the corresponding retrieved spectral phase and amplitude along with the simulated ones. We observe significant differences: the experimental phase jump(1 rad) is less than the simulated one and the shape of the two $2\omega_0$ amplitudes differs. Moreover, the measured amplitude and phase appear to be smoother and less contrasted than the simulated ones in the ideal case. In order to better approach the experimental results we need to take into account a number of different experimental parameters as will be presented in the following sections.

6.2.1.1 Spectrometer resolution

The resolution of the detection system is one of the main factors that limits the spectral resolution of a RABBIT measurement. In [Gruson et al., 2016a] and [Busto et al., 2018] 2-m long MBES with energy resolution of 190 meV and 89 meV ±5 meV respectively, were used. In order to simulate this effect, the sideband signal (equation 6.48) is convoluted with the electron spectrometer response function f_{sp}

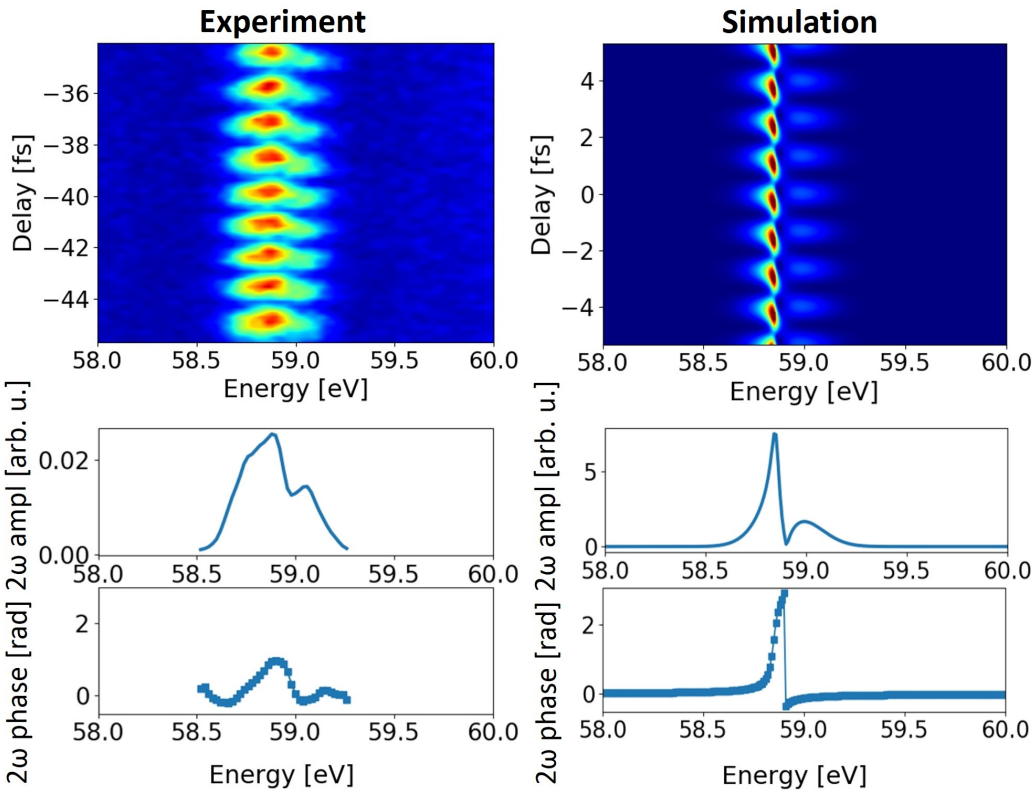

Figure 6.8: RABBIT traces of sideband 38 and the corresponding spectral phases and amplitudes retrieved by the Rainbow RABBIT method for experimental data (left panel) and simulation (right panel) for the sp2+ resonance in helium.

for each delay: $SB_R(\tau,E) \otimes f_{sp}$. We describe the response function as the following Gaussian:

$$f_{sp} = \frac{1}{s_{sp}\sqrt{2\pi}} e^{-E^2/2s_{sp}^2} \tag{6.51}$$

with

$$s_{sp} = \frac{FWHM_{sp}}{2\sqrt{2ln2}} \tag{6.52}$$

For this study the position of the harmonic with respect to the resonance along with the harmonic spectral width are kept constant (Etun = 60.22 eV, $FWHM_{harm}$ = 200 meV) while the spectrometer resolution $FWHM_{sp}$ is varied. By using the analysis described in the previous section (chapter 5.1) we extract the spectral amplitudes and phases reported in Figure 6.9.

In the spectral domain, the main effect of a low spectrometer resolution (increasing $FWHM_{sp}$), is the smoothing of both amplitude and phase. More specifically, the amplitude's asymmetric shape converges to a gaussian and the maximum signal level is decreased. The phase jump becomes less than π and is shifted towards higher energies following the local minimum of the amplitude caused

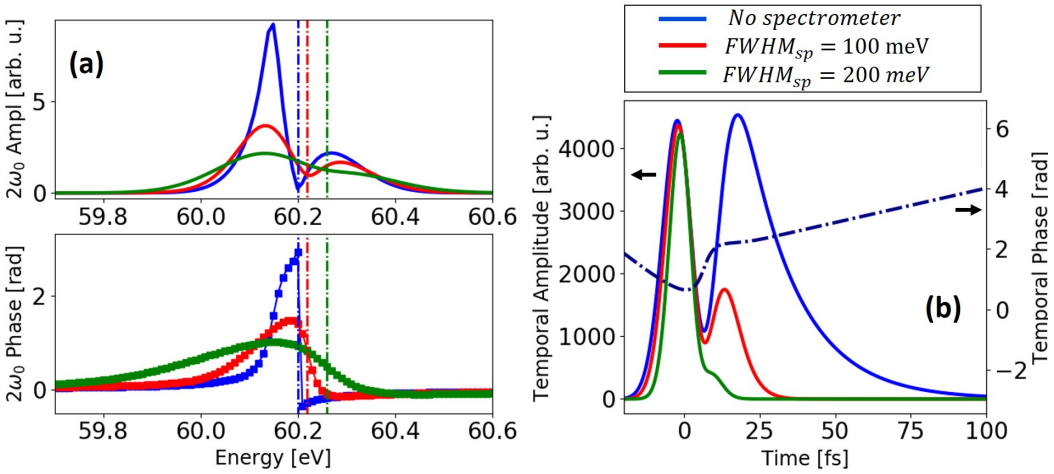

Figure 6.9: (a) Spectral amplitude (top panel) and phase (bottom panel) extracted by the rainbow RABBIT algorithm, for a 200meV wide resonant harmonic, tuned at $E_{tun} = 60.22eV$. The values of the spectrometer resolution vary: (blue curve) no spectrometer; (red curve) 100 meV, similar value to [Busto et al., 2018];(green curve) 200 meV ,similar value to [Gruson et al., 2016a]. The vertical lines show the drifting position of the phase jump along with the position of the dip on the amplitude which occur to the resonance energy position. (b) Corresponding temporal profiles of the resonant EWP $\widetilde{M}_R(t) = FT[M_R(E)]$.

by the resonance. By expressing the resonant EWP in the spectral domain as $M_R(E) \approx M_{2\omega_0}(E)e^{\phi_{2\omega_0}(E)}$ and by applying a Fourier transform we obtain the corresponding temporal profile (section 6.2.5):

$$\widetilde{M}_R(t) = \frac{1}{2\pi}\int_{-\infty}^{+\infty} |M_R(E)|e^{i\phi_{2\omega_0}(E)}e^{iEt/\hbar}dE \tag{6.53}$$

The normalized temporal profiles are shown in Figure 6.9 (b). As was discussed in [Gruson et al., 2016a] and further detailed later in this chapter (section 6.2.5), the shape of the temporal amplitudes has two peaks: the first one, centered around 0 fs, corresponds to the ionization via the direct path and thus is related to the characteristics of the ionizing harmonics, while the second peak is associated with the resonance decay. It now becomes clear that a low spectral resolution measurement will affect mainly the indirect path contribution and thus the interference will be less contrasted and the signal will decay faster, extending to shorter times: $t_{no-spectrometer} \approx 100fs$, $t_{sp=100meV} \approx 30fs$, $t_{sp=200meV} \approx 18fs$. On the contrary, the temporal phase is not affected since a convolution in the energy domain is translated, in the time domain, into a simple multiplication with f_{sp} which is a real function without any phase factor.

6.2.1.2 Width of the resonant harmonic

The width of the harmonics depends on various experimental parameters like the wavelength, duration, energy of the generating pulse as well as on the generat-

ing gas conditions, like its pressure, the use of a jet or a cell and their respective specifications, etc (Chapter 2). In this section we will discuss the effects of different harmonic spectral widths on the retrieved spectral phases and amplitudes and their result on the reconstructed ionization dynamics.

For this study we tune the resonant harmonic at E_{tun} = 60.22 eV and we do not take into account the convolution with the spectrometer. By changing the width of the resonant harmonic we obtain the spectral amplitudes and phases of Figure 6.10 (a). As the width of the harmonic increases, the spectral amplitude becomes also broader. However the position of the local minimum doesn't shift and its asymmetric shape is not distorted. The $FWHM_{harm}$ values were chosen to be larger than the resonance itself, similar to the conditions of Ref. [Gruson et al., 2016a] and Ref. [Busto et al., 2018]. In the case where the harmonic width is close to the resonance width, the shape of the spectral amplitude would be severely distorted since only a part of the resonance would be excited. The corresponding spectral phases are not affected since it is just a multiplication with a real number.

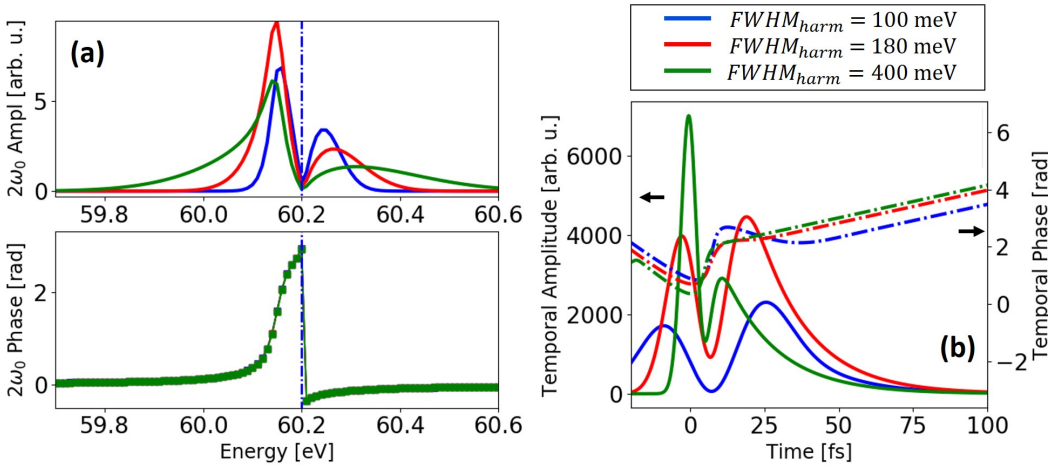

Figure 6.10: (a) Spectral amplitude and phase for E_{tun} = 60.22 eV, without spectrometer resolution for three different harmonic widths: (blue curve) $FWHM_{harm}$ = 100 meV; (red curve) $FWHM_{harm}$ = 180 meV similar to [Busto et al., 2018] and (green curve) $FWHM_{harm}$ = 400 meV similar to [Gruson et al., 2016a]. (b) Corresponding temporal amplitudes and phases of the resonant EWP.

In contrast to the previous section, where the effect of the spectrometer was only measurement induced, now there is a physical meaning. This is clear in Figure 6.10 (b) and the corresponding temporal profiles of the resonant electron wavepacket. As the spectral width of the harmonic increases, the contribution of the direct path to the temporal amplitude becomes more important with a first peak more intense and narrower ($FWHM_{harm}$ = 400 meV), and the destructive interference occurs earlier ($FWHM_{harm=100meV}$ = 7.3fs,$FWHM_{harm=180meV}$ = 6.8fs, $FWHM_{harm=400meV}$ = 5fs). Even though the contributions of the direct and indirect path differ for the three cases, the amplitude decay is very similar, extending to 100 fs. The temporal phases are also affected. The position of the phase jump happens

earlier as the harmonic width increases since it follows the destructive interference the overall shape and size are very similar (phase jump$_{harm=400meV}$ = 1.6 rad, phase jump$_{harm=180meV}$ = 1.5 rad, phase jump$_{harm=100meV}$ = 1.8 rad).

6.2.1.3 Finite pulse effect

The ideal case for RABBIT measurements is a spectrally short dressing pulse so the assumption that the two-photon EWP created after the absorption/emission of a dressing IR photon is an exact replica of the initial one-photon EWP is valid. However, experimentally this is not always the case. When spectrally large dressing pulses are used, they will contain more frequency components than ω_0. Therefore, for a given final energy in the sideband, the energy conservation condition will be satisfied by several different pairs of frequency components, which results in separate contributions that interfere to give rise to the total transition amplitude as was detailed in Chapter 6.1.4. The following simulations were performed by David Busto of Lund University.

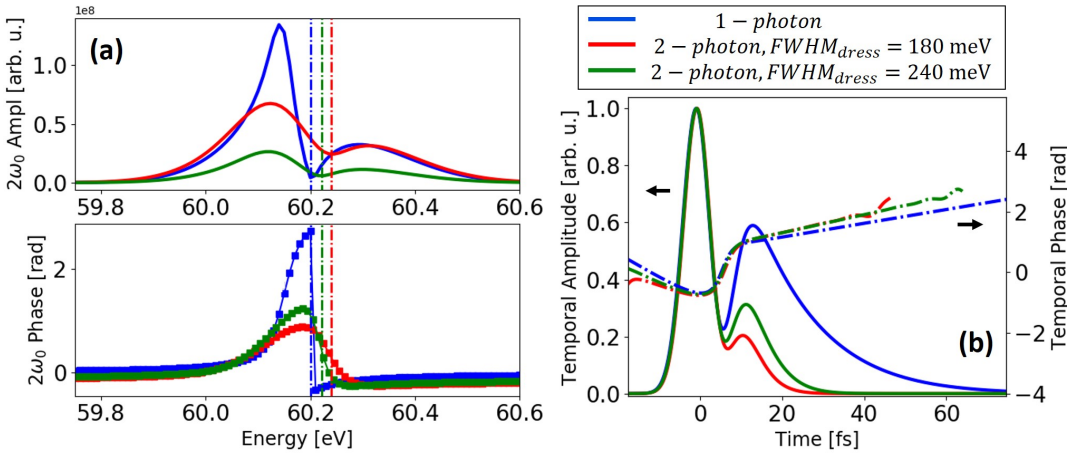

Figure 6.11: (a) Spectral amplitude (top panel) and phase (bottom panel) extracted by the rainbow RABBIT algorithm, for a 310 meV wide resonant harmonic, tuned at E_{tun} = 60.22eV and two values of the probe's pulse spectral width: (red curve) $FHWM_{dressing}$=180 meV, similar value to [Busto et al., 2018]; (green curve) $FHWM_{dressing}$= 248 meV ,similar value to [Gruson et al., 2016a]. The blue curve shows the one-photon EWP for reference. The vertical lines show the drifting position of the phase jump along with the position of the dip on the amplitude. (b) Corresponding temporal profiles.

In Figure 6.11 (a) we compare the retrieved spectral phases and amplitudes for the three following cases: the one-photon EWP, the two-photon EWP with a dressing pulse of $FWHM_{dres}$ = 180 meV or $FWHM_{dres}$ = 248. The width of the harmonic ($FWHM_{harm}$ = 310 meV) and its position (E_{tun} = 60.22eV) are kept constant. The spectrometer convolution is not taken into account. Looking at the spectral amplitude, the effect of the finite dressing pulse is similar to the spectrometer resolution

since as it is getting broader the amplitude is smoothed out. The spectral phase is also smoothed but its evolution is not linear as a function of the pulse width. More specifically, the phase jump that corresponds to a 248 meV pulse is 0.3 rad bigger than the one for the pulse of 180 meV. This makes evident the fact that this is not a simple convolution. In addition, both phase jumps are almost half of the one-photon case and shifted towards higher energies. The corresponding temporal profiles are presented in Figure 6.11 (b). Concerning the amplitudes, the strength of the interference is decreased and the decay is faster between the one-photon and the two-photon cases however, the spectrally wider dressing pulse will result in a higher contribution of the indirect path than the 180 meV case. The temporal phases are almost identical with a sub-femtosecond shift that corresponds to the destructive interference minimum of the amplitudes that exhibit the same shift.

6.2.1.4 Energy position of the resonant harmonic (E_{tun})

The way by which the harmonic will excite the resonance depends on the energy tuning around it. This will result in different population ratios between the direct and indirect paths and thus the interference between these two quantum paths will differ. An example is shown in Figure 6.12 (a) where the energy position of the harmonic as compared to the resonance varies while the harmonic width is kept constant (300 meV) and the convolution with the f_{sp} is not taken into account. Therefore the induced effects on the retrieved phases and amplitudes are purely physical. In more details, even though the spectral phase is not affected the amplitude gets dramatically distorted as we move the harmonic away from the resonance. The physical meaning of this change is better understood by looking at the amplitudes in the temporal domain (Figure 6.12 (b)). When the harmonic is more centered around the resonance (E_{tun} = 60.22 eV), the intensity of the second peak is larger. On the other hand, when the resonance is excited by the tail of the gaussian harmonic (E_{tun} = 60.51 eV) the dominant contribution originates from direct ionization with the resonant path being almost zero. However the corresponding temporal phase exhibits a 1.8 rad jump at a very delayed time (and thus reduced amplitude) which indicates the presence of the resonance even though it is not visible in the amplitude. The temporal phases differ in size and position of the jump depending on the shape of the temporal amplitudes. Therefore, by scanning the harmonic around the resonance one can shape the resonant EWP. However the physical meaning of the measured characteristics can be distorted by the spectrometer resolution and the finite pulse effect as is discussed below.

Spectrometer Resolution

In order to approach better the real experimental conditions, we now include the effect of the spectrometer. As was detailed earlier (chapter 6.2.1.1) the effect introduced by the convolution with the f_{sp} is the smoothing of the corresponding amplitudes and phases which also leads to a shift of the corresponding phase jumps in the spectral domain. For this part of the study a spectrometer with relatively low resolution of $FWHM_{sp}$ = 200 meV is used similar to the [Gruson et al., 2016a]

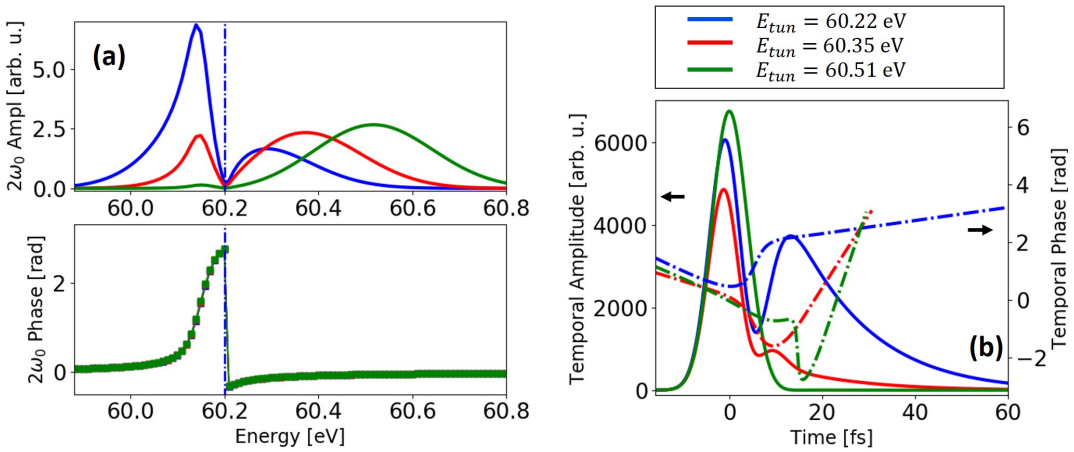

Figure 6.12: (a) Spectral amplitude (top panel) and phase (bottom panel) extracted by the rainbow RABBIT algorithm, for a 300meV wide resonant harmonic, without any effect of the spectrometer. The position of the harmonic with respect to the resonance is varied: (blue curve) E_{tun} = 60.22 eV; (red curve) E_{tun} = 60.35 eV; (green curve) E_{tun} = 60.51 eV. (b) Corresponding temporal profiles.

conditions. The results are shown in Figure 6.13 (a), where the effects are clear with both amplitude and phase being smoothed out: the phase jump is reduced to 1 rad, and the amplitude is ~ 30% of the non-convoluted one. The maximum shift is ~140 meV between E_{tun} = 60.22 eV and E_{tun} = 60.51 eV. Furthermore, by comparing the temporal profiles of Figure 6.13 (b) with the ones of Figure 6.12 (b) where there is no spectrometer effect, one can see that the temporal phases remain the same as was expected from chapter 6.2.1.1. On the contrary, the temporal amplitudes show a faster decay of the EWP as was expected.

Finite pulse effect

As demonstrated in chapter 6.2.1.3, the effects of a finite dressing pulse on the spectral phase and amplitude are different from the simple convolution with the spectrometer. In order to approach more the experimental conditions of [Busto et al., 2018] where the main resolution limiting factor was the large spectral width of the dressing pulse, we will use the two extreme cases of Figure 6.12 and add a dressing pulse with spectral width of $FWHM_{dres} \approx 250$ meV. Comparing 6.14 (a) with Figure 6.13 (a), it is evident that even though a spectrally broad dressing pulse results in a smoothing of the spectral amplitudes and phases, the effect of a low spectrometer resolution is more invasive on the measurement. The amplitude still decreases, its shape is less deformed. Additionally, the phase jump is ~ 1.5 rad and there is a shift of only 10 meV between the phases corresponding to the two different energy tuning. In the temporal domain (Figure 6.14 (b)) the amplitudes are less affected since the smoothing effect is less than for the spectrometer, for E_{tun} = 60.22 eV the resonance now will decay at 30 fs instead of 15 fs that was the spectrometer case. By looking at these two examples it is evident that a low spectrometer resolution

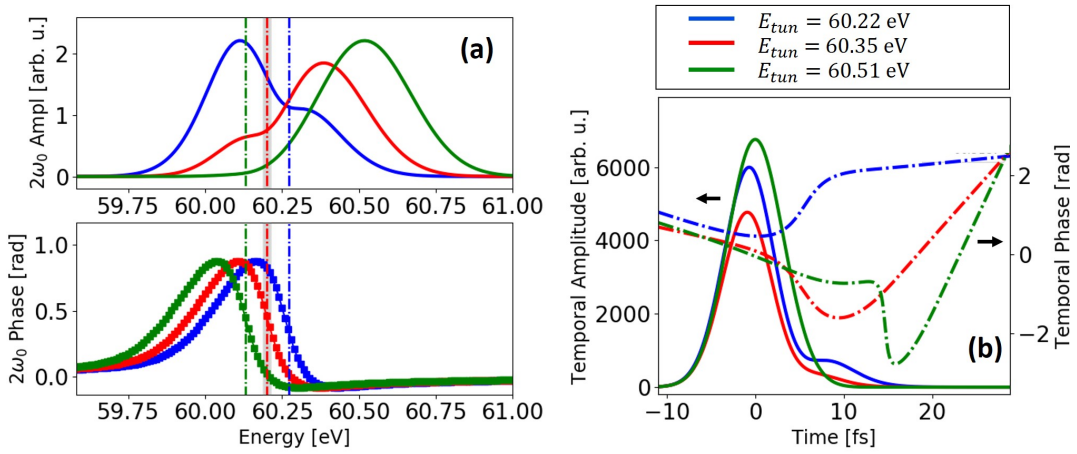

Figure 6.13: (a) Spectral amplitude (top panel) and phase (bottom panel) extracted by the rainbow RABBIT algorithm, for a 300 meV wide resonant harmonic, convoluted with a spectrometer of $FWHM_{sp}$=200 meV. The position of the harmonic with respect to the resonance is varied: (blue curve) E_{tun} = 60.22 eV; (red curve) E_{tun} = 60.35 eV; (green curve) E_{tun} = 60.51 eV. (b) Corresponding temporal profiles.

will be more invasive on the measurement as compared to the width of the dressing pulse. Nonetheless, the effect that will dominate depends on each specific experiment.

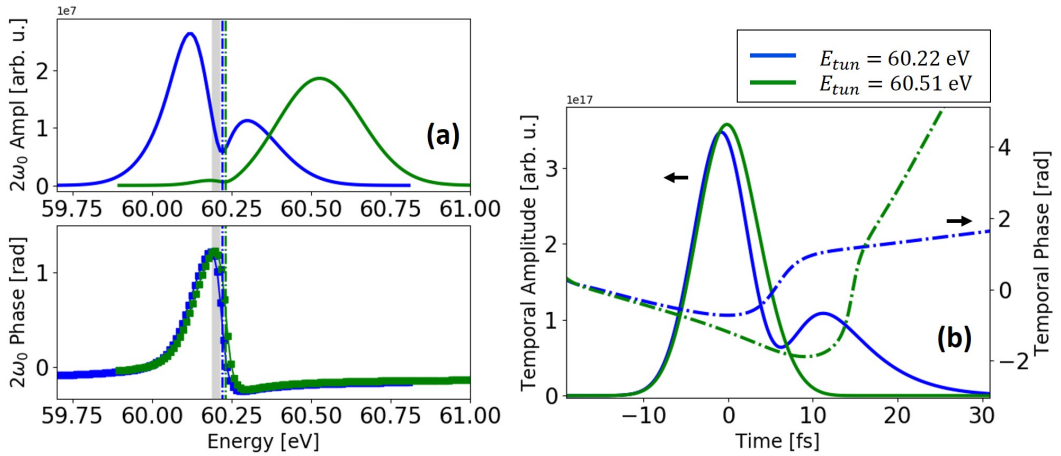

Figure 6.14: (a) Spectral amplitude (top panel) and phase (bottom panel) extracted by the rainbow RABBIT algorithm, for a 300meV wide resonant harmonic, without any effect of the spectrometer for dressing pulse with spectral width of 250 meV. The position of the harmonic with respect to the resonance is varied: (blue curve) E_{tun} = 60.22 eV; (green curve) E_{tun} = 60.51 eV. (b) Corresponding temporal profiles.

Experimental examples The purpose of the above studies was the better understanding of the experimental parameters affecting the spectral amplitude and phase extraction using the Rainbow rabbit technique in order to be able to disentangle the

physical processes from the various measurement induced factors. In this section we demonstrate the effect of some parameters discussed above on experimentally measured spectral phases and amplitudes in the same conditions as [Gruson et al., 2016a] and [Busto et al., 2018]. In both of these cases, the rainbow RABBIT method was utilized for the retrieval of the EWP dynamics in the vicinity of the sp2+ resonance in helium. The main experimental differences of the two independent experiments are listed in Table 6.1. In the case of [Gruson et al., 2016a] the main limiting factor was the spectrometer whereas in [Busto et al., 2018] it was the spectrally large dressing pulses.

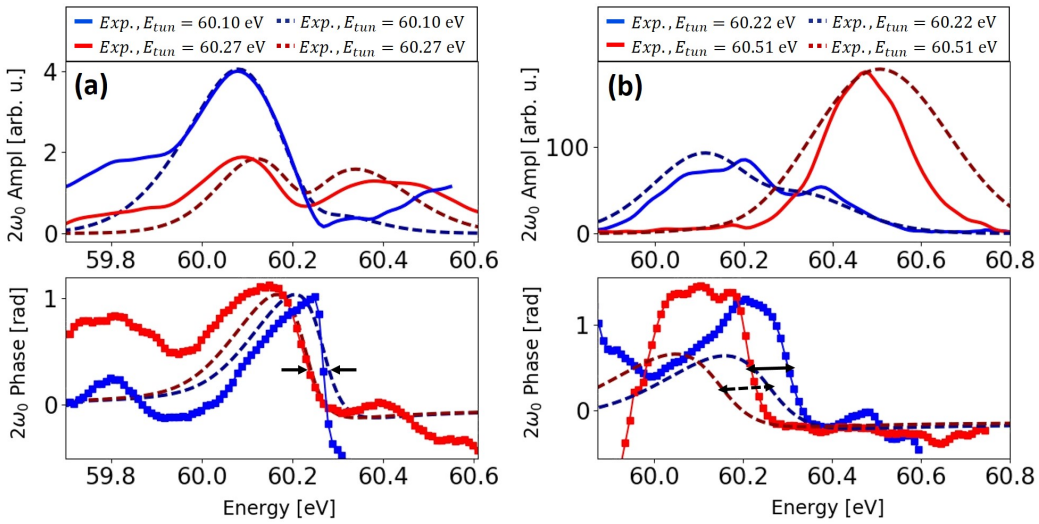

Figure 6.15: Simulations compared with experimental measurements for different E_{tun} in the [Gruson et al., 2016a] conditions (a) and in the [Busto et al., 2018] conditions (b).

In Figure 6.15 (a) we plot the measured spectral amplitudes and phases for two different harmonic energy tunings. These measurements are realized in the same conditions as [Gruson et al., 2016a]. Looking at the phases, there is a ~80 meV shift of the phase jump towards higher energies as the E_{tun} decreases. The main parameter responsible for this effect is the restricted spectrometer resolution of ~190 meV. Indeed by including only the spectrometer convolution we are able to simulate very similar results.

A similar set of measurements was realized in the conditions of [Busto et al., 2018], shown in Figure 6.15 (b). As the E_{tun} decreases we obtain the same behavior as in Figure 6.15 (a). In this case as the main resolution limiting factor is indicated the spectral width of the dressing pulse. However, as was discussed in chapter 6.2.1.4, the energy shift of the phase jump induced only by the finite pulse effect is small and not enough to reproduce the experimental result. By adding the contribution of the spectrometer we are able to obtain a similar phase shift of ~50 meV, even though in this case the comparison with our experiments is only qualitative with slightly different positions and amplitudes of the phase jumps.

	λ (nm)	Δt (fs)	$FWHM_{sp}$ (meV)	$FWHM_{dressing}$ (meV)	$FWHM_{harm}$ (meV)
Gruson *et al.*	1295	70	190	26	400
Busto *et al.*	800	30	89	125	180

Table 6.1: Experimental parameters for Ref. [Gruson et al., 2016a] and Ref. [Busto et al., 2018].

6.2.1.5 Conclusions

To summarize, we presented a complete study on the effects of various experimental parameters on the retrieved spectral phases and amplitudes by the Rainbow RABBIT method, on the prototype example of sp2+ resonance of helium. It was demonstrated that measurement-induced effects related to the spectrometer resolution or the spectral width of the dressing pulses could distort the extracted phases and amplitudes and thus lead to a distorsion of the recontructed EWP dynamics. The ideal experimental conditions for Rainbow RABBIT measurements were found to be a spectrally narrow dressing pulse in order to create exact replicas of the one-photon EWP and spectrally large harmonics, enough to fully excite the resonance which has a specific spectral width (Γ_{sp2+} = 37 meV). Figure 6.16 summarizes the most important points. Additionally, a comparison between our numerical simulations and experimental data for two independent experiments was realized. Despite the differences between the two experiments, the similarity of the results show the flexibility and the robustness of the Rainbow RABBIT technique.

The goal of this work was to point out the possible experimental factors that could contaminate the spectral phases and amplitudes measured by the Rainbow RABBIT technique so one can later decouple them from the actual results as was done in [Busto et al., 2018] by deconvoluting from the spectrometer response, or at least be aware of the effect that they could have on the results. As the Rainbow RABBIT is a largely applicable technique that is being increasingly used in attosecond spectroscopy, this detailed study could serve as a textbook for experiments similar to the ones described above or to any case that involves fast phase variations and structured amplitude variations.

6.2.2 Rainbow RABBIT measurements for single resonances: sp2+, sp3+

These experiments aim at pushing forward the analysis of autoionization dynamics in helium that was presented in Gruson *et al.* [Gruson et al., 2016a]. The experiments are performed in different experimental conditions, over a broader energy range that allows us to investigate both the sp2+ resonance and the next sp3+ resonance. The characteristics of the two Fano resonances including their energy E_{res}, asymmetry parameter q, linewidth Γ and lifetime $\tau = \hbar/\Gamma$ are summarized in Table 6.2. The influence of the different experimental parameters such as the spectrometer resolution and the spectral width of the IR and XUV pulses is discussed and linked to the numerical calculation presented in Chapter 6.2.1. We then investigate different

Parameter	Spectral Phase	Spectral Amplitude
Spectrometer resolution	Smoothing and shift towards higher energies 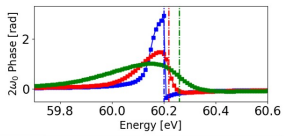	Smoothing and decrease of contrast 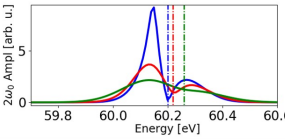
Harmonic width	Not affected 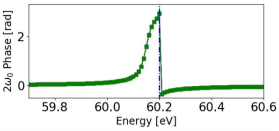	Broadening 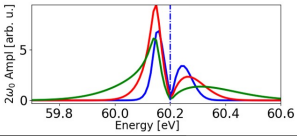
Finite pulse effect	Smoothing and shift towards higher energies 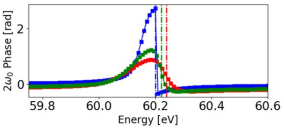	Smoothing and decrease of contrast 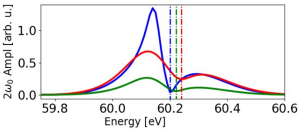
Tuning + spectrometer resolution	Shift towards higher energies as E_{tun} decreases 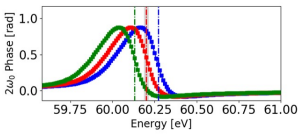	Shape distortion 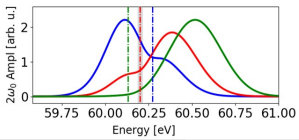
Tuning + finite pulse effect	Shift towards higher energies as E_{tun} decreases 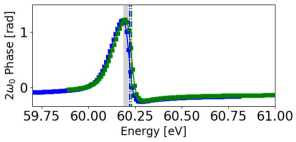	Shape distortion 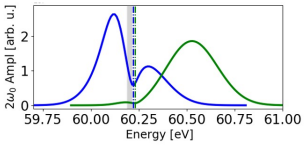

Figure 6.16: Summary of the effects of the different experimental parameters on the retrieved spectral phases and amplitudes by the Rainbow RABBIT technique.

time–frequency representations and we fully characterize the sp2+ resonant EWP using short time Fourier transforms (STFT) and Wigner time–frequency representations. This, together with theoretical calculations, allows us to resolve the ionization dynamics, and in particular, to disentangle the contributions of the two ionization paths.

We use the Rainbow RABBIT method in order to access and study both the spectral amplitude and phase of the resonant EWPs. The experimental set up used here is the one detailed in Chapter 4.3. Briefly we use a tunable Ti:Saph laser system that gives pulses of ~5 mJ with duration of 25 fs FWHM at 1 kHz repetition rate. We use a comb of coherent harmonics generated in neon to photoionize helium atoms. The remaining IR radiation is blocked with a 200 nm -thick Al filter. The ejected photoelectrons are detected with a MBES of sub-100 meV spectral resolution. By adding a weak IR field and varying its delay with the XUV field, we are able to

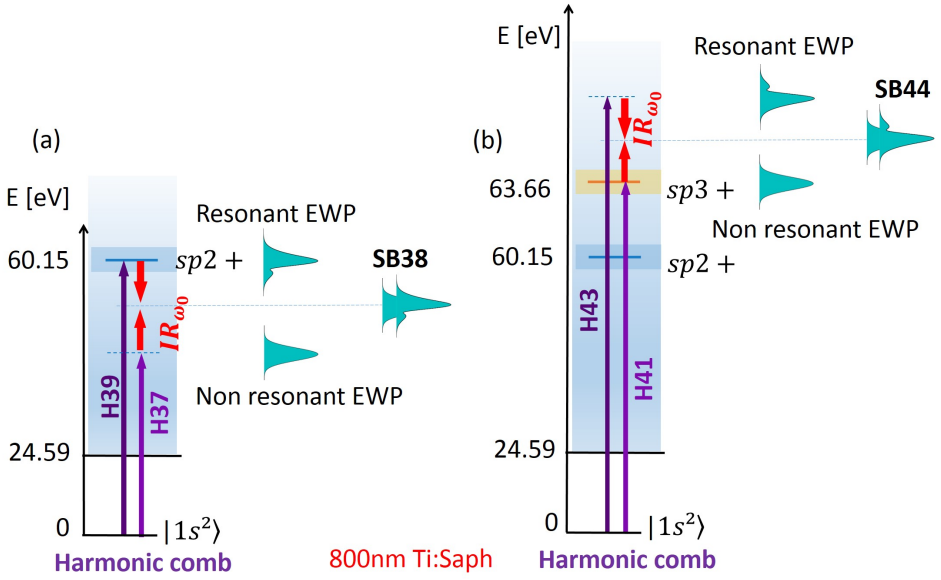

Figure 6.17: Principle of the RABBIT measurement for the study of the (a) first (sp2+) and (b) second (sp3+) autoionizing resonance.

obtain the RABBIT spectrograms. As detailed in Chapter 4.3, a Dazzler allows us to tune the central wavelength of the laser pulses, and thus, to tune the harmonic energies around the sp2+ and sp3+ resonances. The EWP interferometry schemes are shown in Figure 6.17.

	E_{red} [eV]	q	Γ [meV]	τ [fs]
sp2+	60.15	-2.77	37	17
sp3+	63.66	-2.58	8	82

Table 6.2: Spectroscopic characteristics of sp2+ and sp3+ autoionization resonances of helium [Domke et al., 1996].

Part of the work of this chapter is based on the results of Article I available at the end of this manuscript.

6.2.3 Experimental limitations

In this section a number of limitations inherent to the measurement process are presented. Their influence on the retrieved spectral amplitudes and phases, and on the reconstructed dynamics have been studied in detail through simulations earlier in this chapter (6.2.1).

Spectrometer resolution

The low spectrometer resolution has a direct influence on the measured spectral amplitudes and phases. In the case of Gruson *et al.* this was the main reason for

the widening of the phase curve and the reduction of the phase jump. In the series of experiments that we performed in Lund a deconvolution process was applied in order to avoid this effect.

The procedure described below was developed by Margherita Turconi and differs from the one used in Busto *et al.*, however it exhibits very similar results. The effect of the spectrometer is modeled by a convolution with a Gaussian function $\mathcal{S}$ of width DE (here DE = 100 meV):

$$G = \mathcal{S} \otimes \mathcal{F}, \tag{6.54}$$

where G is the measured spectrum and F the spectrum to be determined. In the Fourier domain, the convolution becomes a multiplication and subsequently we get the following relation between the Fourier transforms of the previously defined quantities:

$$\tilde{\mathcal{F}} = \frac{\tilde{G}}{\tilde{\mathcal{S}}} \tag{6.55}$$

In practice, the experimental noise will make the quantity of expression 6.55, diverge beyond a certain interval. The method of Biraud [Biraud, Y.G., 1976] is then used to extrapolate the function $\tilde{\mathcal{F}}$ over a larger range. The deconvoluted spectrum $\mathcal{F}$ is calculated by the inverse Fourier transform of the extrapolated function. This procedure is applied to each delay of the RABBIT spectrogram in order to reconstruct a "deconvoluted" spectrogram. This spectrogram is then analyzed by the Rainbow RABBIT method. Figure 6.18 shows the comparison between the spectral amplitudes and phases from SB38 to SB42, before and after the deconvolution treatment. The effect of the deconvolution is clear on the amplitudes, with more marked local minima at the resonance, and a little less effective on the phases, with slightly sharper phase jumps. Thus, the spectral broadening due to the spectrometer resolution is not the dominant process in this experiment

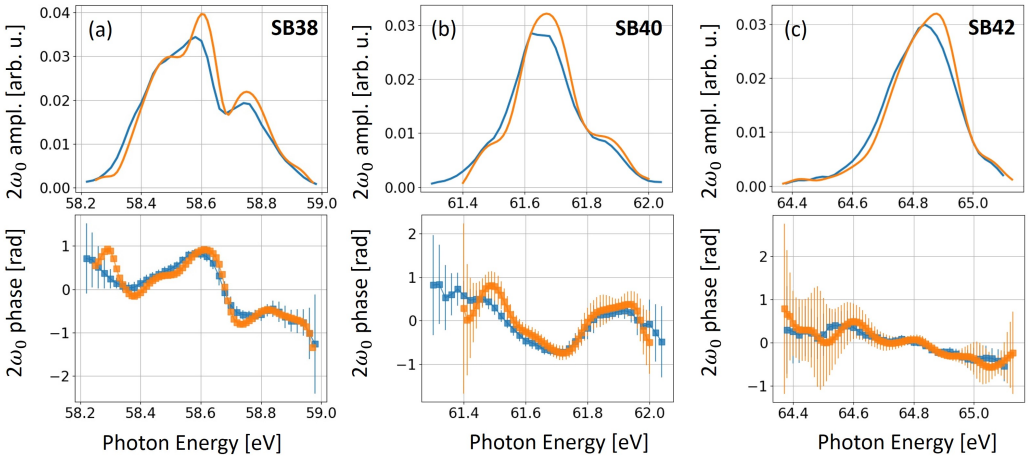

Figure 6.18: Rainbow RABBIT amplitudes (top panels) and phases (bottom panels) for raw (blue) and deconvoluted (orange) data for the resonant sidebands SB38 (a) and SB40 (b) and the non-resonant SB42 (c).

Finite pulse effect

The spectral width of the dressing pulses used in Lund was ≈130 meV (for 70 nm bandwidth) whereas Gruson *et al.* used Fourier limited pulses of 26 meV. This means that in our case the dressing pulses will have a stronger effect on the measured spectral amplitudes and phases (see Chapter 6.2.1.3). In Ref. [Jiménez-Galán et al., 2016] a complete model of the two-photon transition amplitude via a Fano resonance that includes the effect of the dressing pulse is presented. If the harmonic and the dressing pulse are broad spectrally, a particular energy of the sideband can be reached by different $\omega + \Omega$ combinations of the IR and XUV photons, respectively. Thus the amplitudes of two-photon transitions will be "mixed" in the sideband, which deforms the phase $arg[\mathcal{M}^{(2)}_{\vec{k},Fano}]$ (equation 6.44). The wider the IR spectrum is, the more the phase will be distorted with the phase variations becoming weaker and spectrally broader. This effect is more complex than a simple convolution by the width of the IR pulse, so it is not possible to avoid it with a simple deconvolution algorithm. In these conditions, the two-photon EWP is not an exact replica of the one-photon resonant EWP. In addition, if the dipole coupling between the resonance and the final continuum (quantified by the parameter γ) is strong, the IR bandwidth will have an even bigger distorting effect on the phase measured in the sideband.

Harmonic blue shift

During the high harmonic generation process, when the initial laser beam is focused in the gas cell, the laser intensity is high enough so that the front of the pulse may partially ionize the medium, thus creating a low density plasma in which the pulse propagates. The interaction of the IR pulse with the plasma leads to a blue shift of the laser central frequency that results in harmonics separated in frequency by $2(\omega_0 + \delta\omega)$ [Wahlström et al., 1993]. Since the probe IR pulse does not propagate through the gas cell and is thus not blue-shifted, the contributions from the lower and higher harmonics to the sideband do not perfectly overlap in frequency. In the absence of blue shift, the quadratic phase variation inside the harmonic lines (due to the harmonic chirp, not to be confused with the attochirp [Salières et al., 1995],[Varjú et al., 2005]) does not influence our measurement. Indeed, the variations of ϕ_{n+2} and ϕ_n are similar over the pulse bandwidth so that $\Delta\phi_{XUV}$ only contributes by a constant phase in equation 4.1.In the presence of a blue shift, $\Delta\phi_{XUV}$ varies linearly with frequency, with a coefficient equal to $-8\delta\omega\phi_n''$, where ϕ_n'' is the harmonic group delay dispersion. In the experimental results, a linear phase variation was indeed observed inside the non-resonant sidebands. This linear phase is removed in all the results presented below. To do so, we apply a linear fit on the measured phase of each sideband and then the corresponding linear slope is subtracted for.

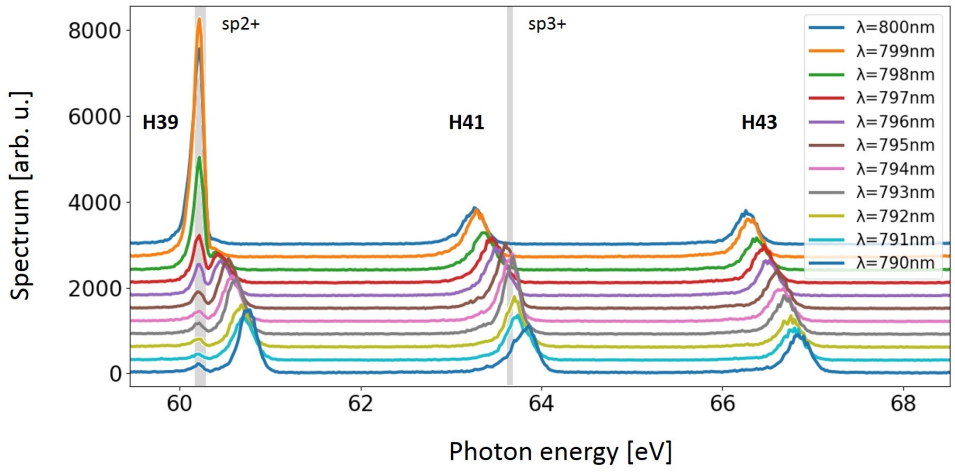

Figure 6.19: Photoelectron XUV spectra for different wavelengths of the driving laser with a bandwidth of 70 nm. At λ=799 nm we excite only the sp2+ resonance, whereas for λ=794 nm we reach sp3+ with a very weak excitation of sp2+. For a wavelength in between 795 nm and 796 nm we excite simultaneously both with significant amplitudes.

6.2.4 Results

The sp2+ and sp3+ resonances are independently excited by tuning, respectively, harmonics H39 and H41 to the autoionizing states' energies (Figure 6.19). Figure 6.20 displays the phases measured for sidebands SB38, SB40 and SB42 when harmonic H39 is resonant with the sp2+ state (upper row) and when harmonic H41 is resonant with the sp3+ state (lower row). For both resonances, we can measure a clear phase variation induced by the resonance while the third non-resonant sideband, shown for comparison (either SB42 in the first row or SB38 in the second row), exhibits a flat phase, since the two-photon ionization occurs through a smooth continuum.

Due to the broad harmonic profile, the amplitude exhibits a double structure which results from the ionization via both resonant and non-resonant continua. The first peak, centered at 58.89 eV and the dip at 59 eV result from ionization via the sp2+ resonance and present the typical constructive and destructive interference characteristic of the Fano profile. The second peak, centered at 59.1 eV, originates from the ionization via a non-resonant continuum which is probed by the high energy part of the harmonic. When harmonic H41 is resonant with the sp3+ state, the amplitude of M_{41-1} is smoother than that of M_{39-1} in the previous case. The width of the sp3+ resonance (8 meV) is extremely small compared to that of the harmonics (180 meV) and IR pulses (125 meV), so that the sp3+ signature in the sideband is subject to a strong broadening due to the finite pulse effects.

This behavior is well reproduced by theory and indicates that, in our experimental

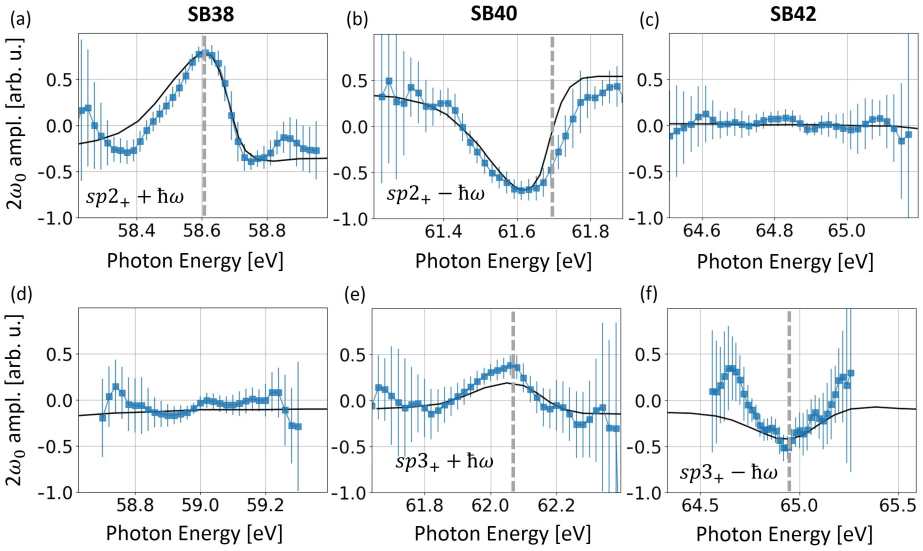

Figure 6.20: Phases measured (blue) in SB38 (first column), SB40 (second column) and SB42 (third column) in the cases where H39 is resonant with the sp2+ state (first row) and where H41 is resonant with the sp3+ state (second row). A clear phase variation linked to the two resonances is observed on the sidebands originating from the resonant harmonics (SB38 and SB40 for sp2+, SB40 and SB42 for sp3+), while the phase on the other sidebands is flat. The theoretical calculations (black line) agree very well with the measured phases.

conditions, the modification of the amplitude of the two-photon wave packet due to the sp3+ resonance cannot be resolved. The corresponding theoretical calculations were performed by the group of Fernando Martin of Madrid University, using a model based on second-order perturbation theory and Fano's theory. The phase variations observed for the sidebands where the resonance is one IR photon above or below are similar, except for an opposite sign. For the sp2+ resonance, a fast phase variation of 1.2 rad is observed across the resonant part of the sideband. For the sp3+ resonance, despite the smooth amplitude of the resonant wave packet, a phase variation of 0.3 rad is measured, indicating that the EWP is affected by the sp3+ state. Despite their similar q values, the phase jump measured for the sp3+ is smaller than the one measured for the sp2+ state. This difference originates from the finite pulse effects that lead to a broadening and dilution of the phase jump.

Furthermore, our measurements are in very good agreement with the ones carried out by Gruson *et al* including the amplitude of the phase jump for sp2+. However, as already mentioned, the limitations to the spectral resolution in the two experiments have different origins. Table 6.1 summarizes the different experimental parameters in the two studies. In Gruson *et al*, the IR bandwidth was smaller than the resonance width, strongly reducing the influence of the finite pulse effects so that the limiting factor was the MBES resolution. In our case, the RABBIT spectrogram is deconvolved from the MBES response but the broad IR bandwidth limits our spectral resolution. Despite the different experimental parameters in the two

experiments, the good agreement between the results shows the flexibility of the Rainbow RABBIT technique and its applicability to a wide range of experimental conditions (see Chapter 6.2.1 for a detailed study).

6.2.5 Spectro-temporal representation of the sp2+ resonance

Having measured the spectral amplitudes and phases of the $2\omega_0$ oscillations of the Rainbow RABBIT trace, we can get the spectral amplitude and phase of the resonant two-photon EWP (see Chapter 5.2):

$$M^{res}(E) \approx M^{res}_{39-1}(E)e^{\phi_{39-1,atom}(E)}. \tag{6.56}$$

In order to study its dynamics, we will use three different types of analysis: cumulative Fourier transform, Gabor representation and Wigner representation.

Temporal domain The resonant two-photon EWP can be expressed in the time domain as [Desrier et al., 2018]:

$$\widetilde{M}^{res}(t) = \frac{1}{2\pi}\int_{-\infty}^{+\infty} |M^{res}_{39-1}(E)|e^{i\phi_{39-1,atom}(E)-iEt/\hbar}dE. \tag{6.57}$$

Here we use the approximations $\phi_{39-1,atom}(E) \approx \Phi_{38}(E)$ and $|M^{res}(E)| \approx A_{38}(E)$ as is discussed in Chapter 5.2 as well as in Ref. [Gruson et al., 2016b] and Ref [Barreau, 2017].

Using the amplitudes and phases deconvoluted from the spectrometer response, Figure 6.18 and the expression 6.57 for the temporal profile of the resonant EWP, we obtain its corresponding temporal amplitude and phase as shown in Figure 6.21.

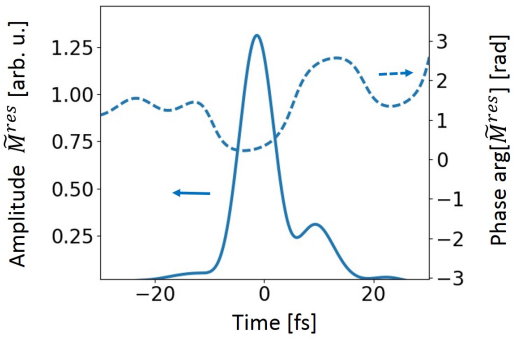

Figure 6.21: Temporal amplitude of the two-photon resonant EWP obtained from the Fourier transform of the spectral amplitude and phase of SB38.

The temporal profile shows a large Gaussian-like peak centered at t=0 fs corresponding to the ionizing XUV pulse. On this time scale, the dominant ionization channel is the direct one. As the autoionizing state decays in the continuum, the

contribution of both paths becomes comparable and strong destructive interferences between the two channels lead to a sharp decrease of the temporal intensity around t=7 fs which is followed by a revival of the EWP. When the intensity goes to this minimum the temporal phase exhibits a jump of ~2.5 rad. The intensity decreases rapidly after ~10 fs, much faster than the theoretical lifetime of 17 fs (Table 6.1). This apparently faster decay of the autoionizing state results from the finite pulse effects which occur because the short IR pulse probes the decay during a limited amount of time (less than 15 fs). The measured lifetime of the decay, along with the exact position in time of the interference depend on the excitation and dressing conditions as was also presented in Chapter 6.2.1. We note that in Gruson *et al.* the apparent lifetime of the resonance was also reduced, but this was due to the spectral broadening caused by the photoelectron spectrometer. In our case, the latter does not play any role since the experimental results are deconvoluted from this effect.

Cumulative Fourier transform (CFT) From the amplitude and phase of the resonant EWP, it is possible to obtain the buildup of its spectral profile over time as it was shown theoretically by Wickenhauser *et al.* [Wickenhauser et al., 2005]. For this, we introduce a time-energy analysis based on a local Fourier transform that shows how the spectral profile is built up to a time of accumulation t_{acc}:

$$W(E,t_{acc}) = \int_{-\infty}^{t_{acc}} \widetilde{M}^{res}(t)^{iEt/\hbar} dt. \tag{6.58}$$

The results are presented in Figure 6.22 where the evolution of the resonance profile $|W(E,t_{acc})|^2$ is plotted as a function of the accumulation time t_{acc}. Up to $t_{acc} \approx 7$ fs, the spectrum is quasi-Gaussian and reproduces the spectrum of the ionization pulse. At these short times, only direct ionization contributes to the spectrum of photoelectrons. When t_{acc} increases, the contribution of the autoionizing resonance is becoming more important and we observe the progressive appearance of spectral interferences. After 20 fs, the spectrum converges towards the spectral intensity measured by the experiment (Figure 6.18 (a), top panel).

Gabor representation Using a different local Fourier transform, it is possible to obtain the spectrum of photoelectrons emitted at different moments of the interaction. Here we use the Gabor transformation of the EWP, which is the inverse Fourier transformation of $\widetilde{M}^{res}$ multiplied by a time window $g(t)$:

$$G(E,\tau) = \int_{-\infty}^{+\infty} g(t-\tau)\widetilde{M}^{res}(t)e^{iEt/\hbar} dt \tag{6.59}$$

In contrast to the Cumulative Fourier Transform case showing the spectral amplitude accumulated until time t, the Gabor representation depicts the spectral amplitude emitted within a time window and shows the evolution of the 'instantaneous' frequencies emitted in the continuum. In Figure 6.23 we plot the corresponding results. As in the previous case, during the first 7 fs a Gaussian-like EWP emerges in

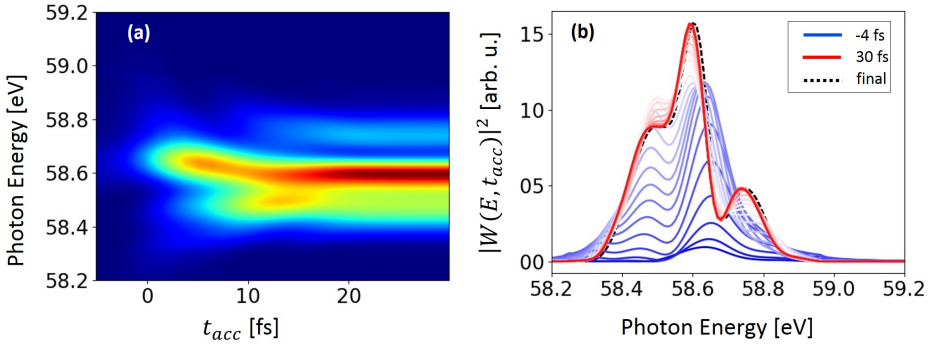

Figure 6.22: (a) Intensity of the cumulative Fourier transform $|W(E,t_{acc})|^2$ as a function of the accumulation time t_{acc}. (b) Lineout of (a) every 2 fs, where we first distinguish the construction of the profile of the direct ionization up to a maximum towards ~6 fs, then the appearance of spectral interference and after ~24 fs the convergence towards the measured spectrum (dashed black line).

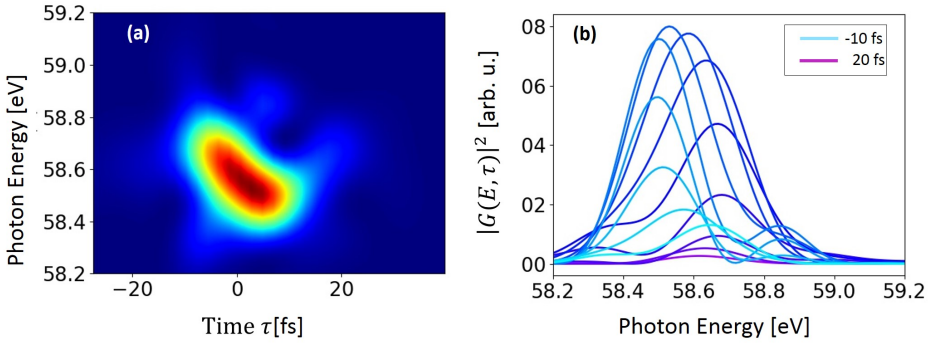

Figure 6.23: (a) Square modulus of the Gabor transform of the EWP $|G(E,t)|^2$ with a g Gaussian window of 20 fs width at FWHM. (b) Lineouts of (a) every 2.3 fs.

the continuum, with its shape reflecting the ionizing pulse, revealing that the direct ionization path is dominant. Passed this time, the direct and resonant paths start interfering giving rise to destructive interferences at the center of the wave packet (around 58.7 eV) and constructive interferences on both sides. After 8 fs, the two representations start to differ. The Gabor representation shows that the interferences disappear and a weak, spectrally narrow decay is observed around 58.6 eV. This energy corresponds to the sp2+ resonance position shifted down by one IR photon (60.15-1.55=58.6eV) . The XUV pulse has then passed the interaction region and the atoms cannot be directly ionized. However, the sp2+ state can still decay in the continuum thus giving rise to this weak decay. In contrast, the $|W(E,t_{cc})|^2$ barely changes after 8 fs because of the small contribution from the decay to the accumulated spectral amplitude.

Wigner representation The two previous time-energy representations rely on local Fourier transforms. The first one allows to observe progressive modification of

the photoelectron spectrum over time due to interference between direct and resonant ionization paths; it does not allow though to temporally separate these two processes (except at short times dominated by the direct path). The second, shows the spectrum of 'instantaneous' photoelectrons and highlights symmetric spectra at short and long times due to direct and resonant paths and asymmetric spectra at intermediate times due to their interference, but the temporal and spectral resolutions are limited by the principle of uncertainty (or Fourier). David Busto from the university of Lund proposed to represent the dynamics of the resonant EWP by a pseudo-probability distribution of Wigner-Ville [Wigner, 1932]. This distribution is defined in the time and frequency domain:

$$WV(E,t) = \int_{-\infty}^{+\infty} \widetilde{M}^{res}(t+\tau/2)\widetilde{M}^{res*}(t-\tau/2)e^{iE\tau/\hbar}d\tau \tag{6.60}$$

$$= \int_{-\infty}^{+\infty} M^{res}(E+\xi/2)M^{res*}(E-\xi/2)e^{-i\xi t/\hbar}d\xi. \tag{6.61}$$

It can be seen as the Fourier transform of the auto-correlation function of the EWP. Additionally, one of the properties of this distribution is that the projections along the time (respectively, frequency) axes (referred to as marginals in the literature) generates the spectral (respectively, temporal) intensity of the wave packet: $\int W(E,t)dt = |M^{res}(E)|^2$ and $2\pi \int W(E,t)dE = \left|\widetilde{M}^{res}(t)\right|^2$. Finally, an interesting feature of this representation is that it is not a positive distribution. In the WV of coherent multicomponent signals, the different components interfere with each other and the distribution can take negative values.

Figure 6.24 (a) shows the experimental WV of the two-photon EWP emitted through the sp2+ resonance. The spectrally large peak centered at t=0 fs represents, like for the Gabor representation, the direct ionization path. The temporally long and spectrally narrow feature centered at 58.6 eV describes the decay of the sp2+ state. Because these two processes have such distinct spectral–temporal representations, it is very easy to disentangle the direct ionization to the continuum states from the autoionization through the sp2+ state. The negative peak (in blue) and the shoulder between 58.7 eV and E = 58.8 eV represent the interferences between the two ionization paths. These results agree very well with the theoretical calculations as shown in Figure 6.24 (b). These interference effects provide information on the correlation between the direct and resonant ionization amplitudes. In our experimental conditions, the IR pulses were too short to allow a complete visualization of these correlation effects. In Figure 6.24 (c) we show the simulation of the WV that would be obtained using the same XUV pulses but spectrally narrower IR pulses of 10 nm bandwidth corresponding to a pulse duration of roughly 100 fs. Very clear oscillations appear between 58.6 and 58.9 eV compared to the simulation in the experimental conditions (Figure 6.24 (b)). These oscillations are characterized by a frequency that increases linearly with the detuning and an amplitude that is damped as a function of time.

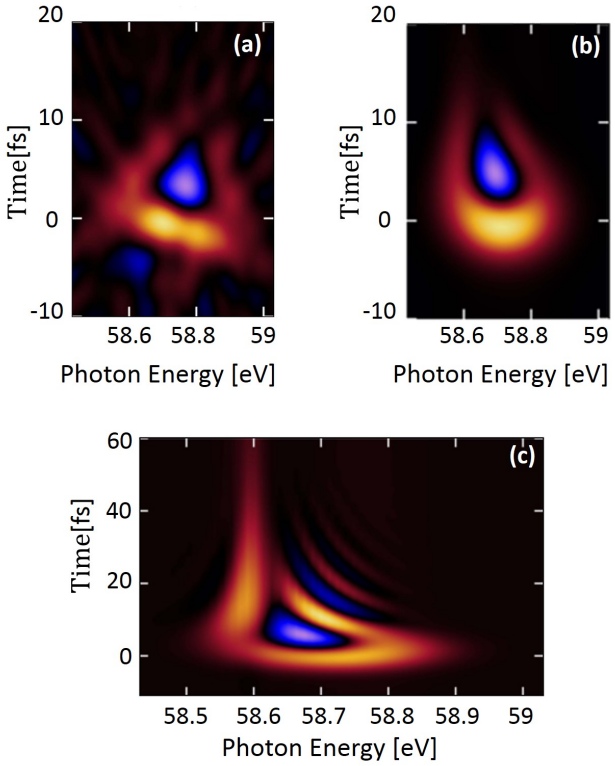

Figure 6.24: Wigner-Ville distribution of the resonant EWP. (a) Experimental WV, (b) simulated WV using the finite pulse model with experimental parameters for the XUV and IR pulses, (c) simulated WV using the finite pulse model with experimental parameters for the XUV and a 10 nm broad IR pulse. Taken from Busto *et al.* [Busto et al., 2018].

6.2.6 Dressing IR Intensity dependence: study on sp2+

A big advantage of the RABBIT technique is the fact that it is a perturbative technique. This means that the IR dressing beam is weak enough (of the order of I~ $10^{11} W/cm^2$), in order to act only as a 'reader' of the photo-ionization event without perturbing the dynamics. However, the increase of the dressing power can give us interesting information about the system under study and additionally one can pass from the observation to the control of the corresponding ionization dynamics. In particular, it has been shown in transient absorption experiments that a high dressing power can alter the q parameter of a Fano resonance and thus change the corresponding line profiles [Ott et al., 2013b]. Regarding the RABBIT method itself it has been shown that the phase information imprinted in the sidebands can also be extracted from the harmonics by analyzing higher Fourier components [Swoboda et al., 2009].

In this section, the effect of an increasing dressing IR intensity on the sp2+ resonance will be presented, both on the resonant line shape, and on the RABBIT phase.

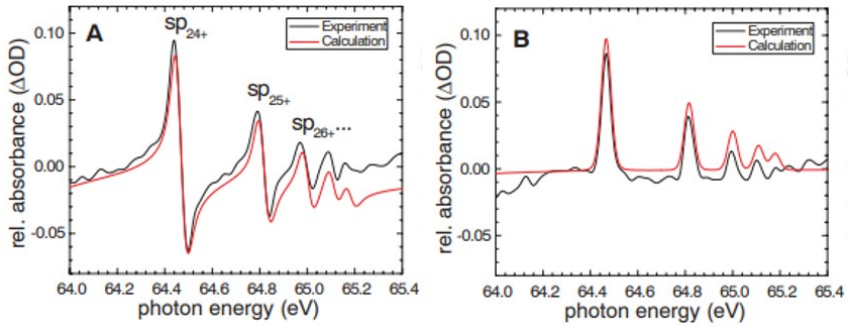

Figure 6.25: Modification of the absorption profiles of doubly excited resonances in helium. (a) Absorption spectrum of helium after being ionized by a single attosecond pulse without any dressing IR. (b) Absorption spectrum of helium when a pulse of 7 fs at 730 nm is focused at an intensity of $\sim 2 \times 10^{12} W/cm^2$, arriving 5 fs after the few-pulse XUV train. Taken from Ref. [Ott et al., 2013b].

6.2.6.1 Effect on the resonant line shape

As a reminder, we recall in Figure 6.25 A the spectactular results of Ref. [Ott et al., 2013b] which shows the absorption spectrum of helium after the excitation of doubly excited Fano resonances located below the N=2 threshold of He+ by a single broadband attosecond pulse. It exhibits the characteristic Fano line profiles, for example in the case of sp4+ resonance where q_{sp4+}= -2.55. After adding a probe pulse centered at 750 nm, of 7 fs duration (at FWHM) and of intensity I~ $2 \times 10^{12} W/cm^2$ the absorption line profiles are modified as shown in Figure 6.25 B, where is now clear that the observed lines are almost Lorentzian (q = 0).

The question we address in this section is whether it is possible to observe a change in the line profile in a RABBIT type scheme, that is to say in photo-ionization spectroscopy rather in transient absorption spectroscopy, using XUV pulse trains and a longer driving laser pulse.

Taking advantage of the active stabilization system of the Lund beam-line we were able to measure the photoelectron spectra at a constant delay, varying the intensity of the dressing pulse. In order to change the dressing intensity without affecting the temporal overlap of the XUV and IR fields, or the size of the focus in the photoelectron spectrometer, a $\lambda/2$ waveplate in combination with a polarizer was used instead of a varying diaphragm.

Figure 6.26 shows the photoelectron spectra measured when the harmonic H39 is resonant with sp2+ state (λ = 793 nm, IR bandwidth 85 nm) for several dressing intensities. Under these conditions, the harmonic H41 is not resonant with the sp3+ state. The dressing power is measured after the spectrometer (behind the window of the vacuum chamber) and as a consequence, we cannot unfortunately link these values to the actual IR intensity in the focus and thus an exact quantitative study is not possible. However, the general behavior is evident. When the dressing power increases, there is an increase of the sidebands' signal while at the same time the

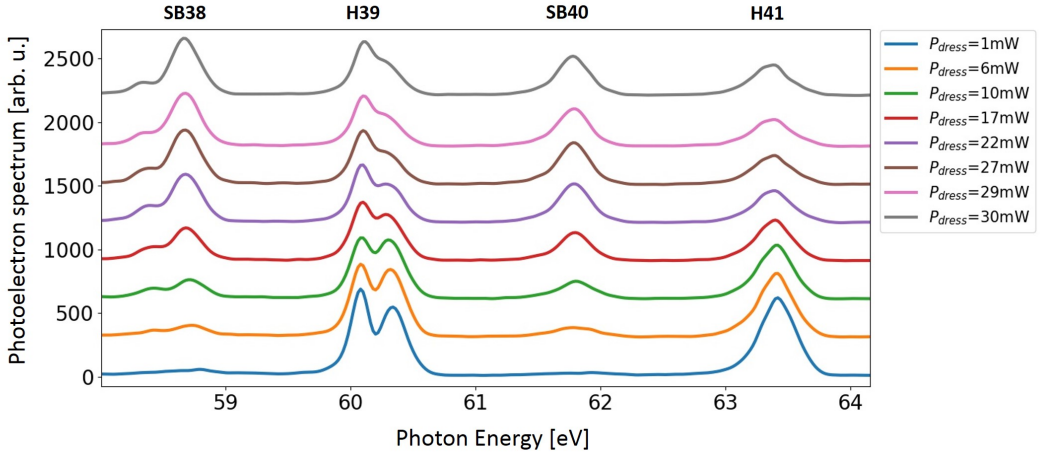

Figure 6.26: XUV photoelectron spectra for different powers of the dressing IR field. H39 is resonant with the sp2+ state.

signal of the non-resonant harmonic H41 decreases up to P = 22 mW. For the power values between 22 mW and 30 mW, the signals of the sidebands and harmonic H41 reach saturation and remain the same. The line-shape of the non-resonant H41 is not modified with the increase of the dressing power, in contrast to the behavior of the resonant H39, which undergoes a large change.

In order to quantify this profile modification, we calculated the parameter q corresponding to the line shape observed at each intensity according to the following procedure developed by Lou Barreau: The profile of the non-resonant harmonic H41 for the lowest dressing power value, is used to determine the shape of the harmonic profile. The photoelectron peak measured at the energy of H41 is the harmonic profile multiplied by the cross section of helium at this energy (considered constant), convoluted by the response function of the MBES. The photoelectron spectrum is then deconvoluted from the spectrometer response function with an algorithm of blind deconvolution (deconvblind function of Matlab) to obtain the harmonic profile. The response function at the energy of harmonic H41 has a width of 150 meV at FWHM. The harmonic profile is shifted by two photons to the position of the resonant harmonic H39, then multiplied by a Fano profile with Γ = 37 meV and E_R = 60.15 eV and finally convoluted with a Gaussian corresponding to the response function extracted from H41. We thus assume here that the width is not significantly different at H39 despite the 3 eV lower electron energy. The value of q is optimized on the difference between the calculated profile and the measured spectrum.

$$S = \left[H(E_{41} - 2\hbar\omega) \times \frac{(q+\epsilon)^2}{1+\epsilon^2} \right] \otimes f_{sp}, \tag{6.62}$$

where f_{sp} is given by equation 6.51. The measured spectra are compared with the results of the optimization in Figure 6.27 (a) and the corresponding q values for the different intensities are shown Figure 6.27 (b). At the minimum intensity we

obtain $q = q_{sp2+}$ = -2.77. When the dressing intensity increases, the photoelectron line profile becomes less asymmetrical, which corresponds also to an increase of the q value.

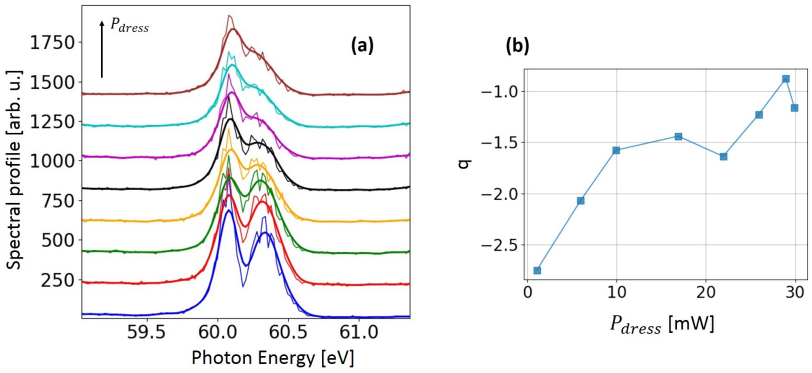

Figure 6.27: (a) Photoelectron spectral profile of harmonic H39 as measured (thin lines) and simulated (thick lines) and after the q optimization procedure (b) Corresponding q values as a function of the incresing dressing power.

The interpretation of these observations remains open for the moment. Simulations in the strong field approximation are in progress, in collaboration with Marcus Dahlström from Lund University.

6.2.6.2 Effect on the RABBIT phase

Having shown that the q parameter can be altered by an increasing dressing IR intensity, the subsequent question that arises is what is the effect on the spectral phase extracted from RABBIT spectrograms. In order to investigate this, we performed Rainbow RABBIT measurements for different probe intensities as shown in Figure 6.28. From left to right, the probe pulse power changes from 20 mW to 110 mW. At the lowest intensity, the presence of a weak IR field leads to weak sidebands between the odd harmonic orders. These sidebands originate from $\Omega \pm \omega_0$ two-photon transitions as is shown in Figure 6.29 (a). The two possible pathways to each final state lead to the observed interference pattern. This probe intensity regime is the so-called RABITT regime.

With increasing dressing IR intensity, the amplitude of the sidebands becomes comparable to direct photoionization by the harmonics. These two-photon processes induce a depletion of the peaks at odd harmonic energies, at the delays where the sidebands are maximum. At higher probe intensities, processes involving more than one IR photon become significant. When the dressing intensity reaches a few $10^{12} W/cm^2$, the so-called streaking regime is reached, where the AC-streak camera becomes the preferred characterization method [Mairesse and Quéré, 2005]. In our measurements we didn't have intense enough IR dressing pulses to reach the streaking regime. We observe however up to four-photon transitions.

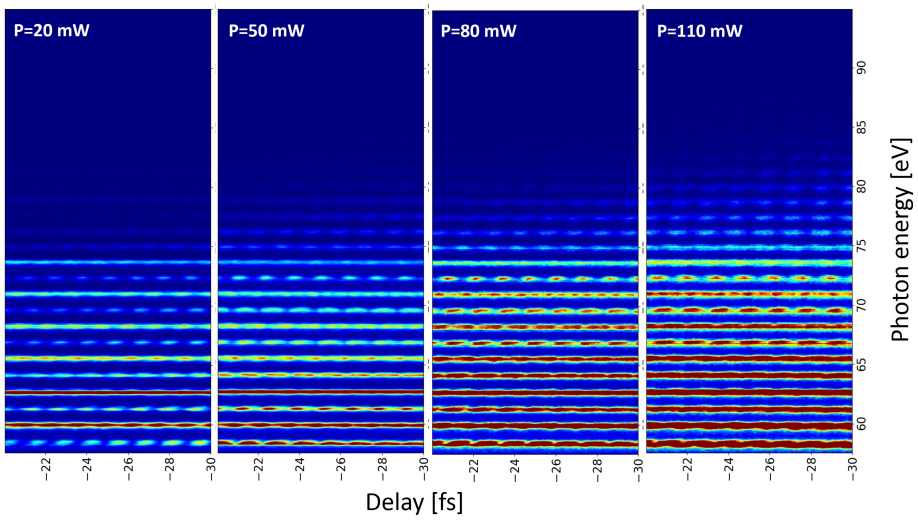

Figure 6.28: RABBIT scans for increasing dressing power.

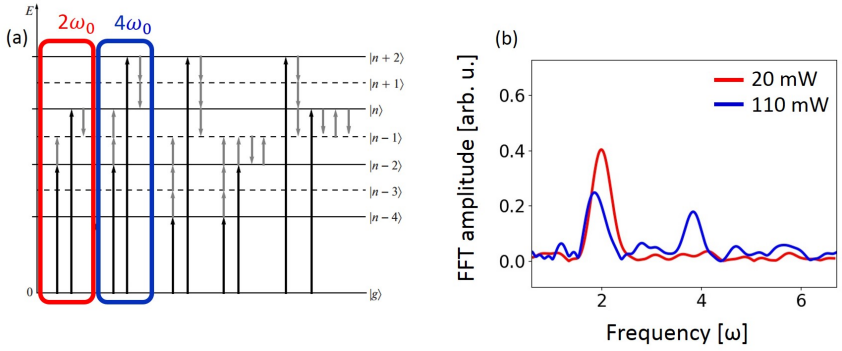

Figure 6.29: (a) Possible transitions involving a single harmonic and multiple IR photons. (b) Amplitude of the FFT of the oscillating RABBIT signal at two different dressing powers, showing the appearance of a $4\omega_0$ peak at 110 mW power.

Swoboda *et al.* [Swoboda et al., 2009] have shown analytically based on third-order perturbation theory, that the intensity of the $4\omega_0$ modulation of a harmonic H_{2n} will be

$$S_{2n}^{(4\omega_0)} \propto cos(4\omega_0\tau + \underbrace{\Delta\phi_{XUV}}_{\phi_{2n-2}-\phi_{2n+2}} + \Delta\phi_{atom}^{(2)}) \tag{6.63}$$

where $\Delta\phi_{atom}^{(2)}$ corresponds to the phase difference of the 3 photon (XUV + 2IR) dipole matrix elements. The next order of perturbation leads to a $6\omega_0$ component in the sidebands and the next to an $8\omega_0$ component again in the harmonics. Higher IR intensities lead to new couplings of states lying further apart and thus higher modulation frequencies. A Fourier transform that isolates these components will allow us to access the spectral phase $\Delta\phi_{atom}^{(i)}$ in the same way as with the conventional RABBIT.

Consequently, the presence of the resonance will be now imprinted on the phase and amplitude of harmonics H37 and H41. After applying the Rainbow RABBIT analysis we obtain Figure 6.30 where for a dressing power of ~80 mW, we plot the $4\omega_0$ phases and amplitudes of the harmonics H37 and H41. For comparison we also show the $2\omega_0$ phases and amplitudes of sidebands SB38 and SB40, for a low dressing power of 20 mW.

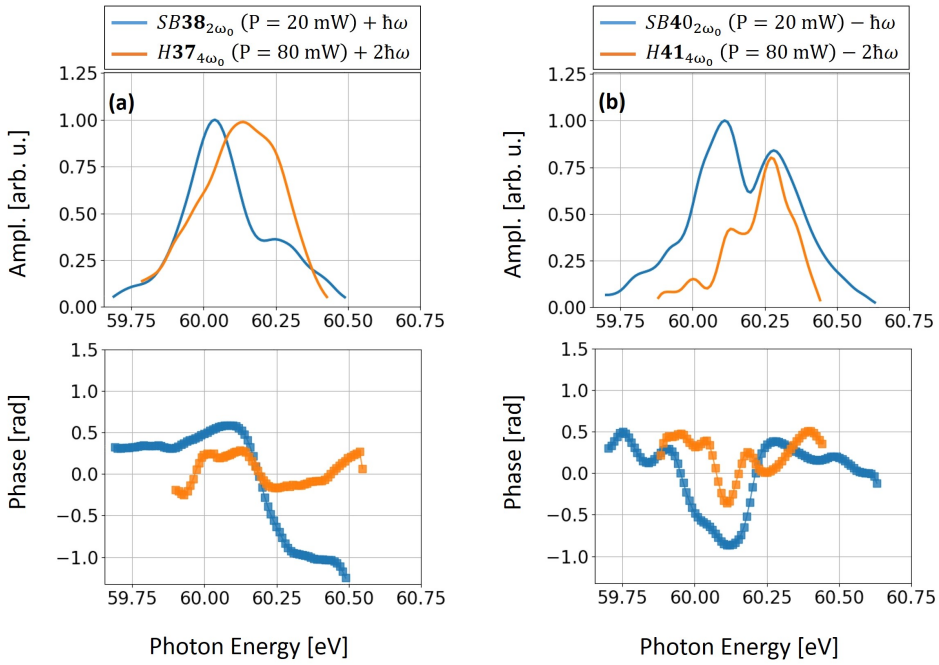

Figure 6.30: RABBIT amplitudes (top pannels) and phases (bottom pannels) extracted from the $2\omega_0$ oscillations of sidebands SB38(a) and SB40(b) (blue) and from the $4\omega_0$ oscillations of H37 (a) and H41(b) (orange)

It seems that the $4\omega_0$ spectral phase of the harmonics, carries some information on the resonance. It is however less pronounced, with the phase jump of H41 being ~1.5 times smaller than the corresponding $2\omega_0$ one of SB40. Similarly, the phase jump of H37 is ~3.3 times smaller than that of of SB38. The comparison between the amplitudes is more difficult since, as discussed throughout this thesis, they are more sensitive as a parameter to the experimental conditions. Thus the effect of the sp2+ resonance on the $4\omega_0$ spectral amplitudes is not so evident.

A complementary investigation in order to support the assumption that for high dressing IR intensities the harmonic $4\omega_0$ spectral phase may carry similar information as the sideband $2\omega_0$ spectral phase for low IR intensity, is to compare the attochirp measured by the classic RABBIT method for both cases as was performed in Ref. [Swoboda et al., 2009].

The attochirp measured for the two cases is $atto_{4\omega_0}$= 28 as per harmonic order and $atto_{2\omega_0}$= 39 as per sideband order. Even though the two values are not the same they are of the same order of magnitude. A possible reason for this discrepancy is the fact that the dressing IR intensity is not high enough as in the case of Ref.[Swoboda et al.,

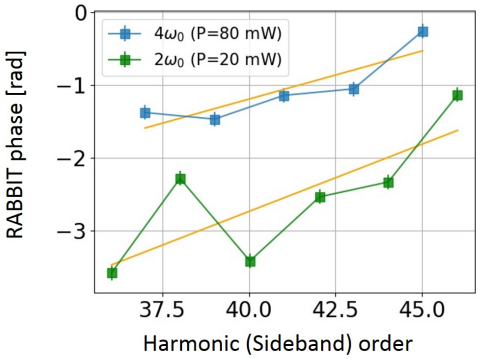

Figure 6.31: Classic RABBIT phases measured for high ($4\omega_0$) and low ($2\omega_0$) dressing power .

2009], something that could also justify the fact that the harmonic $4\omega_0$ Rainbow phases exhibit smaller phase jumps than the corresponding $2\omega_0$ sideband phases.

6.2.7 Simultaneous excitation of sp2+ and sp3+

Earlier in this chapter it was shown that by tuning the wavelength of the driving laser we were able to excite either the sp2+ or the sp3+ resonance (Figure 6.19). However, for a proper wavelength and pulse bandwidth it is possible to ionize simultaneously and thus in coherent way both resonances and create a complex two-electron wave packet. The dynamics of a system like this can be probed either by transient absorption experiments [Ott et al., 2014] or by photoionization spectroscopy. In Figure 6.32 the RABBIT principle is outlined schematically for this particular case.

For these measurements we tuned the central laser wavelength at λ=795 nm with a pulse bandwidth of 90 nm. After applying the Rainbow RABBIT analysis we obtain the spectral amplitudes and phases of Figure 6.33. The phases of SB38 and SB42 have a clear imprint of the sp2+ and sp3+ resonances respectively. Interestingly, the phase of SB40 includes the contribution of both resonances, well separated. It is worth-mentioning at this point, that the energy distance between the two autoionizing states is $\Delta E_{sp3^+-sp2^+}$=3.5 eV. On the other hand we use photons of ~1.5 eV ($\Delta E_{IR_--IR_+}$ ~3.1 eV) thus due to this energy difference of 0.4 eV we are not able to couple directly with the dressing field the two resonances. The phase of SB40 is the proof that the two resonances are coherently excited. As was already mentioned for the case of the single resonances, also here, the experimentally measured spectral phases are in good agreement with numerical simulations performed by Alvaro Jiménez-Galàn based on second order perturbation theory and the Fano formalism taking also into account the finite pulse effect.

We have seen previously that under the experimental conditions of the Lund set

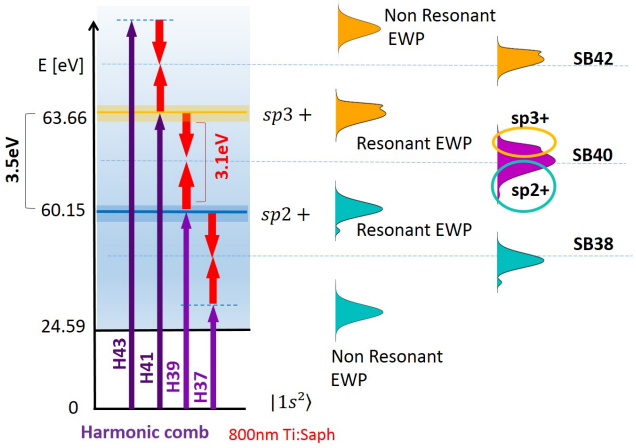

Figure 6.32: Schematic representation of the measurement principle. H39 excites the sp2+ resonance and in parallel H41 excites the sp3+ resonance. The energy difference between the two resonances is 0.4 eV larger than the energy of 2 IR photons so we are not able to couple directly the two resonances with the IR field, but indirectly in the intermediate sideband. Indeed, the signature of this double excitation is imprinted in the Rainbow RABBIT amplitude and phase of SB40.

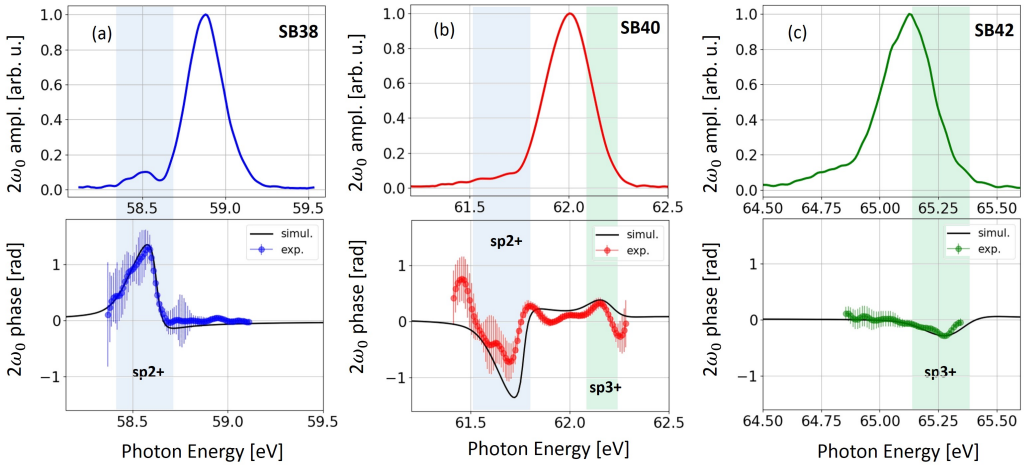

Figure 6.33: Rainbow RABBIT amplitudes and phases of SB38, SB40 and S42 for a driving pulse centered at λ=795 nm with a bandwidth of 90 nm in order to excite simultaneously both sp2+ and sp3+. SB38 and SB42 carry the signature of only sp2+ or sp3+ separately while SB40 has the imprint of both resonances due to their coherent excitation. The black solid lines in the bottom pannels are the results of calculations by the group of Fernando Martin.

up, the sidebands are not an exact replica of the initial one-photon EWPs, especially when the bandwidth of the IR pulses is 90 nm. However, the similarities between the reconstructed dynamics in the preceding paragraph and those of Gruson *et al.* [Gruson et al., 2016a], indicate that this approximation remains qualitatively valid and that the spectral broadening by the dressing photon mainly modifies the

the apparent lifetimes of the resonances. We can therefore approximate the amplitudes and phases of this complex one-photon EWP as:

$$M^{2res}(E) = M_{39}(E) + M_{41}(E) \tag{6.64}$$

$$= A_{39}(E)e^{i\phi_{39,atom}(E)} + A_{41}(E)e^{i\phi_{41,atom}(E)}) \tag{6.65}$$

$$\approx A_{38}(E+\hbar\omega)e^{i\Phi_{38,atom}(E+\hbar\omega)} + A_{42}(E-\hbar\omega)e^{-i\Phi_{42,atom}(E-\hbar\omega)}) \tag{6.66}$$

In Equation 6.66, the replicas extracted from sideband SB38 and SB42 are repositioned at the energies of harmonics H39 and H41, respectively.Note that a minus sign is applied on the phase extracted from SB42 to account for the inverted phase in the sidebands located above resonances. The spectral amplitude and phase of the reconstructed doubly resonant EWP M^{2res} are shown in Figure 6.34 (deconvoluted from the spectrometer response). The dynamics of the corresponding EWP are described by the temporal evolution of $\widetilde{M}^{2res}(t)$ as

$$\widetilde{M}^{2res}(t) = \frac{1}{2}\int_{-\infty}^{+\infty} M^{2res}(E)e^{-iEt/\hbar}dE \tag{6.67}$$

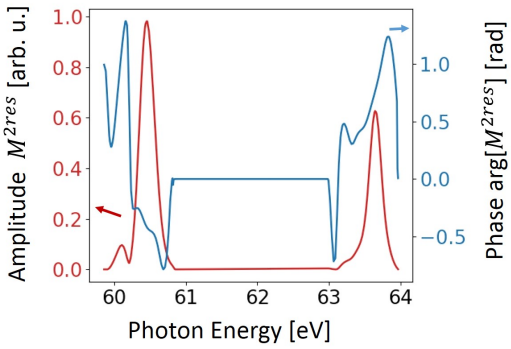

Figure 6.34: Amplitude and phase of the complex EWP created by the coherent excitation of the sp2+ and sp3+ resonances by the harmonics H39 and H41 respectively.

In order to study the influence of resonances on the wave packet, we compare it with a non-resonant, reference wave packet M^{ref} defined as

$$\widetilde{M}^{ref}(t) = \frac{1}{2}\int_{-\infty}^{+\infty} M^{ref}(E)e^{-iEt/\hbar}dE \tag{6.68}$$

with

$$M^{ref}(E) \approx A_{44}(E-5\hbar\omega)e^{i\Phi_{44,atom}(E-5\hbar\omega)} + A_{44}(E-3\hbar\omega)e^{i\Phi_{44,atom}(E-3\hbar\omega)}) \tag{6.69}$$

In equation 6.69, we build the reference, non-resonant EWP by duplicating the wave packet of sideband SB44 and positioning the two replicas to the energies of harmonics H39 and H41. This assumes that harmonics H39 to H45 have rather similar characteristics and that the spectral resolution does not vary too much on this electron energy range.

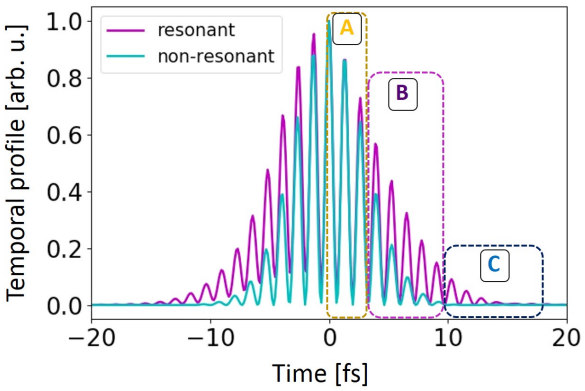

Figure 6.35: Temporal profile of the complex EWP created by the coherent excitation of the two resonances (magenta). This profile is compared with the reference non-resonant one created by the coherent excitation of a smooth continuum (cyan).

Figure 6.35 shows the temporal evolution of $\widetilde{M}^{2res}(t)$ and $\widetilde{M}^{ref}(t)$. The spectral width of the harmonics increases with the order and thus the reference EWP produced from the data of SB44 has a smaller temporal width than the corresponding resonant one where the data of SB38 and SB42 were used. The two highly structured, with fast oscillations EWPs are interestingly enough, getting gradually out of phase for t> 0. Looking more into detail, one can distinguish three regions where the dephasing between the resonant and reference EWP is different. This is presented more clearly in Figure 6.36, where we zoom in the three temporal regions A, B and C. In addition we plot the results of preliminary simulations that were built according to the procedure detailed in Chapter 6.2.1. In the left column ((a),(b),(c)) we plot experimental data and in the right ((d),(e),(f)) the corresponding results of our preliminary simulations. The comparison between the experiment and the theoretical curves is only qualitative. Full TDSE simulations from Antoine Desrier of LCPMR, Université Pierre et Marie Curie are in progress.

Between t=0 fs and ~3 fs (region A) the beating period for both resonant and reference EWPs is T_A=1.3 fs that corresponds to an energy difference of $\Delta E \approx 3.1$ eV. Later on (region B : ~4 fs - 12 fs) an increasing dephasing between the two EWPs is observed with the resonant being in advance from $\Delta\tau$ ~40 as at t= 6.5 fs to $\Delta\tau$ ~150 as at t= 9.1 fs. Finally, after 12 fs (region C : ~12 fs - 40 fs) the non-resonant EWP does not oscillate any more whereas the resonant one continues with a change of the beating period at T_A=1.15 fs that corresponds to $\Delta E \approx 3.5$ eV.

We can explain these three different dynamics as follows. Around t = 0, the two continua are excited by the harmonics and the two direct ionization paths interfere, resulting in a beating of $\Delta E = 2\hbar\omega$. For t greater than the width of the pulse, we observe a beating between the two resonant paths at $\Delta E = E_{sp3+} - E_{sp2+}$. During the intermediate times, all the four paths of ionization interfere and the frequency of oscillations corresponds to a transition between these two limit frequencies. When

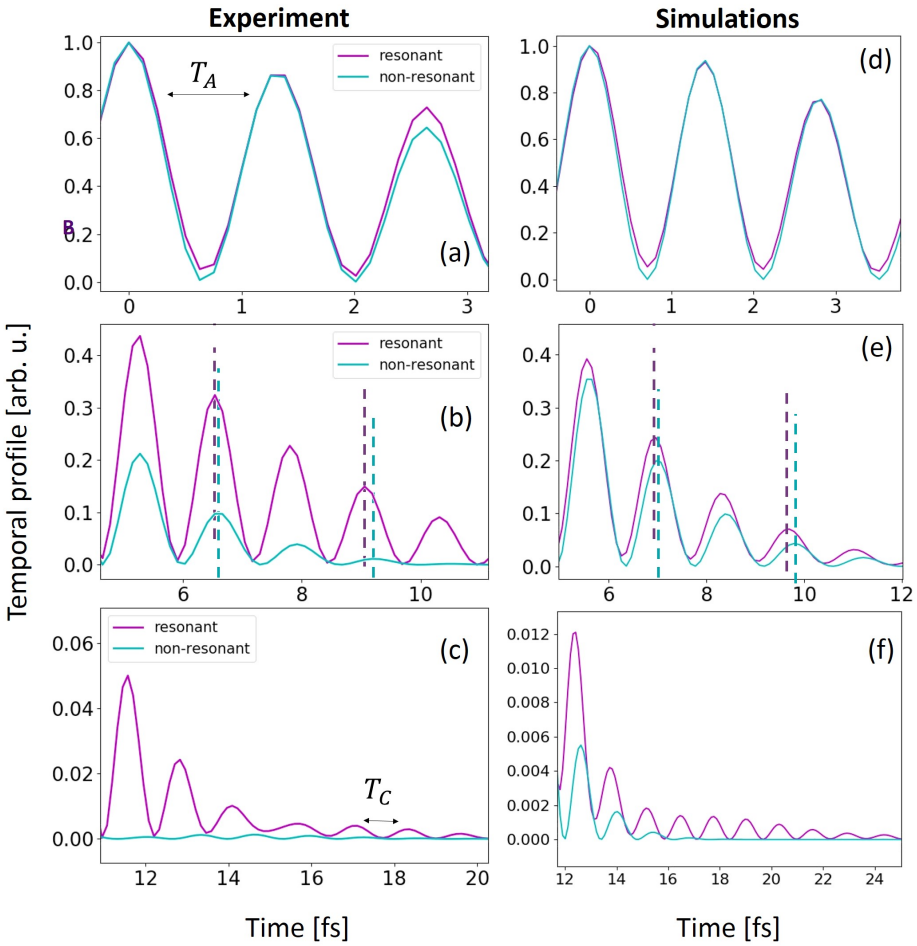

Figure 6.36: Zoom in the three different regions of Figure 6.35. Temporal region A: (a),(d) the beating period is 1.3 fs, corresponding to $\Delta E_{IR_+-IR_-}$ = 3.1 eV; Temporal region B: (c),(e)there is a dephasing between the resonant and non-resonant EWP which increases gradually; Temporal region C: (c),(f) There is a tail only in the resonant EWP that oscillates with a period of 1.15 fs, that corresponds to $\Delta E_{sp3_+-sp2_+}$ = 3.5 eV. The resonant EWP is shown in magenta and the non-resonant one in cyan.

t increases, the oscillation period decreases. Even though the comparison between experiment and theory can only be qualitative, we find very similar behavior (Figure 6.36 (d)-(f)).

6.3 Argon

The first experiment that measured the spectral phase close to a Fano resonance was performed in argon and its $3s^2 3p^6 \rightarrow 3s^1 3p^6 4p$ resonance by Kotur *et al.* [Kotur et al., 2016]. The presence of autoionizing resonances in argon was known since 1935 (Ref.[Lukirskii et al.]). Synchrotron experiments have measured very precisely photoionization cross-sections like the one in Figure 6.37 (a) where one recognizes

the asymmetric form of the absorption line profiles. These line shapes exhibit a different form than that the helium resonances discussed above, due to a very different q parameter ($q_{sp2+,He} = -2.77$, $q_{3s4p,Ar} = -0.25$). The result in this case is a well-shaped resonance which is often called a 'window-resonance'.

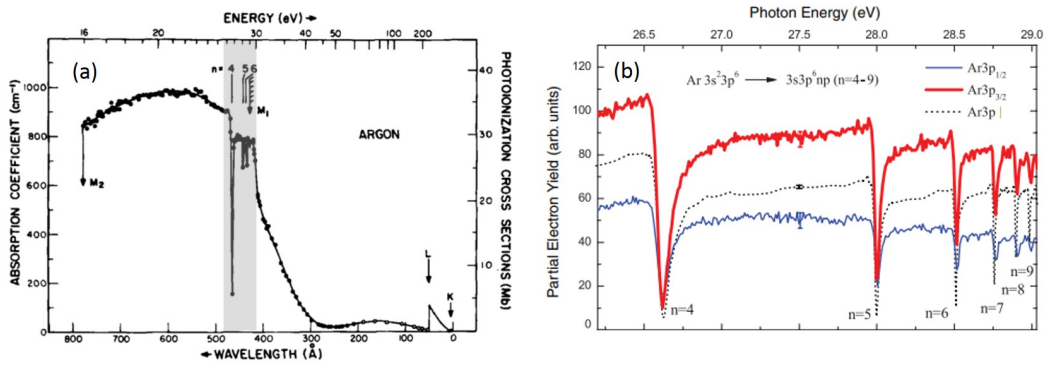

Figure 6.37: (a)Photoionization cross-section of argon taken from Ref [Samson, 1966]. (b) Spin–orbit-resolved partial electron yield across the $3s^2 3p^6 \rightarrow 3s3p^6np$ (n = 4–9) resonances in argon atoms. Taken from Ref [Zhang et al., 2009].

In Kotur *et al.* by using the classic RABBIT method they were able to measure the spectral phases of the two resonant sidebands in the vicinity of the 3s4p Fano resonance as is shown in Figure 6.38. There, the authors measure a phase variation of ~ 0.6 rad for the two sidebands SB16 and SB18 located on either side of the resonance. In order to record the phase through the entire width of the resonance they used a Dazzler to tune the wavelength of the driving laser which is initially centered at 800 nm. The set up used for this experiment is very similar to the one detailed in Chapter 4.3. A comparison with the theory developed in Jiménez-Galán *et al.* [Jiménez-Galán et al., 2014] was performed showing a rather good agreement.

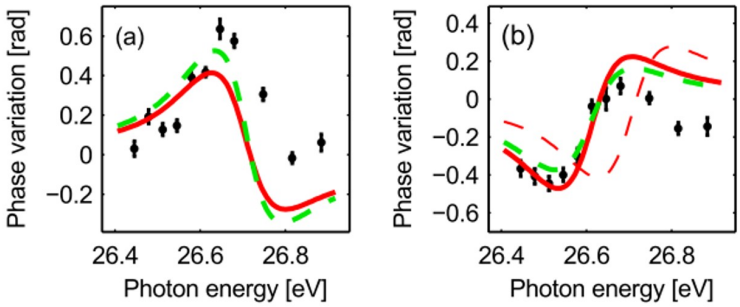

Figure 6.38: Spectral phase of (a) SB16 and (b) SB18 measured with the standard RABBIT technique as a function of the photon energy shifted to the position of harmonic H17. Experimental results correspond to squares. The theoretical results are represented by the green / red curves with / without taking into account the laser coupling between the resonant state and the final state in the continuum. Taken from Ref. [Kotur et al., 2016]

Earlier this year, Cirelli *et al.* [Cirelli et al., 2018] carried out a similar experiment where by using a VMI, they were able to measure the corresponding angle-resolved

delays in the vicinity of 3s4p and 3s5p autoionizing resonances as is shown in Figure 6.39. The presence of an autoionizing state is clear in SB16 where a fast decrease of the measured delays is recorded for different emission angles. This effect of the resonance on the angular dependence of the atomic delay is due to the existence of several open channels with different angular emission properties and with a varying amplitude across the resonance. The anisotropy parameters extracted from time-integrated photoelectron angular distributions generated by two-photon absorption, were also recorded. These results demonstrate not only that the phase of the EWP can be distorted in the presence of resonances, which prevents one from interpreting the Wigner delay as the photoemission time delay, but also that this distortion depends on the electron emission angle.

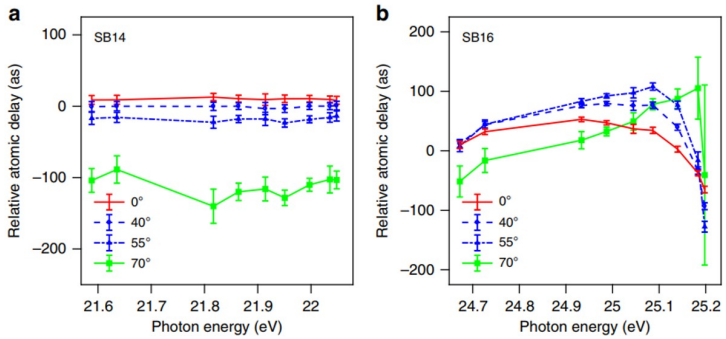

Figure 6.39: Energy and angle-resolved time delays as a function of sideband photon energy for different emission angles for SB14 (a) and SB16 (b). Taken from Ref. [Cirelli et al., 2018]

In both previous studies however, a very interesting aspect that was not taken into account, is the spin-orbit (S-O) splitting. The S-O splitting is essentially an energy shift due to the interaction between the magnetic field that is created by the relative motion between the nucleus and the electron, and the electron's spin angular momentum.

An interesting case is also that of krypton and xenon who exhibit a S-O splitting of E_{Kr} = 0.67 eV and E_{Xe} = 1.31 eV, respectively. Jordan *et al.* [Jordan et al., 2017] measured the photoionization delay differences between the two S-O channels. The presence of the S-O splitting complicates the RABBIT spectrograms since for a 800 nm driving wavelength, the energy distance between a harmonic and a sideband is 1.55 eV. Consequently, in xenon harmonics $J = 1/2$ are overlapping significantly with sidebands $J = 3/2$. In order to measure the corresponding delays, they measure for each delay a photoelectron spectrum without dressing field and then subtract it from the RABBIT spectrogram for each delay step. In the case of krypton a small delay of ~ 6 as was measured in between 20 and 40 eV, while in xenon delays up to 30 as that vary a lot with the energy were extracted. These experimental results were compared with theoretical simulations based on the Time-Dependent Configuration-Interaction Singles (TDCIS) and Relativistic Random Phase Approximation (RRPA) model (Figure 6.40). For xenon, a disagreement between the theoretical calculations and the experimental results is obtained especially in the vicinity

of the Fano resonances around 30 eV (gray dashed lines in Figure 6.40). These resonances were not taken into account in the simulations.

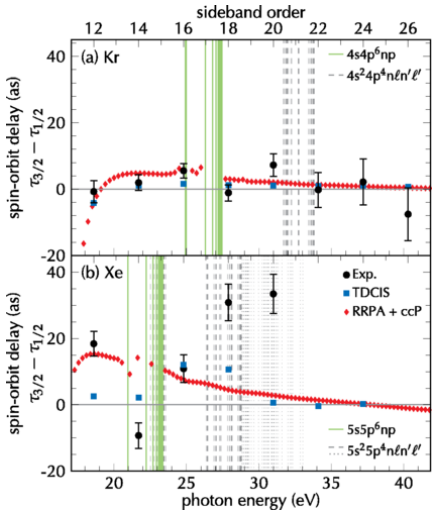

Figure 6.40: Delay between photoelectrons associated with states $^2P_{1/2}$ and $^2P_{3/2}$ of Kr^+ (a) and Xe^+ (b). RABBIT measurements (black circles) are compared to two types of calculations (red and blue symbols). The green and gray lines represent respectively single and double excited states of the atom. Taken from Ref. [Jordan et al., 2017]

In the case of argon this energy shift between the $J = 1/2$ and $J = 3/2$ component is ~180 meV which makes it comparable with the 76 meV-width of the 3s4p Fano resonance. In Figure 6.37 (b) one can see the corresponding cross-sections for each S-O component, compared with the total signal as measured in Ref [Zhang et al., 2009]. The question that arises now is whether this is an effect of the S-O splitting can be resolved in the spectral phase of the resonant sidebands and whether the two S-O components have a different resonant phase evolution. In the following chapter we are going to address these questions by carrying out experimental measurements similar to the ones presented for helium and complementing them with numerical simulations of the examined experimental system.

6.3.1 Rainbow RABBIT measurements : resolution of the S-O splitting

The following experiments were also a collaboration with the group of Anne L'Huillier from Lund university and the group Raimund Feifel from university of Gothenburg, as part of the same campaign. The experimental set up that was used, is the same as in section 6.2.2.

In Figure 6.41, the scheme of the experiment is outlined schematically. The harmonic peaks in the photoelectron spectra exhibit complicated line-shapes as is shown by the spectra in Figure 6.42. The 3s4p resonance lies at 26.6 eV [Samson and Stolte, 2002] and thus affects harmonic 17 of the 800 nm driving laser. As the

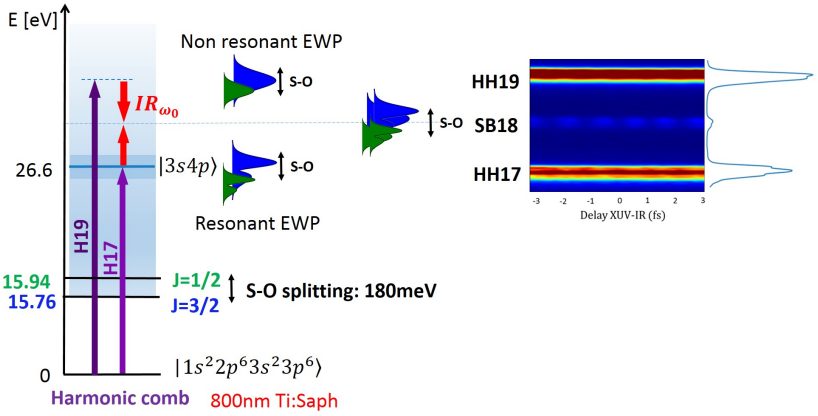

Figure 6.41: Schematic representation of a RABBIT measurement in argon close to the 3s4p Fano resonance, taking also into account the S-O splitting.

wavelength of the driving radiation changes (the tunability is achieved by a Dazzler, see Chapter 4.3), the line-shape of the resonant harmonic H17 changes dramatically. More specifically, while the non-resonant harmonics (H19 and H21) exhibit a double structure due to the S-O splitting that is not affected by the wavelength change, H17 for lower wavelengths shows a similar but more pronounced structure (λ = 783 nm) probably due to the better spectrometer resolution at this lower electron energy. As we move to higher wavelengths (λ = 785 nm and λ = 786 nm), there are now be three peaks whose ratio changes with the wavelength. Finally, for λ = 789 nm the line-shape goes back to its initial shape meaning that we have scanned through the entire resonance.

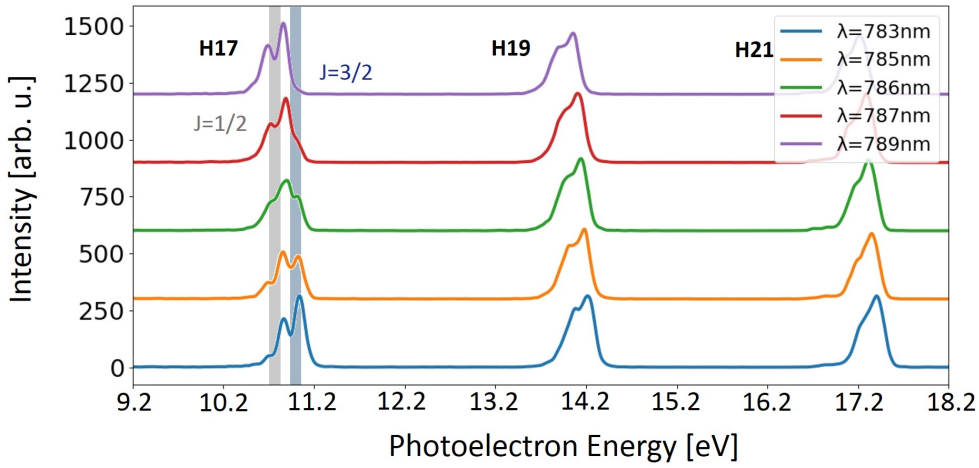

Figure 6.42: Photoelectron spectra produced in argon by the harmonic beam only for different wavelengths of the driving laser. The grey and blue areas in harmonic 17 mark the position of the $|3s4p\rangle$ resonance at E_{kin} = 10.66 eV for the J=1/2 component and at E_{kin} = 10.84 eV for the J=3/2 component (photon energy: 26.6 eV).

The goal of this study is to disentangle the contribution from the two S-O components and to study the influence of the Fano resonance as imprinted on the spectral phase and amplitude of the photoionized EWPs. This can give us insight in electron-electron correlation in more complicated systems than He.

6.3.2 Algorithm for the S-O separation

In order to separate the two S-O contributions numerically, a method that was first demonstrated by Zürch *et al.* [Zürch et al., 2017] in transient absorption experiments was used. There they were interested in the electron-hole dynamics in germanium, which has a larger S-O splitting of 0.58 eV. The idea, transposed to our case, is that one can describe the measured photoelectron spectra as the incoherent sum of the independent spectra corresponding to the J=1/2 and J=3/2 S-O components:

$$S_{tot}(E) = S_{1/2}(E) + S_{3/2}(E). \tag{6.70}$$

If we consider that the two spectra are identical but shifted by the E_{S-O} of the S-O splitting and that are scaled in amplitude by the degeneracy then $S_{1/2}(E) = S(E)$ and $S_{3/2} = 2S(E - E_{S-O})$, equation 6.70 will become:

$$S_{tot}(E) = S_{1/2}(E) + 2S_{1/2}(E - E_{S-O}) \tag{6.71}$$

and its Fourier transform writes:

$$\tilde{S}_{tot}(\eta) = (2e^{-i\eta E_{S-O}} + 1)\tilde{S}_{1/2}(\eta). \tag{6.72}$$

By dividing by the phase factor $(2e^{-i\eta E_{S-O}} + 1)$ and after applying an inverse Fourier transform one can recover the contribution of a single channel:

$$S_{1/2}(E) = FT^{-1}\left[\frac{\tilde{S}_{tot}(\eta)}{(2e^{-i_{S-O}} + 1)}\right]. \tag{6.73}$$

The spectrum of the other channel is obtained by simply multiplying this result by the degeneracy and applying the energy shift E_{S-O}. As the energy calibration of the photoelectron spectrum may be imperfect, the value of E_{S-O} is optimized by an algorithm minimizing the difference between the experimentally measured spectrum and the spectrum calculated from $S_{1/2,exp}(E) = S_{1/2}(\eta)$:

$$S_{tot,exp}(E) = S_{1/2,exp}(E) + 2S_{1/2,exp}(E - E_{S-O,opt}) \tag{6.74}$$

The extracted value $E_{S-O,opt}$ = 180 meV, is very close to the values found in the literature. An example is shown in Figure 6.43 where this algorithm is applied on a spectrum for λ = 789 nm.

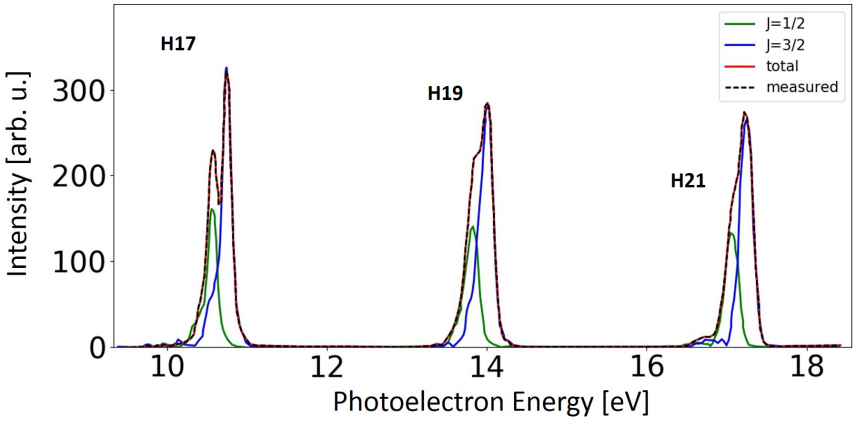

Figure 6.43: Photoelectron spectra produced in argon by the harmonic beam only, generated with λ = 789 nm, decomposed into the two S-O components (J=1/2: green line, J=3/2: blue line). The total retrieved signal (red line) is in excellent agreement with the measured harmonic signal (black dashed line).

Note that possible discrepancies between the retrieved data and the actual measurements could be caused by the fact that we impose the ratio between the two components to be $P_{3/2} = 2P_{1/2}$. Ref. [Canton-Rogan et al., 2000] measured the ratio of the two S-O cross-sections as $\sigma_{P_{3/2}} \approx 1.9\sigma_{P_{3/2}}$. Moreover, according to Ref.[Caldwell et al., 2000] this ratio can vary in the vicinity of Fano resonances and for the specific case of the 3s4p resonance it can vary between 1.7 and 2.2.

6.3.3 Rainbow RABBIT phase measurements in the vicinity of the 3s4p resonance

A typical spectrogram is shown in Figure 6.44. We generate and detect in argon with driving pulses of λ= 786 nm, pulse bandwidth of 50nm which means that the finite pulse effect is less present as compared to the helium data. The deconvolution from the spectrometer response was also applied in this case however the result was very similar to the raw data. We are interested in harmonic H17 which is the resonant one and its corresponding sidebands SB16 and SB18, thus a retarding potential of 9 V is applied to the MBES in order to shift the sidebands of interest to lower kinetic energies, where the electron spectrometer exhibits its best resolution.

Applying the algorithm described above to the spectrum of each delay of the RABBIT spectrogram, we end up with two separate RABBIT traces for each S-O component that then are analyzed with the Rainbow RABBIT method described in Chapter 5.1. The resulting spectral amplitudes and phases are shown in green and blue

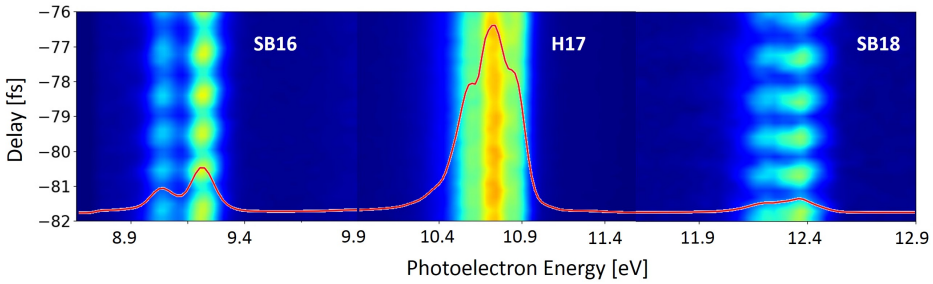

Figure 6.44: RABBIT spectrogram of SB16, H17 and SB18. The integrated signal over the delay is plotted as the red line.

for the two S-O components in the two resonant sidebands SB16 and S18 along with a non-resonant one (SB20) in Figure 6.46. A spectrogram is recalculated by applying the relation 6.71. Like in the spectra without any dressing IR (Figure 6.43), the agreement with the analysis of the measured spectra is very good, especially on the higher energy sidebands, such as SB20. The reason for this effect is that SB16 for example, that is detected on the lower kinetic energies and thus that is better resolved, it is also more sensitive to the electronic noise of the detector.

To highlight the good agreement between the analysis and the measured data we plot in Figure 6.45, the raw RABBIT trace (a), the retrieved one (b) and the difference between the two (c) and it is clear that the residual difference is very small. Additionally, in figure 6.46, are also plotted the measured data (black dashed lines), that are in very good agreement with the retrieved total curves (red curves) for both amplitudes and phases. This overall good agreement tells us that the assumptions performed for extracting the two S-O components are consistent with the measured trace.

The green traces correspond to the retrieved spectral amplitudes and phases of the J=1/2 component whereas the blue ones to the J=3/2 component. In SB18, the amplitude of each component has the imprint of the window resonance and a phase jump of ~0.5 rad in the vicinity of the minimum of the amplitude at 28.45 eV (J=1/2) and 28.65 eV (J=3/2). For SB16 the phase jumps are larger ~1 rad at 25.43 eV (J=1/2) and 25.61 eV (J=3/2). The phase variations between the two resonant sidebands are symmetric but the size of the phase jump is twice larger for SB16. This however, could be explained by the fact that the q_{eff} parameters differ between the two sidebands if γ is significantly nonzero since $q^{\pm}_{eff} = q \mp 2(q-i)\beta\omega/\Gamma$, as already invoked in Ref. [Kotur et al., 2016]. Related examples will be given in the section that follows where our preliminary simulations are presented. As was expected, the spectral phase of the non-resonant SB20 exhibits a flat behavior with no fast variations. The comparison between the measured total phases is shown in Figure 6.47.

At this point it is interesting to compare with the results of Kotur *et al.* [Kotur et al., 2016], where the classic RABBIT in combination with the tunability of the driving laser were used in order to extract the corresponding phases. A comparison is pre-

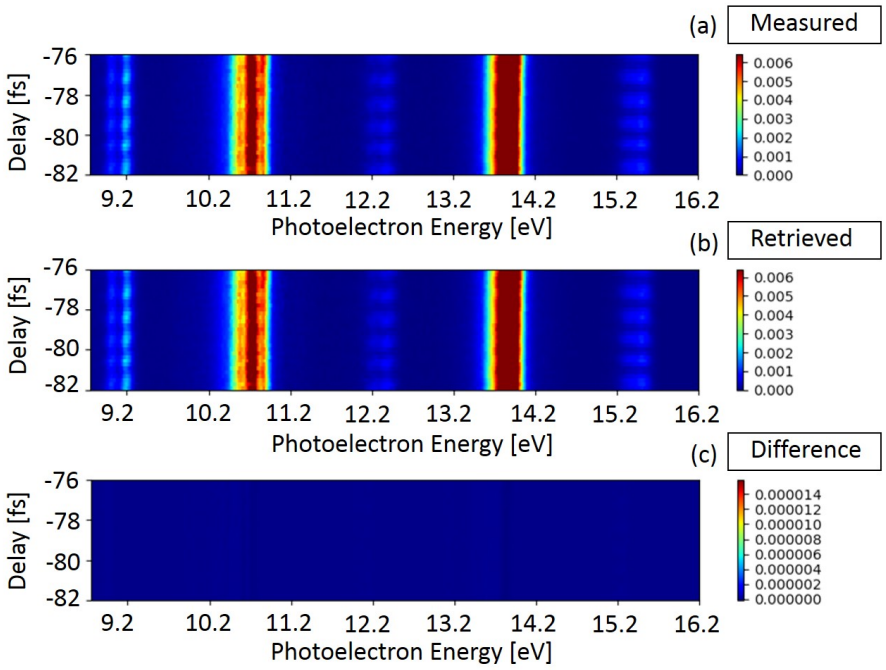

Figure 6.45: (a) Measured RABBIT trace, (b) reconstructed RABBIT trace using the procedure described in the text and (d) the residual difference when the trace (b) is subtracted from the trace (a).

sented Figure 6.48. A striking difference is that the phase evolution in Kotur *et al.* is much smoother and of smaller amplitude (especially for SB16) than the Rainbow rabbit results. In particular, it has no sign of the double structure related to the S-O components. This is a consequence of the integration of the sideband signal over the entire spectral width that smears out the fast structures due to the resonance in both S-O components. The phase of the integrated sideband is not just a mean phase in the arithmetic sense of the term, but rather a weighted average value by the intensity distribution of the sideband(Chapter 5.1).

Now that the spectral phase and amplitude of the two S-O components have been resolved and taking into account the propensity rule which favors transitions to states with larger angular momenta [Fano, 1985], it is possible to obtain the two-photon EWP of the J=3/2 component in the time domain. After applying a Fourier transform to the two-photon electron wave packet with amplitude and phase as given below:

$$|M^{17+1,3/2}(E)| = \frac{A_{18,3/2}(E)}{\sqrt{2A_{20,3/2}(E+2\hbar\omega)}} \tag{6.75}$$

$$\Phi_{17+1,3/2}(E) \approx -\phi^{atom}_{17+1,3/2}(E) \tag{6.76}$$

$$\widetilde{M}^{(2)}_{res}(t) = \frac{1}{2}\int |M^{17+1,3/2}(E)| \cdot e^{i\phi^{atom}_{17+1,3/2}(E)} \cdot e^{-iEt/\hbar} dE, \tag{6.77}$$

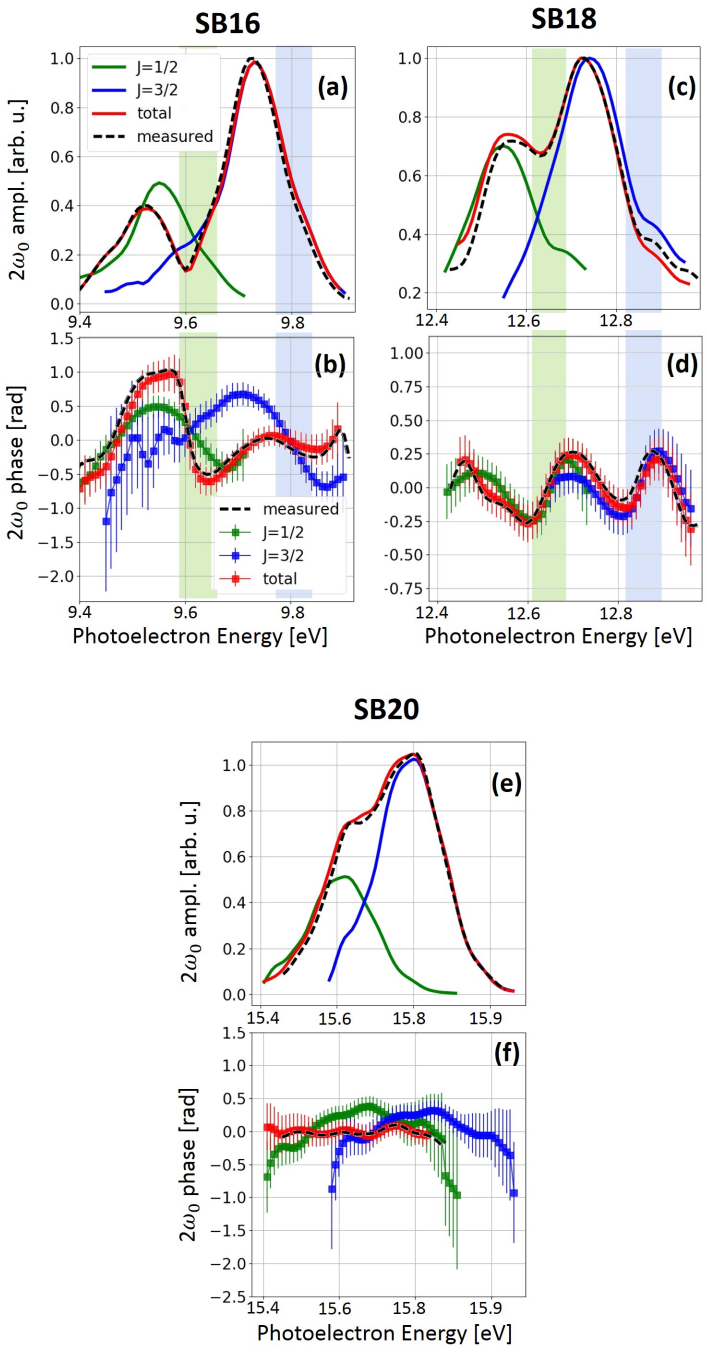

Figure 6.46: Experimentally measured Rainbow RABBIT amplitudes and phases for SB16, SB18 and SB20 (black dashed lines). The phases of the two S-O components retrieved using the procedure detailed in the text are shown in green for J=1/2, blue for J=3/2 and red for the total, respectively. The linear slope has been removed from all the plotted phases.

we obtain the temporal amplitude and phase of Figure 6.49 (a). We observe a Gaussian component centered in t = 0 fs followed by an amplitude minimum associated with a phase jump of 2.5 rad characteristic of the interference between direct ionization and ionization via the auto-ionizing state, and finally a small bump corre-

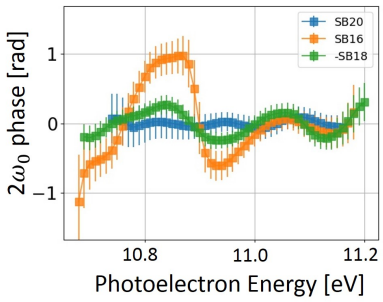

Figure 6.47: Measured RABBIT phases of SB16, SB18 and SB20. All have been shifted on the resonance energy position (SB16 $+1\hbar\omega_0$, SB18 $-1\hbar\omega_0$, SB20 $-3\hbar\omega_0$). The phase of SB18 has been inverted.

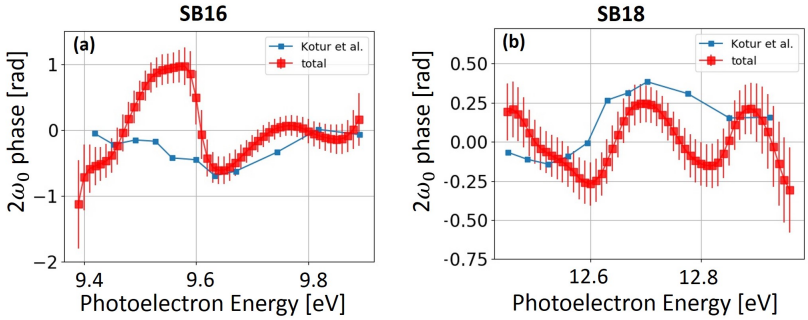

Figure 6.48: Comparison between the phases of SB16 and SB18 measured by the Rainbow (red squares) and the classic (blue squares) RABBIT method.

sponding to the decay of the latter. The build up of the resonant two-photon EWP in time, $|W(E,t_{acc})|^2$, is also calculated as described in section 6.2 and presented in Figure 6.49 (b). The spectrum first reproduces the excitation harmonic spectrum and then we observe the appearance of the window resonance for a photon energy ~ 28.65 eV at tacc ~3 fs.

6.3.4 Preliminary simulations

In order to understand the above experimental results we performed preliminary numerical simulations similar to the ones described in Chapter 6.2.1.

Resonant Harmonic

We first illustrate the simulation technique in the simple case of the resonant one-photon transition. As already mentioned in section 6.1.3 the presence in argon of two continua (s and d) to which the resonance is coupled by CI, results in a modified expression of the resonant one-photon (as well as two-photon) transition, as follows

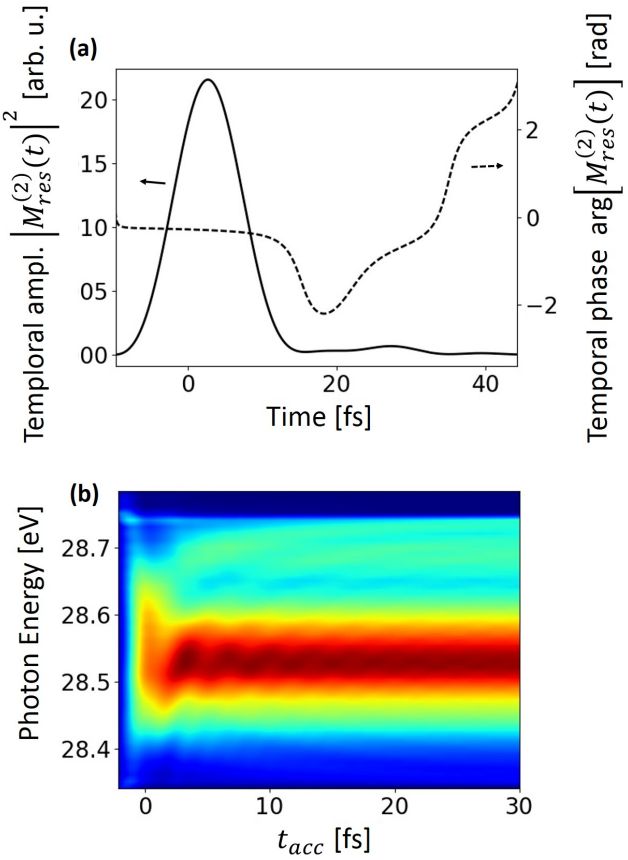

Figure 6.49: (a) Temporal profile and phase of the EWP corresponding to the J=3/2 component of SB18. (b) Temporal build up of the resonant sideband $\left|W_{3/2,SB18}(E,t_{acc})\right|^2$

[Kotur et al., 2015]:

$$\mathcal{M}^{(1)}_{res} = M^{1,(1)}\frac{q+\epsilon}{\epsilon+i} + M^{2,(1)}. \tag{6.78}$$

The parameters of the 3s4p resonance are: q = -0.25, Γ=76 meV, E_{res}=26.65 eV and $M^{1,(1)}$ = 3.766 – 9.545i, $M^{2,(1)}$ = 0.459 – 4.462i (values taken from Kotur *et al* [Kotur et al., 2015]) corresponding to the transition via an an 'interacting' and a 'non-interacting' continuum respectively, as detailed in section 6.1.3. The resonant harmonic intensity is then described as a Gaussian (see Chapter 6.2.1 for a detailed expression) multiplied by the resonant amplitude of equation 6.78. In Figure 6.50 (a) we plot the Gaussians (same Gaussian shifted by the E_{S-O} = 180 meV) and the corresponding cross-sections ($\sigma_{3/2} \approx 2\sigma_{1/2} = \left|\mathcal{M}^{(1)}_{res}\right|^2$) for each S-O component. The simulated resonant harmonic H17 is shown in Figure 6.50 (b) where the total yield is the sum of the two S-O contributions.

To estimate the corresponding experimental values as well as the FWHM of the spectrometer response described by a Gaussian (equation 6.51), we fit the profile of a simulated non-resonant harmonic to the experimental one. For this series of experiments we find $FWHM_{harmonic}$=180 meV and a spectrometer resolution of

$FWHM_{sp}$= 90 meV. The resonant harmonic line in these conditions exhibits a three-peak lineshape.

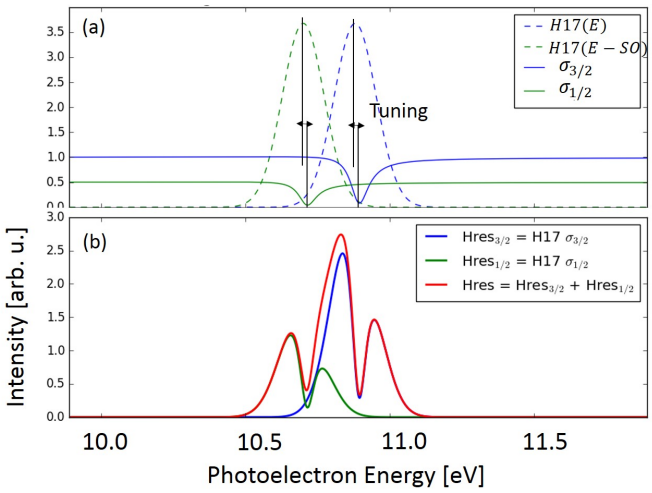

Figure 6.50: (a) cross-sections of the Fano resonance for the two S-O components, scaled by the degeneracy $\sigma_{1/2} = \frac{1}{2}\sigma_{3/2}$ and shifted by ΔE_{S-O} along with the excitation gaussian pulses. (b) The resulting line-profile of the resonant harmonic H17.

RABBIT spectrogram

We now move on to the simulation of the RABBIT spectrogram. For these calculations narrow dressing IR pulses are assumed since the experimental data have been obtained with the narrow 50-nm laser bandwidth and thus we don't take into account the finite pulses effect. The resonant two-photon transition amplitude is now given by Ref. [Kotur et al., 2016]:

$$\mathcal{M}_{res}^{(2)\pm} = M^{1,(2)} \frac{q_{eff}^{\pm} + \epsilon}{\epsilon + i} + M^{2,(2)} \tag{6.79}$$

with

$$q_{eff}^{\pm} = q \mp 2(q - i)\beta\omega_0/\Gamma, \tag{6.80}$$

where $\beta = 0.005$ as calculated by Alvaro Jiménez Galán . $M^{1,(2)} = -0.459 + 5.462i$ and $M^{2,(2)} = 16.36 + 38i$, extracted from Ref. [Kotur et al., 2016] and now q has become a complex number $q_{eff}^{\pm}$ in order to include the effect of the dressing IR pulses with the + sign for SB18 and the - sign for SB16 [Jiménez-Galán et al., 2014].

In order to build the RABBIT trace of a resonant sideband we first construct the RABBIT traces of the two S-O components J=1/2 and J=3/2 by using the expression 6.48, with harmonic intensity $\left|A(E)_{J=1/2}\right|^2 = 1/2\left|A(E)_{J=3/2}\right|^2$. After summing the two, the total trace is convoluted with the spectrometer response function as is shown schematically in Figure 6.51 for the resonant SB16.

Results

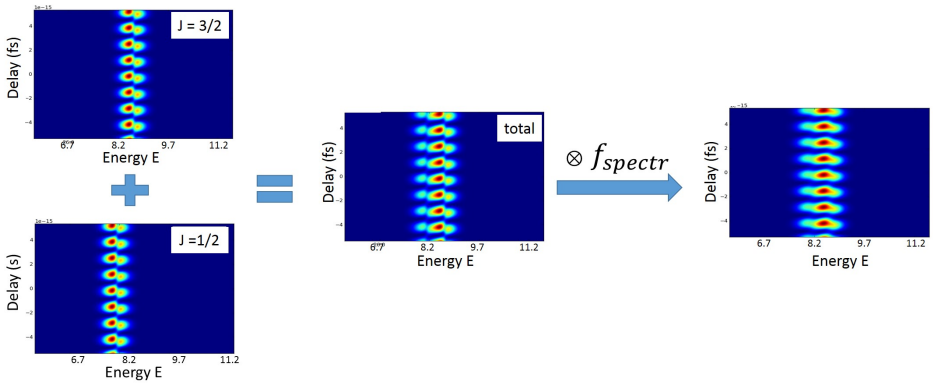

Figure 6.51: Schematic representation of the procedure followed for simulation of the resonant sidebands. First the RABBIT traces of both S-O components (scaled by the degeneracy) are calculated separately, then they are summed to give the total RABBIT trace that is finally convoluted with the spectrometer response function.

After applying the Rainbow RABBIT analysis to the simulated RABBIT traces of the resonant sideband SB18 for different driving wavelengths (tunings) we obtain the results of Figure 6.52. The effect of the different tuning is clear in both the spectral amplitudes and phases. It is worth-mentioning that when the resonant harmonic is red(blue)-tuned compared to the resonance, the phase jump corresponding to the J=3/2(J=1/2) is entirely retrieved as is shown in (a),(b)(in (e),(f))). The simulated results show a very similar behavior with the experimental measurements when compared to the case of λ=794 nm. However, for a more rigorous comparison, simulations of the exact phase in the vicinity of the window resonance 3s4p and for the two S-O components should be performed. Simulations based on second order perturbation theory and the Fano formalism are in progress, carried out by the group Fernando Martín of university of Madrid.

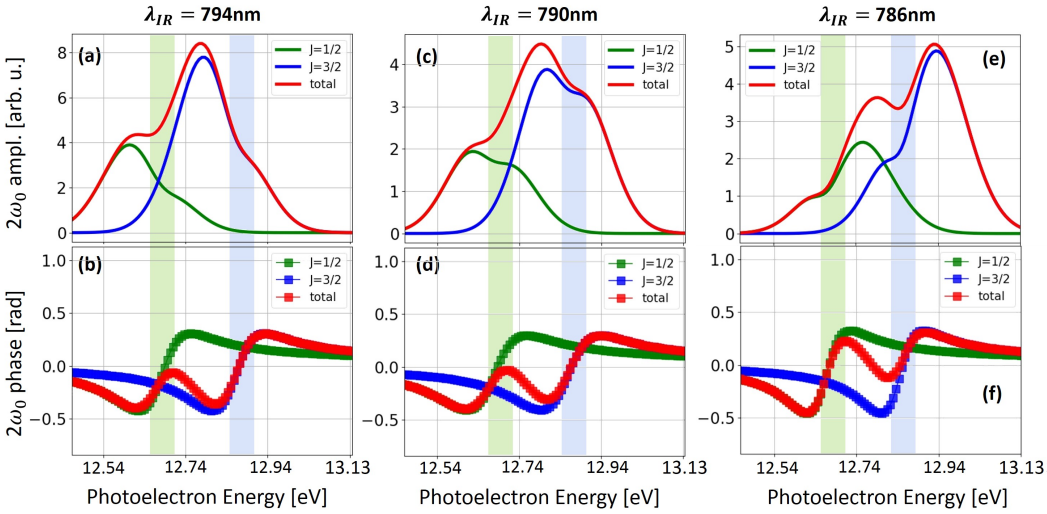

Figure 6.52: Top and middle row: Simulated Rainbow RABBIT amplitudes and phases of the total (red), $P_{1/2}$ (green) and $P_{3/2}$ (blue) contributions for different wavelengths for SB18.

6.4 Conclusions

In this chapter an extended study on the photoionization dynamics in the vicinity of Fano resonances was presented. First, the theoretical background of the original work of Fano was reminded along with its extension to the two-photon ionization conditions (performed by the group of F. Martin) in order to simulate the RABBIT measurement technique.

The experimental work of this chapter is divided into two main parts: i) the study of the sp2+ and sp3+ resonances in Helium and ii) the study of the 3s4p resonance in Argon. Starting by *Helium*, we first discuss the influence of the experimental conditions on the spectral phase and amplitude extraction procedure via the Rainbow RABBIT technique. We studied the influence of the following parameters: the spectrometer resolution, the spectral width of the resonant harmonic and the dressing pulses' as well as the energy position of the resonant harmonic. We saw that they can potentially distort both the retrieved spectral phase and amplitude which may lead later on to a misinterpretation of the corresponding dynamics. These aspects were studied theoretically for the prototypical case of sp2+ resonance however the above results apply for every feature that exhibits fast spectral phase and amplitude variations.

Next, in the spirit of Gruson *et al.* and in order to push further this analysis of autoionization dynamics, we performed measurements around the sp2+ and sp3+ resonances. First, after ionizing each resonance separately, which was possible thanks to the tunability of the driving wavelength provided by a Dazzler, we recorded the corresponding Rainbow RABBIT phases and amplitudes. The influence of the different experimental parameters such as the spectrometer resolution and the spectral

width of the IR and XUV pulses was discussed and linked to the numerical calculation above. We then investigated different time–frequency representations and we fully characterized the sp2+ resonant EWP using short time Fourier transforms (STFT) and Wigner time–frequency representations. This, together with theoretical calculations, allowed us to resolve the ionization dynamics, and in particular, to disentangle the contributions of the two ionization paths.

Then, the influence of the increasing dressing intensity was explored. We first investigated its effect on the line-shape of the sp2+ resonance. The observed distortion was linked to a change of the value of the q parameter. The effect on the RABBIT phases was also discussed. There it was shown that when the dressing intensity is sufficiently high, the information encoded in the sidebands' $2\omega_0$ oscillations is transferred, somewhat smeared out, to the $4\omega_0$ oscillations of the harmonics.

Finally, for a proper wavelength and pulse bandwidth we were able to ionize simultaneously this time the two resonances sp2+ and sp3+ creating a complex two-electron wave packet. The dynamics of this complex EWP revealed that there are different processes involved in different times.

In the case of *Argon* we were able to resolve its spin-orbit splitting of 180 meV due to the sub-100 meV resolution of the electron spectrometer. The Rainbow RABBIT phases and amplitudes in the vicinity of the 3s4p resonance were measured and then separated into the two spin-orbit components using a numerical procedure. This gave consistent results, allowing us to reconstruct the build up in time of the resonant EWP of the J=3/2 component. Preliminary simulations were performed and gave a physical insight into our experimental results.

CHAPTER 7

COOPER MINIMUM IN ARGON

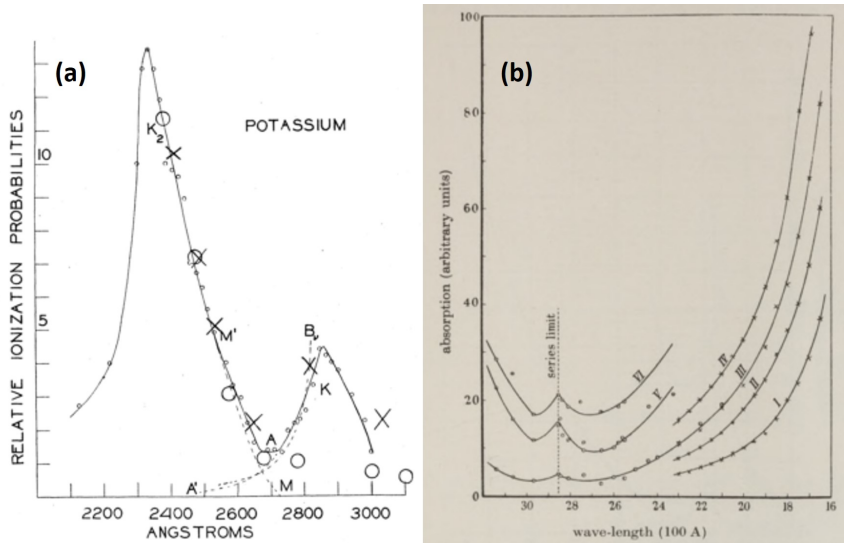

Figure 7.1: (a)[Lawrence and Edlefsen, 1929]: The ionization per unit light intensity B_v as a function of the wavelength. The small circles represent the data of the reported experiments. The large circles represent earlier observations by Lawrence, and the crosses Williamson's data [Williamson, 1923]. (b) [Ditchburn, 1943]: Absorption curves in the vapor-pressure range 1.6-8.5 mm.

Historically, the first measurement of a Cooper minimum (CM) was performed in 1923 by Williamson [Williamson, 1923] who was studying the photo-electric emission from potassium vapors using ultra-violet light. Later on in 1929 [Lawrence and Edlefsen, 1929] Lawrence and Edlefsen (Figure 7.1 (a)) performed a similar experiment with improved resolution and along with the complementary work of [Ditchburn, 1943] in 1943 (Figure 7.1 (b)), who measured the continuous absorption spectrum of the potassium vapors, showed that as the frequency of the incident radiation increases, the cross-section falls, reaches a minimum and then rises rapidly. Even though the conditions at the time were exceptionally difficult and as stated in [Ditchburn, 1943] 'The experiments have been interrupted owing to war conditions', these first experiments revealed the presence of a minimum that was not affected by experimental parameters such as the vapor pressure and was positioned at a specific energy. The basic explanation for the phenomenon in the alkali-metal atoms was given by Bates ([Bat, 1947] ,[Bates and Massey, 1946]) and extended to include relativistic interactions by Seaton ([Sea, 1951]). However it was only after more than twenty years that John W. Cooper showed that this phenomenon was not limited to the outer shells of the alkali-metal atoms but was a very general occurrence and interpreted the origin of this minimum as a result of the cancellation of the radial integral for some transitions, depending on the overlap between the

wavefunctions of the initial and final quantum states of the atoms [Cooper, 1962].

Around the same time, in the 1960's, the advent of synchrotron radiation allowed the measurement of the photoionization cross sections of atoms and molecules up to high energies. A particular interest was then drawn towards the CM since it constitutes a signature of the atomic structure. Numerous theoretical studies have been performed along with experiments studying the Cooper minima in atoms, molecules and solids([Aymar et al., 1976], [Alexander, 1965], [Becker and Shirley, 1996], [Kim et al., 1981], [Rossi et al., 1983], [Abbati et al., 1983], [Lahiri and Manson, 1982], [Manson, 1985], [Berezhko et al., 1978], [Carlson et al., 1982], [Carlson et al., 1984], [Lahiri and Manson, 1982], [Beterov et al., 2012]). However, due to their simpler and more convenient theoretical description, noble gases became a main topic of discussion both experimentally and theoretically especially when Cooper minima were found in argon, krypton, xenon and radon. One of the first measurements of the CM in argon was performed by Houlgate et al. in 1974 ([Houlgate et al., 1974]), who measured the photoionization cross section in both 3s and 3p ionization channels. Later on a large number of studies confirmed these preliminary results ([Samson and Gardner, 1974], [Houlgate et al., 1976], [Yeh and Lindau, 1985] , [Adam et al., 1985], [Chan et al., 1992], [Huang et al., 1981], [Kennedy and Manson, 1972], [Duzy and Hyman, 1980], [Samson et al., 1991], [Möbus et al., 1993], [Samson and Stolte, 2002]).

Nowadays, with the advent of ultrashort XUV table top sources, new possibilities are being opened. By using techniques like RABBIT (Chapter 4.1) one can access not only the spectral amplitudes but also the spectral phases of the emitted photoelectron wavepackets and thus retrieve the ionization dynamics in the vicinity of structures like the CM. Moreover, a new type of nonlinear spectroscopy namely the High-order harmonic spectroscopy, based on the advanced characterization of the harmonic emission, is able to retrieve structural information about the generating atom and thus give supplementary information about the CM and its effect on the HHG process itself.

In this chapter, a brief description of Cooper's original work will be given in Chapter 7.1, followed by our experimental study of the CM in argon using both Photoionization and High-order Harmonic spectroscopy (Chapter 7.2 and Chapter 7.3). In Chapter 7.4 we discuss the electron dynamics in the sense of ionization delays, close to the CM of both 3s and 3p ionization channels. This is followed in Chapter 7.5 by preliminary simulations in order to test the validity of our experimental results. Finally, a comparison with different theoretical models is carried out (Chapter 7.6).

7.1 Theoretical aspects

7.1.1 Cooper's original work

The motivation behind Cooper's theoretical calculations was the fact that at the time the experimental work on atomic photoionization at lower energies, i.e. in the range from threshold to 100 eV, was very poor. Work on rare gases was very difficult since the spectral region of interest lies in the far ultra-violet and synchrotron radiation as well as XUV attosecond pulses were not available. Alkalis were the other option since they could also be studied as free atoms, but their low cross-sections and the difficulty of obtaining purely monochromatic vapors resulted in very complicated experiments, limited in an extremely narrow range of energies.

In this section the work of [Cooper, 1962] will be presented, where Cooper calculated the radial wavefunctions $P_{nl}(r)$ and $P_{\epsilon l}(r)$ (see below) using the Hartree-Fock wavefunctions [Kennedy and Manson, 1972]. Even though this method provides qualitative agreement with experiment, it is often inaccurate in its prediction of the exact energy of spectral features. Much better accuracy can be obtained by taking into account electron-electron correlations by using the Random-Phase Approximation with Exchange (RPAE or simply RPA) ([Amusia et al., 1971], [Kheifets, 2013]), Many-Body Perturbation Theory (MBPT) ([Dahlström et al., 2012a]), or the Time-Dependent Local Density Approximation (TDLDA) ([Dixit et al., 2013], [Magrakvelidze et al., 2015a]). Pseudopotential methods ([Worner et al., 2009], [Miller et al., 1977], [Miller and Dow, 1977]) show similar accuracy as RPAE but are much simpler to implement [Swarts et al., 1979]. The outer subshells of heavy atoms, Kr and Xe for instance, require a relativistic treatment such as the Relativistic RPAE (RRPAE) ([Johnson and Cheng, 1979], [Huang et al., 1981],[Fink and Johnson, 1986], [Johnson, 1989], [Johnson and Lin, 1979], [Saha et al., 2014]). For a more detailed description of the methods and a comparison with experimental results see Chapter 7.6.

In the non-relativistic approximation, the cross section for absorption of photons with energy E_{ph}=hv>I_p, where I_p is the first ionization potential of the atom, in the dipole approximation depends on the radial overlap between the ground state wave function and the final continuum wave function. Thus it can be written as:

$$\sigma(E_{ph}) = \frac{4\pi\alpha a_0^2}{3} h\nu \left| \int \psi_0(r_1,r_2,...r_N) \sum_i \mathbf{r_i} \psi_f(r_1,r_2,...r_N) d\tau \right|^2, \tag{7.1}$$

where a_0 is the atomic radius, α the fine-structure constant, ψ_0 and ψ_f are the wave functions of a single atom before and after absorption, respectively, expressed in terms of electron coordinates $\mathbf{r_i}$. The wave functions are expressed in atomic units, the integration is over the entire electron configuration space τ, the sum is over all atomic electrons and ψ_0 is normalized to unit amplitude and ψ_f per unit energy.

The multiple ionization is ignored and thus ψ_f represents a system consisting of an ion plus a free electron of energy ϵ.

In order to numerically evaluate equation 7.1, Cooper made the following assumptions to estimate the ψ_0 and ψ_f. First, he assumes that ψ_0 and ψ_f are antisymmetrized products of one-electron wave functions which leads to the Hartree-Fock equations and the central-field description of the atomic structure. The second hypothesis is that out of the N one-electron wave functions that form the ψ_0 and ψ_f, N-1 are exactly the same for initial and final states. This implies that the ionic core is unrelaxed which leads to the interpretation of the one-electron orbital energies for the various electron orbitals of an atom, as ionization potentials for the electrons in the respective subshells. Taking also into account that the one-electron wave functions are separable in radial and angular coordinates (spin is ignored here) and that the cross section is averaged over the orientation of the axis of quantization, the integral of equation 7.1 is now reduced to $M = \int \phi_0(r_1) r_1 \phi_f(r_1) d\tau_1$. The last assumption made is that the one-electron free wave functions are eigen-functions of the same effective central potential as the ground state functions $\phi_0(r_1)$. This means that the effects of electron exchange are ignored since the ionized electron is described as moving in the same effective central field both before and after ionization.

In order to estimate the one-electron wave functions $\phi_0(r_1)$ and $\phi_f(r_1)$, Cooper defines a central potential $V_{nl}(r)$ for the nl subshell by means of the radial Schrödinger equation:

$$\left[\frac{d^2}{dr^2} + V_{nl}(r) + \epsilon_{nl} - \frac{l(l+1)}{r^2}\right] P_{nl}(r) = 0, \tag{7.2}$$

where $P_{nl}(r)$ is the Hartree-Fock radial bound-state orbital and ϵ_{nl} is the orbital energy. By combining equation 7.2 with the radial Hartree-Fock equation for an electron in the nl subshell of an atom:

$$\left[\frac{d^2}{dr^2} + G_{nl}(r) + \epsilon_{nl} - \frac{l(l+1)}{r^2}\right] P_{nl}(r) = X_{nl}(r), \tag{7.3}$$

with $G_{nl}(r)$ and $X_{nl}(r)$ are the potential and exchange terms, Cooper finds $V_{nl}(r) = G_{nl}(r) - X_{nl}(r)/P_{nl}(r)$ and then he is able to evaluate the $P_{nl}(r)$ numerically through equation 7.2.

For the continuum states he replaces $P_{nl}(r)$ and $\epsilon_{nl}(r)$ by $P_{\epsilon l}(r)$ and ϵ in equation 7.2, and obtains the continuum state radial wave functions $P_{\epsilon l}(r)$ for positive electron energy ϵ. After normalization at large distances ($r \to \infty$) they become

$$P_{\epsilon l}(r) \sim \pi^{-1/2} \epsilon^{-1/4} \sin[\epsilon^{1/2} r - \frac{l\pi}{2} - z\epsilon^{-1/2}(\ln 2\epsilon^{1/2} r) + \sigma_l(\epsilon) + \delta_l(\epsilon)] \tag{7.4}$$

with $\sigma_l(\epsilon) = \arg(l+1-i\epsilon^{(-1/2)})$ being the Coulomb phase shift, $\delta_l(\epsilon)$ a constant non-Coulombic phase shift and z the ionic charge (=1)([Manson, 1985]).

7.1.1.1 Radial Matrix Elements and Photoionization Cross Sections

The photoionization cross section of equation 7.1 now becomes

$$\sigma_{nl}(\epsilon) = \frac{4\pi\alpha a_0^2}{3}(\epsilon - \epsilon_{nl})(C_{l-1}R_{l-1}^2 + C_{l+1}R_{l+1}^2), \tag{7.5}$$

where the numerical factors $C_{l\pm1}$ arise from averaging over all the initial states of angular momentum quantum number m and summing over all the final states. The dipole matrix elements will be

$$R_{l\pm1} \equiv \langle P_{nl}|r|P_{\epsilon,l\pm1}\rangle \int_0^\infty P_{nl}(r)rP_{\epsilon,l\pm1}(r)dr \tag{7.6}$$

with $P_{nl}(r)$ and $P_{\epsilon,l\pm1}(r)$ the radial parts of the discrete and continuum wave functions described above.

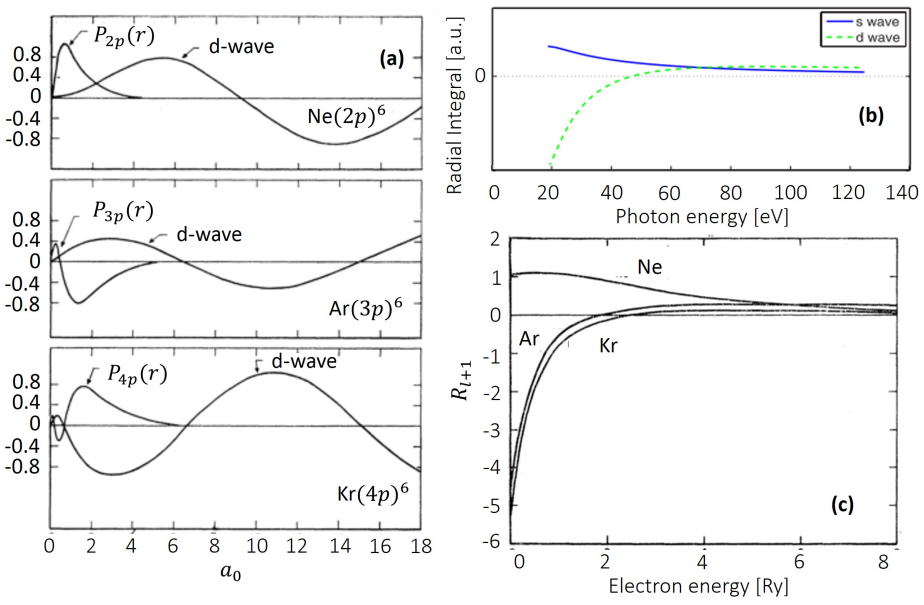

Figure 7.2: (a) Outer subshell radial wave functions and d waves for $\epsilon = 0$ for Ne, Ar and Kr. (b) Radial integrals $R_{l\pm1}$ for s waves (full line), d waves (dashed line) for argon as a function of the emitted photon energy as calculated by [Worner et al., 2009]. (c) Matrix elements for p→d transitions in Ne, Ar, and Kr.

Figure 7.2 illustrates the origin of the CM: In Figure 7.2 (b), taking the example of argon, the radial matrix element R_{l-1} which corresponds to the 3p → ϵs transition, decreases slightly and remains positive. On the other hand the value of the R_{l+1} element (transition 3p → ϵd) undergoes much larger modulations, and in particular

goes to zero and changes sign for a photoelectron energy of 30.6 eV, which corresponds to a photon energy of 30.6 + I_p = 46.3 eV. This change in the sign of the integral R_{l+1} can be explained by studying the radial wave functions of valence and continuum. These functions are represented in 7.2 (a) (middle panel):
- For low photon energies, the main contribution to the radial integral comes from the part between r ≈ 0.5 a_0 and r ≈ 6.5 a_0, where $P_{nl} = P_{31}$ is negative and $P_{\epsilon,l\pm1} = P_{\epsilon 2}$ positive and therefore the total radial integral is generally negative, $\int P_{31}(r)P_{\epsilon 2}(r)rdr < 0$.
- At 70 eV, the corresponding d wave oscillates much faster so that $P_{\epsilon 2}$ becomes negative in the $(0.5-6.5)a_0$ region. The radial integral will then be globally positive. This change of sign on the 3p → ϵd component, and thus the crossing from zero of the radial integral for this term, is the origin of the CM in the photoionization cross section. The contribution of the 3p → ϵs component, which does not change sign, prevents the cross section from passing through a zero. In general for atoms in their ground state, zeros are found in the $l \to l+1$ transitions, not in the $l \to l-1$. There is, usually a single zero for a given $l \to l+1$ transition. This zero crossing of the radial matrix element of one angular momentum channel is equivalent to an instantaneous π phase jump in that channel. For transitions involving a bound orbital with nonzero angular momentum (l > 0), the two dipole-allowed transition channels $l \to l \pm 1$ interfere, causing the phase jump of the total transition dipole, to be spread out in energy, rather than instantaneous. In Figure 7.3 the corresponding cross sections for neon, argon and krypton calculated by Cooper are plotted. The calculations take into account only the ionization from outer subshells.

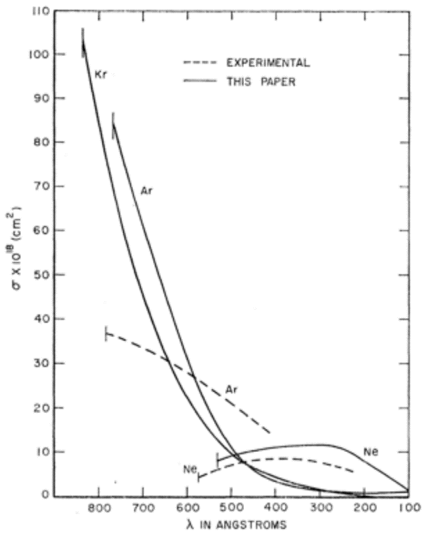

Figure 7.3: Photoionization cross sections for Ne, Ar and Kr.

Later on, it was shown theoretically that the photoionization cross section of specific atoms could exhibit multiple minima. An example is the atom of Cs where three zeros were found in 9d→ ϵf transition and one in the 9d→ ϵp transition ([Lahiri and Manson, 1982]). The dependence of the minima on the atomic number Z has been also studied by numerical calculations which showed that minima occur over the entire periodic table for all outer and near-outer subshells whose wavefunctions

have nodes, except for the 2s state ([Manson, 1985]).

7.1.2 Cooper minimum in photoionization of Argon

Within the non-relativistic SAE approximation, the photoionization cross section for a transition from an initial bound state ψ_i to the final continuum state ψ_k^- due to a linearly polarized field, is proportional to the modulus square of the transition dipole:

$$d_{k,n}(\omega) = \langle \psi_k^- | \mathbf{r} \cdot \mathbf{n} | \psi_i \rangle \tag{7.7}$$

with **n** being the direction of the light polarization and **k** the momentum of the ejected photoelectron. In spherical coordinates, the bound wavefunction can be factorized into radial and angular terms:

$$\psi_i(\mathbf{r}) = R_{nl_i}(r) Y_{l_i}^{m_i}(\Omega_\mathbf{r}), \tag{7.8}$$

where $R_{nl_i}(r)$ is the radial and $Y_{l_i}^{m_i}(\Omega_\mathbf{r})$ the angular term. The incoming scattering wave will then be expanded in terms of partial waves as:

$$\psi_k^-(\mathbf{r}) = \frac{1}{\sqrt{k}} \sum_{l=0}^{\infty} \sum_{m=-l}^{+l} i^l e^{[-i(\sigma_l + \delta_l)]} R_{\epsilon l}(r) Y_l^m(\Omega_\mathbf{r}) Y_l^{m*}(\Omega_\mathbf{k}) \tag{7.9}$$

with σ_l and δ_l the same as in equation 7.4. When the polarization direction **n** is parallel to the z axis the transition dipole writes:

$$d_z(\omega) = \langle \psi_k^- | z | \psi_i \rangle = \frac{1}{\sqrt{k}} \sum_{lm} i^l e^{-i(\sigma_l + \delta_l)} \langle R_{\epsilon l} | r | R_{nl_i} \rangle \langle Y_l^{m*} | cos\theta | Y_{l_i}^{m_i} \rangle \tag{7.10}$$

In the specific case of the 3p ionization channel of argon, it becomes ([Le et al., 2013]):

$$d_z(\omega) = \frac{1}{\sqrt{3\pi k}} [\underbrace{e^{-i(\sigma_0 + \delta_0)} \langle R_{\epsilon 0} | r | R_{31_i} \rangle / 2}_{s-wave} - \underbrace{e^{-i(\sigma_2 + \delta_2)} \langle R_{\epsilon 2} | r | R_{31_i} \rangle}_{d-wave}], \tag{7.11}$$

where we have only the contributions of l=l_i-1=0 (s-wave) and l=l_i+1=2 (d-wave) with the latter being in general the dominant component. When the real d-wave radial dipole matrix element approaches zero, a minimum in the photoionization cross-section appears at an energy where the interference between the two terms in equation 7.11 is the most destructive. In the following section a comparison between the experimentally measured CM in the photoionization and in the recombination process will be performed.

7.2 Cooper minimum in Photoionization (PI) and Photorecombination (PR)

7.2.1 State of the art

As discussed above, the CM has been extensively studied in PI cross-sections. A possibility to study it in PR was brought about by the advent of high harmonic spectroscopy. In 2002, M. Lein ([Lein et al., 2002]) showed theoretically that minima encoding the molecular structure could appear in the harmonic spectra generated from aligned H_2 and H_2^+ molecules. Further works [Itatani et al., 2004], [Haessler et al., 2011] then established that the harmonic dipole in the strong-field approximation could be factorized in a form involving the field-free PR dipole moment. This amounts to neglecting the presence of the strong laser electric field during the PR step of the HHG process ([Worner et al., 2009], [Le et al., 2008b], [Jin et al., 2011], [Frolov et al., 2011]). The assumption of time-reversal symmetry between PR and PI which follows the principle of detailed balancing [Landau and Lifshitz, 1977] then allows to connect the PR and PI dipoles. Therefore, for the case where the XUV light is polarized along the z direction, one can write the PR and PI dipole matrix elements as:

$$d_{rec} = \langle \psi_i | z | \psi_k^+ \rangle, \tag{7.12}$$

$$d_{ion} = \langle \psi_k^- | z | \psi_i \rangle \tag{7.13}$$

In the case of an atom with ground state of angular momentum l, and for electron emission/recombination in the same direction, one gets the simple expressions(for the detailed proof see Appendix D of [Schoun, 2015]):

$$d_{z,rec} = \begin{cases} d_{z,ion} & \text{, for } l \text{ odd} \\ -d_{z,ion} & \text{, for } l \text{ even} \end{cases} \tag{7.14}$$

In fact, the PI and PR differential cross-sections are related by:

$$\frac{d^2\sigma^{rec}}{\omega^2 d\Omega_n d\Omega_k} = \frac{d^2\sigma^{ion}}{k^2 d\Omega_k d\Omega_n} \tag{7.15}$$

and the corresponding spectral phases as:

$$\arg[d_{z,rec}] = \begin{cases} \arg[d_{z,ion}] & \text{, for } l \text{ odd} \\ \pi + \arg[d_{z,ion}] & \text{, for } l \text{ even} \end{cases} \tag{7.16}$$

According to that, one would expect that measurements from high-order harmonic spectroscopy and photoionization spectroscopy would give very similar results.

However this is not the case neither for the cross-sections nor for the spectral phases.

Cross-section

As was already mentioned in the discussion above, the first measurements of the argon CM were performed in PI experiments as the ones of [Marr and West, 1976], [Samson and Gardner, 1974] using synchrotron radiation. Later on the CM was measured also in the high-order harmonic spectra [L'Huillier and Balcou, 1993], [Wahlström et al., 1993] but it was only almost 20 years later that studies on the nature of this minimum and its dependence on experimental conditions were carried out [Worner et al., 2009], [Jin et al., 2011], [Farrell et al., 2011], [Higuet et al., 2011], [Minemoto et al., 2008]. In Figure 7.4 we plot the harmonic (PR) and PI signals for different phase matching conditions as well as for variations of the laser field parameters.

There are two interesting points to discuss:
- Firstly, the position of the CM differs from 49 eV for PI to ~54 eV for PR. A possible reason for this uncertainty is the different experimental conditions for HHG. Minemoto *et al.* [Minemoto et al., 2008] and Farrell *et al.* [Farrell et al., 2011] showed that the position of the laser focus relative to the gas jet can shift the CM. In addition, Schoun *et al.* [Schoun et al., 2014] reported different positions of the CM when two different wavelengths of the driving laser are used. On the other hand, Wörner *et al.* [Worner et al., 2009], Minemoto *et al.* [Minemoto et al., 2008] and Higuet *et al.* [Higuet et al., 2011] measured no difference in the CM position when the intensity and the wavelength of the driving laser is changed. Furthermore, Higuet *et al.* [Higuet et al., 2011] showed that conditions like the backing pressure, the laser beam aperture and the laser focus position do not affect the position of the CM.
- Secondly, the PR CM is redshifted compared to the PI one. The reason of this effect will be discussed below.

Spectral Phase

In order to measure the total dipole phase, one needs an interferometric technique. A perfect tool for this type of measurements is the RABBIT method for the reasons detailed in 4.1. In 2014 Schoun *et al.* [Schoun et al., 2014] was the first to measure this phase in the PR process by using the RABBIT method. Later the same year Palatchi *et al.* [Palatchi et al.] performed similar measurements studying the PI process. In Figure 7.5 we plot these results along with our corresponding measurements, presented below.

7.2.2 Cross-section and phase measurements at ATTOlab

The driving laser used for this experiment has a central wavelength around 800 nm with pulse duration of 25 fs at 1 kHz repetition rate. For the PR case we generate

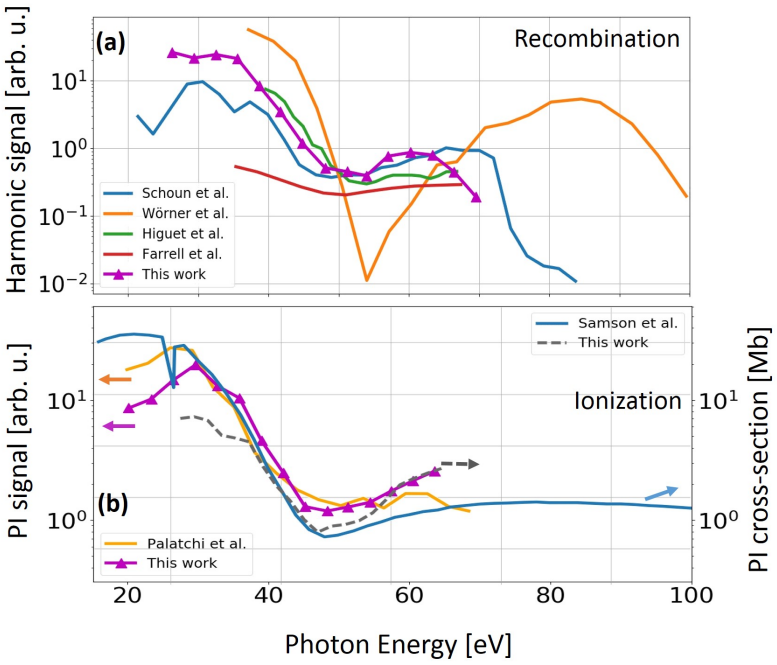

Figure 7.4: **(a)** Harmonic signal generated in argon. The position of the CM differs between measurements. (orange curve): Generation: λ= 780 nm, I= 2.5 – 3.5 × $10^{14} W/cm^2$, duration= 8 fs , Detection: XUV spectrometer, CM position: 53 eV ±3 eV [Worner et al., 2009]; (green curve): Generation: λ= 1800 nm, I= $8 \times 10^{13} W/cm^2$, duration= 50 fs, Detection: XUV spectrometer, CM position: 53.8 eV ±0.7 eV [Higuet et al., 2011]; (red curve): Generation: λ= 780 nm, duration= 30 fs, the Detection: XUV spectrometer, CM position: 51 eV [Farrell et al., 2011]; (blue curve): Generation: λ= 1300 nm, I= $1.6 \times 10^{14} W/cm^2$, duration= 60 fs, Detection: MBES, detection gas= neon, CM position: 49 eV [Schoun et al., 2014]; (magenta triangles) our measurements: Generation: λ= 800 nm, I= $3.7 \times 10^{14} W/cm^2$, duration= 25 fs , Detection : MBES, detection gas= neon, CM position: 53.9 eV. **(b)** PI signal and cross section of argon. (blue curve): Ionization cross-section from Synchrotron experiment with CM position at 48 eV [Samson and Gardner, 1974]; (orange curve): PI signal for generation conditions: λ= 780 nm, I= $9 \times 10^{14} W/cm^2$, duration= 60 fs, generation gas= neon, Detection: MBES, CM position: 50.3 eV [Palatchi et al.] ; (magenta triangles) our measurements: Generation: λ= 800 nm, I= $4 \times 10^{14} W/cm^2$, duration= 25 fs, generation gas= neon, Detection: MBES, CM position: 48.3 eV. (gray dashed curve): Ionization cross-section extracted from the magenta triangles (see text) with CM position at 47 eV.

harmonics in argon using a gas cell of 10 mm and the estimated laser intensity at the focus is $\sim 2 \times 10^{14} W/cm^2$. As detection gas in the MBES we used neon due to its relatively structureless cross section and atomic phase around the energies of interest. For the PI case the generation gas is neon and for the detection argon is now used. For the same conditions we take also reference measurements with neon as generation and detection gas. The estimated laser intensity at focus is $4{\times}10^{14} W/cm^2$. The proper calibration of our MBES spectra (Chapter 4.2.3) is crucial to accurately determine the position of the CM. A reference is provided by using a 200 nm aluminum filter since it transmits energies between 20 eV and 73 eV. The latter energy corresponds to the sudden absorption L-edge, and is thus very useful to determine the order of the last measured harmonic.

The magenta triangles shown in Figure 7.4 correspond to the peak intensity of the photoelectron harmonic spectra generated in argon for PR and in neon for PI. In the case of PI in order to access the cross-section we need to subtract the influence of the HHG process which is achieved by calibrating with a reference measurement as the one mentioned above. We can then extract the cross-section in the following way: the measured argon photoelectron spectrum S_{Ar}^{PI} can be expressed as the multiplication of the generating neon harmonics H_n^{Ne} by the argon PI cross-section σ_{Ar}^{PI}:

$$S_{Ar}^{PI} = \sigma_{Ar}^{PI} \times H_n^{Ne}. \tag{7.17}$$

For the reference measurement the neon photoelectron spectrum is:

$$S_{Ne}^{PI} = \sigma_{Ne}^{PI} \times H_n^{Ne}. \tag{7.18}$$

The ratio between the two gives $\sigma_{Ar}^{PI} = \sigma_{Ne}^{PI} \frac{S_{Ar}^{PI}}{S_{Ne}^{PI}}$ and with the neon PI cross-section known from the literature we can indeed estimate the PI cross-section of argon as plotted in Figure 7.4 (b) as the gray dashed line. On the other hand, the PR case is more complicated and in the frame of this experiment it was not possible to access the PR argon cross-section. Here the measured neon photolectron spectrum writes $S_{Ne}^{PI} = \sigma_{Ne}^{PI} \times H_n^{Ar} \approx \sigma_{Ne}^{PI} \sigma_{Ar}^{PR} |a_n|^2$, where a_n is a complex amplitude including the accumulated phase and the spreading of the EWP during its excursion and before recombining with the parent ion (for a more detailed discussion see Chapter 2.2.2). The reference in this case should be an element with the same I_p as argon (for example nitrogen) which would allow to replicate the same HHG conditions and thus the same value of a_n. Unfortunately, such measurement was not performed.

The phase values shown in Figure 7.5 correspond to the sideband phases extracted by the traditional RABBIT method. For each sideband we integrate over the FWHM which is approximately 400 meV however this depends on the order since for higher energies the spectrometer resolution decreases. The plotted curves are averaged over a number of independent measurements. It should also be emphasized that we lack the knowledge of the absolute delay between the APT and the IR field, which leads to an unknown constant shift in the delay of the RABBIT scans. We thus shift vertically the curves of Figure 7.5 to zero in order to overlap them with Palatchi *et al.* and Schoun *et al.* and facilitate the comparison.

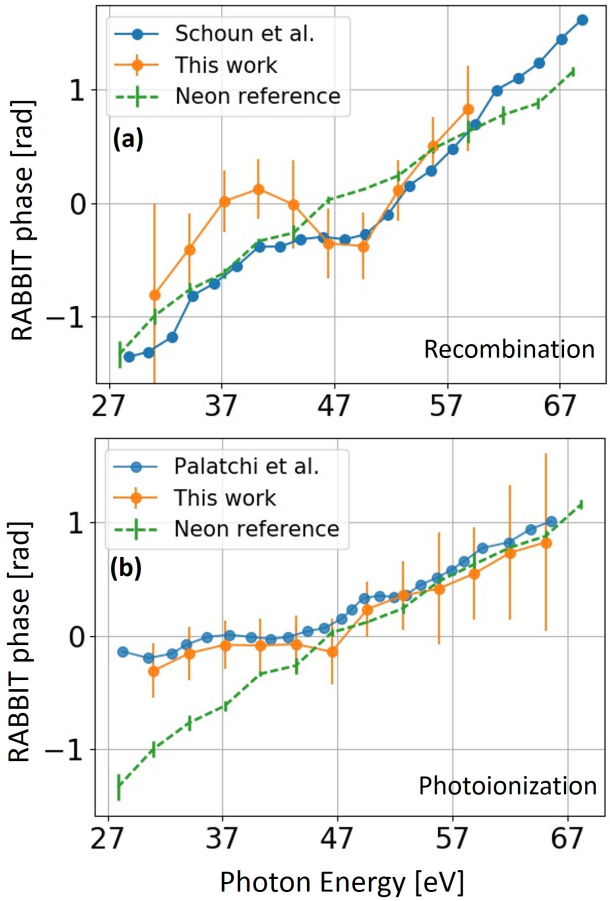

Figure 7.5: (a) RABBIT phases for the PR scheme measured in this work (orange circles) along with similar measurements of [Schoun et al., 2014] (blue circles) and the reference neon phases (green dashed line). (b) RABBIT phases for the PI scheme measured in this work (orange circles) along with similar measurements of [Palatchi et al.] (blue circles) and the reference neon phases (green dashed line).

Figure 7.5 shows that the CM appears as a jump in the sidebands' phase that deviates from the normally linear evolution. In the PR case, the phase jump is ~0.9 rad at 49.6 eV and for PI is ~0.4 rad at 46.5 eV. For both PR and PI, our measurements are in good agreement with previous experiments (±2 eV): Schoun *et al.* finds a minimum of ~0.5 rad at ~49.7 eV and Palatchi *et al.* measures ~0.2 rad at ~45.8 eV. Another interesting point is that even though Schoun *et al.* finds an energy shift of the CM when they use different driving laser wavelengths (for λ = 1300 nm the CM is at ~49.7 eV while for λ = 2000 nm it is found at ~52 eV), we agree perfectly with the λ = 1300 nm case even though we use λ = 800 nm. This is in agreement with the work of [Worner et al., 2009],[Minemoto et al., 2008] and [Higuet et al., 2011] who claim that the driving laser conditions do not affect the position of the CM, as was discussed earlier.

In Figure 7.6 (a,b), we report our measured PI and PR intensities and phases. In the PI case, the measured phases correspond to: $\Delta\phi^{Ne,Ar}_{RABBIT} = \Delta\phi^{Ne}_{XUV} + \Delta\phi^{Ar}_{atom}$. The con-

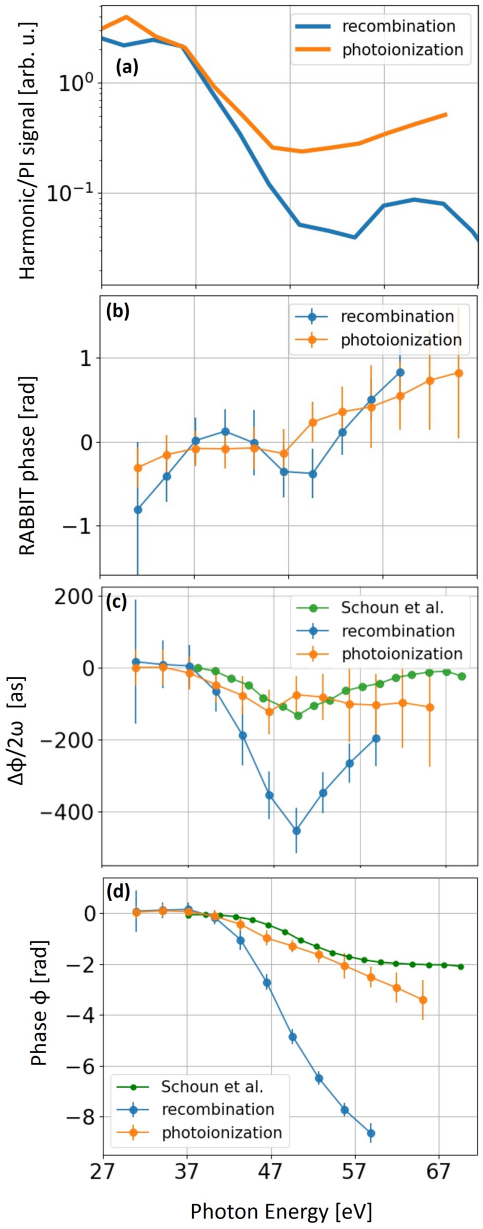

Figure 7.6: (a) Harmonic signal for the PR (blue line) and PI signal (orange line) measured in argon. (b) PR (blue line) and PI (orange line) spectral phases measured by RABBIT. (c) Group delays for PI (orange line) , PR (blue line) which after integration will result in the phases ϕ^{Ar}_{atom} (orange line) and ϕ^{Ar}_{PR} (blue line) of (d). In green we plot previous PR measurements from Ref [Schoun et al., 2014].

tribution of the phase difference between consecutive harmonics $\Delta\phi^{Ne}_{XUV}$, namely the attochirp (Chapter 2.1.3) appears as a global linear slope that needs to be removed in order to access the atomic phase of argon. To do so we calibrate with the reference measurement shown as a green dashed line in Figure 7.5. This will give: $\Delta\phi^{Ne,Ne}_{RABBIT} = \Delta\phi^{Ne}_{XUV} + \Delta\phi^{Ne}_{atom}$ and after subtracting it from $\Delta\phi^{Ne,Ar}_{RABBIT}$ one gets $\Delta\phi^{Ar}_{atom} - \Delta\phi^{Ne}_{atom}$ and since $\Delta\phi^{Ne}_{atom}$ is slowly varying we can consider it negligible compared to argon's atomic phase. We thus get $\Delta\phi^{Ar}_{atom}$, shown in Figure 7.6 (c)

when divided by 2ω to get the corresponding group delay.

In the PR case, the measured phases correspond to: $\Delta\phi^{Ar,Ne}_{RABBIT} = \Delta\phi^{Ar}_{XUV} + \Delta\phi^{Ne}_{atom}$. Here the first term contains both the attochirp and the recombination dipole phase. Thanks to the factorization of the HHG field given by equation 2.27, one can write:

$$|\mathcal{E}^{Ar}_n|e^{i\phi^{Ar}_{XUV}} = |a^{Ar}_n|e^{i\phi^{Ar}_{EWP}}|d^{Ar}_{PR}|e^{i\phi^{Ar}_{PR}}, \tag{7.19}$$

with ϕ_{PR} and ϕ_{EWP} the phases of the PR transition dipole and of the EWP (related to the attochirp), respectively. This means that the measured phase $\Delta\phi^{Ar}_{XUV} \propto \Delta\phi^{Ar}_{PR} + \Delta\phi^{Ar}_{EWP}$. The atomic phase $\Delta\phi^{Ne}_{atom}$ can be considered negligible also in this case.

In order now to access $\Delta\phi^{Ar}_{PR}/2\omega$ one needs to subtract the group delay $GD_{EWP} = \Delta\phi^{Ar}_{EWP}/2\omega$ related to the attochirp. This is shown in Figure 7.6 (c). Mairesse *et al.* [Mairesse et al., 2003b], [Mairesse et al., 2004] have shown that the GD increases linearly up to the cutoff region and then stays constant. In our conditions, the estimated laser intensity is about $I \sim 1.8 \times 10^{14} W/cm^2$, which corresponds to a cutoff around 50 eV. Thus, we subtract an attochirp of 50 as per harmonic order up to SB32 and for the rest a constant value is subtracted. By integrating over energy the quantities of Figure 7.6 (c) one can access ϕ^{Ar}_{atom} and ϕ^{Ar}_{PR} as shown in Figure 7.6 (d). Previous PR results by Schoun *et al.* are also plotted for comparison. Looking the $\Delta\phi^{Ar}_{atom}$ the position of the minimum remains at 46.5 eV while $\Delta\phi^{Ar}_{PI}$ exhibits a slightly shifted minimum at ~ 49.5 eV, which is in good agreement with Schoun *et al.* Our PR measurements however, exhibit a deeper minimum.

The comparison between the PI and PR phases and the corresponding signals of Figure 7.6 highlights two points: i) a much stronger CM effect in PR leading to a deeper cross section minimum and a larger phase jump; ii) a blue shift of the CM position in PR observed in both cross section and phase. There are two main reasons for this behavior. HHG is an inherently differential process that allows the coherent summation of the s and d waves ([Worner et al., 2009], [Higuet et al., 2011], [Farrell et al., 2011]) and thus gives a much deeper interference effect. Indeed, during the PR process, the quantization axis of the atomic orbital, the electron ejection direction and the XUV photon polarization are parallel which leads to a coherent sum over the s and d partial waves. On the contrary, the integration over the angles in PI leads to an incoherent sum of the s and d waves which partly shifts the position of the minimum and smoothes out the interference effect. The second contribution according to [Higuet et al., 2011] comes from the structure of the recombining electron wave packet. In the frame of the classical trajectory Monte Carlo quantum electron scattering theory (CTMC-QUEST), they calculated the corresponding density of the returning wave packet $\rho_{ret}(E)$ and found, for the short trajectories, a significant decrease with increasing energy. This results in a shift of the minimum observed in the PR probability distribution to higher energies.

To summarize, in this section a comparison between the PR and PI process was pre-

sented, by measuring the spectral phases and cross-sections of argon in the vicinity of the 3p CM. Although at first sight PI and PR appear to be strictly reverse processes, which would lead to a simple conjugation relation between the associated transition dipoles, the experimental observations show a systematic shift of the CM in both the cross section and the spectral phase and a much stronger CM effect in PR on both observables. This is compatible with the behavior predicted by the theoretical work of [Higuet et al., 2011].

7.3 Loss of contrast in RABBIT traces

Another way that the CM is expressed in our PI measurements, is by a loss of contrast that was observed in the RABBIT traces around that region, as is shown in Figure 7.7. In the same figure, we plot as reference the contrast from measurements where neon is used as the generation and detection gas. It is clear that in that case the contrast shows a constant behavior. Further on, we have used two ways to calculate the contrast in order to ensure the validity of the result. One is to fit a cosine function on the oscillating signal of each sideband and then calculate the $I_{max} - I_{min}/I_{max} + I_{min}$ value. The other is to calculate from the Fourier transform of the RABBIT oscillations the ratio between the 2ω peak intensity multiplied by a factor of 2 and the zero order peak intensity that corresponds to the background of the measurement. In both cases, we get almost identical results. The plotted curves correspond to the average value over a number of independent measurements while the error bars are calculated by the standard deviation.

The fact that the contrast of our measurements is not 1 (Figure 7.7 (b)), could be the result of many different factors. First, there are physical parameters like the fact that the two interference paths $H_n + IR$, $H_{n+2} - IR$ may not end up at exactly the same energy (due to, e.g., a blueshift of the fundamental) and thus the interference between the two is weaker. The fact that the interfering pathways have different amplitudes due to the ionization cross-section of argon as well as due to the harmonic generation process, can also play a role to the decrease of the contrast, not to mention an intrinsic asymmetry between the +/- IR two-photon transitions close to the ionization threshold that disappear at high energy where the soft photon approximation applies. Additionally, there are technical parameters related to the experimental conditions/set-up that affect the contrast. The stability of the interferometer, the spatio-temporal overlap of the XUV and IR foci in the interaction region of the MBES as well as the common phase variation of the two beams at focus, is of great importance for the overall contrast. Additionally, the electronic noise sets an offset to the measured signal which decreases the overall contrast as the signal to noise ratio decreases.

The minimum in the contrast observed in the energy region of the CM is probably caused by two different effects. First, it can be due to the argon photoionization cross section. This is shown in Figure 7.8. There we plot the contrast calculated as

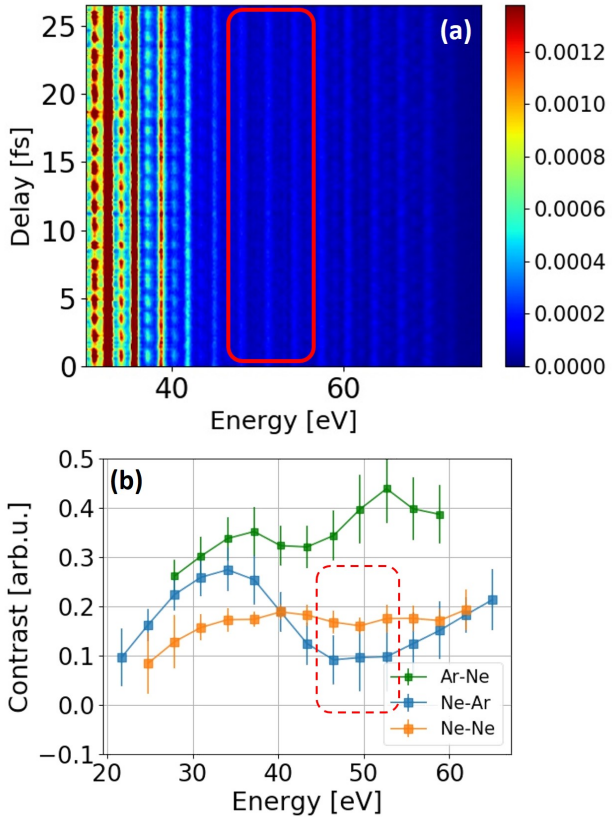

Figure 7.7: (a) Raw RABBIT spectrogram in the photoionization scheme (generation in neon - detection in argon). The loss of contrast happens in the region of the 3p CM that is enclosed in the red square. (b) The corresponding measured contrast (blue squares) along with the contrast of a RABBIT spectrogram where neon is used both as the generation and detection gas and serves as the reference (orange squares) as well as for the case where we generate in argon and detect in neon (green squares).

explained above (blue curve) along with the "spectrum contrast" (red curve) which is extracted from the expression:

$$c = \frac{S/N - 1}{S/N + 1}, \tag{7.20}$$

where S is the intensity of the photoelectron spectrum and N is the noise level. When N is varied, the overall behavior of this "spectrum contrast" remains the same, with a local minimum around 50 eV. This means that its shape is due to argon's PI cross-section. The two quantities in Figure 7.8 exhibit a similar trend up to ~ 56 eV, even though for higher energies the contrast increases in opposition to the "spectrum contrast". This suggests that the strong decrease of the PI signal due to the argon Cooper minimum probably plays a role in the decreased contrast.

Another possible cause originates from the fact that the detection system used for these photoionization experiments is a 4π collection angle MBES, thus our measure-

ments are angle-integrated. As was discussed earlier in this chapter, this suggests

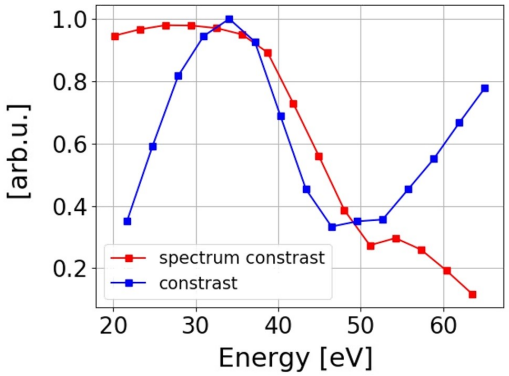

Figure 7.8: Contrast extracted from equation 7.20 (red curve) compared with the contrast calculated by the procedure detailed in the text (blue curve). Both are normalized to 1.

the incoherent summation of the transition dipoles to the s and d partial waves of the 3p ionization channel. Since the s-dipole phase is flat and the d-dipole phase exhibits a π jump at E_{CM} (energy position of the Cooper minimum) the corresponding RABBIT oscillations will get dephased at some point. Below E_{CM}, they will initially oscillate in phase. Then, when passing by E_{CM} they will get dephased and eventually will get back again in phase after moving away from the CM energy region. This process is depicted figuratively in Figure 7.9.

In order to understand the process in depth, we performed simple simulations where we describe the oscillating signal of a sideband $S_{(n+1)}$ as follows. If we define the signal of the neighboring harmonics as

$$H_n = |\mathcal{E}_n|^2 \cdot \sigma(E_n) \tag{7.21}$$

then the sideband will be:

$$S_{(n+1)s \text{ or } d} = \left|\sqrt{H_n}\right|^2 + \left|\sqrt{H_{n+2}}\right|^2 + 2\left|\sqrt{H_n}\right|\left|\sqrt{H_{n+2}}\right| \cdot cos(2\omega\tau + \Delta\phi_{s \text{ or } d}), \tag{7.22}$$

where E_n the central energy of the n^{th} harmonic, $\mathcal{E}_n$ a Gaussian as defined by equation 6.49, $\sigma(E_n)$ the photoionization cross-section as calculated by [Dahlström and Lindroth, 2016], ω the frequency of the driving laser, τ the delay between the XUV and the IR pulse and $\Delta\phi_{s \text{ or } d}$ the phases of the s and d partial waves as calculated by [Magrakvelidze et al., 2015b]. Then the total signal of sideband $S_{(n+1)}$ will be:

$$S_{(n+1)\ total} = s_{branch} \cdot S_{(n+1)\ s} + d_{branch} \cdot S_{(n+1)\ d}, \tag{7.23}$$

with s_{branch} and d_{branch} are the branching ratios for s and d waves respectively taken from [Magrakvelidze et al., 2015b]. Finally, both harmonic and sideband signals are convoluted with f_{sp}, the response function of the spectrometer.

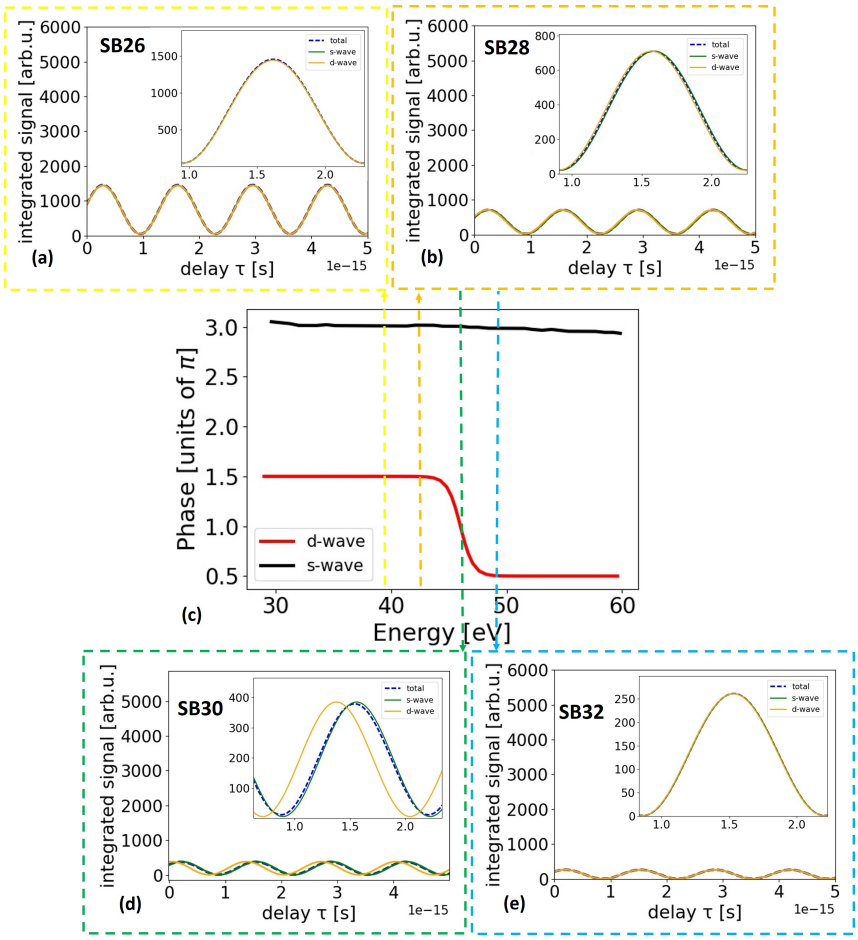

Figure 7.9: The central panel (c) shows the s and d dipole phases. In the other panels one can see the oscillating signal of the sidebands that correspond to the s and d wave separately and the total one. In (a) and (b) SB26 and SB28 are plotted which are positioned before the π phase jump of the d-wave thus the partial s and d sidebands are in phase. SB30 plotted in (d) falls on exactly on the π phase jump and there the dephasing between the partial s and d sidebands is clear. This subsequently results in a decrease of the contrast of the oscillations of the total signal. Finally, SB32 is shown in (e) where the two partial sidebands are back in phase since the s and d wave phases are both flat in that energy region.

By taking into account the decreasing signal and spectrometer resolution as the energy increases, we obtain the contrast of Figure 7.10 which is qualitatively similar to the experimental results. It is worth mentioning that by taking into account only the photoionization cross-section without the incoherent sum of s and d waves the retrieved contrast does not exhibit the characteristic decrease and then increase around the CM position.

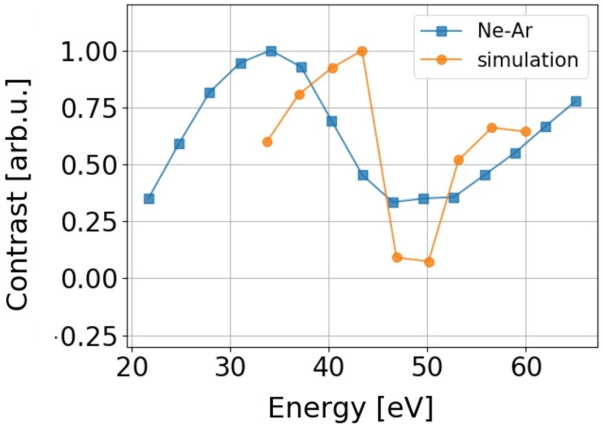

Figure 7.10: Experimentally measured (blue squares) and simulated contrast (orange circles) of a RABBIT trace in the photoionization scheme, normalized to 1.

7.4 Delay difference between 3s and 3p ionization channels

Half a century after their theoretical description by Wigner [Wigner, 1955], scattering time-delays can now be measured with experiments combining high-harmonic generation and electron interferometry. They characterize the dephasing of the emitted electron wave-packet as compared to a free electron and as such are sensitive probes of the system's potential. Since reference free electron wavepackets are not available in experiments, the delay measurements are performed either between different atomic/molecular shells or bands in solids, or between different systems, e.g., atoms in a gas mixture. Following the observation of attosecond delays in the photoemission from core-states and conduction band of a metal [Cavalieri et al., 2007], time-delays -or equivalently, phase differences- have been measured in the valence ionization of molecules [Haessler et al., 2009] , [Huppert et al., 2016], [Vos et al., 2018], atoms [Palatchi et al.] ,[Guénot et al., 2014], [Jordan et al., 2017] and in-between different atomic shells [Schultze et al., 2010], [Klünder et al., 2011], [Guénot et al., 2012], [Isinger et al., 2017]. The latter might appear as the most straightforward to interpret. However, the first experiment at 110 eV in the s and p shells of neon by Schultze *et al.* triggered extensive theoretical work regarding the understanding of laser-induced delays [Ivanov and Smirnova, 2011], [Dahlström et al., 2013] and electron correlation effects [Kheifets and Ivanov, 2010], [Moore et al., 2011], [Dahlström et al., 2012a], [Kheifets, 2013]. Only in 2017 did the experimental capabilities make the measurement of these atomic delays possible over a ≥ 30 eV spectral range [Isinger et al., 2017]. The authors measured a negative $\tau_A(2s) - \tau_A(2p)$ between 70 and 100 eV, implying that the $2p$ electron wavepacket is formed after the $2s$. The results of [Isinger et al., 2017] also showed that intershell interactions need to be accounted for in the photoionization of neon s electrons, but their influence remains small [Dahlström et al., 2012a], reflecting the fairly unstructured ionization cross-section [Bizau and Wuilleumier, 1995].

The case of the argon M-shell is even more challenging. Indeed, the $3p$ and $3s$ partial photoionization cross-sections show signatures of intrashell and intershell electronic correlations. The sign change in the $3p$ radial wavefunction leads to a zero of the dipole transition to the electronic continuum d-wave around 53 eV [Cooper, 1962] and subsequently, the $3p$ cross-section goes through a minimum [Samson and Gardner, 1974] as was discussed in the previous sections of this chapter. The appearance of the CM allows the otherwise negligible $3p \rightarrow \epsilon s$ ionization channel to dominate. Furthermore, the $3p \rightarrow \epsilon d$ channel is strongly coupled to the $3s \rightarrow \epsilon p$ by intershell correlation [Amusia et al., 1972], resulting in the appearance of a "replica" of the Cooper minimum in the $3s$ partial ionization cross-section around 42 eV ([Möbus et al., 1993]) as is schematically shown in Figure 7.11 (b).

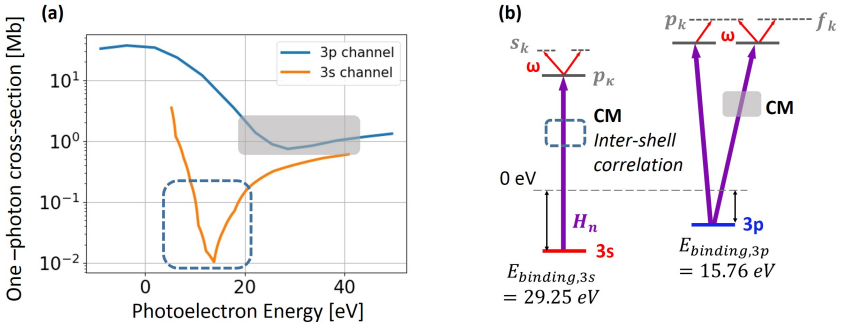

Figure 7.11: (a) Photoionization cross-sections of the 3s and 3p channels as a function of the photoelectron kinetic energy as measured by [Möbus et al., 1993] and [Samson and Stolte, 2002]. (b) Schematic representation of the two-photon (XUV and IR) ionization of both 3s and 3p subshells including the different channels and the corresponding CM. Inspired from [Guénot et al., 2012].

A number of calculations have been performed in order to predict the ionization delays between the $3s$ and $3p$ electrons of argon [Klünder et al., 2011], [Guénot et al., 2012], [Kheifets, 2013], [Dahlström and Lindroth, 2016] , [Magrakvelidze et al., 2015b], [Bray et al., 2018]. The different methods qualitatively agree on the behavior of the $3p$ atomic delays, the zero in the $3p \rightarrow \epsilon d$ dipole transition being associated with a π phase jump and therefore large negative delays around the Cooper minimum, which are however smoothed by the incoherent addition of the $3p \rightarrow \epsilon s$ channel. However, for the $3s$ shell the atomic delays can differ in magnitude and in sign depending on the degree of correlation included [Dahlström and Lindroth, 2016]. Up to now, two experiments using the classic RABBIT technique have aimed at measuring the photoionization time-delay difference in the M-shell of argon [Klünder et al., 2011], [Guénot et al., 2012]. Unfortunately, for experimental reasons the results of [Klünder et al., 2011] and [Guénot et al., 2012] are limited to the 34-40 eV photon energy range, that is before the strong correlation region of argon, preventing the comparison with conflicting theories.

In this section, as an extent to the work of [Klünder et al., 2011] and [Guénot et al., 2012], the photoionization delays of 3s and 3p shells of argon will be examined for a more extended energy range (32 - 68 eV). Consequently, the Cooper minima of

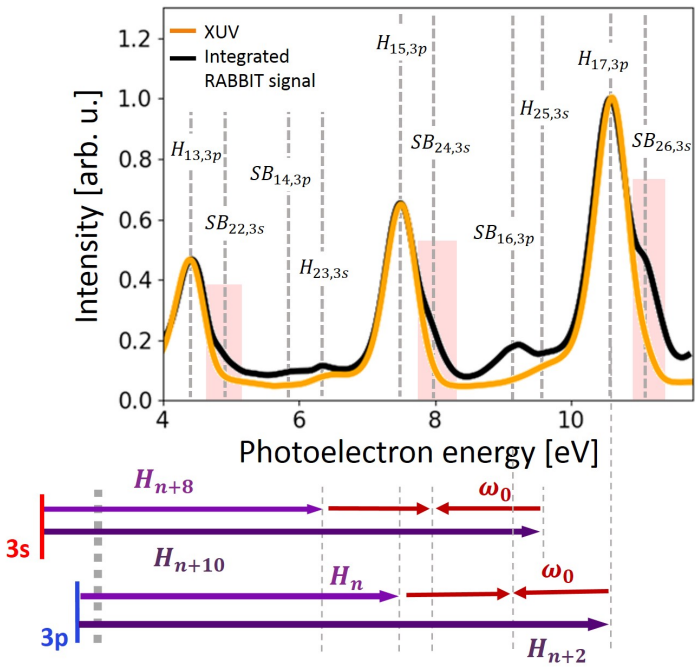

Figure 7.12: Bottom panel: schematic representation of the RABBIT process. Photoionization of the 3s and 3p channels is achieved by using the same harmonic comb. Due to the difference of 13.5 eV in the binding energy of the two channels, the corresponding harmonic and sideband peaks are almost overlapping as is shown by the intensity of the XUV+IR spectrum (top panel: black line). The spectrum of the XUV alone is plotted for reference (top panel: orange line).

3s and 3p shells, located around 43 eV and 48 eV respectively [Möbus et al., 1993], [Samson and Stolte, 2002] will be included.

The measurements were performed using the experimental set up of the SE1 beamline in ATTOlab which is detailed in Chapter 4.2. To extract the corresponding delays the Rainbow RABBIT method was used. In Figure 7.12 the principle of the RABBIT measurement is schematically outlined for this particular experimental case (lower panel) along with the corresponding intensity spectrum for a narrow photoelectron energy range of 7 eV (upper panel). By Fourier transforming the oscillating signal (Equation 4.1) of the sidebands of interest one can access $(\Delta\phi_{XUV} + \Delta\phi_{atom})$, where $\Delta\phi_{XUV} = \phi_{n+2} - \phi_n$ is the phase difference between two consecutive harmonics and $\Delta\phi_{atom}$ is the phase difference that arises from the two-photon ionization process. The atomic phase difference has two contributions $\Delta\phi_{atom} = \Delta\eta + \Delta\phi_{cc}$, where $\Delta\eta$ is the phase accumulated by the EWP when scattering out of the potential after the one-photon (XUV) transition and is intrinsic to the target atom; ϕ_{cc} is a measurement induced phase shift due to the electron being probed by the IR laser field in a long-range potential with a Coulomb tail [Dahlström et al., 2012b].

The corresponding ionization delays are calculated through Wigner's formula $\tau \approx$

$\partial\phi/\partial\omega$, as follows (Chapter 3.2.3)

$$\tau_{atom} = \tau_{Wigner} + \tau_{cc} \tag{7.24}$$

where

$$\tau_{Wigner} = \frac{\eta_{n+2} - \eta_n}{2\omega} \quad and \quad \tau_{cc} = \frac{\Delta\phi_{cc}}{2\omega} \tag{7.25}$$

where η_n, η_{n+2} are the scattering phases corresponding to the one-photon ionization by harmonics H_n and H_{n+2}. In a similar way we define $\tau_{XUV} = \Delta\phi_{XUV}/2\omega$ which can be seen as the group delay of the attosecond pulses, related to the attochirp. Since the 3s and 3p photoelectrons are ionized by the same harmonic comb this contribution of the ionization radiation can be removed from the final 3s-3p delay difference and thus access directly the τ_{atom}. It should be emphasized that our measurement is conducted without absolute knowledge of the delay between the APT and IR field, which leads to an unknown constant shift in delay of the RABBIT scans. This however does not affect our study since we are interested in the delay differences that are extracted from the 3s and 3p phases measured simultaneously in one RABBIT scan.

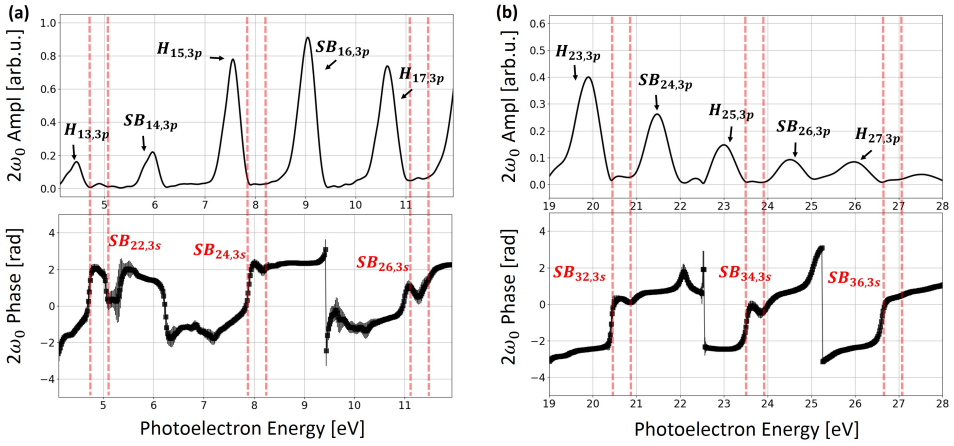

Figure 7.13: Rainbow RABBIT amplitude and phase of the entire RABBIT spectrogram. A typical case for the lowest energies is shown in (a) and for higher ones in (b). In between the red lines we show the contributions of the 3s sidebands. In both cases a sudden phase jump between the 3p harmonics and the 3s sidebands is apparent.

The specific nature of the experiment makes it a difficult task to be accomplished, which is also underlined by the fact that up to now there have been only two similar attempts. The main experimental difficulty, is the separation of the 3s and 3p contributions since the 3s ionization cross section is much lower than the corresponding 3p one (Figure 7.11(a)). Moreover, the 3s sidebands fall only 0.46 eV from the 3p harmonic peaks ($\Delta E_{3s-3p} = 13.49eV = 9\omega_0 - 0.46eV$). The previous two studies of [Klünder et al., 2011] and [Guénot et al., 2012] managed to spectrally isolate the two contributions by using a combination of Cr and Al filters, 200 nm-thick each, while

generating the ionizing harmonics in argon in order to benefit from its relatively large cross-section (before the CM) and thus of the intense XUV light generated. The main drawback of this approach is that it constrains the usable energy range to only a 10 eV window and thus allows measurements only up to ~ $41eV$. As a result the delays in the vicinity of the 3s and 3p CM were not accessible.

In the present work, harmonics generated in neon were used as the excitation radiation. Even though it has a lower cross section than argon, neon exhibits a quite flat behavior for the energy region of interest and has a longer cut-off energy for the same generation conditions ($E_{cutoff} = I_p + 3.17U_p$). In combination with the use of a single 200 nm-thick Al filter we obtain a spectrum that includes harmonics from H13 to H45. However the two peak families are almost completely overlapped with the 3p harmonics overshadowing the 3s sidebands. In order to separate the two contributions, the Rainbow RABBIT technique is used. As was demonstrated throughout this thesis, by using the Rainbow RABBIT technique one can resolve fast variations inside the spectral phase and amplitude of a structured EWP. Taking advantage of this technique's unique property, we apply the Rainbow RABBIT analysis to the entire spectrum and record the evolution of the phase and amplitude of the $2\omega_0$ oscillations of all harmonics and sidebands that lie between the energies of 20 eV to 73 eV (photon energy). An example is shown in Figure 7.13 for two different energy regions. In (a) the 3s-3p pairs measured also by [Klünder et al., 2011] and [Guénot et al., 2012] are plotted whereas (b) shows the spectral phases and amplitudes for higher order harmonics and sidebands.

By looking at the corresponding phases, it is clear that after each 3p harmonic, there is a sudden phase jump. It is expected that between consecutive harmonics and sidebands of the same ionization channel, a dephasing of π occurs as a result of the conservation of the total number of electrons. Indeed, in RABBIT, the dressing field is a weak perturbation inducing only 2 photon XUV+IR transitions: it only redistributes electrons between the neighboring harmonic peaks and the sidebands. When the sideband signal is maximum, the neighboring harmonic signal is minimum, hence a dephasing of π of the sideband oscillations with respect to the neighboring harmonic ones. However in the case of Figure 7.13, the phase jumps occur almost 1 eV before the 3p sidebands and always on the 'blue' side of the harmonic. We note that the same behavior (phase jump on the 'blue side') can be observed on the 3p sidebands, that are close to the 3s harmonic peaks. In order to find the origin of these phase jumps, we examine the spectral amplitudes. We observe that the 2ω amplitudes of the 3p harmonic and sideband peaks are of similar magnitude, despite their very different integrated intensities in the RABBIT trace (see Figure 7.12). This is another consequence of the electron conservation mentioned above.

At the energy regions where the phase jumps occur, one can distinguish small but clear peaks. Having excluded the possibility that these peaks are due to noise of the spectrometer since in that case they wouldn't oscillate at $2\omega_0$ and after comparing with the spectrum of the 3s ionization channel, we conclude that these correspond to the 3s channel contribution. To strengthen this argument, in the upper

panel of Figure 7.12 we plot the integrated RABBIT signal (XUV+IR) and the XUV spectrum alone. There, one can distinguish the contribution of the 3s SBs on the XUV+IR spectrum, as a shoulder on the blue side of the 3p harmonics, which then disappears when the IR field is blocked. It is worth-mentioning that in this kind of measurements, the spectral phase is a more robust quantity, less affected by the external experimental conditions than the corresponding amplitudes and intensities. In general, phase measurements are more sensitive to the presence of features that induce fast variations than amplitude measurements. In the absence of a features like this, the phase is flat, while the amplitude reflects that of the excitation pulse. Phase measurements are thus background-free, while amplitude measurements are not.

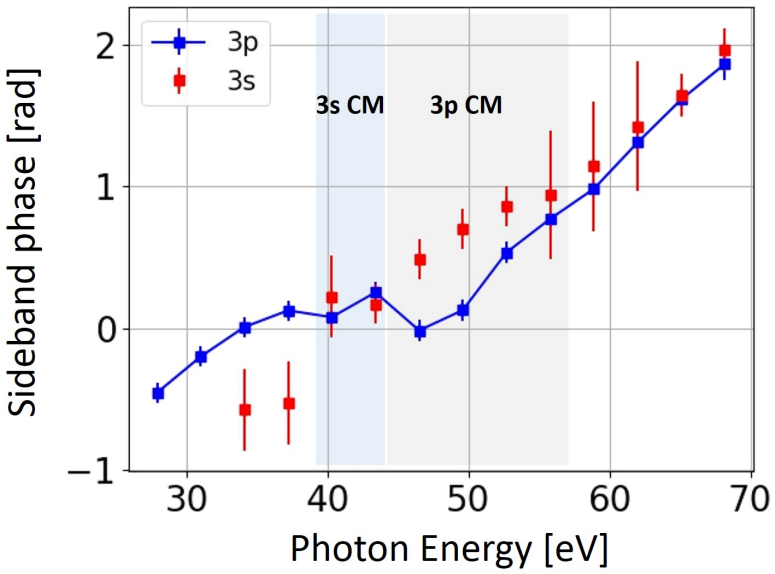

Figure 7.14: Measured sideband phases ($\Delta\phi_{XUV} + \Delta\phi_{atom}$) for the 3s (red squares) and 3p (blue squares) ionization channels as a function of the photon energy. The measured phases include the phase term due to the ionizing radiation which is responsible for the linear slope. This slope is the same for both channels since they were ionized by the same harmonic comb and thus is removed when calculating the corresponding delay differences giving access to the $\Delta\tau_{atom}$. The blue and grey shaded area corresponds to the region of the 3s and 3p CM respectively.

As mentioned earlier, using only one 200 nm - thick Al filter, gives the advantage of obtaining a large spectrum (21 eV - 73 eV, photon energies) which allows us to study the effect of the 3s and 3p CM on our measurements. However the spectrometer resolution decreases with the energy which renders the spectral separation of the 3s and 3p channels more and more difficult. To avoid that, an increasing retarding potential is added to shift the sidebands of interest towards lower kinetic energies where the spectrometer performs best. This way, the spectral phases inside the 3s and 3p sideband peaks, are quite flat without any fast variations apart from a linear slope that could be attributed to the harmonic blue shift ([Busto et al., 2018],

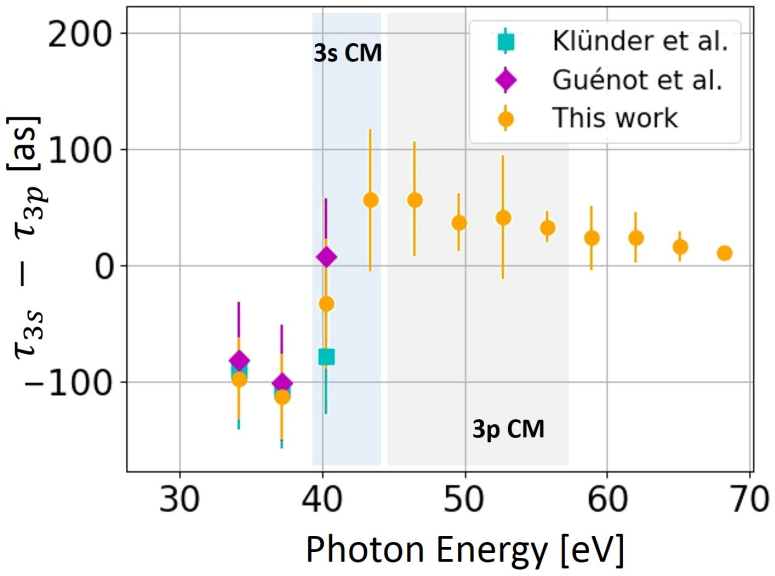

Figure 7.15: Atomic delay differences between 3s and 3p ionization channels in the vicinity of the two corresponding minima. Comparison between experimental data of this work (orange circles) and previous measurements by [Klünder et al., 2011] (cian squares) and [Guénot et al., 2012] (magenta diamonds). The blue and grey shaded area corresponds to the region of the 3s and 3p CM respectively.

Chapter 6.2.3). However this does not affect the measurement and therefore we can integrate in energy to improve the signal to noise ratio and extract one phase value for each sideband. The energy range in which the 3s phases are integrated, is narrow (typically ~ 400 meV), and often confined by two phase jumps on either side. The 3p contributions are easily distinguishable with well defined $2\omega_0$ oscillations and thus in this case the size of the energy integral doesn't affect the extracted value.

Using different retarding potentials, we were able to measure the RABBIT phases of the 3s and 3p sidebands up to 68 eV as is shown in Figure 7.14. For photon energies around 60-68 eV, the signal to noise ratio becomes low due to the decrease in the ionizing harmonic signal (end of the plateau of neon emission spectrum). This may affect the extracted 3s phases in this energy region. In order to ensure the accuracy of our results, supplementary measurements were performed by adding a 200 nm - thick zirconium filter. In this case the combination of the two filters will transmit the narrow energy window of 60-73 eV and allows the clear spectral separation of the 3s and 3p peaks. Therefore the phases of the 3p and 3s sidebands 40, 42 and 44 were measured also in these conditions and were found very similar with the ones measured when only one Al filter was used.

The corresponding $\tau_{3s} - \tau_{3p}$ delay differences are plotted in Figure 7.15. Each value corresponds to the average of independent measurements and the corresponding

3s - 3p delay difference			
	SB22	SB24	SB26
Guénot *et al* [as]	-80 (±50)	-100 (±50)	10 (±50)
Klünder *et al* [as]	-90 (±50)	-110 (±50)	-80 (±50)
This work [as]	-97 (±37)	-112 (±37)	-36 (±56)

Table 7.1: 3s - 3p delay differences for SB22, SB24, SB26, measured in different experiments.

error bars are their standard deviation. Additionally, in Table 7.4, we compare our measurements for SB22, 24 and 26 with the previous results of [Guénot et al., 2012] and [Klünder et al., 2011] and find a good agreement within the error bars. Thanks to the large range of our measurements, we are able to observe a very interesting fact: the change of sign at 41 eV. This means that between 34 eV - 41 eV the 3p photoelectrons leave the argon atom later than the 3s ones. However this changes as we go through the 3s CM where we observe a maximum at 57 as with the 3s photoelectrons being now emitted later than the 3p ones. A local maximum is also noted in the region of the 3p CM. The delay difference is converging towards zero for higher energies where the 3s and 3p cross sections are mostly flat. Indeed, away from resonances, the Wigner delay in a given channel decreases as $E^{-3/2}$ (equation 3.40), and thus is quickly dampened at high energy.

In order to explain the physical meaning behind these measurements, a comparison with simulations based on different theories will be conducted in Chapter 7.6. Before that however, it is worth testing the robustness and the reliability of the above phase measurements as well as the possible effects of the 3p harmonics on the 3s sidebands phases. To answer these questions we perform the numerical study presented in the following section.

7.5 Preliminary simulations

A delicate point of the analysis above is the ability of the Rainbow RABBIT to resolve the spectral phases of the two ionization channels despite the fact that the corresponding sidebands and harmonics are almost overlapping. The reasonable question that arises is how and if the spectral phase of the less intense 3s channel is affected by the presence of the 3p channel. In order to answer this question and show the validity of our measurements a series of simulations were performed and will be presented in this section.

We are interested in simulating the RABBIT traces of the combination $H_{2n-1,3p}$ + $SB_{2N,3s}$ + $SB_{2n,3p}$, where n and N symbolize the different orders of the two peak families. The case of $H_{25,3p}$, $SB_{34,3s}$ and $SB_{26,3p}$ will be used here as an example to demonstrate the working principle of our simulations. The two sidebands can be described as:

$$SB_{26,3p}(E,\tau) = \left|M_{25,3p}\right|^2 + \left|M_{27,3p}\right|^2 + 2\left|M_{25,3p}\right|\left|M_{27,3p}\right| \cdot \cos(2\omega\tau + \phi_{SB26,3p}) \quad (7.26)$$

and

$$SB_{34,3s}(E,\tau) = |M_{33,3s}|^2 + |M_{35,3s}|^2 + 2\,|M_{33,3s}|\,|M_{35,3s}| \cdot \cos(2\omega\tau + \phi_{SB34,3s}), \quad (7.27)$$

where $|M_{n,3i}| = |\mathcal{E}_n|\sqrt{\sigma_{n,3i}}$ are the amplitudes of the harmonic fields described by the gaussian curves of equation 6.49 detailed in Chapter 6.2.1 and multiplied by the square root of the corresponding one-photon ionization cross-sections given by [Möbus et al., 1993] for the 3s and [Samson and Stolte, 2002] for the 3p channel (depicted in Figure 7.11). We assume that the peak amplitudes of the different harmonic orders are identical since they are in the emission plateau of the neon generating gas. For the sideband phases $\phi_{SB26,3p}$ and $\phi_{SB34,3s}$ that decompose into the XUV phase difference and the atomic phase difference, we assume: i) for the former, no attochirp leading to a 0 value; and ii) for the latter, we use the values calculated by Marcus Dahlström using the RPAE model including the interaction with all orbitals (averaged over the electron emission angle for the 3p electrons and at 0^o for the 3s electrons[Dahlström and Lindroth, 2014]) (see next section).

To describe the oscillating signal of a harmonic one needs to know the corresponding spectral phase which demands some additional approximations ([Ruchon and Camper, 2013]). In a first-order approximation, a harmonic peak H_{2n+1} will be modulated due to the loss of electrons that are transferred to the neighboring sidebands SB_{2n} and SB_{2n+2} as:

$$\begin{gathered} H_{2n+1}(E,\tau) \approx \alpha\,|M_{2n+1}|^2 - SB_{2n} - SB_{2n+2} = \\ \alpha\,|M_{2n+1}|^2 - (|M_{2n-1}|^2 + |M_{2n+1}|^2 + 2|M_{2n-1}||M_{2n+1}|\cos(2\omega\tau + \phi_{SB,2n}) + \\ |M_{2n+1}|^2 + |M_{2n+3}|^2 + 2|M_{2n+1}||M_{2n+3}|\cos(2\omega\tau + \phi_{SB,2n+2})) \end{gathered} \quad (7.28)$$

where α accounts for the difference in intensity of the harmonic and SB peaks (1-photon with respect to 2-photon transitions, typically a factor 10). Assuming now a slowly-varying cross-section and harmonics with similar intensity, equation 7.28 becomes:

$$\begin{gathered} H_{2n+1}(E,\tau) = (\alpha - 4)\,|M_{2n+1}|^2 - 2\,|M_{2n+1}|\,|M_{2n-1}| \\ \cdot\cos\left(2\omega\tau + \frac{\phi_{SB,2n} + \phi_{SB,2n+2}}{2}\right) \cdot \cos\left(\frac{\phi_{SB,2n} - \phi_{SB,2n+2}}{2}\right) \end{gathered} \quad (7.29)$$

and for the specific case of $H_{25,3p}$ will be:

$$H_{25,3p}(E,\tau) = 10\left|M_{H25,3p}\right|^2 - 2\left|M_{H25,3p}\right|\left|M_{H23,3p}\right| \cdot \cos\left(2\omega\tau + \frac{\phi_{SB24,3p} + \phi_{SB26,3p}}{2}\right) \cdot \cos\left(\frac{\phi_{SB24,3p} - \phi_{SB26,3p}}{2}\right) \tag{7.30}$$

where $\alpha = 14$ was chosen to fit as well as possible the experimental measurements. The attochirp is not taken into account. After convolving the oscillating signals of the two sidebands and the harmonic with the spectrometer response function f_{sp} (Chapter 6.2.1) for each delay, we add them incoherently:

$$RABBIT_{total}(E,\tau) = H_{25,3p}(E,\tau) \otimes f_{sp} + SB_{34,3s}(E,\tau) \otimes f_{sp} + SB_{26,3p}(E,\tau) \otimes f_{sp} \tag{7.31}$$

and eventually obtain the RABBIT trace in Figure 7.16. Even though $SB_{34,3s}$ is very weak compared to $H_{25,3p}$, it is clear that they oscillate in opposite phase. This can be easily seen when applying the Rainbow RABBIT analysis.

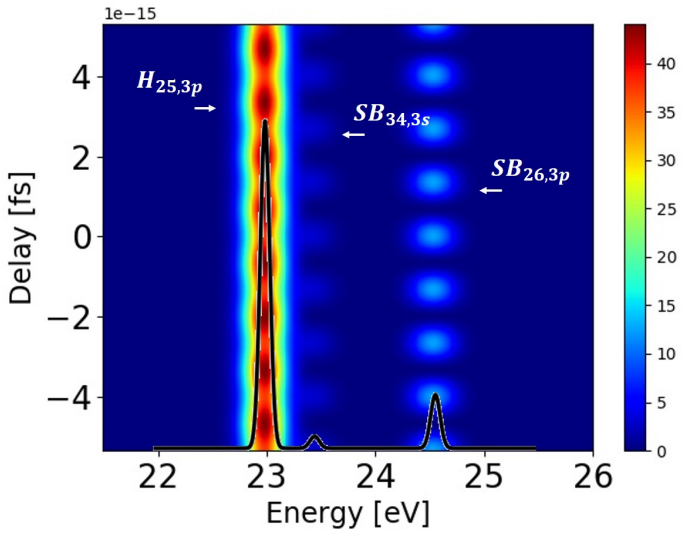

Figure 7.16: Simulated RABBIT spectrogram of harmonic 25 and sideband 26 of the 3p ionization channel and sideband 34 of the 3s channel. The black line is the intensity averaged over the delays.

The treatment of the simulated RABBIT spectrograms is identical to the one of the experimental data described in Chapter 5.1. The extracted spectral amplitudes and phases are plotted in Figure 7.17 for different values of the spectrometer resolution which constitutes the main limiting factor of this specific experimental set up. Between the phase of $H_{25,3p}$ and $SB_{34,3s}$ we obtain a jump of π as was expected. The decrease of the spectrometer resolution doesn't seem to affect the size of the jump however it shifts it towards higher energies. An interesting point is that a smaller phase jump of ~0.04 rad appears between the sidebands of the two different ionization channels which is due to the fact that they correspond to different orders and thus different atomic phases. The decreasing spectrometer resolution shifts the

jump towards smaller energies and it smooths it out. For less spectral resolution this second phase jump disappears completely. Note that if we take into account the intrinsic GDD of the ionizing harmonics, related to the attochirp, then the amplitude of this second phase jump is modified by the difference in group delay between SB24 and SB36 (i.e., 19 as $*8 \sim 150$ as amounting to 0.7 rad).

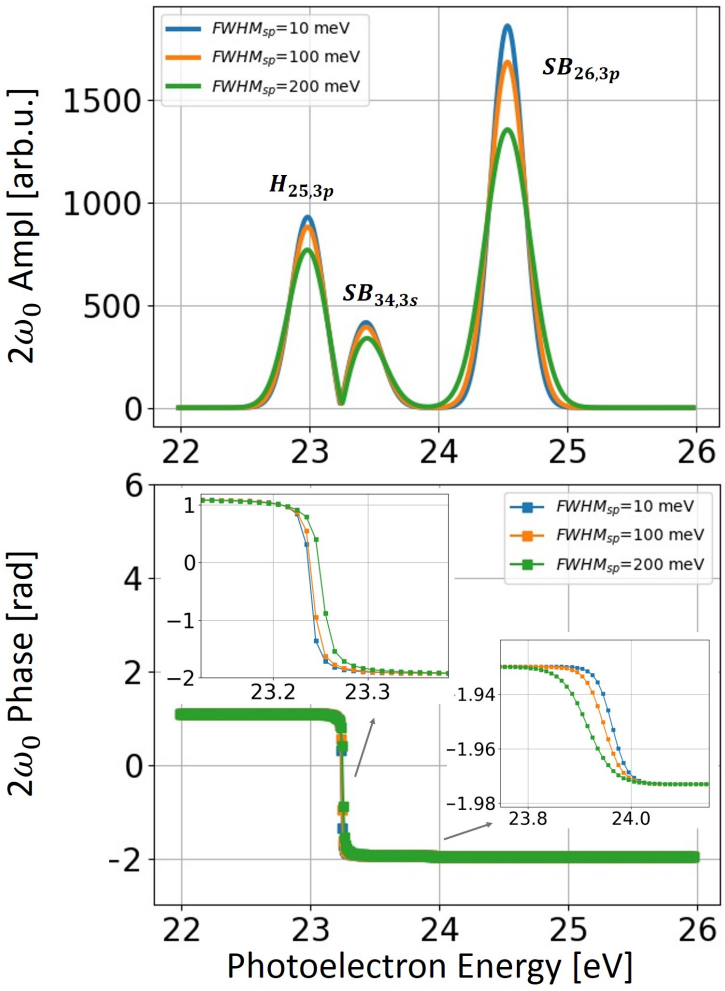

Figure 7.17: Simulated spectral amplitude and phase of harmonic 25, sideband 26 (3p channel) and sideband 34 (3s channel) for different values of the spectrometer resolution. The width of the harmonics is kept constant at 300 meV. The insets show in more detail the effect of the spectrometer resolution on the two phase jumps.

The use of the 200 nm filter (spectral window : 15-73 eV) to block the remaining IR radiation in combination with the use of neon as the generation gas, has the advantage of allowing the transmission of a large number of harmonics (H13-H45 of the 3p channel). In Figure 7.18 the simulated spectral phases and amplitudes for the entire spectrum including the 3s sidebands are plotted. In order to highlight the effect, the spectrometer resolution is not taken into account and the width of the harmonics is kept relatively small (100 meV). The spectral phases show the same behavior as in Figure 7.13 with a π jump between the 3p harmonics and the 3s sidebands and a smaller one between the two families of sidebands. It is worth

mentioning the fact that even for the lower order 3s sidebands that lie in the vicinity of the 3s Cooper-like minimum and have a small cross section (inset in the top panel Figure 7.18) the corresponding phases are well resolved. This shows that the spectral phase extracted by the Rainbow RABBIT method is less affected by the experimental conditions than the corresponding spectral amplitudes. Note that we did not include in these simulations the harmonic peaks of the 3s channel that induce opposite jumps on the blue side of the 3p sidebands.

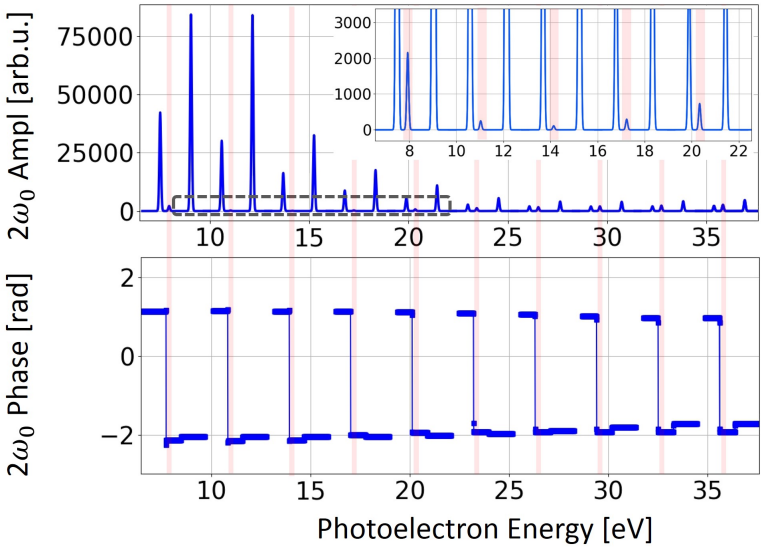

Figure 7.18: Simulated spectral amplitudes and phases extracted by the Rainbow RABBIT algorithm for a range of kinetic energies [7-40] eV. The red highlighted areas correspond to the 3s sidebands. The inset is a zoom in energies [7-22] eV, to highlight the presence of the 3s sidebands even in the vicinity of the corresponding Cooper minimum. For this figure the harmonic width is 100 meV and the spectrometer resolution is not taken into account.

Another interesting case that demonstrates the ability of our technique to resolve the spectral phase is shown in Figure 7.19. There the combination of $H_{15,3p}$+$SB_{24,3s}$+$SB_{16,3p}$ is simulated including the convolution with a spectrometer resolution of 100 meV and a relatively large harmonic width of 300 meV. In Figure 7.18, due to the low cross-section, the spectrometer resolution and the harmonic width, the presence of $SB_{24,3s}$ is now almost completely overshadowed by the more intense 3p harmonic. This can be clearly seen in the intensities of Figure 7.19 (a) where the presence of $SB_{24,3s}$ becomes visible only when the RABBIT spectrogram (XUV+IR) is compared with the spectrum of $H_{15,3p}$ alone (XUV). The extracted spectral amplitudes in Figure 7.19 (b), despite being smoothed as compared to Figure 7.18 where the harmonic width was 3 times less broad and the spectrometer was not taken into account, reveal the peak of $SB_{24,3s}$. Moreover, the corresponding spectral phases are not affected displaying the expected π jump between $H_{15,3p}$ and $SB_{24,3s}$ and the second smaller one between $SB_{24,3s}$ and $SB_{16,3s}$. The good agreement between these preliminary simulations and the experimental data is shown in Figure 7.20, where some typical cases throughout the whole spectrum

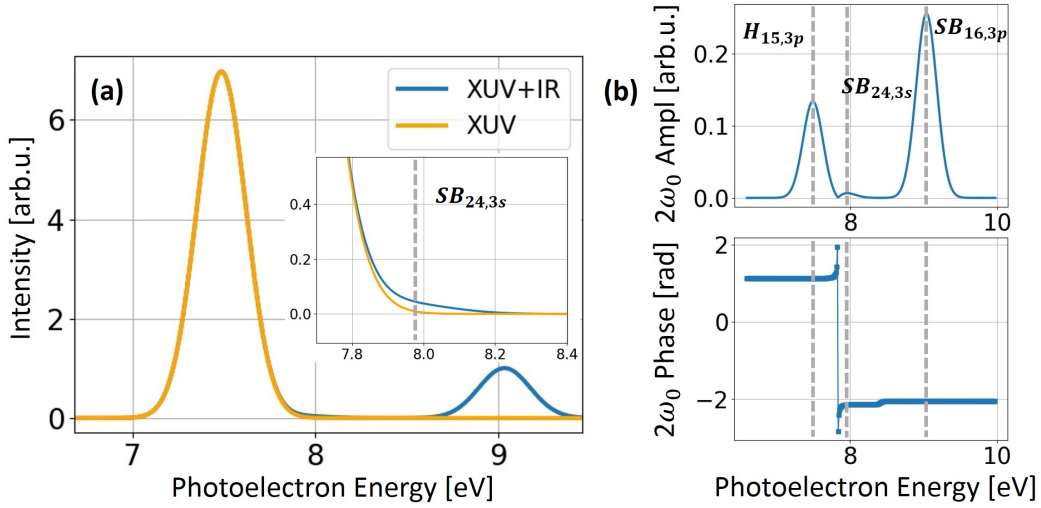

Figure 7.19: (a) Simulated RABBIT spectrogram integrated over the delays of $H_{15,3p}$+$SB_{24,3s}$+$SB_{16,3p}$ (blue curve) and of $H_{15,3p}$ alone normalized to the previous curve (orange curve). (b) Corresponding Rainbow RABBIT amplitudes (top panel) and phases (bottom panel). For this figure the harmonic width is 300 meV and the spectrometer resolution 100 meV.

are plotted. In all the plotted examples the spectral phases are in better agreement with the simulations than the corresponding amplitudes since the latter are more easily affected by the experimental conditions as mentioned above.

7.6 Comparison with theory

Measuring the ionization delays in atomic or molecular systems is of great interest since they evidence the correlated electronic motion and the correlation between electron and nuclear motion. The use of ultrashort XUV radiation has allowed the study of these motions on their natural sub-femtosecond time scale. At the same time, the theoretical description of a process involving electron correlation is extremely challenging where only the most simple systems have been exactly solved. In order to describe more complex multi-electron systems, a number of different approximations have been introduced. Thus comparison with experimental data is of extreme importance for the validation of the different theoretical approaches. In this section a brief overview of the existing theoretical models concerning the specific case of the ionization delays in argon will be presented. The comparison with the experimental data discussed in Chapter 7.4, will follow.

Argon is one of the most convenient atoms for this kind of studies for the following reasons. Firstly, the ionization delay differences between the 3s and 3p ionization channels contain information about the electron - electron intra- and inter-shell interactions, especially in the vicinity of the 3s CM which arises solely due to inter-

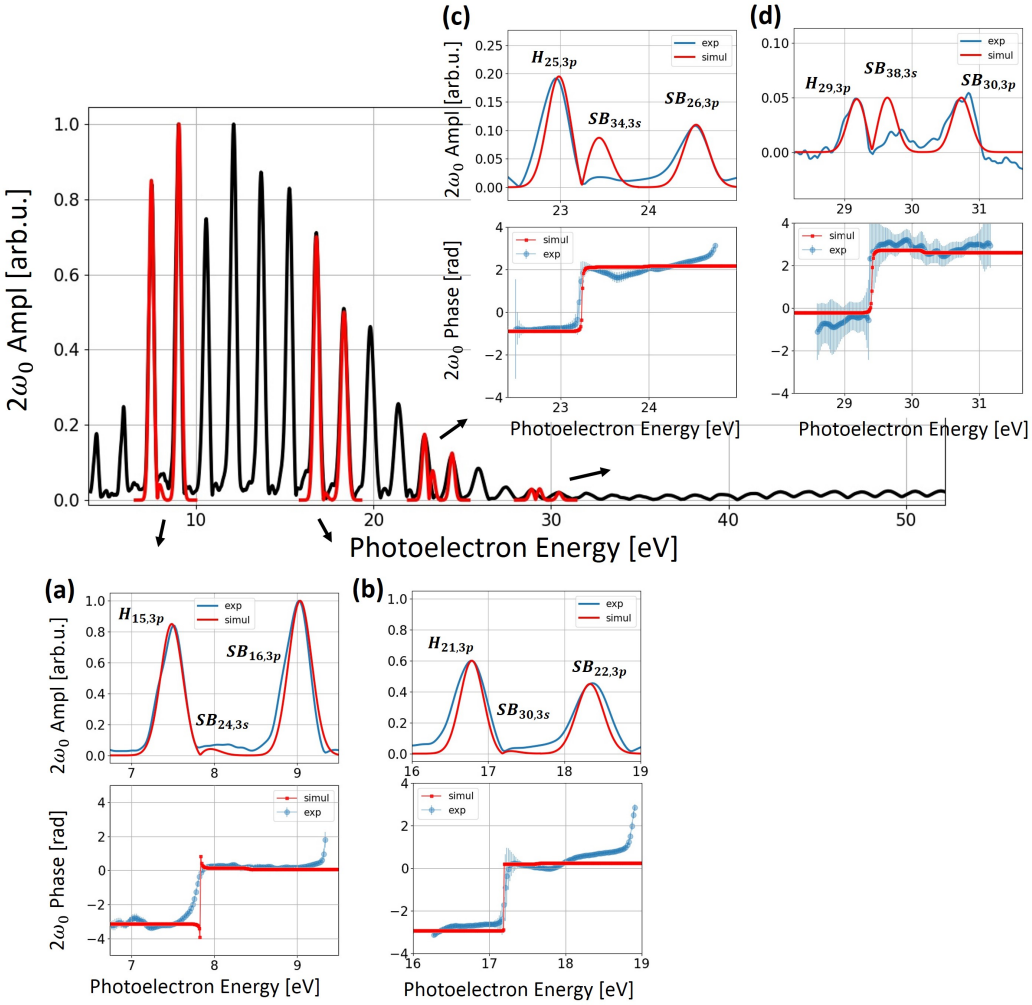

Figure 7.20: Main panel: Measured spectral amplitude of the entire RABBIT spectrogram of neon harmonics photoionizing argon after a 200 nm thick aluminum filter (black line) and the corresponding simulated amplitudes for some harmonics (red lines). Small panels: simulated (red) and measured (blue) spectral phases and amplitudes extracted by the Rainbow RABBIT method for (a) $HH_{15,3p} + SB_{24,3s} + SB_{16,3p}$, (b) $HH_{21,3p} + SB_{30,3s} + SB_{22,3p}$, (c) $HH_{25,3p} + SB_{34,3s} + SB_{26,3p}$ and (d) $HH_{29,3p} + SB_{38,3s} + SB_{30,3p}$.

channel coupling with the 3p photoionization channels ([Amusia et al., 1972]) Secondly, the presence of the 3p CM constitutes a signature of the electronic atomic structure and thus of the intra-shell dynamics and the correlation between the s and d photoelectrons. Additionally, argon provides a good benchmark because it is comparatively light, so a non-relativistic description can be used.

The above characteristics are the reason for which this system has been used as a prototype on which many different theoretical approaches have been developed. The main ones will be now briefly outlined.

Ab-initio

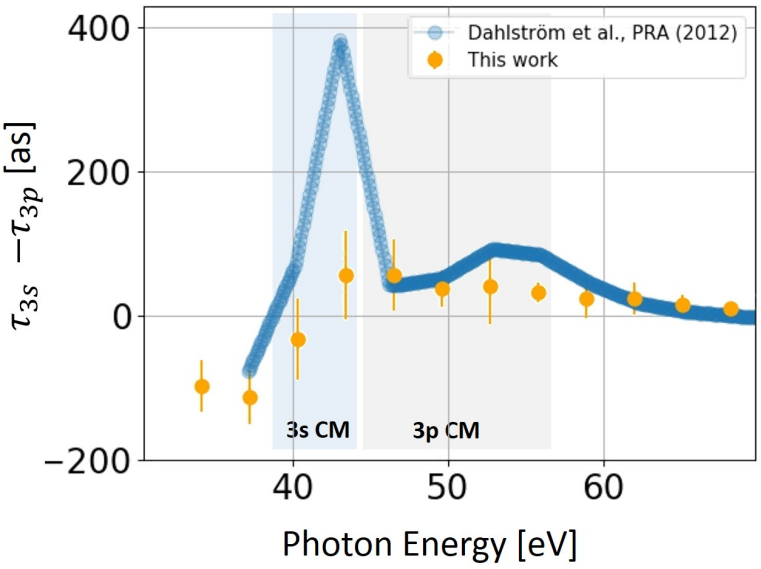

Figure 7.21: Comparison between the theoretical curve calculated in [Dahlström et al., 2012a] (blue circles) and our experimental measurements (orange circles). The τ_{cc} are taken into account. The blue and grey shaded area corresponds to the region of the 3s and 3p CM respectively.

This is a large group of methods that rely on fitting some free parameters to experimental or ab-initio data. A characteristic example is the work of [Carette et al., 2013], where they presented a method, based on the Atomic Structure Package (ATSP2K)([Fischer et al., 2007]), to obtain a general, many-electron atomic wave function in a close-coupling expansion. The structure of the localized part of the wave function is represented using the multiconfiguration Hartree-Fock (MCHF) method, which represents complex many-body effects with a limited number of configurations. By using B-splines to describe the radial components of the photoelectron in the allowed partial-wave channels, they obtain a multichannel method that, for the description of one active electron in a box, is complete. This approach is developed in combination with the exterior complex scaling method of use, in particular, in the description of monochromatic wave packets. Unfortunately they have only investigated up to 42 eV photon energy, which means that neither the 3s nor 3p CM is included.

Another example of ab-initio calculation tested on the case of argon was performed one year earlier by the same group and presented in [Dahlström et al., 2012a] where a large spectrum of energies (20-80 eV) was covered. This study was focused on establishing a connection between the single-photon ionization and the two-photon ionization process used for the measurement. The correlation effects were accounted for "all orders" of single-particle excitations, including the non local exchange interaction and ground-state correlation. The correlated photoelectron and ion are represented using the perturbation diagrams (Fig. 2 of [Dahlström et al.,

2012a]), including linear screening for the absorption of the XUV photon.

Firstly, the two-photon transition amplitude, expressed as a one-photon dipole matrix element from an intermediate to the final state $|s\rangle$ is defined as $\mathcal{M}_{s,\omega,\Omega,a} = \langle s|d_\omega|\rho_{\Omega,a}\rangle$, where $|\rho_{\Omega,a}\rangle$ is the perturbed wave function for absorption of one XUV photon Ω from an initial atomic orbital $|a\rangle$ with energy ϵ_a. A Hartree-Fock (HF) basis with exterior complex scaling in the radial dimension is used to set up the $|\rho_{\Omega,a}\rangle$. A broad range of correlation effects between the photoelectron and the ion are then accounted for using infinite-order, many-body perturbation theory (MBPT). The final form of $|\rho_{\Omega,a}\rangle$ (equation 4 and 5 of Dahlström et al. [2012a]) will contain a term corresponding to the direct and exchange interactions and a term representing the ground-state correlation. This can be solved by numerical iteration including the outermost n orbitals. Once convergence is found, this solution is used to evaluate the two-photon matrix element $\mathcal{M}_{s,\omega,\Omega,a}$. The argument of this complex expression will give the corresponding phases and atomic ionization delays including the measurement induced delay term τ_{cc} (equation 7.24).

Finally, it is shown that the atomic delays from the outer 3p orbital are mostly insensitive to the coupling with the inner orbitals. In contrast, the delays from the inner 3s orbital are strongly altered by the coupling to the outer orbitals which results in the observation of sharp delay structures close to the CM from the 3p and 3s orbitals, respectively. The delay peak from the 3s orbital is only observed in the correlated calculation and not in the single active orbital approximation case as is shown in Fig. 4 of [Dahlström et al., 2012a].

In Figure 7.21 we compare the above simulated 3s-3p atomic delay differences with our experimentally measured ones shown in Figure 7.15. The agreement is good for the energies above 59 eV where both 3s and 3p atomic delays are quite flat since we move away from the two CM. In addition, satisfactory accordance between experiment and theory is found for the energy range 46.5 eV - 49.6 eV and around 37 eV, so between the two CM and before the 3s CM, a region which is quite sensitive to the presence of the τ_{cc} as will be discussed further on. It is important to stress the fact that the above simulations are implemented along the polarization direction of the field which does not correspond to the angle integrated nature of our measurements. This affects however mostly the 3p delays around the corresponding CM.

Time-Dependent Local-Density Approximation [TDLDA]

This category of simulations uses an approach based on firstly calculating the one-photon dipole transition amplitude by using different types of the LDA ([Madjet et al., 2001], [Zangwill and Soven, 1980a], [Stener et al., 1997]) potential in the independent-particle approach. In order then to include collective effects, the TDLDA code ([Zangwill and Soven, 1980b], [Zangwill and Liberman, 1984]) is used and results in the full transition amplitude that includes a complex induced potential, proportional to the induced frequency dependent changes in the electron

density that accounts for the electron correlations.

Two characteristic examples of this method are the work of [Magrakvelidze et al., 2015b] and [Pi and Landsman, 2018]. In both cases the one-photon dipole transition amplitude $d_k = \langle \psi_k | z | \psi_0 \rangle$ is calculated along the polarization axis z, for a transition from a bound state ψ_0 to a continuum state ψ_k. Both initial and final wave functions are calculated using the LDA potential:

$$V_{LDA}(r) = -\frac{Z}{r} + \int \frac{\rho(r')}{|r-r'|} dr' + V_{XC}[\rho(r)] \tag{7.32}$$

, where Z is the atomic number, $\rho(r)$is the charge density and V_{XC} is the exchange-correlation functional. Since the exact V_{XC} is unknown, different approximations are used in the two articles. A change of the charge density $\delta\rho(r,\omega)$ occurs under the influence of the laser field, inducing a change $\delta V(r,\omega)$ in the potential. The dipole transition will then become $D_k = \langle \psi_k | z + \delta V(r,\omega) | \psi_0 \rangle$. The solution of the equation will give the corresponding Wigner delays $\tau_{Wigner} = \frac{d}{dE} arg[D_k]$. In [Magrakvelidze et al., 2015b] they tried to include also the measurement-induced τ_{cc} by finite-differencing their TDLDA phases using 1.55 eV half steps.

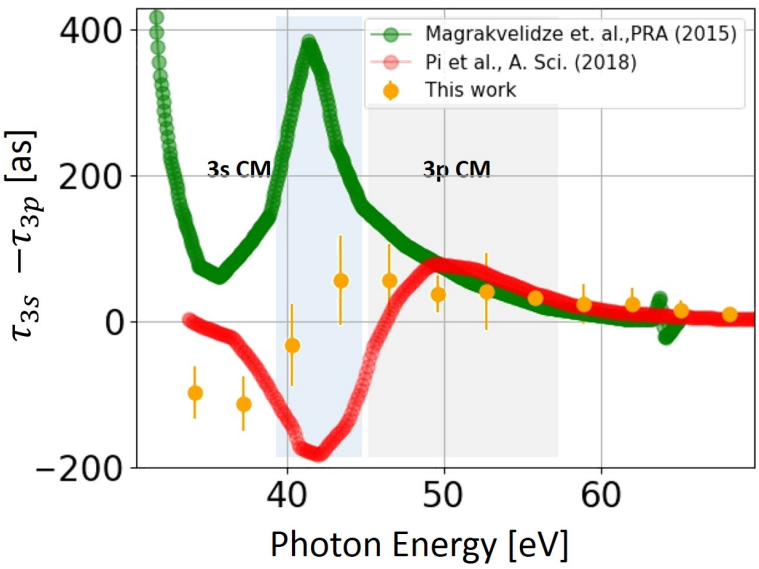

Figure 7.22: Comparison between the theoretical curves calculated in [Magrakvelidze et al., 2015b] (green circles) and in [Pi and Landsman, 2018] (red circles) with our experimental measurements (orange circles). The τ_{cc} are taken into account only in the calculations of [Magrakvelidze et al., 2015b] whereas [Pi and Landsman, 2018] calculates only the τ_{Wigner}. The blue and grey shaded area corresponds to the region of the 3s and 3p CM respectively.

Figure 7.22 shows the comparison between our experimental points and the corresponding simulated TDLDA delays. Even though the model used for the calculation of the two theoretical curves is the same, the change of parameters like

the potential V_{LDA}, results in completely different behavior of the delay differences especially for the 3s CM region. The two curves start converging around 52.7 eV where our results also show a similar tendency. On the other hand, for lower energies the experimental results do not agree with none of the two theoretical cases.

Random Phase Approximation with Exchange [RPAE]

The random phase approximation was applied to calculate photoionization cross sections and angular anisotropy parameters in valence shells of noble gas atoms some forty years ago [12]. Since then, it became a standard technique to account for inter- and intra- shell effects in valence shell photoionization in atoms, based on the work of M. Ya Amusia ([Becker and Shirley, 1996]). As in the previous case the one-photon transition matrix element is first defined using lower-order perturbation theory as $M^{(1)}(k) = -iE_\Omega\langle k|z|i\rangle$, where E_Ω is the complex amplitude of the harmonic field. In order to include the different correlation effects the single photoionization dipole matrix element is then replaced by a "screened" matrix element $\langle k|Z|i\rangle$. In some studies as [Guénot et al., 2012] and [Dahlström and Lindroth, 2016] the model is taken one step further by calculating the corresponding two-photon transition matrix element in order to mimic in the best possible way the experimental measurement process.

About the one-photon matrix element, there are several issues to discuss regarding the choice of basis functions. The first issue is the choice of implementation potential; a common choice is a HF potential with a correction that provides an asymptotically correct long-range interaction for the photoelectrons. A second point is the numerical representation of the basis function; a common choice is the use of the B-splines. Finally, one needs to construct the outgoing wave packet and a numerical stable and efficient way to do so, is provided by the method of complex scaling ([Nicolaides and Beck, 1978]).

In order to include correlated interaction into the photoionization process, a perturbation $\delta V = \frac{1}{r_{12}} - u_{HF} - u_{proj}$ is considered. The screened matrix elements will then be defined by the self-consistent equation:

$$\langle k|Z|i\rangle = \langle k|z|i\rangle + \lim_{\varepsilon\to 0^+} \sum\!\!\!\!\!\!\int_v \left[\frac{\langle v|Z|j\rangle\langle jk|V|vi\rangle}{\Omega - \epsilon_v + \epsilon_j + i\varepsilon} - \frac{\langle j|Z|v\rangle\langle vk|V|ji\rangle}{\Omega + \epsilon_v - \epsilon_j}\right] \tag{7.33}$$

where i and j are 3s or 3p or vice versa and V = $1/r_{12}$ is the Coulomb interaction. The sum is performed over the discrete as well as continuum spectra. The Coulomb interaction matrices $\langle jk|V|vi\rangle$ and $\langle vk|V|ji\rangle$, describe the so-called time-forward and time-reversed correlation processes. For a single dominant channel L, the phase of the one-photon matrix element becomes $arg[M^{(1)}(k)] = \eta_L(k) + \delta_L(k) - L\pi/2$, where $\delta_L(k) = \delta_{i\to kL}$denotes the additional phase due to the correlations accounted within the RPAE.

In Figure 7.23 our experimental data are compared with RPAE simulations from

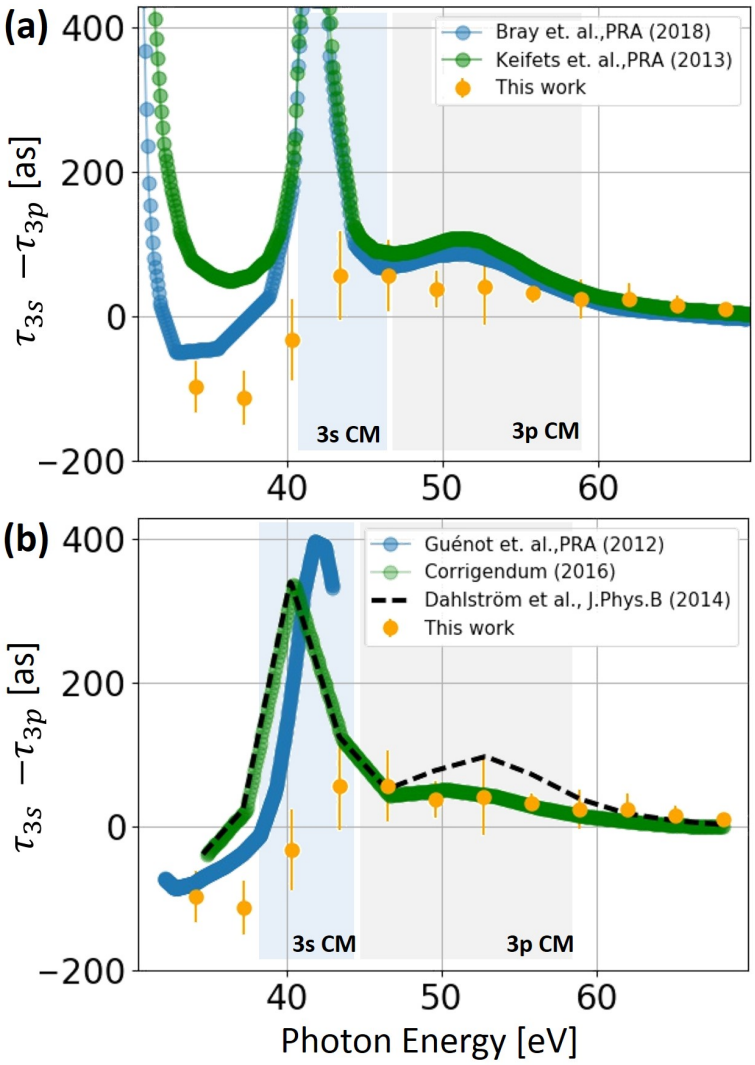

Figure 7.23: (a) Comparison between the theoretical curves calculated in [Kheifets, 2013] (green circles) and [Bray et al., 2018] (blue circles) with our experimental measurements (orange circles). The τ_{cc} are taken into account only in the calculations of [Bray et al., 2018] whereas [Kheifets, 2013] calculates only the τ_{Wigner}. (b) Comparison between our experimental measurements (orange circles) and the theoretical curves calculated in [Guénot et al., 2012] (blue circles), in [Dahlström and Lindroth, 2014] (black dashed line) where delays have been calculated for 0^o electron emission angle for both channels and the corrected version [Dahlström and Lindroth, 2016] (green circles) where the 3p delays are averaged over the electron emission angle. The τ_{cc} are taken into account in all three theoretical curves. The blue and grey shaded area corresponds to the region of the 3s and 3p CM respectively.

different studies. In (a) we compare with the work of [Kheifets, 2013] and [Bray et al., 2018]. The two models are in good agreement with each other from ~40 eV on. For lower energies there is a discrepancy due to the measurement-induced delay τ_{cc} that is not taken into account in [Kheifets, 2013]. The comparison with our

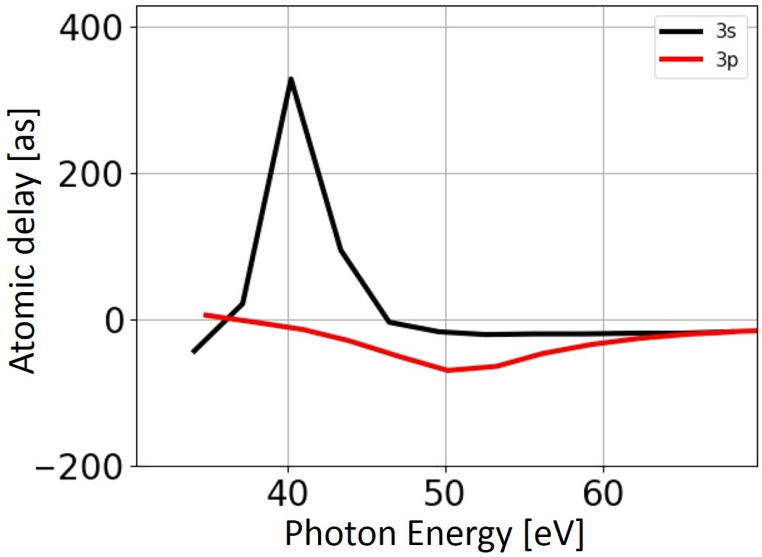

Figure 7.24: Atomic delays in argon as calculated by M. Dahlström, for 0^o electron emission angle for the 3s channel [Dahlström and Lindroth, 2014] and averaged over the electron emission angle for the 3p channel [Dahlström and Lindroth, 2016].

experimental results is very similar as in the case of [Dahlström et al., 2012a] with a good agreement only after 55.9 eV which corresponds to the end of the 3p CM. In the vicinity of both 3s and 3p CM the experimental points are not in good agreement with any of the two theoretical models, with the exception of the delay at 46.47 eV that lies between the two CM. As in the case of [Dahlström et al., 2012a] the two theoretical curves are calculated for electron emission along the XUV polarization axis which does not correspond to the angle-integrated nature of our detection method.

[Dahlström and Lindroth, 2016] has calculated the 3s and 3p delays for multiple correlation combinations. The one that fits best our data accounts for the correlation of the 3s and 3p channels with all the orbitals from the $\mathcal{M}$ and $\mathcal{L}$-shells. It is plotted in Figure 7.23 (b) and corresponds to the angle-integrated 3p delays (On the contrary the 3s delays were calculated along the polarization axis, however the authors claim that the 3s CM is not sensitive to the detection angle). The excellent agreement along the whole range of the 3p CM is clear (from 46.4 eV to 68 eV). Unfortunately, the agreement for lower energies is not very good like in the previous cases.A slightly better agreement at low energy is obtained by [Guénot et al., 2012], in particular for the delay difference at 34 eV. Unfortunately, this curve is given only up to 42 eV. In Figure 7.24 we plot the calculated atomic delays for each channel separately that correspond to the delay difference of the green curve of Figure 7.23 (b).

At this point it is worth-mentioning the effect of the τ_{cc}, the measurement induced delay. As has already been mentioned earlier, this additional delay term is due

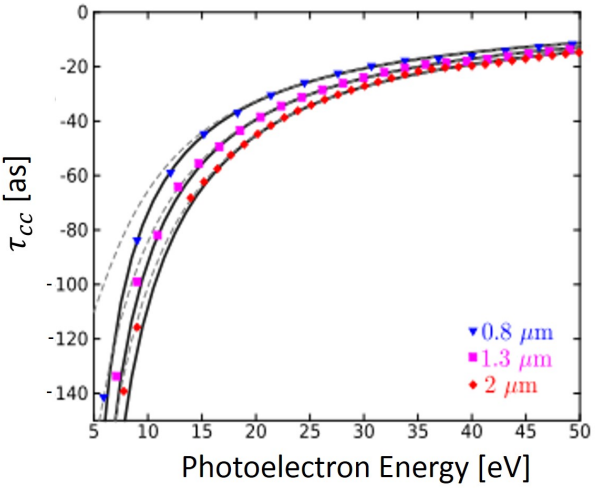

Figure 7.25: Continuum-continuum delays τ_{cc} as presented in [Dahlström and Lindroth, 2014].

to the electron being probed by an IR laser field in a long-range potential with a Coulomb tail ([Dahlström et al., 2012b]). Most of the times it is not taken into account since it is quite small compared to the actual τ_{Wigner} . However, it has been shown that τ_{cc} can play a role in the experimentally measured delays ([Heuser et al., 2016]). In our case the induced effect is a downshift of the delay differences for the lower energies (33 eV - 40 eV) as can be easily understood by looking at Figure 7.25 where the argon τ_{cc} are plotted as calculated in [Dahlström and Lindroth, 2014]. Between ~5 eV and ~35 eV one remarks a fast increase in the τ_{cc} values as a function of the photoelectron energy, whereas for higher energies saturation is obtained. In the previous figures, it was clear that the theoretical curves that included this extra delay term were in better agreement with the experimental measurements at low energy.

Relativistic Random Phase Approximation [RRPA]

The relativistic photoionization theory should take into account the spin-orbit splitting of atomic shells. The relativistic counterpart of RPAE, the RRPA, considers a one-electron transition from an initial state characterized by the quantum number nljm to a final continuum state $\mathbf{k}\overline{lj}\overline{m}$. In Figure 7.26 the corresponding delay differences are plotted as calculated in [Saha et al., 2014]. As compared to the RPAE calculation of [Kheifets, 2013], the relativistic effects induce a global shift in energy of the time delay difference (above 35 eV) by ~-1 eV, the overall shape staying very similar. Like in the previous cases the agreement between experiment and theory is best after 55.8 eV where the impact of the 3p CM is fading out, but still quite bad at lower energy.

In conclusion, in this section the experimentally measured 3s-3p delay differences presented in Chapter 7.4, were compared with the numerous existing theoretical calculations. Using the technique described in Chapter 7.4 we were able to record

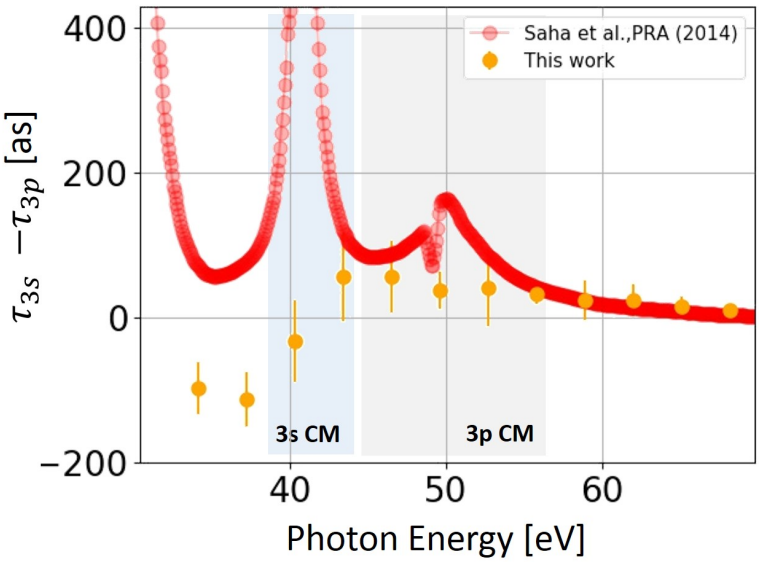

Figure 7.26: Comparison between the theoretical curve calculates in [Saha et al., 2014] (red circles) with our experimental measurements (orange circles). The τ_{cc} are not taken into account. The blue and grey shaded area corresponds to the region of the 3s and 3p CM respectively.

these delays up to 68 eV photon energy, a range that includes both 3s and 3p CM which in our knowledge has never been measured before. This is a valuable input for a stringent test of the various theories. According to this study the best agreement with our experimental measurements is achieved for high photon energies, with the RPAE calculations presented in Dahlström and Lindroth [2016]. The experimental points are in excellent agreement for photon energies between 46 eV - 68 eV where the 3p CM is included. However, for lower energies (34eV -43 eV) we only have a similar qualitative trend between experiment and theory with the best agreement being with the RPAE calculations of Guénot et al. [2012]. A possible reason for not being able to resolve the fast delay variation of the 3s CM could be that the energy spacing of our harmonics generated by 800 nm radiation (~3.1 eV) is not fine enough. This could be resolved by using an OPA to generate the excitation radiation with longer wavelength (the HE-TOPAS available in SE1 can provide from 1100 to 2100 nm). This would provide better sampling and at the same time tunability of the driving wavelengths which would allow us to scan over the 3s CM.

7.7 Conclusions

In this Chapter the Cooper minimum in argon was studied in multiple ways. First, a comparison between the photo-ionization and photo-recombination (from high harmonic spectroscopy) cross-sections and the corresponding atomic phases was

performed in the vicinity of the 3p CM. Even though these two processes are usually considered as time-reversed, the experimental observations show a systematic shift of the CM in both the cross section and the spectral phase and a much stronger CM effect in PR on both observables. This is compatible with the behavior predicted by the theoretical work of [Higuet et al., 2011]. There are two reasons for this behavior: i) the fact that HHG is an inherently differential process that allows the coherent summation of the s and d waves (in contrast to the incoherent summation in PI angle-integrated measurements) and thus gives a much deeper interference effect in the PR case and ii) the structure of the recombining EWP which will result in a shift of the minimum observed in the PR case to higher energies.(Chapter 7.2)

Following this investigation, a study on the RABBIT spectrogram's contrast was performed. In more details, a loss of contrast close to the 3p CM energy region was observed. In order to understand the origin of this behavior, a number of simulations were performed. It was then, showed that this loss was mainly due to two effects: i)The PI cross-section of argon and ii) the incoherent sum of the 3p s and d waves due to the angular-integrated nature of our detection method. (Chapter 7.3)

Further on, since we were able to resolve the 3s photoelectrons, by using the Rainbow RABBIT technique we managed to measure the delay differences between the two ionization channels 3s-3p for an extended energy region spanning from 34 eV to 68 eV. This includes both the 3s and the 3p CM and to our knowledge has never been measured before. (Chapter 7.4)

In order to test the validity of our phase measurements and more specifically the effect of the 3p harmonic peaks on the less intense and almost overlapping 3s sidebands, we performed preliminary simulations of this specific system. The agreement with experimental data was very satisfactory, showing that the phase extraction procedure was meaningful. (Chapter 7.5)

Finally, our measurements can be a valuable input for theories that describe the inter- and intra-shell correlations. We have compared with the predictions of different models. More specifically, in the case of the 3p CM the sign of the delay is negative for all the theoretical models tested above, which is expected since it is an intra-shell effect caused by the annihilation of the $3p \rightarrow \epsilon d$ dipole moment. The negative 3p delay implies that the photoelectron escape faster due to the $-\pi$-shift of the dipole phase. The Cooper minimum is, in this sense, behaving in the opposite way as compared to an autoionizing resonance that holds the photoelectron close to the atom for an extended time.

On the contrary, the 3s delays in the vicinity of the CM can change dramatically from a positive to a negative peak depending on the theoretical model and thus on the correlation effects taken into account. This implies that the 3s atomic delays are very sensitive to inner-shell electron correlation. In the case where the 3s delay peak is positive it is suggested that the photoelectrons are delayed by the correlation-induced CM and that the dipole phase increases by a $+\pi$-shift, in direct contrast

to the case of the 3p-channel. This discrepancy between the different theoretical models highlights the importance of our experimental measurements. In our case the best agreement was found with the RPAE calculations presented in Dahlström and Lindroth [2016] where the correlation with all the orbitals is taken into account. For this particular case the τ_{cc} is included and the 3p delays are calculated for an angle-integrated electron emission with respect to the XUV polarization axis which corresponds to our angle-integrated measurements. A very good agreement is obtained in the region of the 3p CM, but it is much less satisfactory in the region of the 3s CM, despite the same trend. (Chapter 7.6)

Part V

Conclusions

CHAPTER 8

CONCLUSIONS AND OUTLOOK

The work presented in this thesis focuses on the study of the ionization dynamics induced in an atomic system by an XUV pulse train. The main goal was to measure the spectral phases and amplitudes of the emitted EWPs when features like resonances are involved and study the effect that they can induce on the corresponding dynamics. Using the Rainbow RABBIT interferomentric technique, we investigated the case of two structural features with different physical origins, that also happen in different energy scales. First, in the scale of some tens of meV, we studied several autoionizing resonances in helium and argon and second, in the scale of some tens of eV, the Cooper minimum in argon was investigated.

Rainbow RABBIT:

Throughout this work the Rainbow RABBIT along with the classic RABBIT technique was used. The Rainbow RABBIT was introduced for the first time by Gruson *et al.* [Gruson et al., 2016a] in 2016. This energy-resolved version of the classic RABBIT method allows the resolution of fast variations in the spectral phase and amplitude of the emitted EWP. In the study of Fano resonances, we used it in order to record the exact phase evolution inside the resonant sidebands whereas in the case of the Cooper minimum in argon, it allowed us to isolate the contributions from the two ionization channels (3s and 3p), which normally is a difficult task since the two peak families almost overlap. Since the Rainbow RABBIT method is new, the effect of the various experimental parameters on the phase extraction, had not been studied. Thus an in depth study including simulations and comparison with experimental measurements was performed for the possible effects of the spectrometer resolution, the spectral width and detuning of the excitation harmonics (pump beam) as well as the spectral width of the IR pulses (probe beam). The ideal experimental conditions for Rainbow RABBIT measurements were found to be a spectrally narrow dressing pulse in order to create exact replicas of the one-photon EWP and spectrally large harmonics, enough to fully excite the resonance. The spectrometer resolution was shown to potentially induce distortions both of the retrieved spectral phase and amplitude, which may lead to a misinterpretation of the reconstructed dynamics.

Fano resonances [meV scale]:

Helium

Gruson *et al.* [Gruson et al., 2016a] along with Kaldun *et al.* [Kaldun et al., 2016] measured for the first time the temporal evolution of the autoionizing sp2+ resonance in helium. More specifically, it was shown that in the first 3 fs there is

a dominant contribution of the direct ionization path that is then followed by the interference with the indirect path that passes through the doubly excited sp2+ state. In the same spirit, we extended this study with the introduction of different time-frequency representations of the emitted EWP, such as the Gabor and Wigner representations that can give supplementary information in more complicated systems ([Busto et al., 2018]). This set of studies included also the measurements around the sp3+ resonance which is more difficult to investigate since its spectral width (8 meV) is ~5 times narrower than the sp2+ one. Additionally, thanks to the tunability of the driving laser, we were able to excite simultaneously the two above-mentioned resonances in a coherent way and thus create a complex two-electron wave packet, whose complicated dynamics was later investigated. Three different regimes were found: i) a direct excitation to the continuum with 2ω-beatings due to the excitation radiation; then ii) a complex interference between the four ionization channels (two direct and two indirect channels for both resonances) ; and finally iii) the decay of the two resonances into the continuum with beatings at $(E_{sp3+} - E_{sp2+})$.These experimental results agreed qualitatively, with preliminary simulations while exact calculations performed by the group of Richard Taïeb of LCPMR, Université Pierre et Marie Curie are in progress. A study on the intensity dependence of the probe pulse on the spectral phase and amplitude of the EWP emitted through the sp2+ resonance was also conducted. We observed the distortion of the lineshape with a significant variation of the corresponding q parameter and the fact that the phase information is transferred -somewhat smoothed out- to the 4ω-oscillations of the neighboring harmonic peaks.

Argon

In the same spirit, we investigated the 3s4p autoionization resonance in argon. This case becomes more complicated since argon exhibits a spin-orbit splitting of only 180 meV. Thanks to to the Rainbow Rabbit technique and to the sub-100 meV resolution of the MBES, we were able to resolve this structure on the measured photoelectron spectra. Furthermore, we managed to isolate the two S-O contributions both in the measured spectral phase and amplitude of the emitted EWP, by implementing a numeric technique based on the work of Zürch *et al.* [Zürch et al., 2017]. Our findings are consistent with a similar imprint of the resonance on both S-O components. The temporal buildup of the resonance was reconstructed for the J=3/2 case. Preliminary simulations show a very similar behavior and suggest that by tuning the driving laser, it is possible to encode the complete resonant phase variation of a single S-O component in the total measured spectral phase. Exact calculations are in progress by the group of Fernando Martin of Universidad Autónoma de Madrid. A comparison with the classic RABBIT results of Kotur *et al.* [Kotur et al., 2015], was also performed. The results are in good agreement and highlight the properties of the Rainbow RABBIT since the S-O is resolved in the resonant sidebands' phase while we also obtain larger phase jumps for both components.

The above experiments were performed in Lund, in collaboration with the group of Anne L'Huillier from University of Lund, who welcomed us in her laboratory

as well as with the group of Raimund Feifel from University of Gothenburg who provided us with the photoelectron spectrometer.

Cooper minimum [eV scale]:

3p-shell Ionization-Recombination

The first experiments performed on the SE1 beam-line of the new ATTOLab facility at CEA-Orme des Merisiers were the investigation of the Cooper minimum (CM) in argon. We first studied its influence on the amplitude and phase of the photoionization (PI) from the 3p outer shell, and compared it to the photorecombination (PR) as obtained from high harmonic spectroscopy. The comparison between the PI and PR phases and amplitudes highlighted two points: i) a much stronger CM effect in PR leading to a deeper cross-section minimum and a larger phase jump; ii) a blue shift of the CM position in PR observed in both cross section and phase. These differences were attributed mainly to the stronger interference effect in PR due to the coherent summation of the s and d channels whereas the integration over the angles in PI leads to an incoherent sum which partly shifts the position of the minimum.

3s-3p ionization delays

Seven years ago Klünder *et al.* [Klünder et al., 2011], [Guénot et al., 2012], measured the difference of the ionization delays between electrons emitted from the 3s and 3p shells of argon. However in order to separate the two peak families that lie only 0.46 eV apart and with the 3p peaks overshadowing the much less intense 3s ones, they used a combination of Cr and Al filters, that transmitted only a window of 10 eV (four harmonics). This limited the measurement range up to 41 eV, and thus could not reach 43 eV and 46.7 eV where are located the Cooper minima of the 3s and 3p channels respectively. We took this first effort to the next step by measuring these photoionization delay differences up to 68 eV for the first time. By using the Rainbow RABBIT method and only one Al filter (transmits energies up to 73 eV) we managed to separate the two peak families thanks to the phase jumps between the 3p harmonics and 3s sidebands. A numerical study was also performed in order to investigate how much the overlapping of the two peak families could affect the extracted Rainbow RABBIT phase. It recovers the experimental trends , evidencing the meaningfulness of the phase extraction. Our measurements over a large range reveal a previously unknown change of sign of the 3s-3p delay at 41 eV, just on the edge of the spectral region of the CM in the 3s channel. A maximum delay difference is obtained at 47 eV, position of the 3p CM. The measured delays are then compared to various theoretical models. The Cooper minimum in the 3p channel is a feature well described by many theories which is not the case of the 3s CM because the latter originates from inter-shell correlation.The description of electron correlation effects has always been a very demanding task, thus our results can serve as a valuable input for advanced theories. Among the different theories predicting widely conflicting results, the best agreement was found with the RPAE calculations presented in [Dahlström and Lindroth, 2014] where the correlation with all the orbitals was taken into account. However, our measurements

do not show the strong increase in delay predicted at the position of the 3s CM, possibly due to the large energy sampling of 3 eV. This calls for further studies where a finer sampling will be obtained either with mid-IR driving wavelength or with a tunable laser.

OUTLOOK

As for the future work, the Rainbow RABBIT technique that was initially developed by V. Gruson and L. Barreau and that we pushed one step further in this thesis, exhibits enormous potential for the study of all types of fine atomic and molecular resonances, as well as stuctures in solid-state physics. This is a new type of spectroscopy, maybe more complete, where we measure both the transition dipole amplitudes and phases, giving access to the whole ionization dynamics.

One of the perspectives opened by this work is the measurement of angularly resolved photoionization times in atoms and molecules. Indeed, the wave functions of the emitted photoelectrons can be decomposed into different partial waves that exhibit different angular emission distributions. Performing a RABBIT type experiment with a Velocity Map Imaging spectrometer (VMI) or a Cold Target Recoil Ion Momentum Spectrometer (COLTRIMS), it is possible to resolve angularly the sidebands' oscillations and thus measure the angular variation of the photoionization delay for different ejection directions of the electron [Heuser et al., 2016], [Hockett et al., 2016]. Recently, the team of A. L'Huillier in Lund and the team of U. Keller from ETH Zurich , performed RABBIT measurements in the vicinity of the 3s4p resonance in argon with both a VMIS and a COLTRIMS [Cirelli et al., 2018].

These types of measurements are particularly relevant for molecules where a strong spatial variation is expected due to the anisotropic nature of the molecular potential. A first example is provided by photoelectron circular dichroism (PECD).The team of Y. Mairesse in Bordeaux carried out Above Threshold Ionization (ATI) experiments with a circularly polarized pulse in a chiral molecule in the presence of a dressing beam. Photoionization of chiral molecules by circularly polarized radiation gives rise to a strong forward/backward asymmetry in the photoelectron angular distribution[Beaulieu et al., 2016]. Using the Rainbow RABBIT, they measured a delay between electrons ejected forward and backward, which depends on the ejection angle and reaches 24 attoseconds. The asymmetric temporal shape of electron wave packets emitted through an autoionizing state further reveals the chiral character of strongly correlated electronic dynamic [Beaulieu et al., 2017].

Indeed, the presence of resonances can largely influence the spectral and spatial variation of the delays. For example, in the vicinity of Fano resonances, the anisotropy parameter β which characterizes the angular distribution of the electron, varies greatly with energy. We then expect different phase variations for the different partial waves involved. Another example are shape resonances, that induce strong angular variations. H. J. Wörner's group in Zurich measured photoionization delays in N_2O using an MBES, i.e. integration over the angular distribution

of the ejected electrons, that already showed evidence of a population of molecular shape resonances trapping the photoelectron for a duration of up to ~110 as [Huppert et al., 2016]. Resolving completely molecular ionization dynamics is a big challenge. In the molecular frame, the simulations of Ref. [Hockett et al., 2016] reveal many structures, depending on both energy and angle, with delays ranging between -200 and +200 attoseconds, in particular due to the presence of shape resonances that can 'trap' the electron during its emission.

This type of complete study of the photoionization in the molecular frame is planned on the ATTOlab platform, in collaboration with D. Dowek's team, taking advantage of the relatively high rate (10 kHz) of the FAB10 laser for coincidence measurements in a COLTRIMS. A first experimental campaign has already been completed and the measurements are currently under analysis. Using the lower rate (1 kHz) but higher energy per pulse (15 mJ) of the FAB1 laser, one can first align the molecules and then detect angularly the ejected electrons with a VMI. Such an experiment is in the process of mounting. All these measurements will allow the access to all spatial dimensions of the resonant wave packet, allowing a 4D reconstruction (time + space) of the latter. This complete imaging of an ultrafast wave packet is a sort of holy grail for attosecond physics.

ACKNOWLEDGMENTS

First of all I would like to thank Pascal Lablanquie and Eric Constant who agreed to review this manuscript in a rather limited time. Thanks also to the other members of the jury Amelle Zair, John Bozek and Dimitris Charalambidis for their comments and questions. A special thanks goes to Dimitris who as my professor back in Heraklion, was one of the first to introduce me to the world of ultrafast optics.

When I first came in France, a little bit more than three years ago, I could have never dreamt that this journey would be so intense and beautiful. Leaving Greece was a tough decision but at the same time one of the best in my life. Leaving from a lab (UNIS) where I had grate colleagues and most of all friends, it was hard for me to believe that I could find this somewhere else. Apparently I was totally wrong. For this responsible is first of all my supervisor Pascal Salieres who by his excellent guidance, advice and constant support made me appreciate the magic of attosecond delays! His solid knowledge and infinite inspiration made science both interesting and exciting and his love for the details taught me how science should be really done. Thank you Pascal for being soooo patient and enthusiastic!

Then my colleagues Margherita Turconi, Lou Barreau, Antonin Borot, Dominique Platzer. First of all an enormous thank you to Margherita without whom I would have been totally lost in the chaotic world of Python and this thesis would have never been completed. I also want to thank her for not only offering me her great knowledge and experience in the lab but most of all her friendship. Then I would like to thank Lou, an amazingly talented and passionate for science person. Without her ideas and answers to my stupid questions this work would have been much less interesting. And of course Antonin for fixing miraculously all the problems in the lab just by a small magic touch and Dominique for being patient with me while working together (knowing that I can be extremely grumpy sometimes :P).

Merci aussi à Thierry Rouchon et David Bresteau pour les pauses café, le jardin, les sessions de la 'vrais culture française' et les matches de 'atto-pong' qu'ils sont fait mes jours du travaille plus drôle et agréable que jamais ! Thank you also to the newer members of the Atto group : Alice, Mauro and Mekha.

I would also like to thank Bertrand that without his brilliant mind, hard work and great scientific knowledge, ATTOlab would have never been realized. Bertrand apart from a great researcher was a great man, a real "επιστήμονας" having deep knowledge, interest and curiosity not only for science but also for history, music, art, always taking me by surprise when talking about Greek history (which he knew much better than me!).

A great thanks goes to the SLIC team (or else the laser guys) Jean-Francois Hergott, Olivier Tcherbakoff and Pascal D'Oliveira for working hard on the laser system because no laser…no attosecond spectroscopy!!

Furthermore, the biggest thank you goes to the 'κώλοςfaces' Michele Natile and Anna Golinelli my semi-colleagues and full-friends. Michele thank you for your creative English, les dimanches culture, the countless apéros and the corresponding 'voyage en noctilien'. An extra thanks to my office-mate Anna for all the above and most of all for experiencing the 'redaction' together. All that stress and fatigue would have been incredibly more intense without the surrealism of our office. Cette « dernière ligne droite » avait l'air d'être vraiment infinite mais en fin regardes nous, on l'a fini !! On est Dr. !!!!

I would also like to thank the MEDEA project and all the people who worked hard for this. A very well organized and supportive program that made me feel safe as a PhD student and gave me the greatest experiences by travelling around Europe to different labs and allowing me to meet and befriend other young researchers from all around the world!

One of the laboratories that I visited and worked in, in the MEDEA frame, is that of Anne L'Huillier in Lund University that I would like to personally thank for her warm welcoming. Thank you also to all the members of her team for making great science together. Thank you also to the best theorist ever, Richard Taieb and Jérémie Caillat of LCPMR for making theory fun and comprehensible!

Of course a great thanks goes to my friends here in France and those back home. Julius, Dominik, Τζένη, Γεωργία, Κώστα, Ιωάννα και Μπαμπιώ 'thank you' is a small word that cannot contain my gratitude. A special thanks goes also to my friend Pavlos. Παυλή σ' ευχαριστώ για την υπομονή και την αγάπη σου :)

And finally I could not thank enough my family for supporting me more than ever, for being there for me when I was stressed and ready to quit everything and for giving me courage by believing in me. Especially my dad for being always calm and my mom for sending me countless supplies of ΠΑΥΛΙΔΗΣ chocolate and love. The biggest thank you though goes to my godfather Ioannis G. Tsatsaris whom without his guidance and advice this journey would have never been possible.

Merci à tous!
Χριστιάνα.

BIBLIOGRAPHY

The quantal calculation of the photo-ionization cross-section of atomic potassium. Proceedings of the Royal Society of London A: Mathematical, Physical and Engineering Sciences **188**, 350–357 (1947). [Cited on page 131.]

A comparison of theory and experiment for photo-ionization cross-sections ii. sodium and the alkali metals. Proceedings of the Royal Society of London A: Mathematical, Physical and Engineering Sciences **208**, 418–430 (1951). [Cited on page 131.]

Abbati I, Braicovich L, Rossi G, Lindau I, del Pennino U, and Nannarone S. *Solid-state effects on the valence-band 4d-photoionization cross sections at the cooper minimum*. Phys. Rev. Lett. **50**, 1799–1802 (1983). [Cited on page 132.]

Adam MY, Morin P, and Wendin G. *Photoelectron satellite spectrum in the region of the 3s cooper minimum of argon*. Phys. Rev. A **31**, 1426–1433 (1985). [Cited on page 132.]

Agostini P and DiMauro LF. *The physics of attosecond light pulses*. Reports on Progress in Physics **67**, 813 (2004). [Cited on page 48.]

Alexander, R. W. J. *PHOTOIONIZATION OF KRYPTON AND ARGON IN THE 100-300 ANGSTROM RANGE, book*. (1965). [Cited on page 132.]

Amusia M, Ivanov V, Cherepkov N, and Chernysheva L. *Interference effects in photoionization of noble gas atoms outer s-subshells*. Physics Letters A **40**, 361 – 362 (1972). [Cited on pages 150 and 162.]

Amusia MY, Cherepkov NA, and Chernysheva LV. *Cross section for the photoionization of noble-gas atoms with allowance for multielectron correlations*. Sov. Phys. JETP **33**, 90–96 (1971). [Cited on page 133.]

Antoine P, L'Huillier A, and Lewenstein M. *Attosecond pulse trains using high–order harmonics*. Phys. Rev. Lett. **77**, 1234–1237 (1996). [Cited on page 26.]

Argenti L, Jiménez-Galán A, Caillat J, Taïeb R, Maquet A, and Martín F. *Control of photoemission delay in resonant two-photon transitions*. Phys. Rev. A **95** (2017). [Cited on page 35.]

Augst S, Strickland D, Meyerhofer DD, Chin SL, and Eberly JH. *Tunneling ionization of noble gases in a high-intensity laser field*. Phys. Rev. Lett. **63**, 2212–2215 (1989). [Cited on page 12.]

Aymar M, Luc-Koenig E, and Farnoux FC. *Theoretical investigation on photoionization from rydberg states of lithium, sodium and potassium*. Journal of Physics B: Atomic and Molecular Physics **9**, 1279 (1976). [Cited on page 132.]

Balcou P, Sali'eres P, L'Huillier A, and Lewenstein M. *Generalized phase-matching conditions for high harmonics: The role of field-gradient forces*. Phys. Rev. A **55**, 3204–3210 (1997). [Cited on pages 25 and 26.]

Barreau L. *Etude de dynamiques de photo-ionisation résonante à l'aide d'impulsions attosecondes*. Thesis (2017). [Cited on pages 12, 30, and 100.]

Bates DR and Massey HSW. *An approximate formula for the continuous radiative absorption cross-section of the lighter neutral atoms and positive and negative ions*. Monthly Notices of the Royal Astronomical Society **106**, 423–431 (1946). [Cited on page 131.]

Bauer D and Mulser P. *Exact field ionization rates in the barrier-suppression regime from numerical time-dependent schrödinger-equation calculations*. Phys. Rev. A **59**, 569–577 (1999). [Cited on page 12.]

Beaulieu S, Ferré A, Géneaux R, Canonge R, Descamps D, Fabre B, Fedorov N, Légaré F, Petit S, Ruchon T, Blanchet V, Mairesse Y, and Pons B. *Universality of photoelectron circular dichroism in the photoionization of chiral molecules*. New Journal of Physics **18**, 102002 (2016). [Cited on page 178.]

Beaulieu S, Comby A, Clergerie A, Caillat J, Descamps D, Dudovich N, Fabre B, Géneaux R, Légaré F, Petit S, Pons B, Porat G, Ruchon T, Taïeb R, Blanchet V, and Mairesse Y. *Attosecond-resolved photoionization of chiral molecules*. Science **358**, 1288–1294 (2017). [Cited on page 178.]

Becker U and Shirley DA. *VUV and Soft X-Ray Photoionization, book*. (1996). [Cited on pages 132 and 166.]

Bellini M, Lyngå C, Tozzi A, Gaarde MB, Hänsch TW, L'Huillier A, and Wahlström CG. *Temporal coherence of ultrashort high-order harmonic pulses*. Phys. Rev. Lett. **81**, 297–300 (1998). [Cited on page 23.]

Berezhko EG, Kabachnik NM, and Rostovsky VS. *Potential-barrier effects in inner-shell photoionisation and their influence on the anisotropy of x-rays and auger electrons*. Journal of Physics B: Atomic and Molecular Physics **11**, 1749 (1978). [Cited on page 132.]

Beterov II, Mansell CW, Yakshina EA, Ryabtsev II, Tretyakov DB, Entin VM, MacCormick C, Piotrowicz MJ, Kowalczyk A, and Bergamini S. *Cooper minima in the transitions from low-excited and Rydberg states of alkali-metal atoms*. pages 1–12 (2012). [Cited on page 132.]

Beutler H. *Über absorptionsserien von argon, krypton und xenon zu termen zwischen den beiden ionisierungsgrenzen2p32/0und2p12/0*. Zeitschrift für Physik **93**, 177–196 (1935). [Cited on pages 71 and 72.]

Biraud, Y.G. *Les méthodes de déconvolution et leurs limitations fondamentales*. Rev. Phys. Appl. (Paris) **11**, 203–214 (1976). [Cited on page 96.]

Bizau J and Wuilleumier F. *Redetermination of absolute partial photoionization cross sections of he and ne atoms between 20 and 300 ev photon energy*. Journal of Electron Spectroscopy and Related Phenomena **71**, 205 – 224 (1995). [Cited on page 149.]

Bourassin-Bouchet C, Diveki Z, de Rossi S, English E, Meltchakov E, Gobert O, Guénot D, Carré B, Delmotte F, Salières P, and Ruchon T. *Control of the attosecond synchronization of xuv radiation with phase-optimized mirrors*. Opt. Express **19**, 3809–3817 (2011). [Cited on page 20.]

Brabec T and Krausz F. *Intense few-cycle laser fields: Frontiers of nonlinear optics*. Rev. Mod. Phys. **72**, 545–591 (2000). [Cited on page 4.]

Bray AW, Naseem F, and Kheifets AS. *PHYSICAL REVIEW A 97 , 063404 (2018) Simulation of angular-resolved RABBITT measurements in noble-gas atoms*. **063404**, 1–12 (2018). [Cited on pages 150 and 167.]

Bruner BD, Mašín Z, Negro M, Morales F, Brambila D, Devetta M, Faccialà D, Harvey AG, Ivanov M, Mairesse Y, Patchkovskii S, Serbinenko V, Soifer H, Stagira S, Vozzi C, Dudovicha N, and Smirnova O. *Multidimensional high harmonic spectroscopy of polyatomic molecules: Detecting sub-cycle laser-driven hole dynamics upon ionization in strong mid-IR laser fields*. Faraday Discussions (2016). [Cited on page 7.]

Busto D, Barreau L, Isinger M, Turconi M, Alexandridi C, Harth A, Zhong S, Squibb R, Kroon D, Plogmaker S, et al. *Time–frequency representation of autoionization dynamics in helium*. Journal of Physics B: Atomic, Molecular and Optical Physics **51**, 044002 (2018). [Cited on pages 67, 83, 84, 86, 87, 88, 90, 92, 93, 104, 154, and 176.]

Caldwell CD, Whitfield SB, and Krause MO. *Manifestation of spin-orbit interactions in photoemission from free atoms*. Molecular Physics **98**, 1075–1082 (2000). [Cited on page 120.]

Calegari F, Ayuso D, Trabattoni A, Belshaw L, De Camillis S, Anumula S, Frassetto F, Poletto L, Palacios A, Decleva P, Greenwood JB, Martín F, and Nisoli M. *Ultrafast electron dynamics in phenylalanine initiated by attosecond pulses*. Science **346**, 336–339 (2014). [Cited on page 5.]

Canton-Rogan SE, Wills AA, Gorczyca TW, Wiedenhoeft M, Nayandin O, Liu CN, and Berrah N. *Mirroring doubly excited resonances in argon*. Phys. Rev. Lett. **85**, 3113–3116 (2000). [Cited on page 120.]

Carette T, Dahlström JM, Argenti L, and Lindroth E. *Multiconfigurational Hartree-Fock close-coupling ansatz: Application to the argon photoionization cross section and delays*. Physical Review A - Atomic, Molecular, and Optical Physics **87**, 1–13 (2013). [Cited on page 163.]

Carlson TA, Krause MO, Grimm FA, Keller P, and Taylor JW. *Angle-resolved photoelectron spectroscopy of ccl4: The cooper minimum in molecules*. The Journal of Chemical Physics **77**, 5340–5347 (1982). [Cited on page 132.]

Carlson TA, Fahlman A, Krause MO, Whitley TA, and Grimm FA. *Systematic investigation of the cooper minimum for the hydrogen halides*. The Journal of Chemical Physics **81**, 5389–5394 (1984). [Cited on page 132.]

Cavalieri AL, Müller N, Uphues T, Yakovlev VS, Baltuška A, Horvath B, Schmidt B, Blümel L, Holzwarth R, Hendel S, et al. *Attosecond spectroscopy in condensed matter*. Nature **449**, 1029 (2007). [Cited on page 149.]

Chan WF, Cooper G, Guo X, Burton GR, and Brion CE. *Absolute optical oscillator strengths for the electronic excitation of atoms at high resolution. iii. the photoabsorption of argon, krypton, and xenon*. Phys. Rev. A **46**, 149–171 (1992). [Cited on page 132.]

Chang Z. Fundamentals of Attosecond Optics -CRC Press (2011).pdf. [Cited on page 56.]

Chu WC and Lin CD. *Photoabsorption of attosecond xuv light pulses by two strongly laser-coupled autoionizing states*. Phys. Rev. A **85**, 013409 (2012). [Cited on page 6.]

Cireasa R, Boguslavskiy AE, Pons B, Wong MCH, Descamps D, Petit S, Ruf H, Thiré N, Ferré A, Suarez J, Higuet J, Schmidt BE, Alharbi AF, Légaré F, Blanchet V, Fabre B, Patchkovskii S, Smirnova O, Mairesse Y, and Bhardwaj VR. *Probing molecular chirality on a sub-femtosecond timescale*. Nature Physics (2015). [Cited on page 7.]

Cirelli C, Marante C, Heuser S, Petersson CLM, Galán lJ, Argenti L, Zhong S, Busto D, Isinger M, Nandi S, Maclot S, Rading L, Johnsson P, Gisselbrecht M, Lucchini M, Gallmann L, Dahlström JM, Lindroth E, L'Huillier A, Martín F, and Keller U. *Anisotropic photoemission time delays close to a fano resonance*. Nature Communications **9** (2018). [Cited on pages 115, 116, and 178.]

Cohen-Tannoudji C, Diu B, and Laloë F. *Mécanique quantique II*. Hermann (1973). [Cited on pages 33 and 37.]

Constant E, Garzella D, Breger P, Mével E, Dorrer C, Le Blanc C, Salin F, and Agostini P. *Optimizing high harmonic generation in absorbing gases: Model and experiment*. Phys. Rev. Lett. **82**, 1668–1671 (1999). [Cited on page 24.]

Cooper JW. *Photoionization from outer atomic subshells. a model study*. Phys. Rev. **128**, 681–693 (1962). [Cited on pages 132, 133, and 150.]

Corkum PB. *Plasma perspective on strong field multiphoton ionization*. Phys. Rev. Lett. **71**, 1994–1997 (1993). [Cited on pages 5 and 11.]

Dahlström JM and Lindroth E. *Study of attosecond delays using perturbation diagrams and exterior complex scaling*. Journal of Physics B: Atomic, Molecular and Optical Physics **47**, 124012 (2014). [Cited on pages 48, 157, 167, 168, 169, and 177.]

Dahlström JM and Lindroth E. *Corrigendum: Study of attosecond delays using perturbation diagrams and exterior complex scaling (Dahlström and Lindroth 2014 J. Phys. B: At. Mol. Opt. Phys. 47 124012)*. Journal of Physics B: Atomic, Molecular and Optical Physics (2016). [Cited on pages 147, 150, 166, 167, 168, 170, and 172.]

Dahlström JM, L'Huillier A, and Maquet A. *Introduction to attosecond delays in photoionization*. Journal of Physics B: Atomic, Molecular and Optical Physics **45**, 183001 (2012). [Cited on pages 34 and 35.]

Dahlström JM, Carette T, and Lindroth E. *Diagrammatic approach to attosecond delays in photoionization*. Physical Review A - Atomic, Molecular, and Optical Physics **86**, 1–4 (2012)a. [Cited on pages 133, 149, 163, 164, and 168.]

Dahlström JM, L'Huillier A, and Maquet A. *Introduction to attosecond time-delays in photoionization*. Journal of Physics B: Atomic, Molecular and Optical Physics (2012)b. [Cited on pages 151 and 169.]

Dahlström JM, Guénot D, Klünder K, Gisselbrecht M, Mauritsson J, L'Huillier A, Maquet A, and Taïeb R. *Theory of attosecond delays in laser-assisted photoionization*. Chemical Physics **414**, 53–64 (2013). [Cited on pages 38, 39, 42, and 149.]

Desrier A, Maquet A, and Ta R. *Time domain interpretation of spectral amplitudes*. pages 28–30 (2018). [Cited on page 100.]

Ditchburn. *The continuous absorption of light in potassium vapour*. Proceedings of the Royal Society of London A: Mathematical, Physical and Engineering Sciences **181**, 386–399 (1943). [Cited on page 131.]

Dixit G, Chakraborty HS, and Madjet MEA. *Time delay in the recoiling valence photoemission of ar endohedrally confined in* c_{60}. Phys. Rev. Lett. **111**, 203003 (2013). [Cited on page 133.]

Domke M, Schulz K, Remmers G, Kaindl G, and Wintgen D. *High-resolution study of 1Po double-excitation states in helium.* Physical review. A **53**, 1424–1438 (1996). [Cited on pages 3, 83, and 95.]

Doumy G, Wheeler J, Roedig C, Chirla R, Agostini P, and DiMauro LF. *Attosecond synchronization of high-order harmonics from midinfrared drivers*. Phys. Rev. Lett. **102**, 093002 (2009). [Cited on page 26.]

Dudovich N, Smirnova O, Levesque J, Mairesse Y, Strelkov V, Ivanov MY, Villeneuve DM, and Corkum PB. *Measuring and controlling the birth of attosecond xuv pulses*. Nature Physics (2006). [Cited on page 26.]

Duzy C and Hyman HA. *Photoionization of excited rare-gas atoms*. Phys. Rev. A **22**, 1878–1883 (1980). [Cited on page 132.]

Eckle P, Pfeiffer AN, Cirelli C, Staudte A, Dörner R, Muller HG, Büttiker M, and Keller U. *Attosecond ionization and tunneling delay time measurements in helium*. Science **322**, 1525–1529 (2008). [Cited on page 5.]

Einstein A. *Über einen die erzeugung und verwandlung des lichtes betreffenden heuristischen gesichtspunkt*. Annalen der physik **322**, 132–148 (1905). [Cited on page 27.]

Eisenbud L. *The formal properties of nuclear collisions*. Thèses, Princeton University, (1948). [Cited on page 34.]

Fano U. *Sullo spettro di assorbimento dei gas nobili presso il limite dello spettro d'arco*. Il Nuovo Cimento (1924-1942) **12**, 154–161 (1935). [Cited on page 71.]

Fano U. *Effects of configuration interaction on intensities and phase shifts*. Physical Review **124**, 1866–1878 (1961). [Cited on pages 71 and 73.]

Fano U. *Propensity rules: An analytical approach*. Phys. Rev. A **32**, 617–618 (1985). [Cited on pages 37 and 122.]

Farkas G and Tóth C. *Proposal for attosecond light pulse generation using laser induced multiple-harmonic conversion processes in rare gases*. Physics Letters A **168**, 447 – 450 (1992). [Cited on page 18.]

Farrell JP, Spector LS, McFarland BK, Bucksbaum PH, Gühr M, Gaarde MB, and Schafer KJ. *Influence of phase matching on the cooper minimum in ar high-order harmonic spectra*. Phys. Rev. A **83**, 023420 (2011). [Cited on pages 139, 140, and 144.]

Ferray M, L'Huillier A, Li XF, Lompre LA, Mainfray G, and Manus C. *Multiple-harmonic conversion of 1064 nm radiation in rare gases*. Journal of Physics B: Atomic, Molecular and Optical Physics **21**, L31 (1988). [Cited on pages 5 and 11.]

Fink MGJ and Johnson WR. *Low-energy photoionization of alkali-metal atoms: Relativistic random-phase-approximation calculations*. Phys. Rev. A **34**, 3754–3759 (1986). [Cited on page 133.]

Fischer CF, Tachiev G, Gaigalas G, and Godefroid MR. *An mchf atomic-structure package for large-scale calculations*. Computer Physics Communications **176**, 559 – 579 (2007). [Cited on page 163.]

Friedrich H. *Theoretical Atomic Physics*. Springer-Verlag (1991). [Cited on pages 33 and 34.]

Frolov MV, Manakov NL, Sarantseva TS, and Starace AF. *Analytic confirmation that the factorized formula for harmonic generation involves the exact photorecombination cross section*. Phys. Rev. A **83**, 043416 (2011). [Cited on page 138.]

Gaumnitz T, Jain A, Pertot Y, Huppert M, Jordan I, Ardana-Lamas F, and Wörner HJ. *Streaking of 43-attosecond soft-x-ray pulses generated by a passively cep-stable mid-infrared driver*. Opt. Express **25**, 27506–27518 (2017). [Cited on page 20.]

Gilbertson S, Chini M, Feng X, Khan S, Wu Y, and Chang Z. *Monitoring and controlling the electron dynamics in helium with isolated attosecond pulses*. Phys. Rev. Lett. **105**, 263003 (2010). [Cited on page 6.]

Golinelli A, Xiaowei C, B B, Eric G, Pierre-Mary P, Olivier T, d'Oliveira Pascal, and Jean-Francois H. *Cep-stabilized, sub-18 fs, 10 khz and tw-class 1 khz dual output ti: Sa laser with wavelength tunability option*. in preparation (2018). [Cited on page 50.]

Goulielmakis E, Uiberacker M, Kienberger R, Baltuska A, Yakovlev V, Scrinzi A, Westerwalbesloh T, Kleineberg U, Heinzmann U, Drescher M, and Krausz F. *Direct measurement of light waves*. Science **305**, 1267 (2004). [Cited on page 37.]

Goulielmakis E, Schultze M, Hofstetter M, Yakovlev VS, Gagnon J, Uiberacker M, Aquila AL, Gullikson EM, Attwood DT, Kienberger R, Krausz F, and Kleineberg U. *Single-cycle nonlinear optics*. Science **320**, 1614–1617 (2008). [Cited on page 26.]

Gruson V, Barreau L, Jiménez-Galan Á, Risoud F, Caillat J, Maquet A, Carré B, Lepetit F, Hergott JF, Ruchon T, Argenti L, Taïeb R, Martín F, and Salières P. *Attosecond dynamics through a fano resonance: Monitoring the birth of a photoelectron*. Science **354**, 734–738 (2016)a. [Cited on pages 3, 6, 61, 67, 72, 77, 82, 83, 84, 86, 87, 88, 89, 92, 93, 111, and 175.]

Gruson V, Barreau L, Jiménez-Galan Á, Risoud F, Caillat J, Maquet A, Carré B, Lepetit F, Hergott JF, Ruchon T, Argenti L, Taïeb R, Martín F, and Salières P. *Supplementary material: Attosecond dynamics through a fano resonance: Monitoring the birth of a photoelectron*. Science **354**, 734–738 (2016)b. [Cited on pages 62, 63, 64, 67, and 100.]

Guénot D, Klünder K, Arnold CL, Kroon D, Dahlström JM, Miranda M, Fordell T, Gisselbrecht M, Johnsson P, Mauritsson J, Lindroth E, Maquet A, Taïeb R, L'Huillier A, and Kheifets AS. *Photoemission-time-delay measurements and calculations close to the 3s-ionization-cross-section minimum in Ar*. Physical Review A - Atomic, Molecular, and Optical Physics **85**, 1–8 (2012). [Cited on pages 35, 48, and 177.]

Guénot D, Klünder K, Arnold CL, Kroon D, Dahlström JM, Miranda M, Fordell T, Gisselbrecht M, Johnsson P, Mauritsson J, Lindroth E, Maquet A, Taïeb R, L'Huillier A, and Kheifets AS. *Photoemission-time-delay measurements and calculations close to the 3s-ionization-cross-section minimum in argon*. Phys. Rev. A **85**, 053424 (2012). [Cited on pages 149, 150, 152, 153, 155, 156, 166, 167, 168, and 170.]

Guénot D, Kroon D, Balogh E, Larsen EW, Kotur M, Miranda M, Fordell T, Johnsson P, Mauritsson J, Gisselbrecht M, Varju K, Arnold CL, Carette T, Kheifets AS, Lindroth E, L'Huillier A, and Dahlström JM. *Measurements of relative photoemission time delays in noble gas atoms*. Journal of Physics B: Atomic, Molecular and Optical Physics **47**, 245602 (2014). [Cited on page 149.]

Gustafsson E, Ruchon T, Swoboda M, Remetter T, Pourtal E, López-Martens R, Balcou P, and L'Huillier A. *Broadband attosecond pulse shaping*. Opt. Lett. **32**, 1353–1355 (2007). [Cited on page 20.]

Haessler S, Boutu W, Stankiewicz M, Frasinski LJ, Weber S, Caillat J, Taïeb R, Maquet A, Breger P, Monchicourt P, Carré B, and Salières P. *Attosecond chirp-encoded dynamics of light nuclei*. Journal of Physics B: Atomic, Molecular and Optical Physics **42**, 134002 (2009). [Cited on pages 6, 7, 48, and 149.]

Haessler S, Caillat J, Boutu W, Giovanetti-Teixeira C, Ruchon T, Auguste T, Diveki Z, Breger P, Maquet A, Carré B, Taeb R, and Salières P. *Attosecond imaging of molecular electronic wavepackets*. Nature Physics **6**, 200–206 (2010). [Cited on page 7.]

Haessler S, Caillat J, and Salières P. *Self-probing of molecules with high harmonic generation*. Journal of Physics B: Atomic, Molecular and Optical Physics **44**, 203001 (2011). [Cited on page 138.]

Harris S, Macklin J, and Hänsch T. *Atomic scale temporal structure inherent to high-order harmonic generation*. Optics Communications **100**, 487 – 490 (1993). [Cited on page 18.]

Hentschel M, Kienberger R, Spielmann C, Reider GA, Milosevic N, Brabec T, Corkum P, Heinzmann U, Drescher M, and Krausz F. *Attosecond metrology*. Nature **414**, 509 (2001). [Cited on page 5.]

Heuser S, Jiménez Galán A, Cirelli C, Marante C, Sabbar M, Boge R, Lucchini M, Gallmann L, Ivanov I, Kheifets AS, Dahlström JM, Lindroth E, Argenti L, Martín F, and Keller U. *Angular dependence of photoemission time delay in helium*. Phys. Rev. A **94**, 063409 (2016). [Cited on pages 169 and 178.]

Heyl C. *Scaling and gating attosecond pulse generation*. PhD thesis, Lund University, (2014). [Cited on page 24.]

Higuet J, Ruf H, Thiré N, Cireasa R, Constant E, Cormier E, Descamps D, Mével E, Petit S, Pons B, Mairesse Y, and Fabre B. *High-order harmonic spectroscopy of the cooper minimum in argon: Experimental and theoretical study*. Phys. Rev. A **83**, 053401 (2011). [Cited on pages 139, 140, 142, 144, 145, and 171.]

Hockett P, Frumker E, Villeneuve DM, and Corkum PB. *Time delay in molecular photoionization*. Journal of Physics B: Atomic, Molecular and Optical Physics **49**, 095602 (2016). [Cited on pages 178 and 179.]

Houlgate R, West J, Codling K, and Marr G. *The angular distribution of the 3p electrons and the partial cross section of the 3s electrons of argon from threshold to 70 ev*. Journal of Electron Spectroscopy and Related Phenomena **9**, 205 – 209 (1976). [Cited on page 132.]

Houlgate RG, Codling K, Marr GV, and West JB. *Angular distribution and photoionization cross section measurements on the 3p and 3s subshells of argon*. Journal of Physics B: Atomic and Molecular Physics **7**, L470 (1974). [Cited on page 132.]

Huang KN, Johnson W, and Cheng K. *Theoretical photoionization parameters for the noble gases argon, krypton, and xenon*. Atomic Data and Nuclear Data Tables **26**, 33 – 45 (1981). [Cited on pages 132 and 133.]

Huppert M, Jordan I, Baykusheva D, von Conta A, and Wörner HJ. *Attosecond delays in molecular photoionization*. Phys. Rev. Lett. **117**, 093001 (2016). [Cited on pages 149 and 179.]

Isinger M et al. *Photoionization in the time and frequency domain*. Science **358**, 893 (2017). [Cited on page 149.]

Itatani J, Quéré F, Yudin GL, Ivanov MY, Krausz F, and Corkum PB. *Attosecond streak camera*. Phys. Rev. Lett. **88**, 173903 (2002). [Cited on page 5.]

Itatani J, Lavesque J, Zeidler D, Niikura H, Pépin H, Kieffer JC, Corkum PB, and Villeneuve DM. *Tomographic imaging of molecular orbitals*. Nature **432**, 867–871 (2004). [Cited on pages 7, 26, and 138.]

Ivanov M and Smirnova O. *How accurate is the attosecond streak camera?* Phys. Rev. Lett. **107**, 213605 (2011). [Cited on page 149.]

Ivanov MY, Brabec T, and Burnett N. *Coulomb corrections and polarization effects in high-intensity high-harmonic emission*. Phys. Rev. A **54**, 742–745 (1996). [Cited on page 26.]

Jiménez-Galán A, Argenti L, and Martín F. *Modulation of attosecond beating in resonant two-photon ionization*. Phys. Rev. Lett. **113**, 263001 (2014). [Cited on pages 78, 82, 115, and 126.]

Jiménez-Galán A, Martín F, and Argenti L. *Two-photon finite-pulse model for resonant transitions in attosecond experiments*. Phys. Rev. A **93**, 023429 (2016). [Cited on pages 77, 78, 81, and 97.]

Jin C, Le AT, and Lin CD. *Medium propagation effects in high-order harmonic generation of ar and* n_2. Phys. Rev. A **83**, 023411 (2011). [Cited on pages 138 and 139.]

Jin C, Bertrand JB, Lucchese RR, Wörner HJ, Corkum PB, Villeneuve DM, Le AT, and Lin CD. *Intensity dependence of multiple orbital contributions and shape resonance in high-order harmonic generation of aligned n_2 molecules*. Phys. Rev. A **85**, 013405 (2012). [Cited on page 7.]

Johnson W. Relativistic random-phase approximation. volume 25 of *Advances in Atomic and Molecular Physics*, pages 375 – 391. Academic Press, (1989). [Cited on page 133.]

Johnson WR and Cheng KT. *Photoionization of the outer shells of neon, argon, krypton, and xenon using the relativistic random-phase approximation*. Phys. Rev. A **20**, 978–988 (1979). [Cited on page 133.]

Johnson WR and Lin CD. *Multichannel relativistic random-phase approximation for the photoionization of atoms*. Phys. Rev. A **20**, 964–977 (1979). [Cited on page 133.]

Jordan I, Huppert M, Pabst S, Kheifets A, Baykusheva D, and Wörner H. *Spin-orbit delays in photoemission*. Phys. Rev. A **95** (2017). [Cited on pages 116, 117, and 149.]

Kaldun A, Blättermann A, Stooß V, Donsa S, Wei H, Pazourek R, Nagele S, Ott C, Lin CD, Burgdörfer J, and Pfeifer T. *Observing the ultrafast buildup of a Fano resonance in the time domain*. Science **354**, 738–741 (2016). [Cited on pages 6, 82, and 175.]

Kazamias S, Daboussi S, Guilbaud O, Cassou K, Ros D, Cros B, and Maynard G. *Pressure-induced phase matching in high-order harmonic generation*. Phys. Rev. A **83**, 063405 (2011). [Cited on page 25.]

Keldysh L et al. *Ionization in the field of a strong electromagnetic wave*. Sov. Phys. JETP **20**, 1307–1314 (1965). [Cited on page 13.]

Kennedy DJ and Manson ST. *Photoionization of the noble gases: Cross sections and angular distributions*. Phys. Rev. A **5**, 227–247 (1972). [Cited on pages 132 and 133.]

Kheifets AS. *Time delay in valence-shell photoionization of noble-gas atoms*. Phys. Rev. A **87**, 063404 (2013). [Cited on pages 133, 149, 150, 167, and 169.]

Kheifets AS and Ivanov IA. *Delay in atomic photoionization*. Phys. Rev. Lett. **105**, 233002 (2010). [Cited on page 149.]

Kienberger R, Goulielmakis E, Uiberacker M, Baltuska A, Yakovlev V, Bammer F, Scrinzi A, Westerwalbesloh T, Kleineberg U, Heinzmann U, Drescher M, and Krausz F. *Atomic transient recorder*. Nature **427**, 817–821 (2004). [Cited on page 37.]

Kim YS, Pratt RH, and Ron A. *Overlap of shape resonance and cooper-minimum structure in photoionization*. Phys. Rev. A **24**, 1626–1628 (1981). [Cited on page 132.]

Klünder K, Dahlström JM, Gisselbrecht M, Fordell T, Swoboda M, Guénot D, Johnsson P, Caillat J, Mauritsson J, Maquet A, Taïeb R, and L'Huillier A. *Probing single-photon ionization on the attosecond time scale*. Physical Review Letters **106**, 1–4 (2011). [Cited on pages 6, 48, 61, 149, 150, 152, 153, 155, 156, and 177.]

Kothe A, Metje J, Wilke M, Moguilevski A, Engel N, Al-Obaidi R, Richter C, Golnak R, Kiyan IY, and Aziz EF. *Time-of-flight electron spectrometer for a broad range of kinetic energies*. Review of Scientific Instruments **84**, 023106 (2013). [Cited on page 55.]

Kotur M, Guenot D, Jiménez-Galán Á, Kroon D, Larsen EW, Louisy M, Bengtsson M, Miranda M, Mauritsson J, Arnold CL, Canton SE, Gisselbrecht M, Carette T, Dahlström MJ, Lindroth E, Maquet A, Argenti L, Martín F, and L'Huillier A. *Phase measurement of a Fano window resonance using tunable attosecond pulses ´*. arXiv [physics.atom-ph] **5**, 02024 (2015). [Cited on pages 67, 125, and 176.]

Kotur M, Guénot D, Jiménez-Galán , Kroon D, Larsen EW, Louisy M, Bengtsson S, Miranda M, Mauritsson J, Arnold CL, Canton SE, Gisselbrecht M, Carette T, Dahlström JM, Lindroth E, Maquet A, Argenti L, Martín F, and L'Huillier A. *Spectral phase measurement of a fano resonance using tunable attosecond pulses*. Nature Communications **7**, 10566 (2016). [Cited on pages 63, 82, 114, 115, 121, and 126.]

Krause JL, Schafer KJ, and Kulander KC. *High-order harmonic generation from atoms and ions in the high intensity regime*. Phys. Rev. Lett. **68**, 3535–3538 (1992). [Cited on page 14.]

Kroon D. *Thesis*. (2016). [Cited on page 59.]

Kruit P and Read FH. *Magnetic field paralleliser for 2π electron-spectrometer and electron-image magnifier*. Journal of Physics E: Scientific Instruments **16**, 313 (1983). [Cited on page 55.]

Lahiri J and Manson ST. *Multiple minima in photoionization cross sections of excited atoms*. Phys. Rev. Lett. **48**, 614–616 (1982). [Cited on pages 132 and 136.]

Landau LD and Lifshitz EM. *Quantum Mechanics*. (1977). [Cited on pages 36 and 138.]

Lawrence EO and Edlefsen NE. *The photo-ionization of potassium vapor*. Phys. Rev. **34**, 1056–1060 (1929). [Cited on page 131.]

Le AT, Morishita T, and Lin CD. *Extraction of the species-dependent dipole amplitude and phase from high-order harmonic spectra in rare-gas atoms*. Phys. Rev. A **78**, 023814 (2008)a. [Cited on page 26.]

Le AT, Morishita T, and Lin CD. *Extraction of the species-dependent dipole amplitude and phase from high-order harmonic spectra in rare-gas atoms*. Phys. Rev. A **78**, 023814 (2008)b. [Cited on page 138.]

Le AT, Lucchese RR, and Lin CD. *Quantitative rescattering theory of high-order harmonic generation for polyatomic molecules*. Physical Review A - Atomic, Molecular, and Optical Physics **87**, 1–23 (2013). [Cited on page 137.]

Lein M, Hay N, Velotta R, Marangos JP, and Knight PL. *Interference effects in high-order harmonic generation with molecules*. Phys. Rev. A **66**, 023805 (2002). [Cited on page 138.]

Levesque J, Mairesse Y, Dudovich N, Pépin H, Kieffer JC, Corkum PB, and Villeneuve DM. *Polarization state of high-order harmonic emission from aligned molecules*. Phys. Rev. Lett. **99**, 243001 (2007)a. [Cited on page 7.]

Levesque J, Zeidler D, Marangos JP, Corkum PB, and Villeneuve DM. *High harmonic generation and the role of atomic orbital wave functions*. Phys. Rev. Lett. **98**, 183903 (2007)b. [Cited on page 26.]

Lewenstein M, Balcou P, Ivanov MY, L'Huillier A, and Corkum PB. *Theory of high-harmonic generation by low-frequency laser fields*. Phys. Rev. A **49**, 2117–2132 (1994). [Cited on pages 5, 16, and 18.]

L'Huillier A and Balcou P. *High-order harmonic generation in rare gases with a 1-ps 1053-nm laser*. Phys. Rev. Lett. **70**, 774–777 (1993). [Cited on page 139.]

Li W, Zhou X, Lock R, Patchkovskii S, Stolow A, Kapteyn HC, and Murnane MM. *Time-resolved dynamics in n2o4 probed using high harmonic generation*. Science **322**, 1207–1211 (2008). [Cited on page 7.]

Lin N. *Application of attosecond pulses to high harmonic spectroscopy of molecules*. Thesis (2013). [Cited on page 26.]

López-Martens R, Varjú K, Johnsson P, Mauritsson J, Mairesse Y, Salières P, Gaarde MB, Schafer KJ, Persson A, Svanberg S, Wahlström CG, and L'Huillier A. *Amplitude and phase control of attosecond light pulses*. Phys. Rev. Lett. **94**, 033001 (2005). [Cited on page 20.]

Lukirskii A, Rumsh M, and Karpovich I. *Measurements of soft x-ray emission by means of secondary-electron multipliers*. Zavodsk. Lab.,(1963). [Cited on page 114.]

Madden RP and Codling K. *New autoionizing atomic energy levels in He, Ne, and Ar*. Physical Review Letters **10**, 516–518 (1963). [Cited on page 82.]

Madden RP and Codling K. *Two-Electron Excitation States in Helium.* The Astrophysical Journal **141**, 364 (1965). [Cited on page 82.]

Madjet ME, Chakraborty HS, and Rost JM. *Spurious oscillations from local self-interaction correction in high-energy photoionization calculations for metal clusters*. Journal of Physics B: Atomic, Molecular and Optical Physics **34**, L345 (2001). [Cited on page 164.]

Magrakvelidze M, Anstine DM, Dixit G, Madjet MEA, and Chakraborty HS. *Attosecond structures from the molecular cavity in fullerene photoemission time delay*. Phys. Rev. A **91**, 053407 (2015)a. [Cited on page 133.]

Magrakvelidze M, Madjet MEA, Dixit G, Ivanov M, and Chakraborty HS. *Attosecond time delay in valence photoionization and photorecombination of argon: A time-dependent local-density-approximation study*. Physical Review A - Atomic, Molecular, and Optical Physics (2015)b. [Cited on pages 147, 150, and 165.]

Mairesse Y. *Génération et caractérisation d'impulsions attosecondes*. Thesis (2005). [Cited on page 20.]

Mairesse Y and Quéré F. *Frequency-resolved optical gating for complete reconstruction of attosecond bursts*. Phys. Rev. A **71**, 011401 (2005). [Cited on pages 5 and 107.]

Mairesse Y, de Bohan A, Frasinski LJ, Merdji H, Dinu LC, Monchicourt P, Breger P, Kovačev M, Taïeb R, Carré B, Muller HG, Agostini P, and Salières P. *Attosecond synchronization of high-harmonic soft x-rays*. Science **302**, 1540–1543 (2003)a. [Cited on pages 20, 48, and 57.]

Mairesse Y, de Bohan A, Frasinski LJ, Merdji H, Dinu LC, Monchicourt P, Breger P, Kovačev M, Taïeb R, Carré B, Muller HG, Agostini P, and Salières P. *Attosecond synchronization of high-harmonic soft x-rays*. Science **302**, 1540–1543 (2003)b. [Cited on pages 5, 26, and 144.]

Mairesse Y, de Bohan A, Frasinski LJ, Merdji H, Dinu LC, Monchicourt P, Breger P, Kovačev M, Auguste T, Carré B, Muller HG, Agostini P, and Salières P. *Optimization of attosecond pulse generation*. Phys. Rev. Lett. **93**, 163901 (2004). [Cited on pages 20, 21, and 144.]

Mairesse Y, Higuet J, Dudovich N, Shafir D, Fabre B, Mével E, Constant E, Patchkovskii S, Walters Z, Ivanov MY, and Smirnova O. *High harmonic spectroscopy of multichannel dynamics in strong-field ionization*. Phys. Rev. Lett. **104**, 213601 (2010). [Cited on page 7.]

Manson ST. *Systematics of zeros in dipole matrix elements for photoionizing transitions: Nonrelativistic calculations*. Phys. Rev. A **31**, 3698–3703 (1985). [Cited on pages 132, 135, and 137.]

Maquet A. *Notes sur fano phys. rev. 124, 1866 (1961)*. Private discussion (2015). [Cited on page 73.]

Maquet A and Taïeb R. *Two-colour IR+XUV spectroscopies: the soft-photon approximation*. Journal of Modern Optics **54**, 1847–1857 (2007). [Cited on page 66.]

Marcus I, L'Huillier A, and al. *Phase studies of fano resonances in helum and argon*. Poster in GRC 2016 (2017). [Cited on page 60.]

Marr G and West J. *Absolute photoionization cross-section tables for helium, neon, argon, and krypton in the vuv spectral regions*. Atomic Data and Nuclear Data Tables **18**, 497 – 508 (1976). [Cited on page 139.]

Mauritsson J, Gaarde MB, and Schafer KJ. *Accessing properties of electron wave packets generated by attosecond pulse trains through time-dependent calculations*. Phys. Rev. A **72**, 013401 (2005). [Cited on pages 6 and 48.]

Mauritsson J, Johnsson P, Mansten E, Swoboda M, Ruchon T, L'Huillier A, and Schafer KJ. *Coherent electron scattering captured by an attosecond quantum stroboscope*. Phys. Rev. Lett. **100**, 073003 (2008). [Cited on page 6.]

Mauritsson J, Remetter T, Swoboda M, Klünder K, L'Huillier A, Schafer KJ, Ghafur O, Kelkensberg F, Siu W, Johnsson P, Vrakking MJJ, Znakovskaya I, Uphues T, Zherebtsov S, Kling MF, Lépine F, Benedetti E, Ferrari F, Sansone G, and Nisoli M. *Attosecond electron spectroscopy using a novel interferometric pump-probe technique*. Phys. Rev. Lett. **105**, 053001 (2010). [Cited on page 6.]

McPherson A, Gibson G, Jara H, Johann U, Luk TS, McIntyre IA, Boyer K, and Rhodes CK. *Studies of multiphoton production of vacuum-ultraviolet radiation in the rare gases*. J. Opt. Soc. Am. B **4**, 595–601 (1987). [Cited on pages 5 and 11.]

Miller DL and Dow JD. *Atomic pseudopotentials for soft X-ray excitations*. Physics Letters A **60**, 16–18 (1977). [Cited on page 133.]

Miller DL, Dow JD, Houlgate RG, Marr GV, and West JB. *The photoionisation of krypton atoms: A comparison of pseudopotential calculations with experimental data for the 4p asymmetry parameter and cross section as a function of the energy of the ejected photoelectrons*. Journal of Physics B: Atomic and Molecular Physics **10**, 3205–3213 (1977). [Cited on page 133.]

Minemoto S, Umegaki T, Oguchi Y, Morishita T, Le AT, Watanabe S, and Sakai H. *Retrieving photorecombination cross sections of atoms from high-order harmonic spectra*. Phys. Rev. A **78**, 061402 (2008). [Cited on pages 139 and 142.]

Miroshnichenko AE, Flach S, and Kivshar YS. *Fano resonances in nanoscale structures*. Rev. Mod. Phys. **82**, 2257–2298 (2010). [Cited on page 72.]

Möbus B, Magel B, Schartner KH, Langer B, Becker U, Wildberger M, and Schmoranzer H. *Measurements of absolute Ar 3s photoionization cross sections*. Physical Review A **47**, 3888–3893 (1993). [Cited on pages 132, 150, 151, and 157.]

Moore LR, Lysaght MA, Parker JS, van der Hart HW, and Taylor KT. *Time delay between photoemission from the 2p and 2s subshells of neon*. Phys. Rev. A **84**, 061404 (2011). [Cited on page 149.]

Morishita T, Watanabe S, and Lin CD. *Attosecond light pulses for probing two-electron dynamics of helium in the time domain*. Phys. Rev. Lett. **98**, 083003 (2007). [Cited on page 6.]

Morlens AS, Balcou P, Zeitoun P, Valentin C, Laude V, and Kazamias S. *Compression of attosecond harmonic pulses by extreme-ultraviolet chirped mirrors*. Opt. Lett. **30**, 1554–1556 (2005). [Cited on page 20.]

Muller H. *Reconstruction of attosecond harmonic beating by interference of two-photon transitions*. Applied Physics B **74**, s17–s21 (2002). [Cited on pages 5, 37, 47, and 48.]

Nicolaides CA and Beck DR. *The variational calculation of energies and widths of resonances*. Physics Letters A **65**, 11 – 12 (1978). [Cited on page 166.]

Ott C, Kaldun A, Raith P, Meyer K, Laux M, Evers J, Keitel CH, Greene CH, and Pfeifer T. *Lorentz meets fano in spectral line shapes: A universal phase and its laser control*. Science **340**, 716–720 (2013)a. [Cited on page 6.]

Ott C, Kaldun A, Raith P, Meyer K, Laux M, Evers J, Keitel CH, Greene CH, and Pfeifer T. *Lorentz meets fano in spectral line shapes: A universal phase and its laser control*. Science **340**, 716–720 (2013)b. [Cited on pages 104 and 105.]

Ott C, Kaldun A, Argenti L, Raith P, Meyer K, Laux M, Zhang Y, Blättermann A, Hagstotz S, Ding T, Heck R, Madroñero J, Martín F, and Pfeifer T. *Reconstruction and control of a time-dependent two-electron wave packet*. Nature **516**, 374–8 (2014). [Cited on pages 82 and 110.]

Palatchi C, Dahlström JM, Kheifets AS, Ivanov IA, Canaday DM, Agostini P, and Dimauro LF. *Atomic delay in helium , neon , argon and*. Journal of Physics B: Atomic, Molecular and Optical Physics **47**, 245003. [Cited on pages 139, 140, 142, and 149.]

Paul PM, Toma ES, Breger P, Mullot G, Augé F, Balcou P, Muller HG, and Agostini P. *Observation of a train of attosecond pulses from high harmonic generation*. Science **292**, 1689–1692 (2001). [Cited on pages 5, 6, 37, 47, 48, and 57.]

Pi Lw and Landsman AS. *Attosecond Time Delay in Photoionization of Noble-Gas and Halogen Atoms*. Applied Sciences **8**, 322 (2018). [Cited on page 165.]

Platzer D. *master thesis : Ligne de lumière attoseconde pour la spectroscopie de photo-ionisation*. (2017). [Cited on pages 52 and 55.]

Popmintchev T, Chen MC, Bahabad A, Gerrity M, Sidorenko P, Cohen O, Christov IP, Murnane MM, and Kapteyn HC. *Phase matching of high harmonic generation in the soft and hard x-ray regions of the spectrum*. Proceedings of the National Academy of Sciences **106**, 10516–10521 (2009). [Cited on page 15.]

Popmintchev T, Chen MC, Popmintchev D, Arpin P, Brown S, Ališauskas S, Andriukaitis G, Balčiunas T, Mücke OD, Pugzlys A, Baltuška A, Shim B, Schrauth SE, Gaeta A, Hernández-García C, Plaja L, Becker A, Jaron-Becker A, Murnane MM, and Kapteyn HC. *Bright coherent ultrahigh harmonics in the kev x-ray regime from mid-infrared femtosecond lasers*. Science **336**, 1287–1291 (2012). [Cited on page 5.]

Popmintchev T., Chen M. APMMKHjNviymNdnuh. *The attosecond nonlinear optics of bright coherent x-ray generation*. [Cited on page 15.]

Roedig CA. *Application of Strong Field Physics Techniques to X-Ray Free Electron Laser Science*. (2012). [Cited on page 57.]

Rossi G, Lindau I, Braicovich L, and Abbati I. *Cooper-minimum effects in the photoionization cross sections of 4d and 5d electrons in solid compounds*. Phys. Rev. B **28**, 3031–3042 (1983). [Cited on page 132.]

Ruchon T and Camper A. *Notes on attosecond pulse profile measurements with the RABBIT technique*. UVX 2012 - 11e Colloque sur les Sources Cohérentes et Incohérentes UV, VUV et X ; Applications et Développements Récents **01014**, 01014 (2013). [Cited on page 157.]

Ruchon T, Hauri CP, Varjú K, Mansten E, Swoboda M, López-Martens R, and L'Huillier A. *Macroscopic effects in attosecond pulse generation*. New Journal of Physics **10**, 025027 (2008). [Cited on page 26.]

Saha S, Mandal A, Jose J, Varma HR, Deshmukh PC, Kheifets AS, Dolmatov VK, and Manson ST. *Relativistic effects in photoionization time delay near the Cooper minimum of noble-gas atoms*. Physical Review A - Atomic, Molecular, and Optical Physics **90**, 1–9 (2014). [Cited on pages 133, 169, and 170.]

Salières P, L'Huillier A, and Lewenstein M. *Coherence control of high-order harmonics*. Phys. Rev. Lett. **74**, 3776–3779 (1995). [Cited on pages 21, 26, and 97.]

Salières P and Lewenstein M. *Generation of ultrashort coherent xuv pulses by harmonic conversion of intense laser pulses in gases: towards attosecond pulses*. Measurement Science and Technology **12**, 1818 (2001). [Cited on page 16.]

Salières P, Maquet A, Haessler S, Caillat J, and Taïeb R. *Imaging orbitals with attosecond and Ångström resolutions: toward attochemistry?* Reports on Progress in Physics **75**, 062401 (2012). [Cited on page 5.]

Samson J and Stolte W. *Precision measurements of the total photoionization cross-sections of helium, neon, argon, krypton, and xenon*. Journal of Electron Spectroscopy and Related Phenomena **123**, 265 – 276 (2002). [Cited on pages 117, 132, 150, 151, and 157.]

Samson JaR. *The Measurement of the Photoionization Cross Sections of the Atomic Gases*. Advances in Atomic and Molecular Physics **2**, 177–261 (1966). [Cited on page 115.]

Samson JAR and Gardner JL. *Photoionization cross sections of the outer s-subshell electrons in the rare gases*. Phys. Rev. Lett. **33**, 671–673 (1974). [Cited on pages 132, 139, 140, and 150.]

Samson JAR, Lyn L, Haddad GN, and Angel GC. *Recent progress on the measurement of absolute photoionization cross sections*. Journal de Physique IV **1**, C1–99 (1991). [Cited on page 132.]

Sansone G, Benedetti E, Calegari F, Vozzi C, Avaldi L, Flammini R, Poletto L, Villoresi P, Altucci C, Velotta R, Stagira S, De Silvestri S, and Nisoli M. *Isolated single-cycle attosecond pulses*. Science **314**, 443–446 (2006). [Cited on page 5.]

Sansone G, Kelkensberg F, Pérez-Torres JF, Morales F, Kling MF, Siu W, Ghafur O, Johnsson P, Swoboda M, Benedetti E, Ferrari F, Lépine F, Sanz-Vicario JL, Zherebtsov S, Znakovskaya I, Lhuillier A, Ivanov MY, Nisoli M, Martín F, and Vrakking MJJ. *Electron localization following attosecond molecular photoionization*. Nature **465**, 763–766 (2010). [Cited on page 6.]

Schafer KJ, Yang B, DiMauro LF, and Kulander KC. *Above threshold ionization beyond the high harmonic cutoff*. Phys. Rev. Lett. **70**, 1599–1602 (1993). [Cited on pages 5 and 11.]

Schoun SB. *Thesis: Attosecond High-Harmonic Spectroscopy of Atoms and Molecules Using Mid-Infrared Sources*. (2015). [Cited on pages 14 and 138.]

Schoun SB, Chirla R, Wheeler J, Roedig C, Agostini P, Dimauro LF, Schafer KJ, and Gaarde MB. *Attosecond pulse shaping around a cooper minimum*. Physical Review Letters (2014). [Cited on pages 139, 140, 142, and 143.]

Schultze M, Fieß M, Karpowicz N, Gagnon J, Korbman M, Hofstetter M, Neppl S, Cavalieri AL, Komninos Y, Mercouris T, Nicolaides CA, Pazourek R, Nagele S, Feist J, Burgdörfer J, Azzeer AM, Ernstorfer R, Kienberger R, Kleineberg U, Goulielmakis E, Krausz F, and Yakovlev VS. *Delay in photoemission*. Science **328**, 1658–1662 (2010). [Cited on page 149.]

Schultze M, Ramasesha K, Pemmaraju C, Sato S, Whitmore D, Gandman A, Prell JS, Borja LJ, Prendergast D, Yabana K, Neumark DM, and Leone SR. *Attosecond band-gap dynamics in silicon*. Science **346**, 1348–1352 (2014). [Cited on page 4.]

Shan B and Chang Z. *Dramatic extension of the high-order harmonic cutoff by using a long-wavelength driving field*. Phys. Rev. A **65**, 011804 (2001). [Cited on page 15.]

Shiner AD, Trallero-Herrero C, Kajumba N, Bandulet HC, Comtois D, Légaré F, Giguère M, Kieffer JC, Corkum PB, and Villeneuve DM. *Wavelength scaling of high harmonic generation efficiency*. Phys. Rev. Lett. **103**, 073902 (2009). [Cited on page 15.]

Singh R, Cao W, Al-Naib I, Cong L, Withayachumnankul W, and Zhang W. *Ultrasensitive terahertz sensing with high-q fano resonances in metasurfaces*. Applied Physics Letters **105**, 171101 (2014). [Cited on page 72.]

Smith F. *Lifetime matrix in collision theory*. Phys. Rev. (1960). [Cited on page 34.]

Sola IJ, Mével E, Elouga L, Constant E, Strelkov V, Poletto L, Villoresi P, Benedetti E, Caumes JP, Stagira S, Vozzi C, Sansone G, and Nisoli M. *Controlling attosecond electron dynamics by phase-stabilized polarization gating*. Nature Physics (2006). [Cited on pages 5 and 6.]

Stener M, Alti GD, Fronzoni G, and Decleva P. *Tdlda calculations of photoionization cross-section and asymmetry parameter profiles of alkaline-earth atoms*. Chemical Physics **222**, 197 – 213 (1997). [Cited on page 164.]

Swarts CA, Miller DL, and Dow JD. *Comparison of theoretical calculations of angular distributions of photoelectrons emitted from rare-gas atoms*. Phys. Rev. A **19**, 734–740 (1979). [Cited on page 133.]

Swoboda M, Dahlström JM, Ruchon T, Johnsson P, Mauritsson J, L'Huillier A, and Schafer KJ. *Intensity dependence of laser-assisted attosecond photoionization spectra*. Laser Physics **19**, 1591–1599 (2009). [Cited on pages 104, 108, and 109.]

Tate J, Auguste T, Muller HG, Salières P, Agostini P, and DiMauro LF. *Scaling of wave-packet dynamics in an intense midinfrared field*. Phys. Rev. Lett. **98**, 013901 (2007). [Cited on page 15.]

Tehlar, Andres M Kraus PWHJ. *Probing electronic dynamics during photochemical reactions.* (2013). [Cited on page 7.]

Tong XM and Lin CD. *Double photoexcitation of he atoms by attosecond xuv pulses in the presence of intense few-cycle infrared lasers*. Phys. Rev. A **71**, 033406 (2005). [Cited on page 6.]

Tzallas P, Charalambidis D, Papadogiannis NA, Witte K, and Tsakiris GD. *Direct observation of attosecond light bunching*. Nature **426**, 267–271 (2003). [Cited on page 5.]

Uiberacker M, Uphues T, Schultze M, Verhoef AJ, Yakovlev V, Kling MF, Rauschenberger J, Kabachnik NM, Schröder H, Lezius M, Kompa KL, Muller HG, Vrakking MJ, Hendel S, Kleineberg U, Heinzmann U, Drescher M, and Krausz F. *Attosecond real-time observation of electron tunnelling in atoms*. Nature **446**, 627–632 (2007). [Cited on page 6.]

Varjú K, Mairesse Y, Carré B, Gaarde MB, Johnsson P, Kazamias S, López-Martens R, Mauritsson J, Schafer KJ, Balcou P, L'huillier A, and Salières P. *Frequency chirp of harmonic and attosecond pulses*. Journal of Modern Optics **52**, 379–394 (2005). [Cited on pages 22, 26, and 97.]

Véniard V, Taïeb R, and Maquet A. *Two-Color multiphoton ionization of atoms using High-Order harmonic radiation*. Phys. Rev. Lett. **74**, 4161 (1995). [Cited on page 37.]

Véniard V, Taïeb R, and Maquet A. *Phase dependence of (n+ 1)-color (n> 1) ir-uv photoionization of atoms with higher harmonics*. Physical Review A **54**, 721 (1996). [Cited on pages 47 and 65.]

Vos J, Cattaneo L, Patchkovskii S, Zimmermann T, Cirelli C, Lucchini M, Kheifets A, Landsman A, and Keller U. *Orientation-dependent stereo wigner time delay and electron localization in a small molecule*. Science **360**, 1326–1330 (2018). [Cited on page 149.]

Vozzi C, Nisoli M, Caumes JP, Sansone G, Stagira S, De Silvestri S, Vecchiocattivi M, Bassi D, Pascolini M, Poletto L, Villoresi P, and Tondello G. *Cluster effects in high-order harmonics generated by ultrashort light pulses*. Applied Physics Letters **86**, 111121 (2005). [Cited on page 7.]

Vozzi C, Negro M, Calegari F, Sansone G, Nisoli M, De Silvestri S, and Stagira S. *A generalized approach to molecular orbital tomography*. Springer Proceedings in Physics **125**, 277–281 (2012). [Cited on page 7.]

Wagner NL, Wüest A, Christov IP, Popmintchev T, Zhou X, Murnane MM, and Kapteyn HC. *Monitoring molecular dynamics using coherent electrons from high harmonic generation*. Proceedings of the National Academy of Sciences **103**, 13279–13285 (2006). [Cited on page 7.]

Wahlström CG, Larsson J, Persson A, Starczewski T, Svanberg S, Salieres P, Balcou P, and L'Huillier A. *High-order harmonic generation in rare gases with an intense short-pulse laser*. Physical Review A **48**, 4709 (1993). [Cited on page 139.]

Wahlström CG, Larsson J, Persson A, Starczewski T, Svanberg S, Salières P, Balcou P, and L'Huillier A. *High-order harmonic generation in rare gases with an intense short-pulse laser*. Phys. Rev. A **48**, 4709–4720 (1993). [Cited on page 97.]

Weber SJ, Manschwetus B, Billon M, Böttcher M, Bougeard M, Breger P, Géléoc M, Gruson V, Lin N, Picard YJ, Ruchon T, Salières P, Carré B, Weber SJ, Manschwetus B, Billon M, Böttcher M, Bougeard M, and Breger P. *Flexible attosecond beamline for high harmonic spectroscopy and XUV / near-IR pump probe experiments requiring long acquisition times Flexible attosecond beamline for high harmonic spectroscopy and XUV / near-IR pump probe experiments requiring long acqui*. **033108**, 1–12 (2015). [Cited on pages 51 and 53.]

Wickenhauser M, Burgdörfer J, Krausz F, and Drescher M. *Time resolved fano resonances*. Physical Review Letters **94**, 1–4 (2005). [Cited on pages 6 and 101.]

Wigner E. *On the quantum correction for thermodynamic equilibrium*. Phys. Rev. **40**, 749–759 (1932). [Cited on page 103.]

Wigner E. *Lower limit for the energy derivative of the scattering phase shift*. Phys. Rev. (1955). [Cited on pages 27, 34, and 149.]

Williamson RC. *The ionization of potassium vapor by light*. Phys. Rev. **21**, 107–121 (1923). [Cited on page 131.]

Worner HJ, Niikura H, Bertrand JB, Corkum PB, and Villeneuve DM. *Observation of electronic structure minima in high-harmonic generation*. Physical Review Letters **102**, 1–4 (2009). [Cited on pages 133, 135, 138, 139, 140, 142, and 144.]

Wörner HJ, Bertrand JB, Kartashov DV, Corkum PB, and Villeneuve DM. *Following a chemical reaction using high-harmonic interferometry*. Nature **466**, 604–607 (2010). [Cited on page 7.]

Yeh J and Lindau I. *Atomic subshell photoionization cross sections and asymmetry parameters: 1 z 103*. Atomic Data and Nuclear Data Tables **32**, 1 – 155 (1985). [Cited on page 132.]

Zaïr A, Holler M, Guandalini A, Schapper F, Biegert J, Gallmann L, Keller U, Wyatt AS, Monmayrant A, Walmsley IA, Cormier E, Auguste T, Caumes JP, and Salières P. *Quantum path interferences in high-order harmonic generation*. Phys. Rev. Lett. **100**, 143902 (2008). [Cited on page 23.]

Zangwill A and Liberman D. *A nonrelativistic program for optical response in atoms using a time-dependent local density approximation*. Computer Physics Communications **32**, 63 – 73 (1984). [Cited on page 164.]

Zangwill A and Soven P. *Density-functional approach to local-field effects in finite systems: Photoabsorption in the rare gases*. Phys. Rev. A **21**, 1561–1572 (1980)a. [Cited on page 164.]

Zangwill A and Soven P. *Density-functional approach to local-field effects in finite systems: Photoabsorption in the rare gases*. Phys. Rev. A **21**, 1561–1572 (1980)b. [Cited on page 164.]

Zhang H, Rolles D, Bozek JD, and Berrah N. *Photoionization of argon clusters in the ar 3s $\rightarrow$ n p rydberg resonance region*. Journal of Physics B: Atomic, Molecular and Optical Physics **42**, 105103 (2009). [Cited on pages 115 and 117.]

Zhao J and Lein M. *Determination of ionization and tunneling times in high-order harmonic generation*. Phys. Rev. Lett. **111**, 043901 (2013). [Cited on page 18.]

Zhao ZX and Lin CD. *Theory of laser-assisted autoionization by attosecond light pulses*. Phys. Rev. A **71**, 060702 (2005). [Cited on page 6.]

Zürch M, Chang HT, Borja LJ, Kraus PM, Cushing SK, Gandman A, Kaplan CJ, Oh MH, Prell JS, Prendergast D, Pemmaraju CD, Neumark DM, and Leone SR. *Direct and simultaneous observation of ultrafast electron and hole dynamics in germanium*. Nature Communications **8** (2017). [Cited on pages 119 and 176.]

Titre : Spectroscopie attoseconde : Étude de la dynamique de photoionisation de gaz atomiques au voisinage des résonances

Mots clés : Attoseconde, Photoionisation, Dynamique, Résonances d'autoionisation, Minimum de Cooper

Résumé: L'interaction des puissantes impulsions laser avec les gaz atomiques et moléculaires entraîne l'émission de flashs exceptionnellement brefs de lumière XUV grâce au processus de génération harmonique d'ordre élevé (GHOE) de la fréquence laser fondamentale. Ce rayonnement ultra-bref, dans la gamme attoseconde (10^{-18} s), permet des investigations détaillées de la dynamique électronique ultra-rapide dans la matière. Le travail de cette thèse consiste à étudier les délais de photoionisation au voisinage de différents types de résonances, en utilisant la technique Rainbow RABBIT. Il s'agit d'une technique interférométrique à deux couleurs (XUV + IR) qui permet d'accéder au temps nécessaire à l'électron pour s'échapper du potentiel atomique avec une haute résolution. Nous nous intéressons particulièrement à deux cas: i) les résonances auto-ionisantes spectralement étroites (dizaines de meV) et ii) les minima de type Cooper ayant une largeur spectrale de quelques eV. L'effet de ces structures de continuum sur la dynamique d'ionisation correspondante est étudié.

Title : Attosecond spectroscopy: Study of the photoionization dynamics of atomic gases close to resonances

Keywords : Attosecond, Photoionization, Dynamics, Autoionization resonances, Cooper minimum

Abstract: The interaction of intense laser pulses with atomic and molecular gases results in exceptionally short bursts of XUV light, through the process of high-order harmonic generation of the fundamental laser frequency. This ultrashort radiation, in the attosecond (10^{-18} s) range, allows detailed investigations of ultrafast electron dynamics in matter. The work of this thesis consists in studying the photoionization delays close to different types of resonances, using the Rainbow RABBIT technique. This is a two-color interferometric technique (XUV + IR) that allows access to the time required for the electron to escape the atomic potential with high resolution. We are particularly interested in two cases: i) autoionizing resonances which are spectrally narrow (tens of meV) and ii) Cooper-type minima which have a spectral width of some eV. The effect of these continuum structures on the corresponding ionization dynamics is studied.

Université Paris-Saclay
Espace Technologique / Immeuble Discovery
Route de l'Orme aux Merisiers RD 128 / 91190 Saint-Aubin, France